THE UNIVERSITY *of* EDINBURGH

Characterising Weather and Rotation on Substellar Worlds

Johanna Maria Catherine Vos

Doctor of Philosophy
The University of Edinburgh
November 2018

Abstract

Photometric variability monitoring is sensitive to atmospheric inhomogeneities as they rotate in and out of view, and is a key probe of atmospheric features in brown dwarfs and giant exoplanets. The population of young, low-gravity brown dwarfs are an excellent test bed for characterising the gravity dependence of brown dwarf atmospheres while also providing a critical analogue to the population of directly-imaged planets. This thesis aims to expand our current understanding of the variability of brown dwarfs with a focus on the role of gravity on variability properties. In Chapter 2 I present the detection of photometric variability in the L7 planetary-mass object PSO 318.5–22, as well as subsequent multi-wavelength ground-based and space-based monitoring. I use the followup observations to measure the rotational period of PSO 318.5–22 and to investigate the horizontal and vertical structure of its atmosphere. In Chapter 3 I supplement the existing brown dwarf variability data in the literature with new rotational velocities to reveal relations between inclination angle, variability amplitude and colour. These new relations probe the latitudinal cloud structure of brown dwarfs for the first time and will inform future searches for variability on both free-floating exoplanets and directly-imaged companions. In Chapter 4 I present *Spitzer* monitoring of the three lowest-mass members of the AB Doradus moving group. I report mid-IR variability in two late-L exoplanet analogues, W0047 and 2M2244 and place upper limits on the variability of the T5.5 planetary-mass object SDSS 1110. I measure the rotational periods and inclination angles of W0047 and 2M2244 and find that they are consistent with the relations reported in Chapter 3 for the field dwarf sample. Finally, in Chapter 5 I present the first large survey for photometric variability in young low-gravity brown dwarfs. Theory and observations have shown that gravity plays an important role in the atmospheric properties of L and T types objects. Surface gravity significantly affects the height at which condensate clouds form in the atmosphere (Marley et al., 2012) and thus we can expect that gravity will have an effect on variability. I detect variability in 6

low-gravity brown dwarfs, 4 of which are reported in this thesis for the first time. Focusing on the L0-L8/5 objects in the survey, I find a variability occurrence rate of 30^{+16}_{-8}%. I reanalyse the results of Radigan (2014) and find a variability occurrence rate of 11^{+13}_{-4}% for the field dwarf sample. This is the first quantitative indication that the young objects are more likely to be variable than their higher mass counterparts. The work presented in this thesis has provided crucial insight into the role of gravity on variability properties, and acts as a key pathfinder for future studies of variability on directly-imaged planets.

Lay Summary

Brown dwarfs bridge the gap between the lowest mass stars and giant exoplanets. They are often referred to as 'failed stars', their low masses resulting in core temperatures insufficient to sustain hydrogen burning. As a result they are born hot and spend their lives cooling and dimming. Their existence was first predicted independently by Kumar (1963) and Hayashi & Nakano (1963), but it was over 30 years later that the first reliable detection of the brown dwarf companion Gliese 229B was announced by Nakajima et al. (1995). Coincidentally, the first detection of an extrasolar giant planet was announced on the same day by Mayor & Queloz (1995). An avalanche of discoveries followed in both fields, with photometric searches such as the 2 Micron All Sky Survey (2MASS), the optical/far-red Sloan Digital Sky Survey (SDSS) and the DEep Near Infrared Survey (DENIS) revealing a large population of brown dwarfs. These discoveries have led to the definition of three new spectral classes – the L dwarfs, T dwarfs and Y dwarfs. With temperatures ranging from $\sim$ 2000 down to 300 K, the brown dwarfs overlap with the temperature range of the directly-imaged planets. Consequently, brown dwarf atmospheres should have similar atmospheric properties and can thus provide insight into the expected photometric and spectroscopic properties of the directly-imaged exoplanets.

At temperatures below $\sim$ 2200 K, brown dwarfs enter the L spectral type sequence, which is characterised by the formation of condensate clouds composed of iron silicates and metal oxides in the upper atmosphere. As the dwarf continues to cool below temperatures of $\sim$ 1300 K, these clouds gravitationally settle below the photosphere, marking the beginning of the T spectral sequence. The formation, evolution and eventual dispersal of these condensate clouds in L and T brown dwarfs has emerged as one of the most interesting topics in substellar physics. With temperatures $<$ 500 K, the recently discovered Y dwarfs represent the coldest spectral class. There are currently only 24 known Y dwarfs, so the Y

spectral sequence has not yet been well-defined (Leggett et al., 2017).

The rapid rotation of brown dwarfs combined with a potentially inhomogeneous cloud deck has long motivated searches for rotationally modulated brightness fluctuations, or photometric variability. The best example of rotationally-induced photometric variability is caused by the Great Red Spot on Jupiter. Gelino & Marley (2000) studied the photometric variability of an unresolved Jupiter due to its rotation. The Great Red Spot, which appears as a dark patch at 4.78 μm, produces a 0.2 mag peak-to-peak modulation in Jupiter's light curve as it rotates in and out of view. Variability surveys of brown dwarfs at near-IR and mid-IR wavelengths have been carried out, revealing ubiquitous variability in L and T type brown dwarfs (Buenzli et al., 2014; Metchev et al., 2015), with evidence for higher variability amplitudes and higher variability occurrence rates across the L/T transition (Radigan et al., 2014). Perhaps the most compelling evidence for an inhomogeneous atmosphere came from Crossfield et al. (2014), who used Doppler imaging to produce a 2D global map of a T2.5 brown dwarf, revealing patches of brighter and darker regions best explained by patchy clouds in the atmosphere.

While massive field brown dwarfs have now been studied in detail, the variability properties of planetary-mass objects remain relatively unstudied. In recent years observations of directly-imaged planets and isolated planetary-mass objects have revealed a link between low surface gravity and a delay in the L/T transition. Specifically, the spectral type of low-gravity brown dwarfs (such as the 8.3 $M_{\rm Jup}$ L7 dwarf PSO J318.5338 − 22.8603, Liu et al., 2013), and directly-imaged exoplanets (such as the HR8799 system, Marois et al., 2008) tend to be classified with spectral types earlier than their temperatures would have predicted. L type low-gravity objects also become much redder in the near-IR and mid-IR than their higher gravity field brown dwarf counterparts (Liu et al., 2016). These discrepancies may be explained by the persistence of dusty clouds at lower temperatures as well as non-equilibrium chemistry (Barman et al., 2011; Marley et al., 2012), likely to result from the lower surface gravity of young objects. Surface gravity significantly affects the height at which cloud species form in the atmosphere of free-floating and companion brown dwarfs and exoplanets (Marley et al., 2012) and thus it can be expected that surface gravity will have a significant effect on variability. This thesis aims to investigate the role of gravity in the variability properties of free-floating objects.

The population of young, low-gravity brown dwarfs are an excellent test bed

for characterising the gravity dependence of brown dwarf atmospheres while also providing a critical analogue to the population of directly-imaged planets. This thesis aims to expand our current understanding of the variability of brown dwarfs, particularly the low-gravity "exoplanet analogues". In Chapter 2 we report the detection of photometric variability in a planetary-mass object for the first time for the free-floating exoplanet analogue PSO 318.5–22. We also present subsequent multi-wavelength ground-based and space-based monitoring of PSO 318.5–22, which enable us to measure its rotational period and to study the horizontal and vertical structure of its atmosphere. In Chapter 3 we supplement the existing brown dwarf variability data in the literature with new rotational velocities to reveal relations between inclination angle, variability amplitude and colour. These new relations probe the latitudinal cloud structure for the first time and will inform future searches for variability on free-floating exoplanets and the directly-imaged companions. In Chapter 4 we present *Spitzer* monitoring of the three lowest-mass members of the AB Doradus moving group. We detect mid-IR variability in two late-L exoplanet analogues, W0047 and 2M2244+20 and place upper limits on the variability amplitude of the T5.5 object SDSS1110+01. Finally, in Chapter 5 we present the first large survey for photometric variability in exoplanet analogues. In this chapter we find the first qualitative indication that the exoplanet analogues are more likely to be variable than their higher mass, field dwarf counterparts, likely a result of their lower surface gravity.

Declaration

I declare that this thesis was composed by myself, that the work contained herein is my own except where explicitly stated otherwise in the text, and that this work has not been submitted for any other degree or professional qualification except as specified.

Chapter 2 consists of sections that have been published in Biller, Vos et al. (2015; 2018) and has been accepted for publication in Vos et al. (2018b).
Chapter 3 was published in Vos et al. (2017).
Chapter 4 was published in Vos et al. (2018).
Chapter 5 has been accepted for publication in Vos et al. (2018b).

(*Johanna Maria Catherine Vos, November 2018*)

Acknowledgements

I have been very fortunate during my PhD to have met so many people who were willing to guide and support me along the way. First and foremost, I would like to thank my supervisor Dr. Beth Biller for being the best supervisor I could have hoped for. From our very first meetings, her scientific expertise and thoughtful advice have been invaluable. Many thanks go to my collaborators, whose insights have greatly improved various observing proposals and papers over the years. In particular I would like to thank Katelyn Allers, whose boundless enthusiasm is both infectious and inspiring.

I would like to thank everyone at the Observatory, for creating such a vibrant place to conduct research. In particular, I would like to thank my fellow PhD students, past and present, for creating such a welcoming, supportive and exciting environment.

I would also like to thank my oldest and dearest friends Karina, Clare, Orla, Brigid and Kathleen, who have cheered me on from various places around the world. I am also so grateful to all the great friends I've made during my time in Edinburgh, I feel very lucky to have landed on my feet so quickly. Special thanks also go to the brilliant ballet teachers I've met during the past few years, whose challenging classes and beautiful choreography were the highlight of many long days.

None of this would have been possible without the constant encouragement of my family. I would like to thank Han for keeping a close eye on my progress from the very beginning, Mary for helping me to pursue every mad idea I have ever thought up, and Dave for refusing to accept the fundamental laws of physics without a debate.

Last but not least, I would like to thank Jack for his endless kindness, support and understanding, and for always putting a smile back on my face after a long day. I count myself very lucky to have you by my side.

"We are all in the gutter but some of us are looking at the stars."

–Oscar Wilde, Lady Windermere's Fan

Contents

Abstract i

Lay Summary iii

Declaration vii

Acknowledgements ix

Contents xiii

List of Figures xix

List of Tables xxv

1 Introduction 1

1.1 Brown Dwarf Evolution 1

1.1.1 Luminosity 1

1.1.2 Radius 3

1.1.3 Rotation 4

1.2 The L–T Spectral Sequence 5

1.3 Brown Dwarf Atmospheres 7

1.3.1 Energy Transport 8

1.3.2 Condensates 10

1.3.3 Cloud Models of Brown Dwarfs 11
1.3.4 Cloud-Free Models of Brown Dwarfs 15
1.4 Photometric Variability Monitoring 16
1.4.1 First Variability Detections 17
1.4.2 Variability Surveys 18
1.4.3 Simultaneous Multi-Wavelength Variability Monitoring 20
1.4.4 Surface-Mapping Techniques 25
1.5 Atmospheric Dynamics in Brown Dwarf Atmospheres 29
1.6 Directly-Imaged Planets 31
1.6.1 Direct Imaging Surveys 32
1.6.2 Properties of the Directly Imaged Planets 33
1.7 Low-Gravity Brown Dwarfs 34
1.7.1 Membership in Young Moving Groups 34
1.7.2 Spectral Signatures of Youth 35
1.7.3 Low-Gravity Brown Dwarfs as Exoplanet Analogues 38
1.7.4 Variability Studies of Exoplanet Analogues 39
1.8 Outline of Chapters 2-5 40

2 Variability in a Young, L/T Transition Planetary-Mass Object 41

2.1 Abstract 41
2.2 Introduction 42
2.3 Observations and Data Reduction 43
2.4 NTT/SofI Lightcurves of PSO J318.5–22 45

2.5 NTT/SofI Followup of PSO J318.5–22 47

2.5.1 Measuring the Rotational Period using MCMC..... 48

2.6 Simultaneous *HST/Spitzer* Multi-Wavelength Characterisation of PSO 318.5–22..... 51

2.6.1 Observations..... 51

2.6.2 *Spitzer* Data Reduction and Lightcurve Extraction..... 52

2.6.3 *HST* Data Reduction and Lightcurve Extraction 54

2.6.4 Results..... 54

2.7 Discussion 58

2.7.1 Phase Shifts 58

2.7.2 Amplitudes 58

2.7.3 Rotation..... 60

2.8 Conclusions 62

3 The Viewing Geometry of Brown Dwarfs Influences Their Observed Colours and Variability Amplitudes 63

3.1 Abstract 63

3.2 Introduction 64

3.3 The Sample 66

3.3.1 Low-Gravity Brown Dwarfs..... 71

3.3.2 Sample Selection Biases 71

3.4 Data and Observations..... 72

3.5 Data Reduction Methods..... 75

3.5.1 Determining Rotational Velocities 75

3.5.2 Calculating Inclination Angles 77

3.6 Results and Discussion 79
3.6.1 Effects of Inclination on Variability Amplitude 79
3.6.2 Relation between Period and Variability Amplitude 84
3.6.3 Spearman and Kendall Correlation Coefficients 85
3.6.4 Investigating Colour Anomalies of the Sample 88
3.7 Summary and Conclusions 93

4 Variability of the Lowest Mass Objects in the AB Doradus Moving Group 95

4.1 Abstract 95
4.2 Introduction 96
4.3 Keck NIRSPEC High Dispersion Spectroscopy 98
4.3.1 Determining Radial and Rotational Velocities 100
4.3.2 2M2244+20 Membership in AB Doradus 102
4.3.3 The Physical Properties of W0047 and 2M2244 102
4.4 Spitzer and WFCAM Photometry 103
4.4.1 Identification of Variables 105
4.4.2 W0047 105
4.4.3 2M2244 110
4.4.4 SDSS1110 122
4.5 The Inclination Angles of W0047 and 2M2244 124
4.6 Conclusions 127

5 The First Search for Weather Patterns in Exoplanet Analogues 129

5.1 Abstract 129
5.2 Introduction 130

5.3 Sample Selection 132
5.4 Observations and Data Reduction 133
5.4.1 NTT SofI 133
5.4.2 UKIRT WFCAM 137
5.4.3 Lightcurve Analysis 137
5.4.4 Independent Reduction of NTT/SofI Data 138
5.4.5 Identification of Variables 139
5.5 Possible Systematics 143
5.6 Sensitivity to Variability Signals 144
5.7 Significant Detections of Variability 144
5.8 Non-detections 162
5.9 Assessing Evidence of Youth in the Sample 164
5.9.1 Analysing Sample Spectra 164
5.9.2 Assessing Group Membership 167
5.10 Variability Statistics 176
5.11 Follow-up Observations of Variable Objects 182
5.12 Conclusions 184

6 Conclusions 185

6.1 Summary 185
6.1.1 Chapter 2 185
6.1.2 Chapter 3 186
6.1.3 Chapter 4 187
6.1.4 Chapter 5 188

6.2 Future Work 189

6.2.1 Variability Monitoring of Directly-Imaged Planets with JWST 190

6.2.2 Probing Cooler Atmospheres with *JWST* 190

6.2.3 Rotation Rates of Young Free-Floating Objects 191

A Chapter 5 Appendix: Lightcurves and Sensitivity Plots for Non-Variable Objects 193

Bibliography 247

List of Figures

1.1 Evolution of luminosity of isolated solar-metallicity low-mass stars and substellar-mass objects plotted against age. 2

1.2 Evolution of radius of isolated solar-metallicity low-mass stars and substellar-mass objects plotted against age. 3

1.3 Rotational periods of brown dwarfs as a function of age. 4

1.4 L dwarf spectral sequence. 6

1.5 T dwarf spectral sequence. 7

1.6 Schematic depiction of a thermal structure model. 9

1.7 Condensation curves for a variety of species. 10

1.8 Colour-magnitude diagram showing M, L and T spectral type brown dwarfs. 14

1.9 The lightcurves of SIMP 0136+09. 17

1.10 Results from Radigan et al. (2014) survey for photometric variability in field L and T dwarfs. 18

1.11 Results from Metchev et al. (2015) *Spitzer* survey for photometric variability on L and T spectral type brown dwarfs. 20

1.12 Period-folded lightcurves of 2M2228-43 from Buenzli et al. (2012) 22

1.13 Phase shifts of the observed 2M2228 lightcurves as a function of the dominantly probed pressure from Buenzli et al. (2012). 23

1.14 Illustration of possible cloud structure consistent with spectroscopic observations of SIMP0136 and 2M2139. 24

1.15 Surface map of Luhman 16B obtained from Doppler imaging. . . . 25

1.16 Best-fitting surface maps of 2M2139 from Apai et al. (2013). . . . 27

1.17 Lightcurve and best-fitting *Aeolus* model of the variable brown dwarf 2M1324. 28

1.18 Relative vorticity for three 2D non-divergent simulations on a sphere initialised from small-scale isotropic turbulence. 30

1.19 Directly-imaged companions near and below the deuterium burning limit on the near-infrared colour-magnitude diagram. 33

1.20 Evolutionary tracks of $\log_{10} g$ vs. $T_{\rm eff}$ for brown dwarfs and planetary-mass objects. 36

1.21 Low-resolution spectra showing the IR gravity sensitive features for L3 objects. 37

1.22 Colour-magnitude diagram showing young companions and free-floating, low-gravity objects. 38

2.1 Final binned J_S lightcurve and comparison detrended reference stars from 9 October 2014. 44

2.2 Final binned J_S lightcurve and comparison detrended reference stars from 9 November 2014. 45

2.3 Final binned K_S lightcurve of PSO 318.5–22 and comparison detrended reference stars from 11 November 2014. 46

2.4 Detrended lightcurves of PSO 318.5–22 taken over three consecutive nights of follow-up observations at the NTT. 49

2.5 Posterior distributions obtained from MCMC analysis of NTT/SofI J_S lightcurve. 50

2.6 *Spitzer* and *HST* corrected lightcurves for PSO 318.5–22. 53

2.7 *Spitzer* lightcurve and periodogram of PSO 318.5–22. 55

2.8 Posterior probability distributions of parameters from sinusoid MCMC fits to our *Spitzer* 4.6 μm lightcurve of PSO 318.5–22. 56

2.9 Ratio of minimum and maximum PSO 318.5–22 *HST* spectra binned by 0.05 μm. 59

2.10 Mass plotted against equatorial velocity for young free-floating and companion planetary-mass objects. 61

3.1 Observed spectrum of 2M1507–16 (black) compared to our forward model with best-fit parameters (red). 76

3.2 Variability amplitude plotted against inclination angle for our sample. . . . 80

3.3 Histogram showing the distribution of inclination angles calculated for the sample. . . . 80

3.4 Inclination angle i affects the atmospheric path length travelled from flux originating from a certain depth. . . . 81

3.5 Variability amplitude plotted against inclination angle for *Spitzer* 3.6 μm (triangles) and J-band (circles) field objects in our sample. 82

3.6 Variability amplitude plotted against period for *Spitzer* 3.6 μm and J-band variability detections. . . . 85

3.7 Variability amplitude plotted against period for J-band variability detections. . . . 88

3.8 Variability amplitude plotted against period for *Spitzer* 3.6 μm variability detections. . . . 89

3.9 Colour anomaly plotted against inclination for the sample in Table 3.1. . . . 90

3.10 Amplitude plotted against colour anomaly for J-band variability detections. . . . 91

3.11 Variability amplitude plotted against colour anomaly for *Spitzer* variability detections. . . . 92

3.12 Amplitude plotted against colour anomaly for *Spitzer* variability detections. . . . 93

4.1 The observed spectrum of W0047 compared to our best-fitting forward model. . . . 99

4.2 The observed and best-fitting forward model of 2M2244. . . . 99

4.3 Light curve and periodogram of W0047. . . . 106

4.4 Posterior distributions of parameters of the *Spitzer* lightcurve of W0047. . . . 107

4.5 Light curve and periodogram of simulated *HST* data of W0047. . 108

4.6 Posterior distributions of parameters of the simulated *HST* lightcurve of W0047. . . . 109

4.7 Light curve and periodogram of 2M2244 from Sep 15 2016. . . . 111

4.8 Posterior distributions of parameters of the Fourier model fit to the *Spitzer* Sep 2016 lightcurve of 2M2244 112

4.9 Light curve and periodogram of the Morales-Calderon et al. (2006) observation of 2M2244. 114

4.10 Posterior distributions of parameters of the sinusoid fit to the Morales-Calderon et al. (2006) *Spitzer* lightcurve of 2M2244. . . . 115

4.11 Posterior distributions of parameters of the Fourier model fit to the Morales-Calderon et al. (2006) *Spitzer* lightcurve of 2M2244. . 116

4.12 Radius distributions for 2M2244 from our evolutionary models and calculated assuming a rotational period of $14.0^{+3.5}_{-3.8}$ hr and an inclination angle of 90°. 117

4.13 Measured $v\sin(i)$ distribution for 2M2244 and a $v\sin(i)$ distribution calculated assuming a rotational period of $14.0^{+3.5}_{-3.8}$ hr and an inclination angle of 90°. 118

4.14 UKIRT/WFCAM light curve and periodogram of 2M2244. 120

4.15 Light curve, periodogram and sensitivity plot of SDSS1110. 123

4.16 $(J-K_S)_{\rm 2MASS}$ colour anomaly plotted against the inclination angle for variable brown dwarfs. 126

4.17 *Spitzer* [3.6 μm] variability amplitude plotted against $(J-K_S)_{\rm 2MASS}$ colour anomaly for variable brown dwarfs. 127

5.1 Lightcurves of 2M0103 and PSO-318 reduced and analysed using two methods. 138

5.2 β factor plotted against the photometric error for reference stars and targets for the NTT and UKIRT samples. 140

5.3 Maximum periodogram power plotted against the photometric error for reference stars and targets for the NTT and UKIRT samples. 141

5.4 Maximum periodogram power plotted against colour for reference stars in the NTT sample. 143

5.5 Lightcurves of variable targets (red) compared to a sample of reference stars in the field (blue). 146

5.5 (Continued) Lightcurves of variable targets (red) compared to a sample of reference stars in the field (blue). 147

5.5 (Continued) Lightcurves of variable targets (red) compared to a sample of reference stars in the field (blue). 148

5.5 (Continued) Lightcurves of variable targets (red) compared to a sample of reference stars in the field (blue). 149

5.6 Lightcurve, periodogram and sensitivity plot for variable object 2M0045+16, observed on 2014-11-11. 150

5.7 Lightcurve, periodogram and sensitivity plot for variable object 2M0045+16, observed on 2016-11-13. 151

5.8 Lightcurve, periodogram and sensitivity plot for variable object PSO 071.8–12, observed on 2016-10-18. 152

5.9 Lightcurve, periodogram and sensitivity plot for variable object 2M0501–00, observed on 2014-11-11. 153

5.10 Lightcurve, periodogram and sensitivity plot for variable object 2M0501–00, observed on 2016-10-19. 154

5.11 Lightcurve, periodogram and sensitivity plot for variable object 2M1425–36 observed on 2015-08-17. 155

5.12 Lightcurve, periodogram and sensitivity plot for variable object 2M2002-05, observed on 2016-07-09. 156

5.13 Lightcurve, periodogram and sensitivity plot for variable object PSO 318.5–22 observed on 2014-10-09. 157

5.14 Lightcurve, periodogram and sensitivity plot for variable object PSO 318.5–22 observed on 2014-11-09. 158

5.15 Lightcurve, periodogram and sensitivity plot for variable object PSO 318.5–22 observed on 2014-11-10. 159

5.16 Lightcurve, periodogram and sensitivity plot for variable object 2M2244+20 observed on 2016-07-21. 160

5.17 $J - K_S$ colour-magnitude diagram showing the field brown dwarf population and our full sample of objects showing signs of low-gravity. 173

5.18 $H - K_S$ colour-magnitude diagram showing the field brown dwarf population and our full sample of objects showing signs of low-gravity. 174

5.19 Histogram showing the distribution of spectral types in our final sample of 30 low-gravity brown dwarfs. 176

5.20 Spectral type of variable objects plotted against $(J-K)_{\rm 2MASS}$ colour. 177

5.21 Probability distribution of the variability occurrence rate of young objects. 179

5.22 Probability distribution of the variability occurrence rate of the field brown dwarf population (Radigan, 2014). 179

5.23 Top panel shows probability distributions for the variability occurrence rate of the field brown dwarf sample from Radigan et al. (2014)(blue) and our young sample (red), assuming binomial statistics and a uniform prior. The bottom panel shows the difference between these distributions. We find a 98% probability that the planetary-mass sample has a higher variability occurrence rate than the field brown dwarf sample. 181

A.1 Light curves of targets (red) and reference stars (blue) for non-detections in the survey. 194

A.2 Light curves of targets (red) and reference stars (blue) for bad quality observations. 206

A.3 Lightcurves, periodograms and sensitivity plots for non-variable objects. 208

A.4 Lightcurves, periodograms and sensitivity plots for poor quality observations 242

List of Tables

2.1 NTT/SofI observations of PSO 318.5–22. 43

2.2 NTT/SofI followup observations of PSO 318.5–22. 48

3.1 Variable Brown Dwarfs with Known Periods and Archival Spectra. 68

3.2 Rotational Periods and Peak-to-peak Variability Amplitudes for J-band Variable Brown Dwarfs. 69

3.3 Rotational Periods and Peak-to-peak Variability Amplitudes for *Spitzer* [3.6]μm Variable Brown Dwarfs. 73

3.4 NIRPSEC-7 High-dispersion Observing Information. 74

3.5 Rotational velocities, radial velocities, effective temperatures, and gravities calculated in this study. 78

3.6 Best-fit parameters for Equation 3.1. Best-fit functions for both bands are plotted in Figure 3.5. 82

4.1 Physical properties of W0047 and 2M2244 from the Saumon & Marley (2008) $f_{sed} = 2$ evolutionary model. 102

4.2 Calculated rotational velocities, radial velocities, periods, [3.6 μm] peak-to-peak variability amplitudes and inclination angles for W0047 and 2M2244. 124

5.1 Observing log 135

5.2 Measured first epoch variability amplitudes for variability detections. 161

5.3 Spectral Signatures of Youth in Sample 165

5.4 Kinematic Information of Variability Sample 168

5.5 Moving Group Membership Probabilities 170

5.6 Contingency table showing the number of variability detections and non-detections in the Radigan (2014) survey (field objects) and this survey (low-gravity). 180

Chapter 1

Introduction

1.1 Brown Dwarf Evolution

The theoretical study of brown dwarfs began with work by Kumar (1963) and Hayashi & Nakano (1963), who independently predicted that below a minimum mass of 0.075 $M_{\odot}$, a collapsing star would be halted by electron degeneracy before the onset of hydrogen fusion. Objects with masses below this limiting mass never reach temperatures necessary to ignite and sustain thermonuclear fusion of hydrogen in their cores. Thus, without hydrogen fusion in its core, a brown dwarf steadily cools with time, changing its spectral and photometric appearance as it ages (Burrows et al., 2001).

1.1.1 Luminosity

The basic characteristics of low-mass stars, brown dwarfs and giant planets are perhaps best illustrated by considering their evolution in luminosity as a function of time. Figure 1.1 shows evolutionary luminosity tracks for solar metallicity objects (Burrows et al., 2001). Low-mass stars are shown in blue, brown dwarfs with masses above the hydrogen-burning limit ($> 13\ M_{\rm Jup}$) are shown in green and objects with masses below the deuterium-burning limit ($< 13\ M_{\rm Jup}$) are shown in red. After $10^{8.3} - 10^{9.5}$ yr, main sequence stars stabilise at a luminosity for which the power derived from thermonuclear burning in the core compensates for the photon luminosity losses from the surface. Brown dwarfs on the other

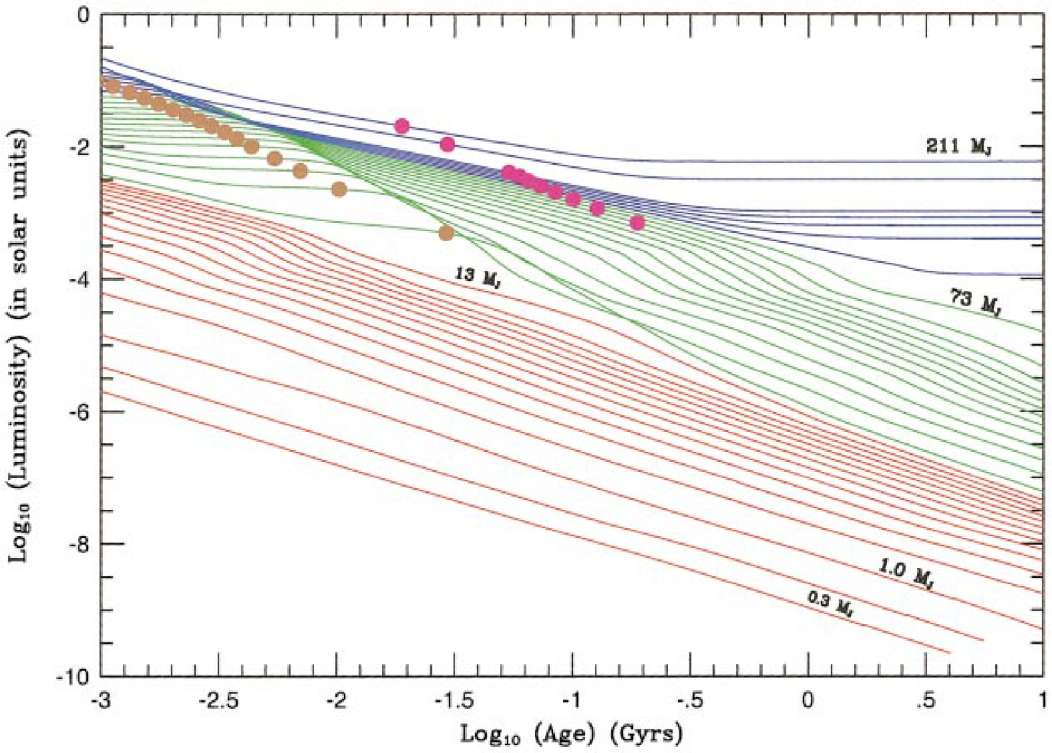

Figure 1.1 Evolution of luminosity of isolated solar-metallicity low-mass stars and substellar-mass objects plotted against age. Stars are shown in blue, brown dwarfs with masses above $13M_{\rm Jup}$ are shown in green and brown dwarfs with masses below $13M_{\rm Jup}$ and giant exoplanets are shown in red. For a given object, the gold dots mark when 50% of the deuterium has burned and magenta dots mark when 50% of the lithium has burned. Figure from Burrows et al. (2001).

hand do not burn hydrogen at a rate sufficient to achieve this balance, though the more massive brown dwarfs burn deuterium for a time (Burrows et al., 2001). Deuterium burning is responsible for the plateaus in luminosity for brown dwarfs at early ages. For a given object, the gold dots mark when 50% of the deuterium has burned and magenta dots mark when 50% of the lithium has burned. The constant cooling of these objects with time leads to an inherent mass-age degeneracy. An object with a measured luminosity, L, could be an old, massive field brown dwarf, or may be a young, very low-mass brown dwarf. Thus, to fully characterise an object, we must constrain two parameters of luminosity-mass-age.

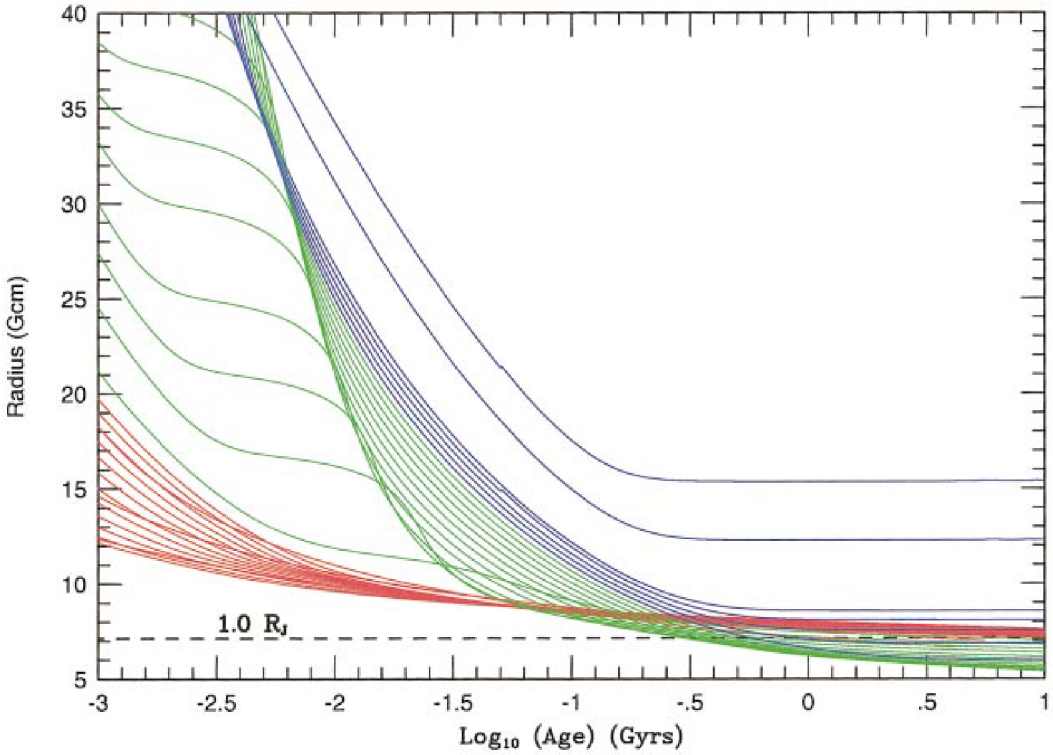

Figure 1.2 Evolution of radius of isolated solar-metallicity low-mass stars and substellar-mass objects plotted against age. Stars are shown in blue, brown dwarfs with masses above $13M_{\rm Jup}$ are shown in green and brown dwarfs with masses below $13M_{\rm Jup}$ and giant exoplanets are shown in red. The radius of Jupiter is shown by the dashed line. Radii are not monotonic with mass and cluster near the radius of Jupiter at late ages, despite a wide range of masses. Figure from Burrows et al. (2001).

1.1.2 Radius

Figure 1.2 shows the evolution of radius, R, for low-mass stars, brown dwarfs and extrasolar giant planets from Burrows et al. (2001). The early plateaus at $\sim 15 - 40\ R_{\rm Jup}$ coincide with deuterium burning which roughly stabilises $T_{\rm eff}$, L and R for $10^6 - 10^8$ yr, depending on mass. Figure 1.2 also shows the non-monotonic dependence of the radius on mass. At early times, the radius is roughly a monotonically increasing function of mass and, for a given mass, the radius is always a decreasing function of age. However, at later stages of evolution, the dependence of mass on radius inverts, with the less massive brown dwarfs having the larger radii. The maximum radius occurs for brown dwarfs with a mass of $\sim 4\ M_{\rm Jup}$ (Burrows et al., 2001). Most importantly, Figure 1.2 shows that for a broad range of masses, from $0.3 - 70\ M_{\rm Jup}$, the older radii are independent of

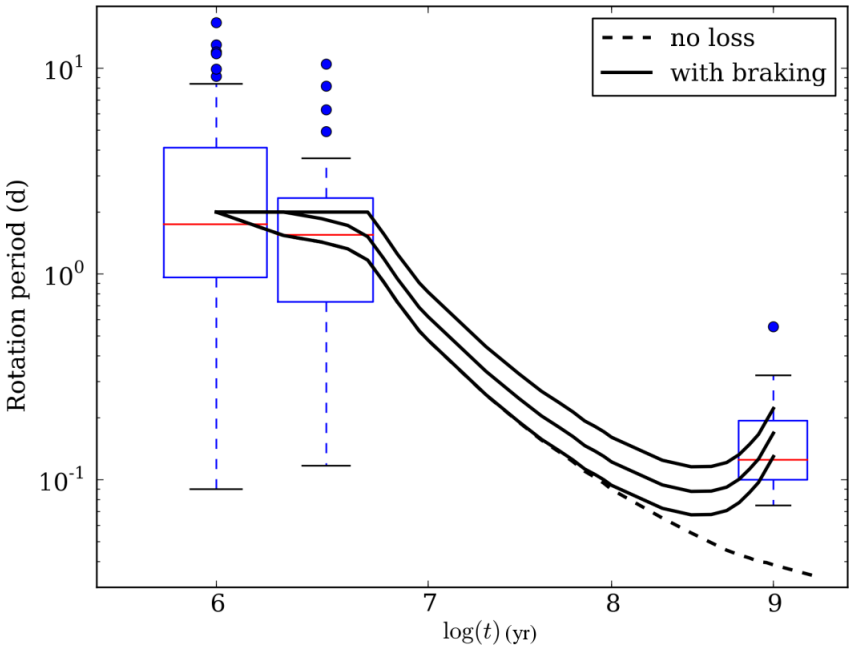

Figure 1.3 Rotational periods of brown dwarfs as a function of age. The plot contains period for brown dwarfs at an age of ~ 1 Myr, ~ 3 Myr and for the field brown dwarf population. The median rotational period is shown by the red line. The lower and upper quartiles are shown by the box and the error bars show the range of measured periods at that age. The dashed line illustrates evolution models without momentum loss. The solid lines correspond to models including saturated angular momentum losses and disk locking phases that last for 1,2 and 5 Myr. The best fit to the current observational constraints is obtained by assuming an angular momentum loss rate for brown dwarfs that is $\sim 10,000$ times weaker than that used for solar-type stars. Figure from Bouvier et al. (2014).

mass to within about 30%. This is due to the competition in the equation of state between Coulomb and electron degeneracy effects. The Coulomb effect would set a fixed density and interparticle distance scale at ~ 1 Å. This would lead to the relation $R \propto M^{1/3}$. On the other hand, electron degeneracy would result in the classical relationship for a low-mass white dwarf ($R \propto M^{-1/3}$). These competing effects cancel each other out, and render the radius constant over roughly two orders of magnitude near the radius of Jupiter (Burrows et al., 2001).

1.1.3 Rotation

Brown dwarfs are characterised by fast rotation from young ages throughout their whole evolution, with a median period of about 2 d at 1 Myr and $3-4$ hr at 1 Gyr

(Bouvier et al., 2014). Over their first ~ 10 Myr, the rotation of brown dwarfs and planetary-mass objects is slowed down by disk and accretion wind braking until the circum-brown dwarf disk dissipates. This is opposed by contraction, which causes the object to spin up during their first $\sim$ 200 Myr. Rotational breaking due to star-disk interaction and accretion-driven winds is strongly mass-dependent, becoming less efficient at substellar masses (Scholz et al., 2015). Figure 1.3 shows measured rotational periods of brown dwarfs at different ages, with evolutionary models overplotted. The current observational constraints on the rotational evolution of brown dwarfs indicate an angular momentum loss rate for brown dwarfs that is $\sim 10,000$ times weaker than that used for solar-type stars (Bouvier et al., 2014).

1.2 The L–T Spectral Sequence

Brown dwarfs were discovered in large numbers with the advent of wide-field imaging surveys such as the Two Micron All Sky Survey (2MASS; Skrutskie et al., 2006) and the Deep Infrared Survey of the Southern Sky (DENIS; Epchtein et al., 1997) in the near-infrared and the Sloan Digital Sky Survey (SDSS; York et al., 2000) in the optical. Near-infrared photometry is calibrated to Vega, while optical photometry is calibrated on the AB system. The magnitudes mentioned throughout this thesis are Vega based. The population of brown dwarfs discovered in these surveys demonstrated the need for a new classification system that extended beyond the OBAFGKM stellar classification scheme. This lead to the introduction of the new L, T and Y spectral types for brown dwarfs with temperatures ranging from $\sim$ 2200 K to $\sim$ 300 K (Kirkpatrick, 2005; Cushing et al., 2011). As with stars, brown dwarfs are characterised based on their spectral absorption features (Reid & Hawley, 2005).

The original classification scheme of L type brown dwarfs based on red optical wavelengths is presented in Kirkpatrick et al. (1999, 2000). The L dwarfs have a temperature range of $\sim$ 2300 K to 1400 K and exhibit some overlapping features with M stars such as TiO and VO. These features diminish in strength with increasing spectral type, disappearing completely by L6 spectral types. The dominant molecular features are metal hydride bands of CaH, FeH, CrH and CrH at far-red wavelengths and MgH shortward of 0.6 μm. The Na I doublet weakens progressively with later spectral type while the resonance lines due to K I, Cs I, Rb I and the sodium D lines increase in strength. The behaviour of the

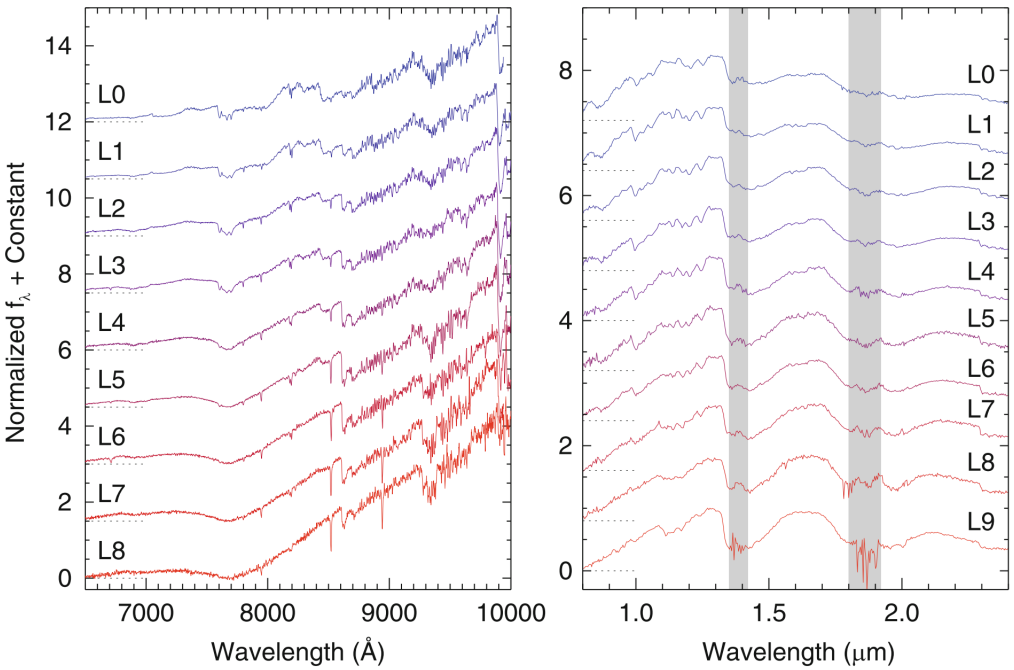

Figure 1.4 *Left:* Red optical spectral sequence of L dwarf spectral standards. *Right:* Near-IR spectral sequence of L dwarf spectral standards. Wavelengths of high telluric absorption, and thus low signal-to-noise data, are denoted by grey bars. Figure from Cushing (2014).

K I doublet at $\sim$ 7700 Å is particularly interesting, broadening considerably at spectral type L4. The two components become indistinguishable, with a combined equivalent width of more than 100 Å. The Na I resonance doublet shows similar behaviour.

As a brown dwarfs evolves its atmosphere continues to cool. At some point, the temperature in the photosphere is sufficiently low such that extensive methane is formed. At this point, strong CH_4 absorption bands appear at near-infrared wavelengths and remove over half of the flux in the H and K passbands (Burgasser et al., 2002). The presence of these absorption bands marks the beginning of the T spectral class, and they strengthen as the brown dwarf evolves to later spectral types. The H_2O absorption bands also continue to strengthen with increasing spectral type and near-infrared colours become increasingly blue ($J - K_S \sim 0$) compared to the L dwarfs. Generally, the features observed in L and T brown dwarfs are thought to be due to the formation of dust in L type atmospheres and their consequent dispersal in T type atmospheres. (Lodders & Fegley, 1999). See Section 1.3.3 for a discussion of these clouds.

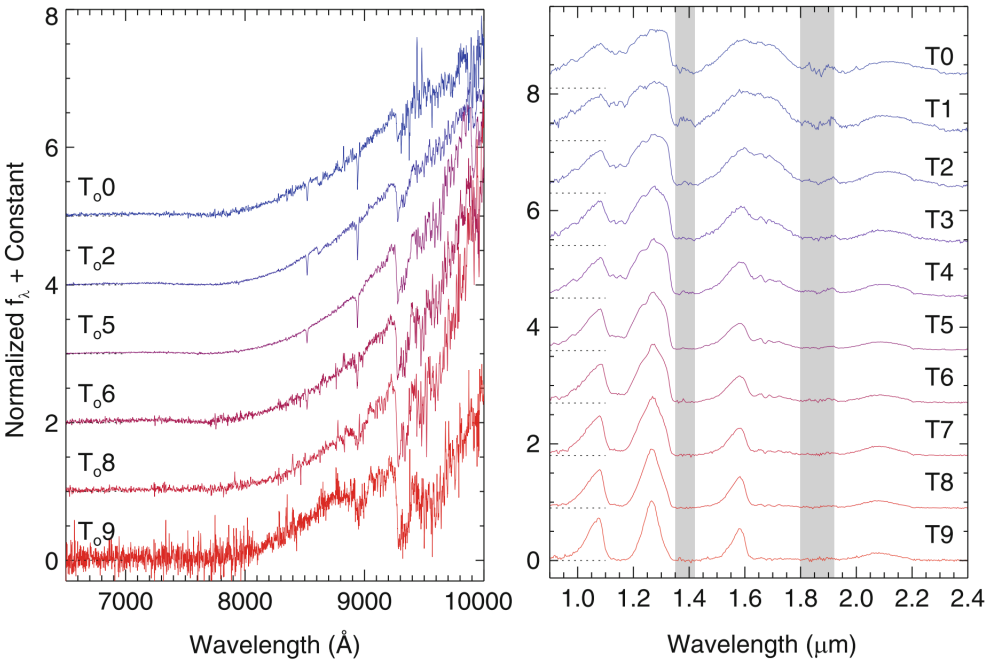

Figure 1.5 *Left:* Red optical spectral sequence of T dwarf spectral standards. *Right:* Near-IR spectral sequence of T dwarf spectral standards. Wavelengths of high telluric absorption, and thus low signal-to-noise data, are denoted by grey bars. Figure from Cushing (2014).

1.3 Brown Dwarf Atmospheres

The atmosphere of a brown dwarf plays a crucial role in controlling the evolution and appearance of the object. By connecting the deep, convective interior with the thermal radiation emitted by the object, the atmosphere regulates how quickly the interior can cool over time. The atmosphere also imprints the varied signatures of gases, condensates, gravity and the temperature profile onto emitted thermal radiation, thereby controlling the spectral signature of the object. Thus, understanding the spectrum and evolution of a brown dwarf requires a working knowledge of the atmosphere.

The atmospheres of brown dwarfs are very complex. Since these objects are relatively cool, chemical equilibrium favours the formation of molecules, whose opacities often vary strongly with wavelength. In addition, condensates can form at these temperatures, adding the complexity of cloud physics to the problem. Unlike stellar atmospheres, whose photosphere is typically well defined, the strongly wavelength dependent opacity in brown dwarf atmospheres leads to a photosphere that varies with wavelength, and whose physical location can vary

by several scale heights (Marley & Robinson, 2015). The gravity, internal heat, energy transport mechanisms, composition and cloud structures of a brown dwarf atmosphere influence the thermal profile and consequently, the properties of its emitted radiation.

1.3.1 Energy Transport

Figure 1.6 shows a schematic of a one-dimensional model atmosphere from Marley & Robinson (2015). The vertical coordinate is pressure, P, which is defined on a grid of model levels. In hydrostatic equilibrium, where the gravitational force acting on any given atmospheric slab is balanced by the vertical pressure gradient force, the fluid atmosphere obeys

$$\frac{dP}{dz} = -g\rho \tag{1.1}$$

where z is altitude, g is acceleration due to gravity, and ρ is the atmospheric mass density. Inserting the ideal gas law and rearranging gives:

$$\frac{dP}{P} = -\frac{gm}{k_{\mathrm{B}}T}dz = -\frac{dz}{H} \tag{1.2}$$

where m is the mean molecular mass in the atmosphere, k_{B} is the Boltzmann constant and T is temperature. Here we have also defined the atmospheric pressure scale height, $H = \frac{k_{\mathrm{B}}}{mg}$, which for an isothermal layer of the atmosphere is the e-folding distance for pressure, such that the pressure-altitude relation is

$$P(z) = P(z_0)e^{-(z-z_0)/H} \tag{1.3}$$

where $P(z_0)$ and z_0 are the pressure and altitude at the base of the layer, respectively.

Pressure-dependant atmospheric properties, such as temperature, chemical composition or wavelength-dependent thermal flux are determined at various model levels or layers. A key model input parameter is the internal heat flux F_i, which sets the effective temperature via $\sigma T_{\mathrm{eff}}^4 = F_i$, where σ is the Stefan-Boltzmann constant. In steady state, this energy flux is constant with pressure throughout the atmosphere, and is represented by the dotted area in Figure 1.6.

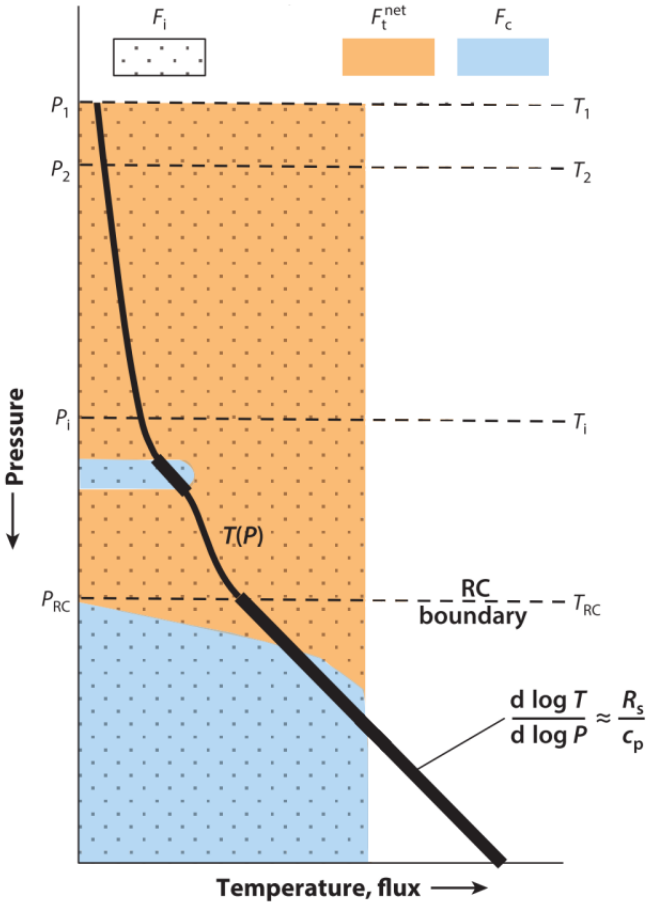

Figure 1.6 Schematic depiction of a thermal structure model. The vertical axis is pressure, which is the independent variable, and the horizontal axis shows, relatively, temperature and energy flux. Model levels are shown by the horizontal dashed lines, and the solid line is the thermal structure (i.e. temperature) profile, in which bolded lengths indicate a convective region. Level pressures and temperatures are indicated with associated subscript symbols and "RC" indicates the radiative-convective boundary. The net thermal flux is shown in orange and the convective flux is shown in blue. Figure modified from Marley & Robinson (2015).

At great depths in the interior of a brown dwarf, the electron density is high and thermal protons cannot propagate far, so energy transport is dominated by convection. Convection in these dense atmospheres is very efficient, so the gradient in the deep thermal temperature profiles is expected to closely follow convective adiabats (i.e. thermal profiles of constant entropy) (Baraffe et al., 2002).

Convection delivers thermal energy to the base of the atmosphere (shown by the blue region at large pressures in Figure 1.6), and thermal radiative transport (shown by the orange region in Figure 1.6) begins to become more important as

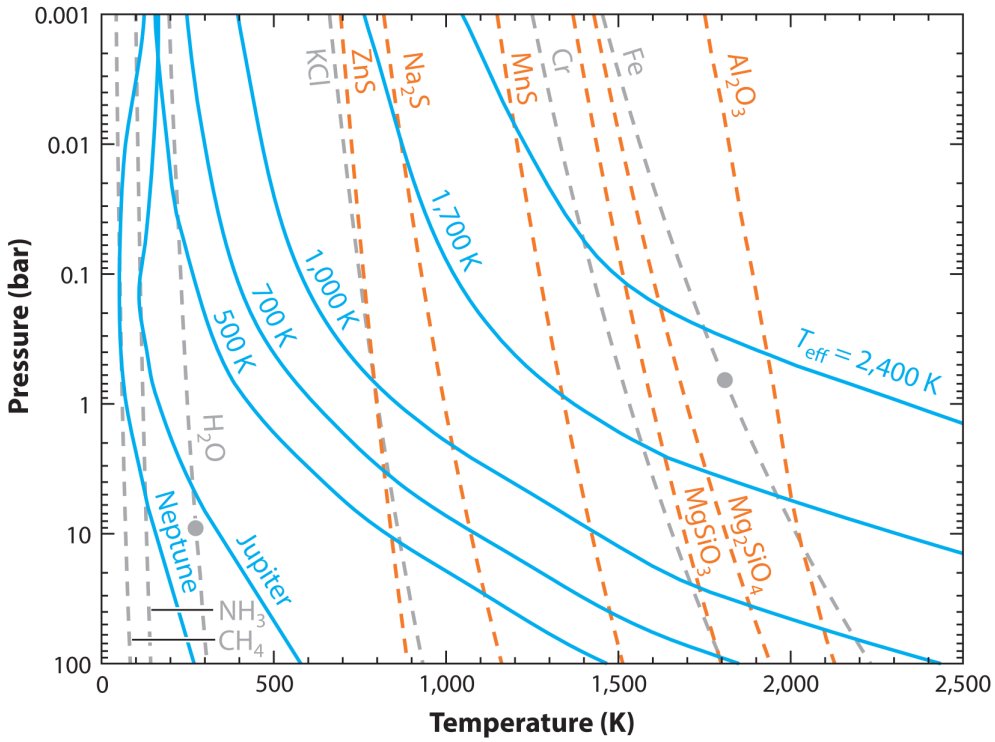

Figure 1.7 Condensation curves for a variety of species (dashed lines), assuming solar abundances from Lodders (2003). Gray curves are for direct condensation, whereas orange curves are for condensates that form as a result of chemical reactions. Filled circles indicate a liquid-solid transition. Several cloud-free model thermal profiles are provided for comparison, as well as empirically derived profiles for Jupiter and Neptune. Figure from Marley & Robinson (2015).

the atmosphere thins with decreasing pressure (Marley & Robinson, 2015). As progressively more energy is carried away by radiation, the temperature profile no longer changes as steeply with altitude, indicating that convection has ceased. Above this level, referred to as the 'radiative-convective boundary', energy is carried away by radiation and the atmospheric thermal profile is governed by radiative equilibrium.

1.3.2 Condensates

At the relatively cool atmospheric temperatures of brown dwarfs, important atmospheric constituents are expected to be found in condensed phases, particularly Fe, Si and Mg, but also the more refractory components such as Al, Ca, Ti and V.

For the case of homogeneous condensation, where the gas phase species condenses to form a liquid or solid of the same species (e.g. H_2O or Fe), condensation first occurs in a rising parcel of gas when the local partial pressure of the condensing gas first exceeds the saturation vapour pressure. This defines the cloud base (Marley & Robinson, 2015). In more complex cases (e.g. Ca and TiO forming $CaTiO_3$), the cloud base is determined through chemical equilibrium calculations. Figure 1.7 shows the condensation curves for many key species along with a selection of model pressure-temperature profiles for reference. The marked boundaries are the locations where the labeled solid or liquid species will form as its progenitor gaseous species are carried upwards in a rising air parcel.

Figure 1.7 shows that there are numerous atmospheric condensates within the brown dwarf pressure-temperature regime. However, not all condensates are of equal importance. Some species, such as TiO, play a leading role in controlling gaseous opacity in the M and early L dwarfs, but due to their low abundances are relatively unimportant cloud opacity sources at at later spectral types. The more abundant Fe-, Si- and Mg-bearing species have a greater contribution to column grain optical depths and thus play an important role in shaping emerging brown dwarf spectra (Marley & Robinson, 2015).

1.3.3 Cloud Models of Brown Dwarfs

There are several approaches to modelling clouds in brown dwarf atmospheres. These treat the microphysics of cloud formation in a variety of levels of detail, from kinetic models that trace each step of cloud nucleation, growth and settling (e.g. Helling et al., 2008) to parametrised models that reduce the number of free parameters in the model (e.g. Ackerman & Marley, 2001; Allard et al., 2003). The second approach is more computationally efficient and allows cloud models to be calculated in tandem with a radiative-convective equilibrium model to calculate pressure-temperature profiles. This approach has been the favoured approach by most groups to model large grids of spectra for comparison with observations.

The Ackerman & Marley (2001) Cloud Model

The Ackerman & Marley (2001) cloud model follows the second method introduced above. This model avoids treating the microphysical processes that form the cloud and instead calculates a mass balance: both gas and condensate

are mixed upwards by turbulent mixing in each layer of the atmosphere, while condensates are transported downward by sedimentation. The model parametrises the efficiency of sedimentation of cloud particles through a scaling factor, $f_{\rm rain}$, while the turbulent mixing is described by the vertical eddy diffusion coefficient, K (Ackerman & Marley, 2001). The balance between upward and downward mass transport can be used to calculate the total amount of condensate at each layer of the atmosphere. The partial pressure of each condensate species is compared with the condensate vapour pressure, and the cloud base is found by determining at which point in the atmosphere the local gas abundance exceeds the local condensate saturation vapour pressure, at which point the atmosphere becomes saturated (Marley et al., 2013). The Ackerman & Marley (2001) model assumes that each material is formed by homogeneous condensation. For condensates that are not formed homogeneously, more recent work by Morley et al. (2012) computes an equivalent vapour pressure curve for these species.

The Ackerman & Marley (2001) cloud model does not require knowledge of the microphysical processes to compute particle sizes. For a given sedimentation efficiency, clouds are simply assumed to have grown large enough to provide the required downward mass flux to balance the turbulent mixing. A broad, lognormal size distribution of particles is used to approximate the bimodal size distribution of terrestrial cloud particles. Since the models are not computationally intensive, a large numbers of models can be computed and compared with data.

Ackerman & Marley (2001) use their model to calculate profiles of condensed water, silicate ($MgSiO_3$) and iron in theoretical atmospheres of brown dwarfs and a giant planet, finding that clouds are an important opacity source for L type objects. Silicate and iron clouds in L dwarfs form in the visible atmosphere and therefore play an important role in controlling opacity and the temperature structure of the atmosphere. For cooler ($T_{\rm eff} \sim 900$ K) T dwarf atmospheres, these clouds form lower in the atmosphere. Although they may still be important to the atmospheric temperature structure, they no longer represent significant opacity sources to an observer (Ackerman & Marley, 2001). Thus, the Ackerman & Marley (2001) model shows that clouds play an important role in shaping the spectral appearance of brown dwarfs. In the next section, we discuss how the consideration of cloud species in brown dwarf atmospheres can explain the spectral and colour evolution of L and T type brown dwarfs.

Condensates Shape the Spectra of L and T Brown Dwarfs

The emergent colours and spectra of cool brown dwarfs are generally thought to be shaped by the presence of condensate clouds in the atmosphere (e.g. Ackerman & Marley, 2001; Burrows et al., 2001; Marley et al., 2002; Tsuji et al., 1999). The colour-magnitude diagram shown in Figure 1.8 shows the colour evolution of a brown dwarf as it cools to later spectral types.

Below temperatures of $\sim$ 2200 K, the temperatures and pressures present in L type brown dwarf atmospheres begin to intersect with the condensation curves of various refractory species such as iron silicate and metal oxide compounds, collectively referred to as dust (Figure 1.7, Marley & Robinson, 2015). The formation of these clouds removes TiO and VO from the atmosphere, as they condense out of the gaseous phase. In the near-infrared (where the peak energy is emitted), L dwarf spectra are shaped by strong H_2O absorption bands that deepen with spectral type. Dust clouds are a major source of opacity in the near-IR, which causes L dwarfs to become progressively redder as the condensate clouds continue to thicken with later spectral type.

Below temperatures of $\sim$ 1200 K brown dwarfs enter the T spectral sequence. The temperatures in T dwarf atmospheres have gotten so low that the condensate clouds gravitationally settle below the photosphere, and we observe a virtually cloud-free atmosphere by mid T type objects. This coincides with the substitution of CO with CH_4 as the dominant carbon species. The suppression of the H and K passbands by CH_4 and H_2O absorption combined with the disappearance of condensate clouds causes a dramatic blueward shift in the colour-magnitude diagram (see Figure 1.8).

The L/T transition is evident in the colour-magnitude diagram (Figure 1.8) as an abrupt blueward shift in $J-K$ colour by $\sim$ 2 mag accompanied by a brightening in the J-band of up to $\sim$ 1 mag (Dupuy & Liu, 2012). Two main ideas have been put forward to explain the L/T transition using cloud models. In one theory, the atmospheric dynamical state changes, resulting in larger particles size which rain out of the atmosphere rapidly, leading to a sudden clearing of the cloud deck (e.g. Knapp et al., 2004). This is supported by fits of brown dwarf spectra to model spectra computed with the Ackerman & Marley (2001) cloud models by Saumon & Marley (2008). Cushing et al. (2008) has shown that progressively later dwarfs from L9 to T4 can be fit by increasing the particle size across the L/T transition at a nearly fixed effective temperature.

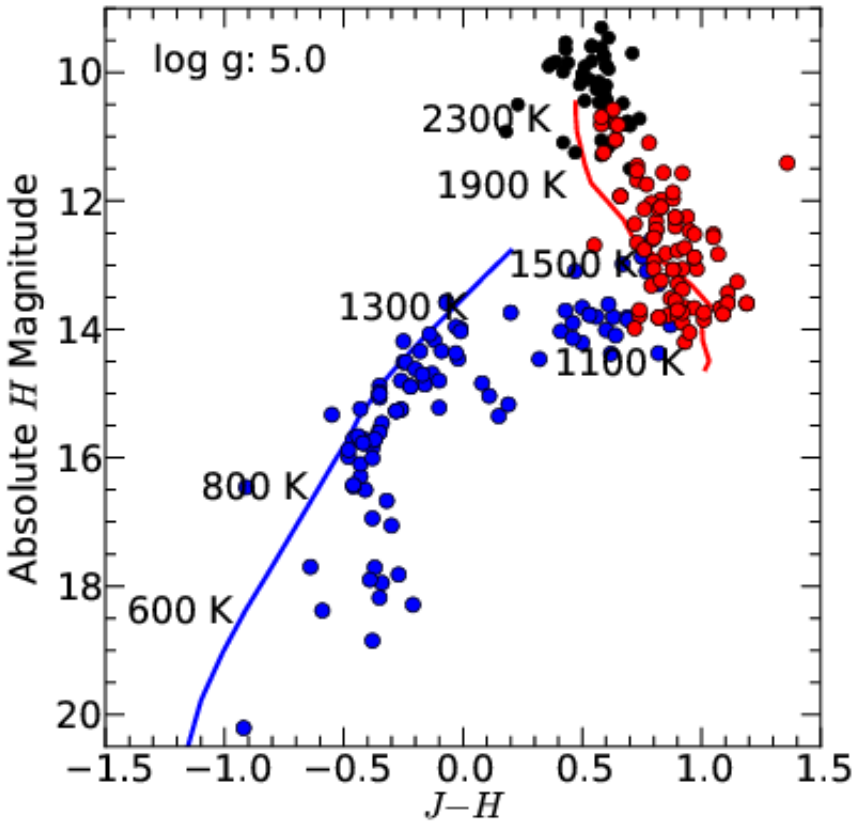

Figure 1.8 Colour-magnitude diagram showing M, L and T spectral type brown dwarfs. Black circles show M spectral type brown dwarfs, red circles show L spectral type brown dwarfs and blue circles show T spectral type brown dwarfs. Figure taken from Morley et al. (2012).

The second idea is based on thermal infrared images of the atmospheres of Jupiter and Saturn at ~ 5 μm. Gaseous opacity is low at this wavelength and clouds stand out as dark patches against a bright background of flux emitted from deeper, warmer levels in the atmosphere. These images of Jupiter and Saturn show that the global cloud decks are not homogenous, but appear quite patchy. Ackerman & Marley (2001) and Marley et al. (2010) have suggested that the arrival of holes in brown dwarf clouds, might also be responsible for the L/T transition. This idea is well supported by the discovery of L/T transition brown dwarfs displaying photometric variability, thought to be driven by dark patches of clouds rotating in and out of view (e.g. Radigan et al., 2014; Metchev et al., 2015).

1.3.4 Cloud-Free Models of Brown Dwarfs

While clouds have been used to explain the observational properties of brown dwarfs for the past ~ 20 years, cloud-free models have recently been proposed to model the spectra and colours of brown dwarfs (Tremblin et al., 2015, 2016, 2017). These models explain the reddening of the L dwarfs as a result of a reduction in the temperature gradient in the atmosphere. This reduced temperature gradient is caused by the onset of fingering convection, triggered by the instability of carbon chemistry in brown dwarf atmospheres. For L type brown dwarfs, CO is the dominant carbon species and for lower temperatures present in T type atmospheres CH_4 is the dominant carbon species. The net reaction:

$$CO + 3\,H_2 \longrightarrow CH_4 + H_2O$$

tells us that the methane dominant part of the atmosphere has a higher mean molecular weight than the CO dominated region. Chemical network studies have shown that this transition can be very slow (Venot et al., 2012). Thus, atmospheres with this chemical transition can develop a thermo-chemical instability. At the CH_4/CO transition, if a perturbation drives some of the "$CH_4 + H_2O$" mixture down into the deeper, hotter "$CO + 3\,H_2$" region, the mixture will stay in its methane-rich state (due to the slowness of the chemical reaction) and sink due to its higher molecular weight. This downward vertical transport of heavier material and upward transport of lighter material is known as fingering convection, and results in a reduced temperature gradient in the atmosphere. Tremblin et al. (2016) show that this process can reproduce the spectra of field brown dwarfs, while also providing a natural explanation for the J-band brightening and resurgence of FeH observed in early T dwarfs. While we cannot presently rule out either the cloudy or cloud-free models, Tremblin et al. (2017) suggest that NIRspec and MIRI observations with the James Webb Space Telescope ($JWST$) in the $3-7$ μm region could help assess which interpretation is correct.

The cloud-free models have recently been challenged by Leconte (2018), who shows that fingering convection, or indeed any kind of turbulent mixing, would in fact increase the thermal gradient, contrary to the assumptions of Tremblin et al. (2017). Leconte (2018) shows that if the chemical gradient were to destabilise the atmosphere of a brown dwarf or giant planet above the troposphere, this would not lead to a more isothermal profile, as advocated by Tremblin et al. (2017). In

contrast, this would actually increase the thermal gradient. Exploring the effects of mixing at the L/T transition, Leconte (2018) shows that turbulent mixing of any kind would lead to a J-band darkening and a disappearance of the FeH feature along the L/T spectral sequence, which is the opposite of what has been observed (e.g. J-band brightening seen in Figure 1.8). This work suggests that for the time being, cloudy models are needed to interpret the observed features of L and T type brown dwarfs and giant planets.

1.4 Photometric Variability Monitoring

The combination of atmospheric inhomogeneities and rapid rotation of brown dwarfs immediately prompted searches for weather phenomena in substellar atmospheres. Photometric variability monitoring is a powerful tool for probing weather patterns in substellar atmospheres as it is sensitive to atmospheric features as they rotate in and out of view.

The first searches for variability focused on early L dwarfs in the red optical (e.g. Tinney & Tolley, 1999; Gelino et al., 2002; Clarke et al., 2003; Enoch et al., 2003; Koen, 2003), but were hindered by the fact that L dwarfs are very faint at optical wavelengths. These searches sometimes revealed inconsistent results – for example, Gelino et al. (2002) reported a rotational period of 31 hr for the L0.5 dwarf 2M0746+20 from variability monitoring. However, Bailer-Jones (2004) measured $v \sin i \sim 25 - 27$ km s^{-1} for this object, implying a maximum rotational period of 5.7 hr.

Concurrently, a number of studies searched for variability in young brown dwarfs in star-forming regions (e.g. Zapatero Osorio et al., 2003; Joergens et al., 2003; Scholz & Eislffel, 2004). With ages < 5 Myr, the objects in these surveys are still hot from formation and have M spectral types. Thus, their variability is likely driven by mechanisms such as accretion from a circum-brown dwarf disk or magnetic phenomena such as starspots. Much of the observed variability is non-periodic and flaring and likely has more in common with magnetically-driven variability observed on M stars.

These initial studies showed that the L and T dwarfs were the most promising candidates for cloud-driven varaibility. Since the atmospheres of late-L and T dwarfs are increasingly neutral, they are less likely to support cool magnetic spots

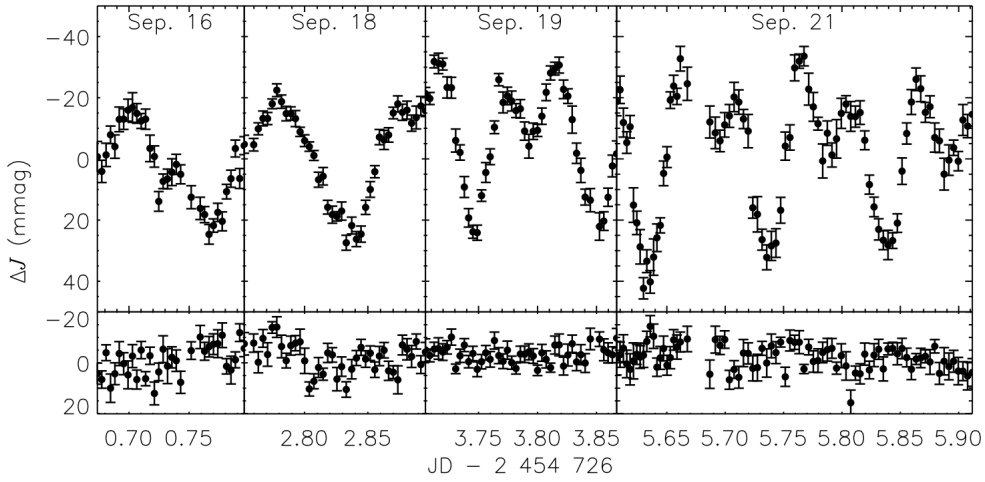

Figure 1.9 The lightcurves of SIMP 0136+09 are shown in the upper panel. The lightcurve of a comparison star is shown in the lower panel. Figure taken from Artigau et al. (2009).

(Gelino et al., 2002). Due to the strong decline in optical flux with increasing spectral type, a move to near-IR wavelengths was necessary, where late-L and T dwarfs are brightest.

1.4.1 First Variability Detections

The detection of high-amplitude, periodic and repeatable variability in a number of brown dwarfs alleviated concerns about the validity of such variability detections. Specifically, the brown dwarfs SIMP 0136+09, 2M2139+10 and Luhman 16B were all found to exhibit high-amplitude, periodic variability (Artigau et al., 2009; Radigan et al., 2012; Gillon et al., 2013). The initial lightcurve of SIMP 0136+09 from Artigau et al. (2009) is shown in Figure 1.9. While the lightcurves of all three brown dwarfs evolve rapidly, they display robust variability overall, with a clear periodicity. The evolution of the lightcurves was believed to be due to rapid evolution of the cloud structures causing the observed variability. SIMP 0136+09, 2M2139+10 and Luhman 16B are situated at the L/T transition, where the condensate clouds that characterise the L spectral class break up and disperse by the mid to late T spectral class. These initial discoveries suggested that the highest variability amplitudes may occur due to the break-up of clouds at the L/T transition.

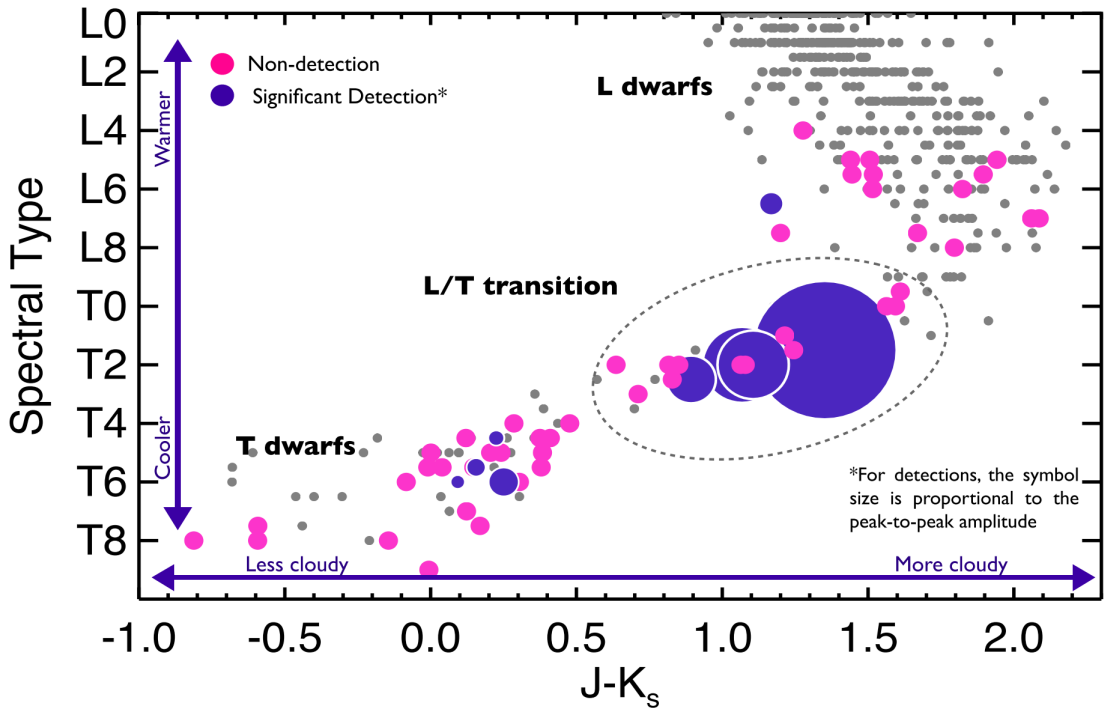

Figure 1.10 Results from Radigan et al. (2014) survey for photometric variability in field L and T dwarfs. near-IR spectral type versus 2MASS $J - K_S$ colour for all targets observed in program. Grey points show the known field L and T dwarf population. Purple circles show variability detections, with the symbol size proportional to the amplitude of variability detected. The grey dashed line encloses the brown dwarfs considered part of the L/T transition sample.

1.4.2 Variability Surveys

Radigan et al. (2014) completed the most comprehensive, ground-based search for J-band variability in L-T spectral type brown dwarf atmospheres, using the *Du Pont 2.5 m* telescope at Las Campanas Observatory and the *Canada France Hawaii Telescope* on Mauna Kea. Figure 1.10 shows the detections and non-detections in the survey on a colour-spectral type diagram. 9 out of 57 (16%) L-T spectral type brown dwarfs observed showed significant ($> 2\%$) variability above photometric noise. Furthermore, enhanced variability occurence rates and amplitudes were detected at the L/T transition, supporting the hypothesis that cloud holes contribute to the abrupt decline in condensate opacity and J-band brightening observed at the L/T transition. A similar ground-based variability survey, the *Brown Dwarf Atmospheric Monitoring* (BAM) survey, was completed by Wilson et al. (2014), who monitored 69 brown dwarfs spanning the L0 to T8

spectral range using the SofI instrument on the 3.5 m *New Technology Telescope*. Significant variability was reported in 14 from 69 brown dwarfs (20%), with no evidence for an enhancement in frequency or amplitude across the L/T transition, a result which differed from the results of the Radigan et al. (2014) survey. Radigan (2014) carried out a reanalysis of the the 13 highly variable objects reported by Wilson et al. (2014) and found significant variability in only 4 from 13. Combining the revised BAM survey with the Radigan et al. (2014) survey, Radigan (2014) found that $3.1^{+2.7}_{-1.7}$% of objects outside the L/T transition exhibit variability compared to 24^{+11}_{-9}% of objects in the L9-T3.5 range.

Space-based observations benefit from much higher photometric stability than ground-based observations and thus can attain much higher precision. Buenzli et al. (2014) conducted a 22 target grism spectroscopy survey at wavelengths of $1.1 - 1.7$ μm using the *Hubble Space Telescope*, attaining point-to-point precision of $0.1 - 0.2$%. Each object was observed for ~ 40 minutes, so only variability slopes could be detected. Low-level (~ 1%) variability was detected in 6 objects in the sample (27%), with no evidence for enhanced frequency across the L/T transition, suggesting that low-level heterogeneities are a frequent characteristic of brown dwarf atmospheres across the entire L-T spectra ranges. Metchev et al. (2015) used the *Spitzer Space Telescope* to search for photometric variability in a sample of 44 L3-T8 dwarfs at 3.6 μm and 4.5 μm, reaching $0.2 - 0.4$% precision. Detections and non-detections from this survey are shown in Figure 1.11. The authors reach a similar conclusion to the Buenzli et al. (2014) survey, finding that photometric variability and hence patchy clouds are common among L and T dwarfs. Metchev et al. (2015) also reported an increase in variability amplitude with later spectral types. Additionally, eight low or moderate gravity dwarfs were included in this survey, to probe the effects of low-surface gravity on variability properties. Metchev et al. (2015) report a tentative correlation (92%) between low-gravity and high amplitude variability, although a larger sample is necessary to confirm this trend. Presently this is the only survey for variability on young, low-gravity objects.

Returning to optical wavelengths, Heinze et al. (2015) monitored a sample of 12 T dwarfs with the Kitt Peak 2.1 m telescope. This survey was inspired by the detection of extremely high amplitude (~ 20%) optical variability in our nearest T dwarf, Luhman 16B (Gillon et al., 2013). Without optical variability data for any other T dwarfs in the field, it was not possible to say how representative Luhman 16B is of its spectral type. This survey detected high-amplitude variability in two

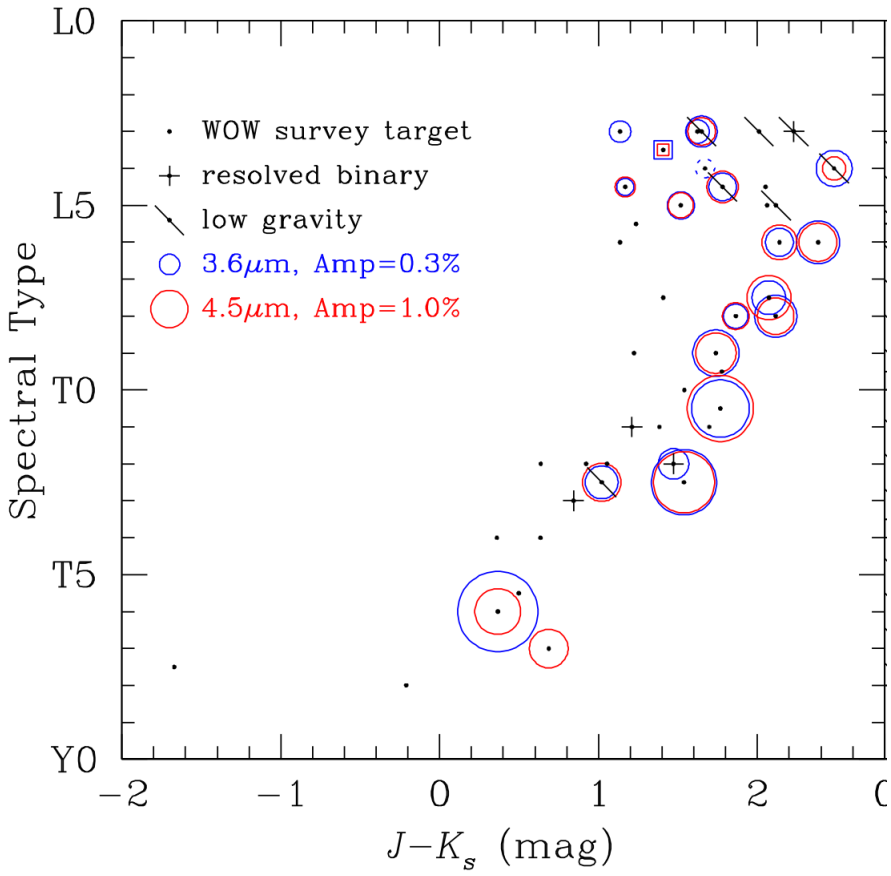

Figure 1.11 Results from Metchev et al. (2015) *Spitzer* survey for photometric variability on L and T spectral type brown dwarfs. Colour, spectral type and variability distribution of full 44 objects L3-T8 sample. Circles enclose the variable targets, where the area of each circle is proportional to the variability amplitude in the IRAC [3.6] band (blue) or [4.5] band (red).

T type brown dwarfs with variability amplitudes $> 10\%$. These results suggest that high-amplitude ($> 10\%$) variability in T dwarfs is more common in the red optical than at infrared wavelengths, and that Luhman 16B is not such an unusual brown dwarf.

1.4.3 Simultaneous Multi-Wavelength Variability Monitoring

Different wavelengths probe different layers of a brown dwarf atmosphere, and by observing spectral variability we can probe the cause of variability as well as the vertical structure of the atmosphere (Morley et al., 2014). Amplitude ratios and phase shifts can be used to differentiate between various variability mechanisms (Biller, 2017). These mechanisms include inhomogeneous cloud cover, hot spots,

temperature perturbations and thermochemical instabilities.

The initial detection of variability in the T2.5 dwarf SIMP 0136+09 (Artigau et al., 2009) made use of the J and K bands to provide clues on the atmospheric cloud structure. The J and K lightcurves were correlated, showing an amplitude ratio of $A_K/A_J \approx 0.5$. Using the models of Allard et al. (2003) and Burrows et al. (2006), the authors found that this amplitude ratio could be reproduced by an atmosphere composed of dusty clouds in an otherwise clear atmosphere, with a temperature difference of $80 - 110$ K between the dusty and cloud-free regions. Radigan et al. (2012) carried out similar observations on the T1.5 dwarf 2M2139+02 in the J, H and K_S bands. Like SIMP 0136+09, all lightcurves were found to be in phase, with $A_K/A_J \approx 0.5$. Radigan et al. (2012) combine amplitude ratios with model grids to rule out the possibility of magnetically-induced spots and conclude that the variability is due to heterogeneous clouds.

In contrast, Buenzli et al. (2012) observed phase shifts in the T6.5 dwarf 2M2228-43 at wavelengths of $1.21 - 4.5$ μm (Figure 1.12). The variability in each band is well-modelled by a sinusoid but the phase varies significantly with each band. These phase shifts were explained by considering the pressure level probed by each wavelength, which were determined using atmospheric models by Burrows et al. (2006) and Morley et al. (2012). As shown in Figure 1.13, the phase shifts were found to correlate with the pressure level, or height in the atmosphere, where phase lag was found to increase with decreasing pressure level, or higher altitude. These phase shifts revealed both horizontal and vertical heterogeneities in ultra-cool atmospheres for the first time. Biller et al. (2013) report similar phase shifts for the T0.5 component of our closest brown dwarf binary, Luhman 16AB at wavelengths of $0.07 - 4.5$ μm. The measured phase shifts were again found to be correlated with the atmospheric pressure probed by each band. Yang et al. (2016) monitored four brown dwarfs simultaneously in the near-IR and mid-IR, finding phase shifts between the near-IR and mid-IR wavelengths for each brown dwarf. These studies have highlighted the diversity of atmospheric structures between high altitudes (probed by mid-IR wavelengths) and lower altitudes (probed by near-IR wavelengths).

Spectroscopic variability monitoring has also yielded critical constraints on the mechanism responsible for the observed variability in brown dwarf atmospheres. Apai et al. (2013) obtained *HST* spectroscopic variability monitoring of the highly variable L/T transition brown dwarfs SIMP 0136 and 2M2139. They interpreted the observed variability as patches of different spectra rotating in and out of

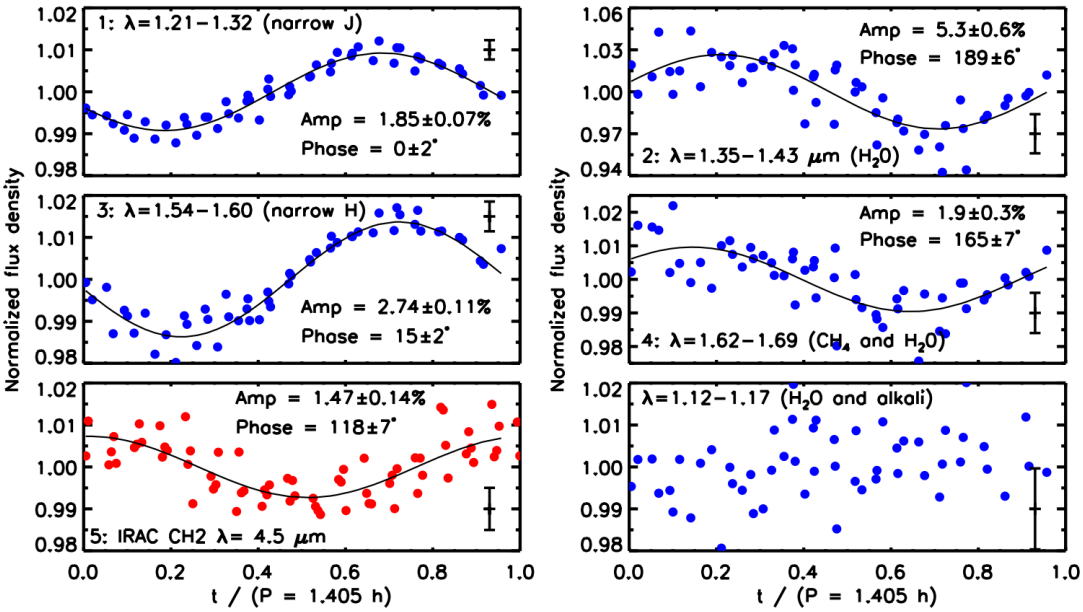

Figure 1.12 Period-folded lightcurves of 2M2228-43 from Buenzli et al. (2012). The black curve shows the best sine fit and the phase is given with respect to the phase of the J band lightcurve.

view. Using Principal Component Analysis (PCA), they found that only two distinct spectra (arising from two distinct regions) are needed to explain the variability. Using 1-D atmospheric models to describe these two spectra, they found that the colour-magnitude variations were not reproduced with cloudy and clear patches, as proposed by Marley et al. (2010). They found that correlated changes in cloud scale height and observed temperature could account for the observed colour-magnitude variations. In other words, the observed variability could be explained by a combination of warm, thin clouds and cold, thick clouds. Figure 1.14 shows an illustration of a possible cloud structure consistent with these observations. The presence of higher clouds limit the observed column to the upper atmospheric levels which are cooler. *HST* spectroscopic monitoring of Luhman 16AB revealed a similar variability mechanism (Buenzli et al., 2015a,b). The observed variability in both components of the L/T transition brown dwarf binary was well-described by a two-component cloud model composed of warm, thin clouds and cold, thick clouds.

The variability in all four L/T transition brown dwarfs SIMP 0136, 2M2139 and Luhman 16AB exhibit their lowest variability amplitude in the water absorption band, but otherwise show an amplitude decreasing gradually from the blue to red edge of the spectrum (Apai et al., 2013; Buenzli et al., 2015a). Yang et al. (2016) carried out similar observations of the L5 brown dwarfs 2M1821+14 and 2M1507–

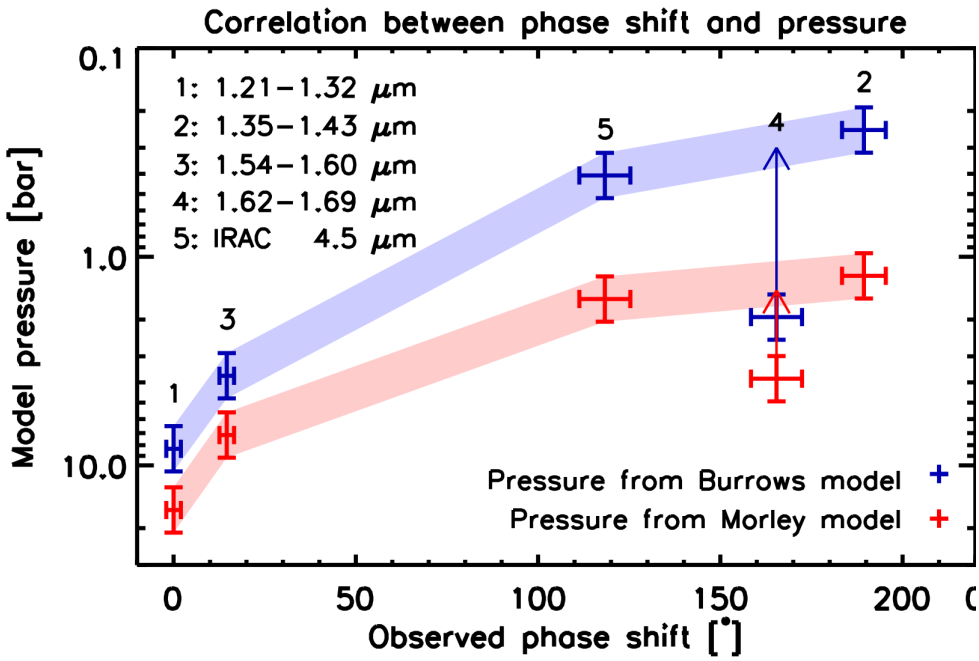

Figure 1.13 Phase shifts of the observed 2M2228 lightcurves as a function of the dominantly probed pressure from Buenzli et al. (2012). There is a correlation between phase shift and pressure. These phase shifts suggest that the modulations seen at lower and higher pressures may be introduced by different cloud layers. Figure from Apai et al. (2013)

16. The time-resolved spectra showed that the water absorption bands varied at similar amplitudes as the adjacent continuum, in contrast to the behaviour of the L/T transition objects. Using a combination of 1D models to describe the observed variability, they found that the variability could be explained by the presence of high-altitude haze layers lying above the condensate clouds. The models suggest that the heterogeneity of these hazes is the variability mechanism for the mid-L brown dwarfs. At high altitudes the water opacity is negligible, so the flux in the water band varies along with the continuum.

While the above approach of combining 1-D models can reveal insights into the atmospheres of variable brown dwarfs, there are some limitations associated with it. Firstly, the existing atmospheric models are not accurate enough to perfectly match the high-quality spectra obtained in these observations. The best-fit spectra match the observed spectra to within $5-10\%$ which is typically considered to be a good fit for brown dwarf atmospheres. However these differences are comparable to the observed variability. For this reason, Apai et al. (2013) explored the colour variations of SIMP 0136 and 2M2139 instead of exploring the

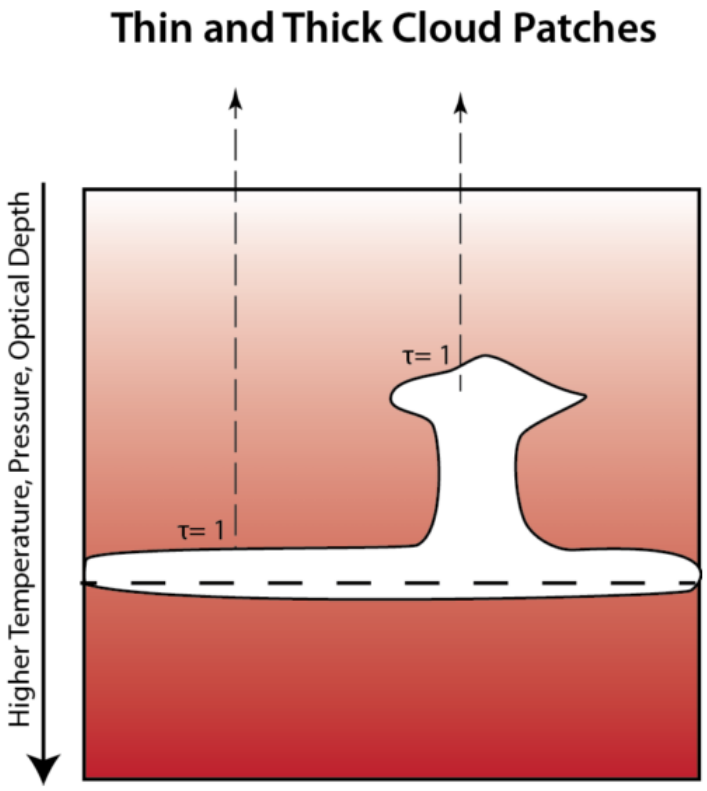

Figure 1.14 Illustration of possible cloud structure consistent with spectroscopic observations of SIMP0136 and 2M2139. The observations are best fit by correlated variations in dust cloud scale height and temperature. Higher clouds will limit the observed column to the cooler upper atmospheres explaining the correlated changes in temperature and cloud scale height.

variability across the full spectrum. Furthermore, modelling patchy cloud cover using a linear combination of independent 1D models is not physically consistent, due to the different temperature-pressure profiles of these models (Marley et al., 2010, 2012).

Spectroscopic variability monitoring can also provide information on the particles present in the condensate clouds. Schlawin et al. (2017) obtained ground-based spectroscopic variability monitoring, using the SpeX instrument on the Infrared Telescope Facility (IRTF). They observed the known variables 2M0835–08 and 2M1821+14, finding low-amplitude variability ($< 0.5\%$) in 2M0835–08 with no clear spectral dependence and higher amplitude ($\sim 1.5\%$) variability in 2M1821+14 with the variability amplitude declining with longer wavelengths. They model the wavelength dependence of the variability amplitude

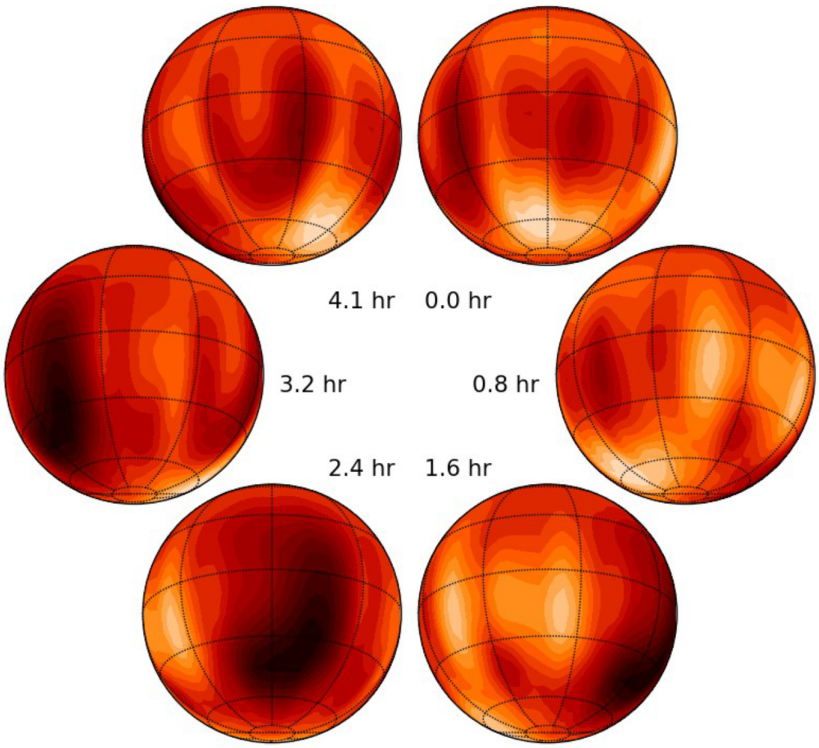

Figure 1.15 Surface map of Luhman 16B obtained from Doppler imaging. The map clearly depicts a bright near-polar region and a darker mid-latitude area consistent with large-scale cloud inhomogeneities. Figure from Crossfield et al. (2014).

of 2M1821+14 with a simple cloud model consisting of an optically thin grouping of clouds composed of particles with sizes that are log-normally distributed. They find that the amplitude spectrum is well-fit by a Mie scattering model with a median particle radius of $r = 0.24^{+0.05}_{-0.07}$ μm. The obtained particle size is consistent with the forsterite grains with mean particle radii of $0.15 - 0.35$ μm used by Hiranaka et al. (2016) to explain the observed spectra of reddened L dwarfs via extinction from a haze layer.

1.4.4 Surface-Mapping Techniques

Variability monitoring probes the existence of atmospheric inhomogeneities. Various techniques have been developed to probe the shape and extent of these atmospheric features across the surface of a brown dwarf.

Doppler imaging can be used to map the surface features of a brown dwarf.

The technique of Doppler imaging relies on the varying Doppler shifts across the face of a rotating object and has been widely used to map the inhomogeneous surfaces of many rapidly rotating stars (Vogt et al., 1987; Rice et al., 1989). This technique exploits the relation between wavelength position across a rotationally broadened spectral line due to Doppler shift and spatial position across the disk. Atmospheric inhomogeneities produce distortions in spectral lines. If the brown dwarf rotates fast enough that the shape of its spectral lines are dominated by rotational Doppler broadening, a high degree of correlation exists between the position of any distortion within a line profile and the position of the corresponding spot on the stellar surface. Thus, a high-resolution spectrum is essentially a one-dimensional image of the star, completely blurred in latitude. If more high-resolution spectra are taken as the object rotates, all of the one-dimensional images can be combined into a two-dimensional image of the brown dwarf surface if the rotational period is known. Crossfield et al. (2014) reported the first Doppler image of a brown dwarf, Luhman 16B. The short rotational period ($\sim$ 4.9 hr), high-amplitude variability and its proximity to Earth makes Luhman 16B the first substellar object suitable for Doppler imaging. The high-resolution spectra were used to produce a global map of Luhman 16B, shown in Figure 1.15. The map clearly depicts a bright near-polar region and a darker mid-latitude area consistent with large-scale cloud inhomogeneities. Furthermore, the atmospheric features obtained from this map are consistent with the variability amplitude observed. With current instruments, this technique can only be applied to $1-2$ bright brown dwarfs, however with the development of giant ground-based telescopes, Doppler imaging will become feasible for many dozens of brown dwarfs and for a handful of the brightest directly-imaged planets (Crossfield, 2014).

Other techniques utilise the lightcurves of variable brown dwarfs to reconstruct their surface features. Kostov & Apai (2013) explored the use of lightcurve inversion (LCI) as a tool to probe the surface brightness distribution and cloud properties of directly-imaged planets. The authors demonstrate that simulated lightcurves can be inverted to a correct, low-resolution longitudinal map of a giant planet. They also find that extremely large telescopes and *JWST* will provide the spectral mapping data necessary for this work. Apai et al. (2013) obtained time-resolved *HST* spectra of two variable brown dwarfs, 2M2139+10 and SIMP 0136+09 and modelled their surface brightness distributions using the *Stratos* mapping routine. This routine describes features as elliptical spots with their axis parallel to the rotational direction (an assumption motivated by simulations of hydrodynamical turbulent flows in rotating spheres; Cho & Polvani, 1996).

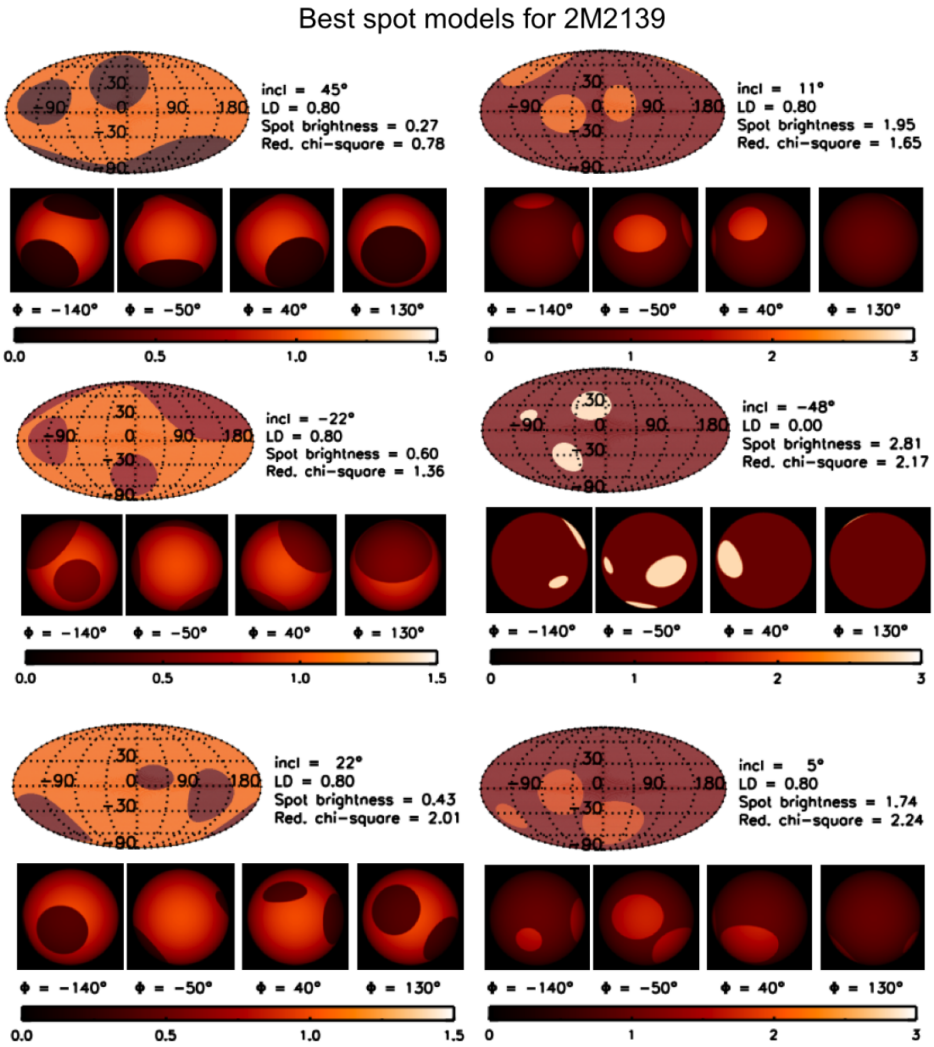

Figure 1.16 Best-fitting surface maps of 2M2139 from Apai et al. (2013). The surface maps produced by *Stratos* are degenerate with inclination, however several of the properties of the solutions are similar, including relative spot sizes and total covering fractions.

The routine produces surface maps that best reproduce the observed lightcurves. For 2M2139+10 and SIMP 0136+09, they found that only two kinds of clouds are needed to describe the observed variability – a thin "background" cloud at low altitudes and a thick higher altitude cloud that needs to be distributed in at least three spots. As shown in Figure 1.16, these maps are degenerate with inclination, as multiple maps with different inclinations reproduce the observed lightcurves equally well. Because of this degeneracy in inclination, no unique solution is found, however several properties of the solutions are similar, including relative spot sizes and total covering fractions.

Karalidi et al. (2015) present the MCMC surface-mapping code *Aeolus*. This

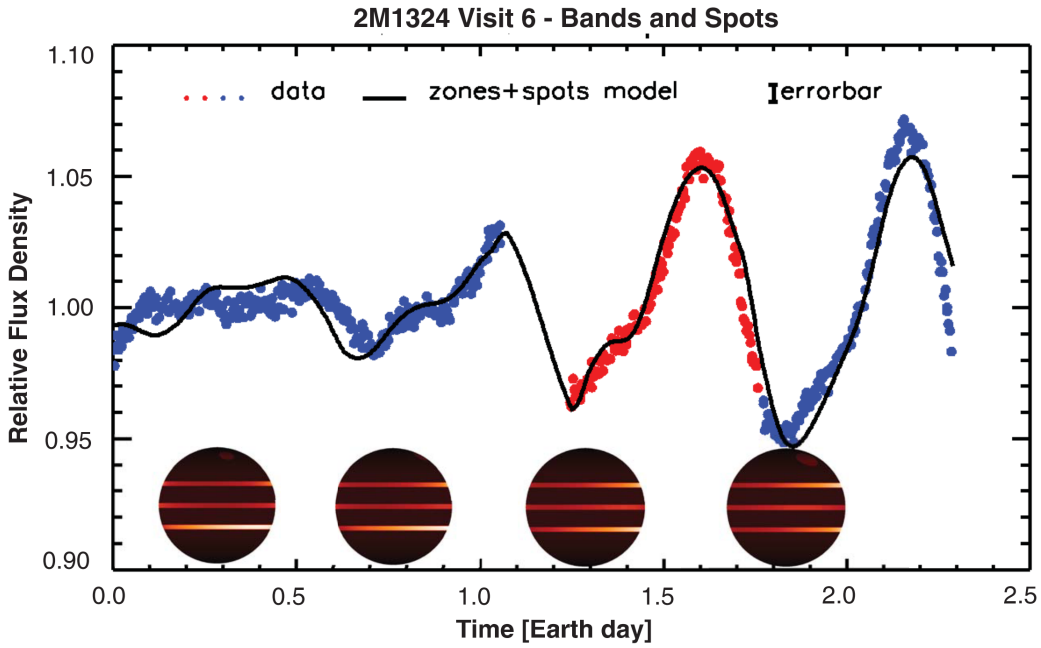

Figure 1.17 Lightcurve and best-fitting *Aeolus* model of 2M1324. The evolving lightcurve was modelled using three sinusoidally modulated bands and a bright spot. The prominent lightcurve evolution is dominated by the beating effect caused by two bands with slightly different periods. The four disks show the hemisphere facing the observer at the times corresponding to the centre of each disk. Figure from Apai et al. (2017).

code maps the surface features of an ultracool atmosphere per observational wavelength using observed rotational lightcurves and assuming fixed values for the limb-darkening parameters and inclination angle. *Aeolus* was tested using *HST* lightcurves of Jupiter, finding that the Great Red Spot and a major 5 μm hot spot were reproduced in the surface maps. Karalidi et al. (2015) also use *Aeolus* to determine the brightness distribution of the brown dwarfs 2M2139+10 and SIMP 0136+09, finding that three spots are necessary to reproduce the observed lightcurves, in agreement with Apai et al. (2013). More recently, Karalidi et al. (2016) presented an updated version of *Aeolus*, which fits the inclination angle and limb darkening of the target as free parameters. In this paper the authors use *Aeolus* to model both components of the brown dwarf binary Luhman 16AB. They constrained the inclination of both brown dwarfs, thus removing degeneracy in their spot models.

Apai et al. (2017) presented an alternative explanation for brown dwarf variability, suggesting that large-scale variability is caused by longitudinal bands with sinusoidal surface brightness modulations, with elliptical spots adding localized

bumps to the lightcurve. The longitudinal bands can have slightly different periods, due to differential rotation. Thus, they can interfere to produce lower-frequency modulations, or beat patterns in the lightcurve. The beat patterns produce high-amplitude variability when the waves are in phase and can produce periods of apparent quiescence when waves are out of phase. They can also produce double-peaked variability when the phase shift between waves is close to 90°. The variability of three brown dwarfs were modelled using an adapted version of *Aeolus*, finding that three longitudinal bands could explain the lightcurve in each case. The lightcurve of 2M1324 and the best-fitting model are shown in Figure 1.17. The evolving lightcurve was modelled using three sinusoidally modulated bands and a bright spot. The prominent lightcurve evolution is dominated by the beating effect caused by two bands with slightly different periods. This new interpretation can explain three types of common behaviour that was previously unexplained: (1) single-peaked lightcurves splitting into double peaked lightcurves (Radigan et al., 2012; Yang et al., 2016); (2) large amplitude changes over short timescales (Yang et al., 2016); (3) recurring features in an otherwise irregularly evolving lightcurve (Karalidi et al., 2016).

1.5 Atmospheric Dynamics in Brown Dwarf Atmospheres

The variability observations discussed in Section 1.4 provide evidence for vigorous motion in the atmosphere of brown dwarfs. In fact, it is thought that the atmospheric dynamics present in brown dwarf atmospheres may be similar to those observed on giant planets in the Solar System. Since heterogenous condensate clouds are essentially tracers of the atmospheric circulation, variability monitoring provides a useful tool in probing the dynamics of a brown dwarf atmosphere.

Brown dwarfs are rapid rotators (Zapatero Osorio et al., 2006), and this exerts a major influence on their atmospheric dynamics. The rotation significantly effects the convective properties of the interior. The interaction of convection with the overlying, stably stratified atmosphere will generate a wealth of atmospheric waves. The interaction of these waves with the mean flow leads to significant atmospheric circulation at regional to global scales (Showman & Kaspi, 2013).

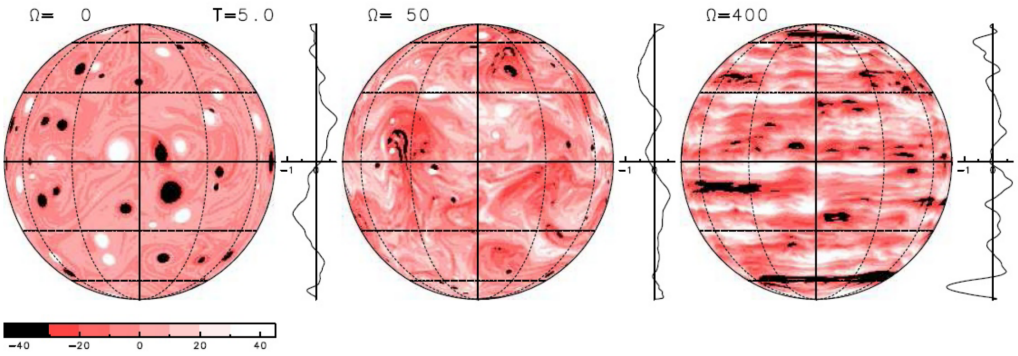

Figure 1.18 Relative vorticity for three 2D non-divergent simulations on a sphere initialised from small-scale isotropic turbulence. The three simulations are identical except for the rotation rate, which is zero on the left, intermediate in the middle and fast on the right. The final state consists of isotropic turbulence in the non-rotating case but banded flow in the rotating case due to the Rhines effect. Figure from Showman et al. (2010).

The nature of atmospheric flow depends on the Rossby number, which is the ratio of the advective and Coriolis accelerations, $R_0 = U/\Omega L$, where U is a characteristic wind speed, L is a characteristic length scale of the flow, and Ω is the rotation rate. If $R_0 \ll 1$, the flow is rotationally dominated, if $R_0 \sim 1$, rotation is important but not dominant, while if $R_0 \gg 1$, the rotation plays a minor role. While the wind speeds and flow length scales are currently unknown, Showman & Kaspi (2013) use reasonable estimates to find that in general, $R_0 \ll 1$ for brown dwarf atmospheres. Thus, it is likely that the large-scale circulation on brown dwarfs will be rotationally-dominated. In this case the flow is known as geostrophic flow, and is governed by the balance between the Coriolis force and pressure-gradient forces (Pedlosky, 1987). The Coriolis force is a force exerted on a mass moving in a rotating system, acting perpendicular to the direction of motion and to the axis of rotation. For example, on Earth the Coriolis force deflects air currents to the right in the northern hemisphere and to the left in the southern hemisphere.

The Coriolis parameter is defined as $f = 2\Omega \sin\phi$, where ϕ is the latitude. Rhines (1975) realised that the variation of f with latitude leads to an anisotropy, causing elongation of structures in the East-West direction relative to the North-South direction. This anisotropy can cause the energy to reorganise into East-West oriented jet streams with a characteristic latitudinal length scale, known as the

Rhines length:

$$L_\beta = \pi \left(\frac{U}{\beta} \right)^{1/2} \tag{1.4}$$

The Rhines length scale can be thought of as a boundary between the regimes of vortices and jets. For length scales smaller than the Rhines length, vorticity advection dominates while for length scales larger than the Rhines length, East-West oriented bands form (Showman et al., 2010). Numerous idealised studies of 2D turbulent flow forced by injection of small-scale turbulence have demonstrated that a banded flow pattern comprised of East-West jet streams spontaneously emerges from the interaction of atmospheric turbulence with planetary rotation (Cho & Polvani, 1996; Zhang & Showman, 2014; Showman et al., 2010). Figure 1.18 shows simulations by Showman et al. (2010) showing the vorticity on three spheres of varying rotation rate. In the non-rotating case, the final state consists of isotropic turbulence but in the rotating case the final state consists of banded zonal jet streams. Since heterogeneous clouds trace atmospheric flows, careful studies of both variability monitoring and atmospheric circulation models will reveal insights into the atmospheric dynamics of brown dwarfs.

1.6 Directly-Imaged Planets

Over the past $\sim$ 20 years, our knowledge of exoplanets has increased dramatically. The majority of giant planets discovered to date have been detected by indirect methods such as radial velocity and transits. Mayor et al. (2011) found that 50% of solar-type stars host planets on orbits with periods shorter than 100 days. The large numbers of detected exoplanets have revealed insights into formation mechanisms, suggesting that RV and transit planets were predominantly formed by the accretion of gas onto a solid core ("core accretion"; Pollack et al., 1996). These studies have also shown that planet scattering and/or migration is needed to explain the population of close-in, retrograde and/or high eccentricity planets; hence, dynamical evolution plays an important role in the building of planetary systems (Lagrange, 2014). Additionally, in a few cases, transit spectroscopy has allowed the first explorations of the atmospheres of hot Jupiters (Sing et al., 2016).

Direct-imaging is necessary to characterise the outer regions of planetary systems, and has already played a critical role in probing separations $>$ 10 au and masses $>$ 1 $M_{\rm Jup}$ (Bowler, 2016). For example, RV techniques are not suitable for

studying the orbits of Saturn, Uranus and Neptune on reasonable timescales, given their rotational periods (Lagrange, 2014). In addition to probing unexplored orbital separations, direct-imaging captures photons that originated in planetary atmospheres, providing unparalleled information about the physical properties of exoplanets.

1.6.1 Direct Imaging Surveys

Direct imaging of exoplanets is an extremely challenging task due to the intrinsic faintness of an exoplanet and the small angular separation between an exoplanet and its bright host star. Detecting exoplanets at separations $< 1''$ requires diffraction-limited images delivered by large aperture ($\sim$ 10 m) telescopes (Lagrange, 2014). A large number of techniques have been developed to attenuate starlight and to suppress artefacts caused by optical defects. These techniques include coronography, saturated imaging, spectral differential imaging and angular differential imaging (Biller, 2013).

As with brown dwarfs, theoretical models predict that giant planets are substantially more luminous during the early stages of their evolution, and thus young exoplanets are more readily observable. For this reason, the majority of imaging surveys target stars that are members of nearby young moving groups (e.g. Biller et al., 2007; Rameau et al., 2013).

Overall, a few hundred targets have been observed in direct imaging surveys, however only a handful of discoveries have been made (Bowler, 2016). The large number of null detections have made it clear that massive planets on wide orbits are extremely rare. Chauvin et al. (2004) imaged the first planetary-mass companion, 2M1207b. This 5 $M_{\rm Jup}$ L3 companion orbits a 25 $M_{\rm Jup}$ brown dwarf in the 10 Myr TWA moving group. With a mass ratio of $\sim$ 0.2 and separation of $\sim$ 41 au, this system is an outlier compared to brown dwarf mass ratio and separation distributions in the field (Burgasser et al., 2007). The unusual spectral shape and extremely red colours of 2M1207b were the first observational indications that the directly-imaged planets would differ from their field brown dwarf counterparts (Barman et al., 2011). This was followed by the detection of four exoplanets orbiting the star HR8799 (Marois et al., 2008, 2010). The HR8799 system is the only directly-imaged system to date hosting more than one exoplanet. Like 2M1207b, some of their spectral features were rather surprising. The HR8799 planets show remarkably red colours compared to the field brown

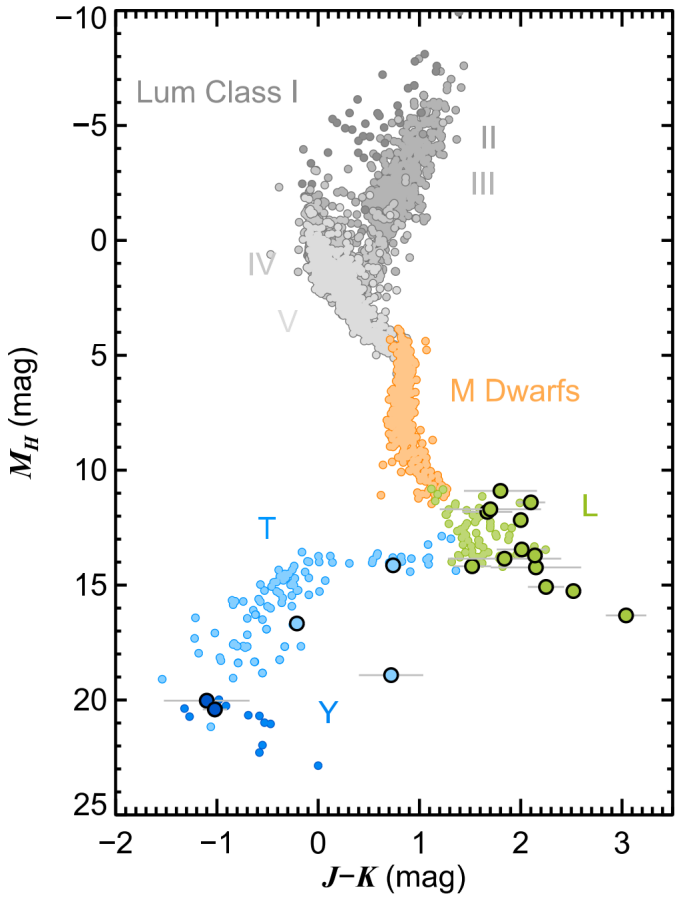

Figure 1.19 Directly-imaged companions near and below the deuterium burning limit on the near-infrared colour-magnitude diagram. The directly-imaged planets (bold circles) extend the the L dwarf sequence to redder magnitudes and fainter absolute magnitudes due to a delayed transition from cloudy atmospheres to condensate-free T dwarfs at low surface gravities.

dwarf population (Barman et al., 2011). Furthermore, their spectra showed no evidence of methane, despite their low temperatures. More surveys have detected 8 "close-in" planets (< 100 au), 8 "wide-orbit" planets (> 100 au), 2 exoplanets orbiting brown dwarfs and ~ 30 candidate exoplanets and companions close to the deuterium burning limit (Bowler, 2016).

1.6.2 Properties of the Directly Imaged Planets

With comparable temperatures but lower masses, young directly-imaged planets were expected to share similar atmospheric properties to old, field L and T spectral type dwarfs, but initial results have yielded some surprises. Most

directly-imaged planets appear much redder in the near-IR and mid-IR than their higher mass brown dwarf counterparts at similar $T_{\rm eff}$ (Barman et al., 2011; Skemer et al., 2012). Furthermore, the $T_{\rm eff}$ at which young exoplanets transition between spectral types is lower than for the field brown dwarf population (Barman et al., 2011). It appears that the directly-imaged planets such as HR8799bcd and 2M1207b may share a temperature with T-type brown dwarfs but exhibit the dusty appearance of L-type brown dwarfs. The position of the directly-imaged exoplanet companions near and below the deuterium burning limit on a colour-magnitude diagram are shown in Figure 1.19. The near-IR colours of these objects are much redder than the population of field brown dwarfs, and the L sequence extends to lower luminosities. These discrepancies may be explained by the persistence of thick, dusty clouds to lower temperatures as well as non-equilibrium chemistry (Barman et al., 2011; Marley et al., 2012), likely to result from the lower surface gravity of young exoplanets. In fact, Bonnefoy et al. (2016) demonstrate that the effects of low surface gravity for the HR8799 d and e planets can explain the deviation of their spectral energy distributions (SEDs) with respect to those of standard L and T dwarfs.

1.7 Low-Gravity Brown Dwarfs

Any given spectral type is comprised of a large variety of objects. For example, the L0 spectral type encompasses old, stably burning stars of fixed mass ($M \sim 0.085\ M_{\odot}$, $t \sim$ few Gyr); to moderate-age, high-mass brown dwarfs ($M \sim 0.075\ M_{\odot}$, $t \sim$ few 100 Myr); to very young, low-mass brown dwarfs ($M < 0.020\ M_{\odot}$, $t <$ 20 Myr) (Kirkpatrick, 2005). To identify the lowest-mass brown dwarfs, we must first break the mass–age degeneracy by finding brown dwarfs that are members of young moving groups and/or by analysing their spectra to detect signatures of low-gravity.

1.7.1 Membership in Young Moving Groups

The discovery of young moving groups has provided us with a sample of age-calibrated brown dwarfs, allowing us to break the mass–age degeneracy and to identify isolated planetary-mass analogues to the directly-imaged planets (e.g. Allers et al., 2016). Nearby young comoving groups are sparse, gravitationally

unbound associations consisting of a few dozen stars and brown dwarfs within $\sim$ 150 pc of the Sun with ages ranging from 5 to a few hundred Myr. These groups form in coeval, cospatial and comoving molecular clouds and spatially disperse over time. We can link them via their common position and space motion within the Galaxy. Due to a projection effect, they display an organised motion in the sky moving toward a convergent point and this can be used to discriminate bona fide members from field stars (Malo et al., 2013; Rodriguez et al., 2013).

A range of algorithms have been built to determine the probability that a given brown dwarf is a member of a known association. These include the relatively simple convergent point tool (Rodriguez et al., 2013) as well as the Bayesian inference tools BANYAN I, II, VII and Σ (Malo et al., 2013; Gagné et al., 2014c, 2015c, 2018a) and LACEwING (Riedel et al., 2017). These tools have made it possible to identify hundreds of candidates and confirmed members of nearby associations of stars, spanning the planetary to stellar-mass domains.

1.7.2 Spectral Signatures of Youth

To first order, objects from low-mass stars to the lowest mass brown dwarfs are believed to have similar radii (Burrows et al., 2001), so their gravities are dependent on their mass. However, the youngest (and lowest mass) brown dwarfs will not yet have contracted to their final radii, meaning that these objects are larger than their higher mass counterparts at similar temperatures. This further widens the gap between high-gravity and low-gravity brown dwarfs. Figure 1.20, taken from Burrows et al. (1997), shows that for a late-L type object, $\log(g)$ can vary from 3.5 for a 3 Myr brown dwarf of mass 0.003 $M_{\odot}$ to 5.5 for a 3 Gyr brown dwarf with a mass of 0.07 $M_{\odot}$. This large range in gravity is evident through gravity-sensitive features in brown dwarf spectra.

Pressure broadening caused by collisions is dependent on the temperature and gravity of the atmosphere. Objects with lower surface gravity will have less pressure broadening in their atmospheres, resulting in weaker absorption lines in the optical and near-IR (Kirkpatrick et al., 2006; Allers & Liu, 2013). Additionally, the H-band continuum of low-gravity objects displays a typical triangular shape due to a combination of less FeH absorption and decreased H_2 collision induced absorption (Allers & Liu, 2013). Furthermore, young, low-gravity objects tend to have near-IR colours that are much redder than their field brown dwarf counterparts (Liu et al., 2016; Faherty et al., 2016). This is

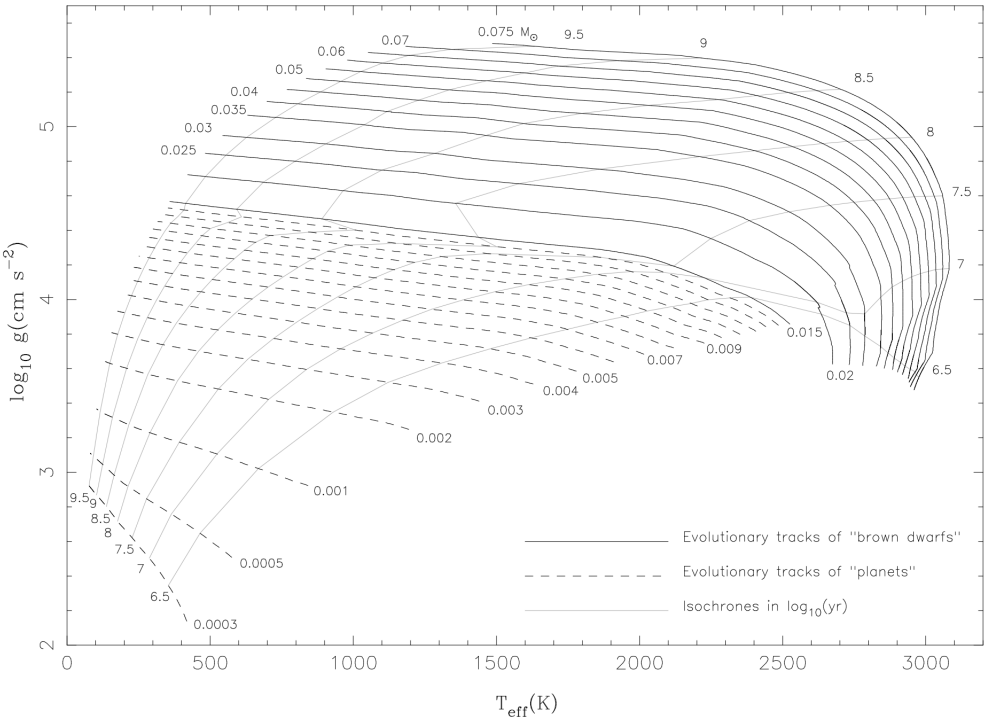

Figure 1.20 Evolutionary tracks of $\log_{10} g$ vs. $T_{\rm eff}$ for brown dwarfs (solid lines) and planetary-mass objects (dashed lines). Gray lines show isochrones and are labelled in $\log_{10}$yr. In all cases, gravity increases with time due to contraction. For a late-L objects ($\sim$ 1600 K), $\log(g)$ can vary from 3.5 for a 3 Myr brown dwarf of mass 0.003 $M_{\odot}$ to 5.5 for a 3 Gyr brown dwarf with a mass of 0.07 $M_{\odot}$. This large range in gravity can be seen in the spectra of brown dwarfs. Figure from Burrows et al. (1997).

due to two complementary processes affecting the formation of clouds in low-gravity atmospheres. Firstly, Helling et al. (2011) demonstrate that the cloud scale height increases with decreasing surface gravity in cloudy atmospheres. These thick, dusty clouds obscure a greater portion of the flux from deeper, hotter layers in the atmosphere, reducing the amount of emergent flux at the shorter wavelengths in the near-IR. Secondly, atmospheric cloud models from Ackerman & Marley (2001) and Helling et al. (2008) predict that mean cloud particle sizes are larger in low-gravity atmospheres. For $T_{\rm eff}$ = 650 K, particle radii for a $\log g = 4.5$ atmosphere can be 10 times larger than that of a $\log g = 5.5$ atmosphere (Burgasser et al., 2010). These larger particles are more efficient at scattering than the sub-micron particles present in high-gravity atmospheres and thus further reduce the emergent flux from deeper layers. Furthermore, Marley et al. (2012) shows that these clouds will persist to cooler effective temperatures in lower gravity objects than higher-gravity dwarfs.

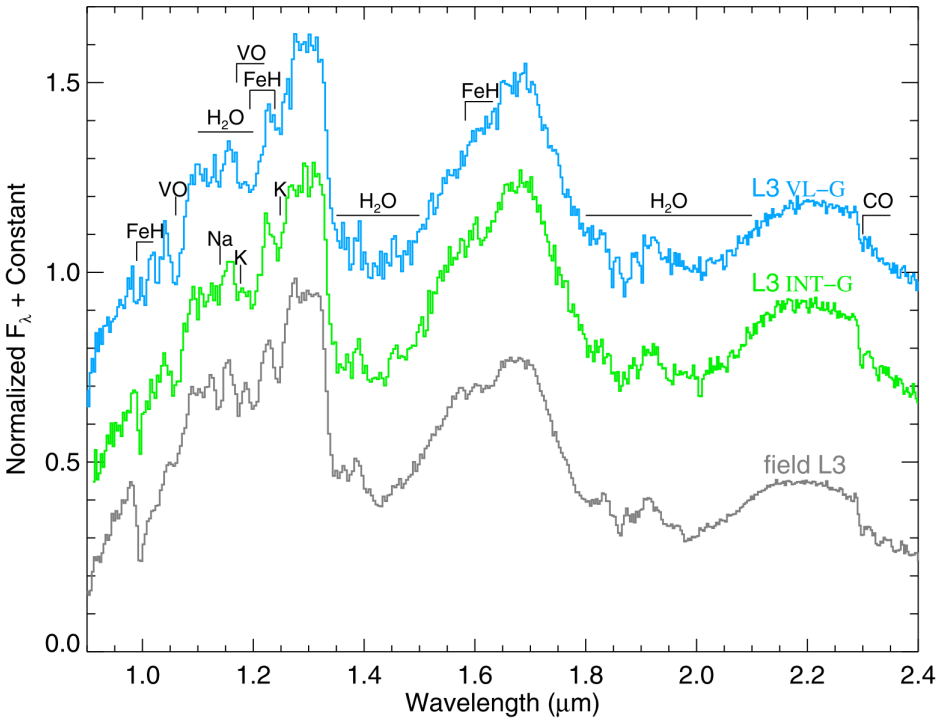

Figure 1.21 Low-resolution spectra showing the IR gravity sensitive features for L3 objects. FLD-G, INT-G and VL-G correspond to objects with normal gravity, intermediate gravity and very low-gravity respectively. FeH, Na I and K I features are weaker and VO is stronger at lower gravities. The *H*-band continuum shows a distinct triangular shape at lower gravities. Figure from Allers & Liu (2013).

These effects can be quantified by building a grid of spectra across a wide spread of age – in star forming regions and clusters ranging from the Orion Nebula (few Myr), to the Pleiades ($\sim$ 125 Myr), as companions to young field stars and as old field objects ($\sim$ few Gyr) (Kirkpatrick, 2005). Cruz et al. (2009) present a spectral classification scheme for L0-L5 brown dwarfs that includes three gravity classes, based on gravity sensitive features in their optical spectra. The three gravity subtypes α, β and γ, denote objects of normal gravity, intermediate gravity and very low gravity respectively. Gagné et al. (2015c) use optically anchored IR spectral average templates for classifying the gravity subtype for L0-L9 dwarfs. This method also assigns α, β and γ subtypes for each object. Allers & Liu (2013) present an index-based gravity classification method that is based on FeH, VO, K I, Na I and *H*-band continuum shape in the infrared. This gravity classification scheme assigns FLD-G, INT-G, VL-G for normal, intermediate and very-low gravity respectively. Figure 1.21 shows the behaviour of these gravity sensitive features in three L3 type objects. These gravity classification systems have been used

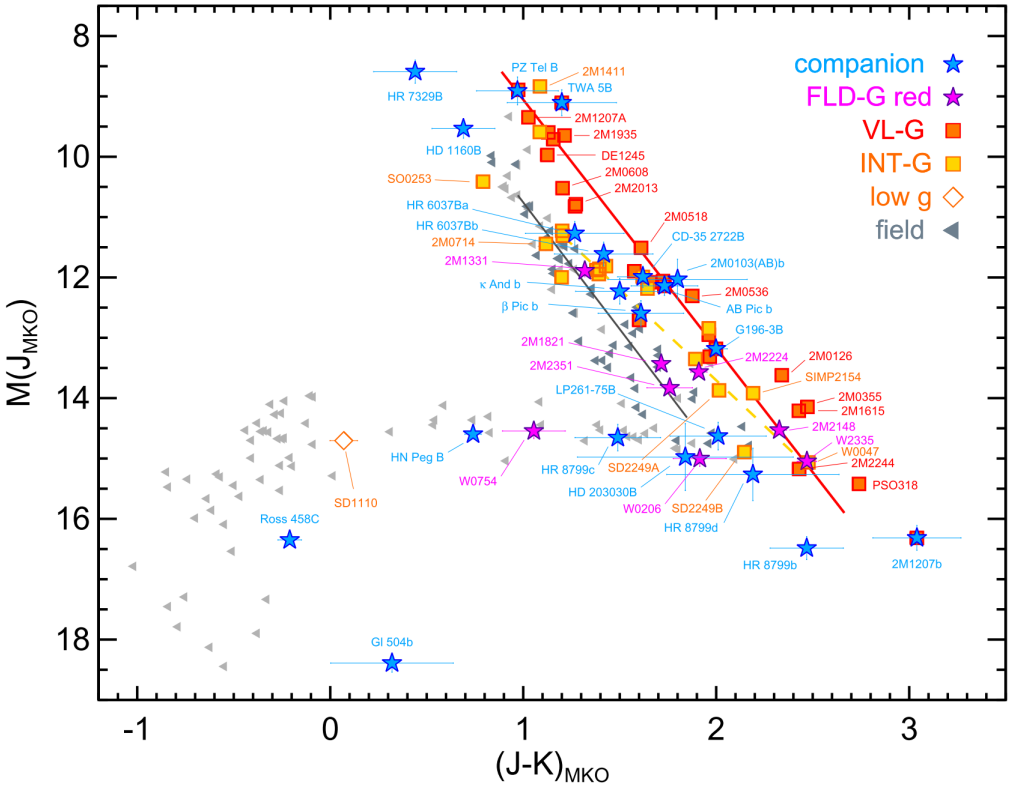

Figure 1.22 Colour-magnitude digram showing young companions (blue stars) and free-floating, low-gravity objects (orange and yellow squares for VL-G and INT-G respectively). Field brown dwarfs are shown in grey. Both the young companions and free-floating objects appear redder than the field brown dwarf population, and the L spectral sequence extends to lower luminosities than is observed for the field brown dwarf population. Figure from Liu et al. (2016).

to identify potential low-gravity objects (Cruz et al., 2009; Allers & Liu, 2013), and combined with moving group membership analysis to identify a population of age-calibrated, bona fide low-gravity brown dwarfs and free-floating planetary-mass objects (Liu et al., 2016; Faherty et al., 2016). These objects have radii, masses, temperatures and spectra that overlap with the population of directly-imaged planets, and can provide insight into the atmospheres of the exoplanet companions.

1.7.3 Low-Gravity Brown Dwarfs as Exoplanet Analogues

Figure 1.22 shows the position of intermediate-gravity and low-gravity free-floating objects on a colour-magnitude diagram, identified using the techniques discussed in Sections 1.7.1 and 1.7.2. These free-floating planetary-mass objects

have temperatures, spectral types and colours that overlap with the directly-imaged companions (Liu et al., 2016; Faherty et al., 2016), and can thus be referred to as "exoplanet analogues". The exoplanet analogues have unusually red colours and a fainter absolute magnitudes when compared to their older spectral counterparts with field surface gravities (Liu et al., 2016). As such, they more closely resemble the colours of the directly-imaged exoplanets. Without the presence of a bright host star, the exoplanet analogues are much easier to observe, and thus are excellent candidates for in depth characterisation.

1.7.4 Variability Studies of Exoplanet Analogues

We have seen that variability is common among L and T spectral type brown dwarfs. Therefore, we expect that the directly-imaged exoplanets will exhibit similar variability. To date, only a handful of directly-imaged planets are amenable to variability studies using planet-finding cameras such as SPHERE and GPI. Apai et al. (2016) obtained time-resolved photometric monitoring of the HR8799 planets using SPHERE at the VLT and attained a photometric precision of $\sim 10\%$. This level of photometric precision would thus be insufficient to detect variability at levels of a few percent. Fortunately, we can probe low-level variability in a larger population of young, low-gravity brown dwarfs. The free-floating exoplanet analogues are ideal candidates for extensive variability studies not currently possible for the directly-imaged companions. As we have seen, surface gravity is a key parameter in the description of dust behaviour in brown dwarf atmospheres. As dust-bearing clouds of varying thicknesses are often invoked to explain variability, it is likely that the variability properties of substellar objects exhibit a gravity dependence. Indeed, Metchev et al. (2015) included a sample of intermediate-gravity L dwarfs in their *Spitzer* variability survey, finding tentative evidence for a correlation between low-gravity and high-amplitude variability. Beyond this small study of variability in moderate to low gravity objects, there have been no other surveys for variability in exoplanet analogues to date.

1.8 Outline of Chapters 2-5

The work presented in this thesis explores photometric variability in substellar atmospheres, with a focus on the role of surface gravity in the variability properties of young, low-gravity brown dwarfs. In Chapter 2 I present the first detection of variability in a planetary-mass object, PSO 318.5–22. I additionally present subsequent ground- and space-based multi-wavelength followup monitoring. I use the followup observations to measure the rotational period and to investigate the vertical atmospheric structure of PSO 318.5–22. In Chapter 3 I supplement the existing brown dwarf variability data in the literature with new rotational velocities to reveal relations between inclination angle, variability amplitude and colour, finding that the inclination angle of a brown dwarf significantly affects its variability properties and atmospheric appearance. In Chapter 4 I present *Spitzer* variability monitoring of the three lowest-mass members of the AB Doradus moving group. I detect variability in two late-L exoplanet analogues, W0047 and 2M2244 and place upper limits on the variability of the T5.5 planetary-mass object SDSS1110. Finally, Chapter 5 describes the first large survey for photometric variability in young, low-gravity brown dwarfs. I show that the L type exoplanet analogues are more variable than their higher mass field brown dwarf counterparts, likely due to their lower gravity. This thesis has contributed to our understanding of variability in both the field brown dwarf population, and in low-gravity exoplanet analogues. The work presented here will inform future variability studies of the directly-imaged planets.

Chapter 2

Variability in a Young, L/T Transition Planetary-Mass Object

2.1 Abstract

As part of a large ground-based survey for photometric variability in young free-floating planets and low-mass brown dwarfs (presented in Chapter 5), we detect significant variability in the young, free-floating planetary-mass object PSO J318.5–22, likely due to inhomogeneous cloud cover. A member of the 23 ± 3 Myr β Pictoris (Mamajek & Bell, 2014) moving group (Allers et al., 2016), PSO 318.5–22 has $T_{\rm eff} = 1160^{+30}_{-40}$ K and a mass estimate of 8.3 ± 0.5 $M_{\rm Jup}$ (Allers et al., 2016). PSO 318.5–22 is intermediate in mass between 51 Eri b and β Pic b, the two known exoplanet companions in the β Pic moving group. This is the first detection of weather on an extrasolar planetary-mass object. Among L dwarfs surveyed at high-photometric precision ($< 3\%$) this is one of the highest amplitude variability detections. In this chapter we present the initial ground-based J-band detections of variability obtained as part of a larger survey as well as subsequent multi-wavelength monitoring over three consecutive nights. The long baseline of the followup observations enables us to measure a rotational period of 8.45 ± 0.05 hr for PSO 318.5–22.

We additionally present simultaneous *HST* and *Spitzer* variability monitoring, detecting significant variability across all wavelengths. We measure a phase shift of $200 - 210^{\circ}$ between the near-IR and mid-IR lightcurves, likely due to the

presence of varying longitudinal structure at different atmospheric depths. We observe a decrease in variability as a function of increasing wavelength, as has been observed in field brown dwarfs. We use the *Spitzer* lightcurve to measure the rotational period of PSO 318.5–22, finding a period of 8.61 ± 0.06 hr, close to the period derived from ground-based monitoring. Given the low surface gravity of this object, the high amplitudes observed in the near-IR and mid-IR preliminarily suggests that planetary-mass objects may be more variable than their higher mass brown dwarf counterparts, although observations of a larger sample are necessary to confirm this.

2.2 Introduction

Of the currently known, free-floating planetary-mass objects, PSO 318.5–22 (Liu et al., 2013) is the closest analogue in properties to directly-imaged exoplanet companions. PSO 318.5–22 is a confirmed member of the 23 Myr (Mamajek & Bell, 2014) β Pictoris moving group (Allers et al., 2016) and a close analogue to directly-imaged exoplanet companions. With an estimated mass of 8.3 ± 0.5 $M_{\rm Jup}$, PSO 318.5–22 is intermediate in mass between 51 Eri b ($\sim$ 2 $M_{\rm Jup}$ Macintosh et al., 2015) and β Pic b ($\sim$ 11 $M_{\rm Jup}$ Lagrange et al., 2010; Bonnefoy et al., 2014), the two known exoplanet companions in the β Pic moving group. Furthermore, with similar magnitudes, colours and spectra, PSO 318.5–22 shares a strong physical similarity with young, dusty planets such as HR 8799bcd and 2M1207b (Marois et al., 2008, 2010). Variability studies are extremely difficult for directly-imaged planets within $1''$ of their host star due to the extreme contrast ratio between star and planet. Thus only a handful are suitable for variability monitoring. However, since PSO 318.5–22 is a free-floating object, it enables high precision characterisation that is not currently possible for exoplanet companions to bright stars.

In this chapter we report the first detection of photometric variability in a young, L/T transition planetary-mass object, PSO 318.5–22. Time-resolved photometric variability monitoring has been a key probe of non-isotropic cloud structures in brown dwarf atmospheres. Recent space and ground-based surveys have revealed that variability is common across the full range of L and T spectral types (Metchev et al., 2015; Buenzli et al., 2014; Radigan et al., 2014; Wilson et al., 2014). Variability has not yet been probed for young, planetary-mass objects. With similar temperatures and spectral types to the previously studied population

Table 2.1 NTT/SofI observations of PSO 318.5–22.

Date	Filter	DIT	NDIT	On-Sky Time
2014 Oct 09	J_S	10 s	6	5.15 hr
2014 Nov 09	J_S	15 s	6	2.83 hr
2014 Nov 10	K_S	20 s	6	3.16 hr

of variable brown dwarfs, we expect the populations of directly-imaged planets and free-floating planetary-mass objects to demonstrate similar variability. For the majority of directly-imaged exoplanets, the contrast between the host star and planet make it difficult to obtain sufficiently high S/N photometry to allow detailed studies of their variability, thus only a handful are amenable to variability studies. In fact, Apai et al. (2016) explored the rotational variability of the HR8799 planets, reaching a photometric precision of $\sim$ 10%, thus insufficient to detect variability on levels of a few percent. However, young brown dwarfs provide an excellent analogue to directly-imaged exoplanets. Recently, a handful of young brown dwarfs with colours and magnitudes similar to directly-imaged planets have been discovered (Gagné et al., 2015c; Best et al., 2015; Schneider et al., 2017). Interestingly, (Metchev et al., 2015) report a tentative correlation between low surface-gravity and high-amplitude variability in a small sample of intermediate-mass L dwarfs. The atmospheres of these young brown dwarfs can provide key insights into the atmospheres of directly-imaged planets.

Here we present the first variability detection from our photometric monitoring survey of young, low-gravity L and T dwarfs, with the goal of investigating the effects of surface gravity on variability properties. The initial observations of PSO 318.5–22 were carried out at the 3.5 m New Technology Telescope (NTT). The full survey for variability in young, low-gravity brown dwarfs is presented in Chapter 5.

2.3 Observations and Data Reduction

We obtained our initial 3 datasets for PSO 318.5–22 with NTT/SofI (Moorwood et al., 1998) in October and November 2014. SofI has a pixel scale of 0.288″/pixel and a 4.92′ $\times$ 4.92′ field of view. Observations are presented in Table 2.1. We attempted to cover as much of the rotational period as possible, however scheduling and weather constraints limited our observations to 2–5 hr on sky. In search mode, we observed in J_S, however we also obtained a K_S followup

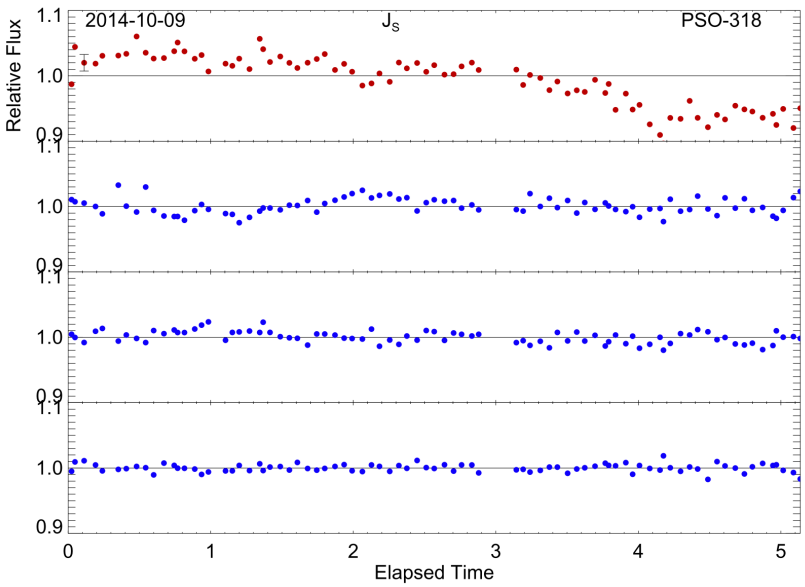

Figure 2.1 Final binned J_S lightcurve and comparison detrended reference stars from 9 October 2014. Typical error bars are shown on the first photometric point. The variability amplitude in this epoch is $> 10\%$ with a period > 5 h.

lightcurve for PSO 318.5–22. An ABBA nodding pattern was used, taking 3 exposures in each nod position. When nodding the target between two positions on the chip, care was taken to ensure that the target was accurately placed on the original pixel in each nod position. This allowed for sky subtraction, while preserving photometric stability.

Data were corrected for crosstalk artefacts between quadrants, flat-fielded using special dome flats which correct for the "shade" (illumination dependent bias) found in SofI images, and illumination corrected using observations of a standard star. Sky frames for each nod position were created by median combining normalised frames from the other nod positions closest in time. These were then re-scaled to and subtracted from the science frame. Aperture photometry for all sources on the frame were acquired using the IDL task APER.PRO with aperture radii of 4–6.5 pixels in steps of 0.5 pixels, and background subtraction annuli from 21–31 pixels.

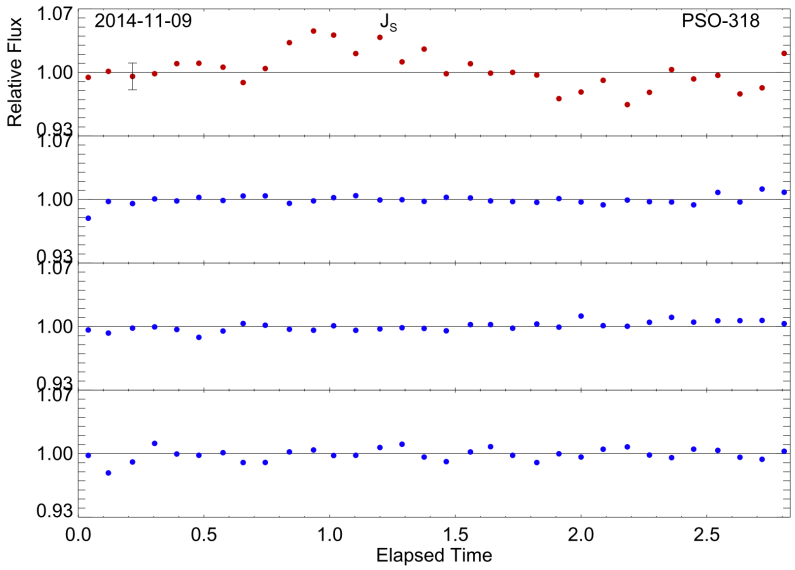

Figure 2.2 Final binned J_S lightcurve and comparison detrended reference stars from 9 November 2014. Typical error bars are shown on the first photometric point. The variability amplitude in this epoch is $> 7\%$ with a period > 3 h.

2.4 NTT/SofI Lightcurves of PSO J318.5–22

We present the final binned J_S lightcurve from October 2014 (with three detrended reference stars for comparison) in Figure 2.1 and the final binned J_S and K_S light curves from November 2014 in Figures 2.2 and 2.3.

Raw light curves obtained from aperture photometry display brightness variations due to changing atmospheric transparency, airmass and residual instrumental effects. To a very good approximation these changes are common to all stars in the field of view and can be removed via division of a calibration curve calculated from a set of iteratively chosen, well-behaved reference stars (Radigan et al., 2012). Firstly, reference stars with peak flux values below 10 or greater than 10,000 ADU were discarded. Different nods were normalised via division by their median flux before being combined to give a relative flux light curve. For each star a calibration curve was created by median combining all other reference stars (excluding that of the target and star in question). The standard deviation and linear slope for each light curve was calculated and stars with a standard deviation or slope $\sim 1.5-3$ times greater than that of the target were discarded. This process was iterated a number of times, until a set of well-behaved reference stars was chosen. Final detrended lightcurves were obtained by dividing the raw

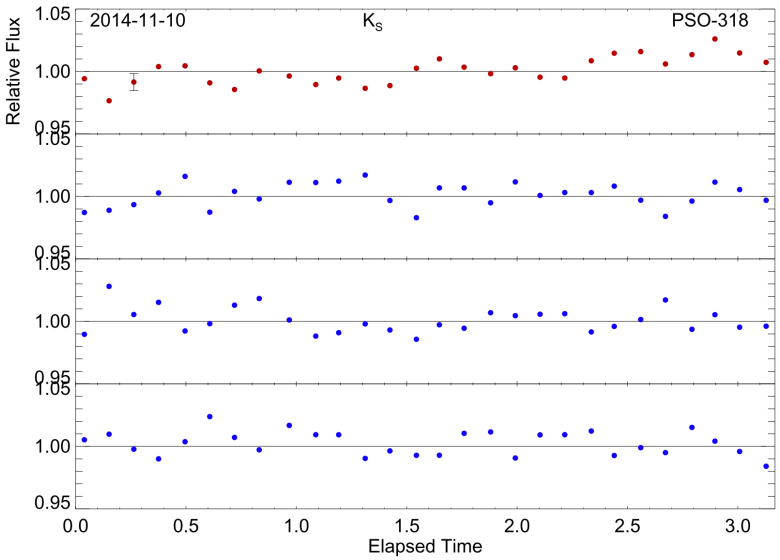

Figure 2.3 Final binned K_S lightcurve of PSO 318.5–22 and comparison detrended reference stars from 11 November 2014. Typical error bars are shown on the first photometric point. We marginally detect K_S variability with an amplitude $< 3\%$ over a 3 hr observation.

curve for each star by its calibration curve. Lightcurves were binned by a factor of 3. Error bars were calculated using the method described in Biller et al. (2013) - a low-order polynomial was fit to the final lightcurve before being subtracted to remove any astrophysical variability and the standard deviation of the subtracted lightcurve was adopted as the typical error on a given photometric point. This error is shown on each lightcurve as the error bar given on the first photometric point. As a check, we also measured photometry and lightcurves using both the publicly available aperture photometry pipeline from Radigan et al. (2014) as well as the PSF-fitting pipeline described in Biller et al. (2013). Results from all three pipelines were consistent.

We found the highest variability amplitude in our J_S lightcurve from 9 October 2014 (Figure 2.1). Over the 5 hr observation the brightness fluctuated by $10 \pm 1.3\%$. The trend seen in the lightcurve of PSO 318.5–22 is not observed in any of the reference lightcurves, and does not correlate with airmass, seeing or xy position on the chip. The flattening of the lightcurve seen at $4 - 5$ hr may be indicative of a minimum in the lightcurve, however since we have clearly not covered a full rotation period, the strongest constraint we can place on the rotational period is > 5 hr. If the variation is sinusoidal, this epoch suggests an even longer period of $> 7 - 8$ hr.

The final detrended J_S lightcurve obtained on 9 November 2014 (Figure 2.2) shows significant variability. Again we did not cover a full rotation period so can only place lower limits on the rotational period and variability amplitude of PSO 318.5–22. We find a smaller variability amplitude of $4.8 \pm 0.7\%$ and constrain the period to > 3 hr. We observe a maximum at ~ 1 hr and a potential minimum at ~ 3 hr. Again, the trend we observe in the lightcurve of PSO 318.5–22 is not observed in any of the reference stars, nor is it correlated with airmass, seeing or xy position. If we assume that the variation is sinusoidal, we find a period of ~ 3 hr, however double-peaked lightcurves have already been observed in field brown dwarfs (e.g. Radigan et al., 2012) so we can only constrain the rotational period to > 3 hr. The lightcurve exhibits a very different shape to that of Figure 2.1, possibly due to cloud evolution and dynamics. This has also been seen in various variability studies of brown dwarfs (Radigan et al., 2012; Artigau et al., 2009; Metchev et al., 2015).

The final detrended K_S lightcurve obtained on 11 November 2014 is shown in Figure 2.3. Given its extremely red colours, PSO 318.5–22 is much brighter in K_S than J_S, and thus we attain much higher photometric precision for this K_S observation (0.7% in K_S compared to $1-1.3\%$ in J_S). Fitting slopes to the target and three similarly bright reference stars, the target increases in flux by 0.9% per hour while the reference stars exhibit slopes of $0.1 - 0.6\%$ per hour (consistent with a flat line within our photometric precision). Thus, we tentatively detect a marginal variability trend of up to 3% during this 3 hr observation. As airmass increased steadily from 1.1 to 2.2 during this observation, further observations are required to confirm the K_S variability of PSO 318.5–22.

2.5 NTT/SofI Followup of PSO J318.5–22

Additional observations of PSO 318.5–22 were taken in August 2016, to more accurately constrain the rotational period and to investigate the wavelength dependence of the variability. On 9 August 2016 we used the J_S filter, followed by the K_S filter on 10 August 2016. Finally, on 11 August 2016, we observed with both filters, swapping over every 20 minutes. The observations are presented in Table 2.2. The normalised, detrended lightcurves for all three nights are shown in Figure 2.4. We detect significant variability in both bands in all three epochs.

The J_S lightcurve obtained on 9 August 2016 shows significant variability with an

Table 2.2 NTT/SofI followup observations of PSO 318.5–22.

Date	Filter	DIT	NDIT	On-Sky Time
2016 Aug 09	J_S	12 s	6	9.12 hr
2016 Aug 10	K_S	10 s	6	9.65 hr
2016 Aug 11	J_S	12 s	6	10.46 hr
2016 Aug 11	K_S	12 s	6	9.84 hr

amplitude of $2.4 \pm 0.2\%$. This is the highest amplitude detected over the course of the three nights but is much lower than the initial variability detection on 9 August 2014 (Section 2.4, Figure 2.1). This suggests that we are observing a quiescent phase of the variability of PSO 318.5–22, as has been observed previously in a number of variable brown dwarfs (Artigau et al., 2009; Radigan et al., 2012; Apai et al., 2017). The K_S lightcurve obtained on 10 August 2016 also shows significant variability. We fit a sinusoid to the lightcurve to obtain a variability amplitude of $0.48 \pm 0.08\%$ in the K_S band. We measure more precise amplitudes in the follow-up observations than the initial epochs because we cover a full rotational period during each observation.

The simultaneous J_S and K_S monitoring obtained on 11 August 2016 allows us to directly compare the variability in both bands during one rotational phase. We observe significant variability in both filters and we measure a A_K/A_J ratio of 0.36 ± 0.25. This is similar to the ratios previously observed for field brown dwarfs (Artigau et al., 2009; Radigan et al., 2012) and suggests a similar variability mechanism for the field brown dwarf and low-gravity populations.

Additionally, we find that the J_S and K_S variability is in phase. Phase shifts have been attributed to different wavelengths probing different heights in the atmosphere (Buenzli et al., 2012; Biller et al., 2013), so this suggests that the J_S and K_S bands probe similar heights in the photosphere of PSO 318.5–22.

2.5.1 Measuring the Rotational Period using MCMC

The long baseline of this observation allows us to constrain the rotational period of PSO 318.5–22. We estimate the rotational period by fitting a sinusoidal model to the full J_S lightcurve using Markov Chain Monte Carlo (MCMC) methods.

MCMC is a Bayesian inference method that provides a sampling approximation of the posterior probability distribution function (PDF). MCMC sampling produces

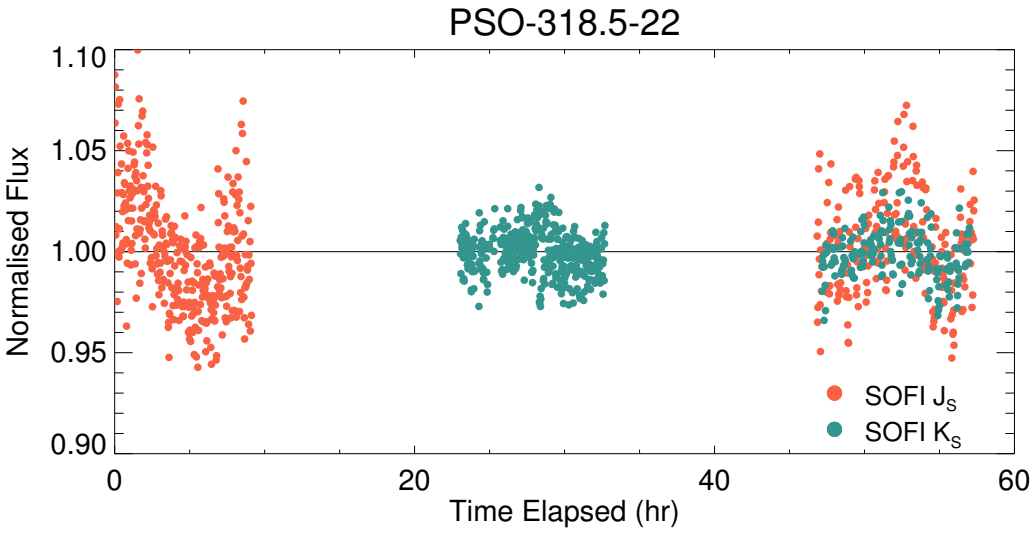

Figure 2.4 Detrended lightcurves of PSO 318.5–22 taken over three consecutive nights of follow-up observations at the NTT. Orange points show observations taken with the J_S filter and the teal points show the K_S filter observation. These three nights allow us to constrain the rotational period of PSO-318 to ~ 8.5 hr.

a chain of positions in parameter space, and these positions are an approximation of the posterior PDF. MCMC allows for more in-depth probabilistic data analysis than a simple least-squares fitting method because in addition to the mean of the posterior PDF, it naturally provides parameter uncertainties and covariances.

The simplest and most commonly used MCMC algorithm is the Metropolis-Hastings algorithm (MacKay, 2003). This is an iterative procedure that generates a single chain of parameter sets that approximate the posterior PDF. To draw samples from the posterior, MCMC starts with an initial guess. A proposal step is generated by adding some random noise, and the likelihood functions of the initial and proposed step are calculated. The ratio of the likelihood functions indicates whether the proposal step gives a better fit to the data. If the proposal step is more probable, the algorithm accepts the proposed parameters and the process repeats. If the proposed step is less probable, the proposed step is accepted with a probability based on the likelihood ratio. In the case of a rejection, the last chain position is repeated (MacKay, 2003). The Metropolis-Hastings algorithm converges to a stationary set of samples when it has located the maximum likelihood parameters. A number of steps are discarded during the initial "burn-in" phase so that the algorithm can start from unbiased parameters.

Goodman & Weare (2010) propose an affine-invariant sampling algorithm that

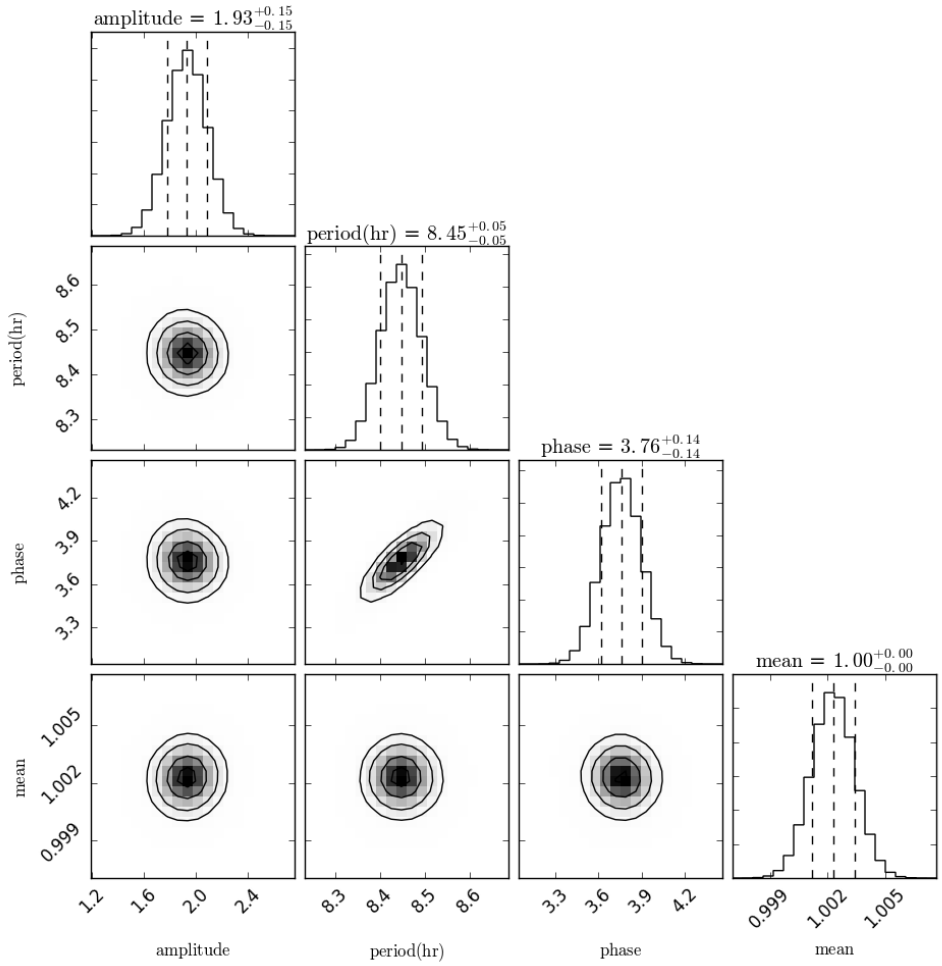

Figure 2.5 Posterior distributions obtained from MCMC analysis of NTT/SofI J_S lightcurve.

significantly outperforms standard Metropolis-Hastings algorithms, producing independent samples with a much shorter autocorrelation time (i.e. with fewer steps in the chain). This method involves simultaneously evolving an ensemble of chains, known was "walkers", where the proposal distribution for one walker is based on the current positions of the ensemble of walkers (Foreman-Mackey et al., 2013).

We use an open-source implementation of the affine-invariant ensemble sampler method (Goodman & Weare, 2010), the EMCEE package (Foreman-Mackey et al., 2013), to obtain the full posterior probability distributions for each parameter of the sinusoidal model. We use 500 walkers with 20000 steps and discard an initial burn-in sample of 1000 steps to explore the four-dimensional parameter space to model the light curve. Figure 2.5 shows the posterior distributions of the amplitude, period, phase and constant parameters of the fit. Each parameter

is well-constrained, and the MCMC method gives a rotational period of 8.45 ± 0.05 hr for PSO 318.5–22.

2.6 Simultaneous HST/Spitzer Multi-Wavelength Characterisation of PSO 318.5–22

2.6.1 Observations

Simultaneous *HST* and *Spitzer* observations of PSO 318.5–22 were obtained on $8-9$ September 2016. *Spitzer* observations lasted from UTC 2016-09-09 08:01:14 to UTC 2016-09-09 02:18:27, with 5 *HST* orbits taken from UTC 2016-09-08 11:38:59 to UTC 2016-09-08 18:44:41, for a simultaneous monitoring period of ~ 7 hr, and a *Spitzer* monitoring period of ~ 17.2 hr.

Spitzer Photometric Monitoring

Spitzer observations were taken with the Infrared Array Cameray (IRAC; Fazio et al., 2004) in Channel 2 (4.5 μm) in staring mode, with 1940×30 s frames acquired (Program ID: 12002). A short dithered sky sequence (9×30 s frames taken at 5 dither positions) preceded the science sequence, as *Spitzer* requires $\sim$ 30 minutes to settle after a target is acquired. A short sky sequence (1×30 s frame taken at 5 dither positions) was taken after the science sequence also. Following established procedure to ensure optimal photometric precision and correct for intrapixel sensitivity variations, care was taken to place the target in the IRAC "sweet spot" during the science sequence, which lies in the upper left quadrant of the full detector.

HST Spectroscopic Monitoring

HST observations were taken with the infrared channel of WFC3 with the G141 grism (Program ID: 14188). The full $123 \times 136''$ frame was used with the SPARS25 readout mode, enabling the observation of the target as well as 6 reference stars. Each 90-minute orbit yielded 59 minutes of usable exposure time, when the target was not occulted by the Earth. At the start of each orbit, a direct image was

taken in the F127M filter with exposure time of 53 s (NSAMP= 3) to determine object positions on the detector. Thereafter, a sequence of 9×278 s (NSAMP= 12) exposures were taken with the G141 grism, covering a wavelength range of $1.077 - 1.7$ μm, with resolution R = 130 at 1.4 μm. With the remaining orbital visibility, an additional 53 s (NSAMP= 3) grism exposure was taken at the end of orbit 1 and an additional 153 s (NSAMP= 7) grism exposure was taken in orbits $2 - 5$. These final, shorter exposures were significantly noisier than the other exposures and were omitted from the final analysis. One 278 s exposure in orbit 4 suffered complete data loss, as the data were not fully read off the *HST* recorder before being overwritten, and is thus omitted from the analysis.

2.6.2 Spitzer Data Reduction and Lightcurve Extraction

We extracted time-resolved photometry from the corrected Basic Calibrated Data frames from the Spitzer Science Center, processed with IRAC pipeline version 19.2.0. The *MJD_OBS* header keyword, which provides the Modified Julian Date was taken as the time for each exposure. Centroids were found for the target as well as a number of reference stars using BOX_CENTROIDER.PRO and photometry was performed about these centroids. A range of apertures were tested and we ultimately chose an aperture size of 2.4 pixels, which produced lightcurves with the lowest RMS.

To robustly remove outliers while avoiding subtracting out any astrophysical variability, we followed the clipping procedure outlined in Heinze et al. (2013). We median-smoothed each lightcurve with a sliding boxcar (width of 25 frames, corresponding to 12.5 minutes). The smoothed lightcurve is subtracted from the original data, removing astrophysical and systematic signals with timescales longer than 12 minutes. Thus, any outliers remaining in the subtracted curve must be artefacts and can be confidently removed using a 6-σ clip.

The flux of an object on a given point of the IRAC detector will vary depending on exactly where a point source falls with respect to the centre of a pixel - this is known as the "pixel phase effect". We correct for the pixel phase effect using the PIXEL_PHASE_CORRECT_GAUSS.PRO routine from the *Spitzer* IRAC website, which models the pixel phase response as a double-Gaussian, a summation of Gaussians in the orthogonal pixel directions. The pixel phase corrected flux is then binned into 2.5 minute bins.

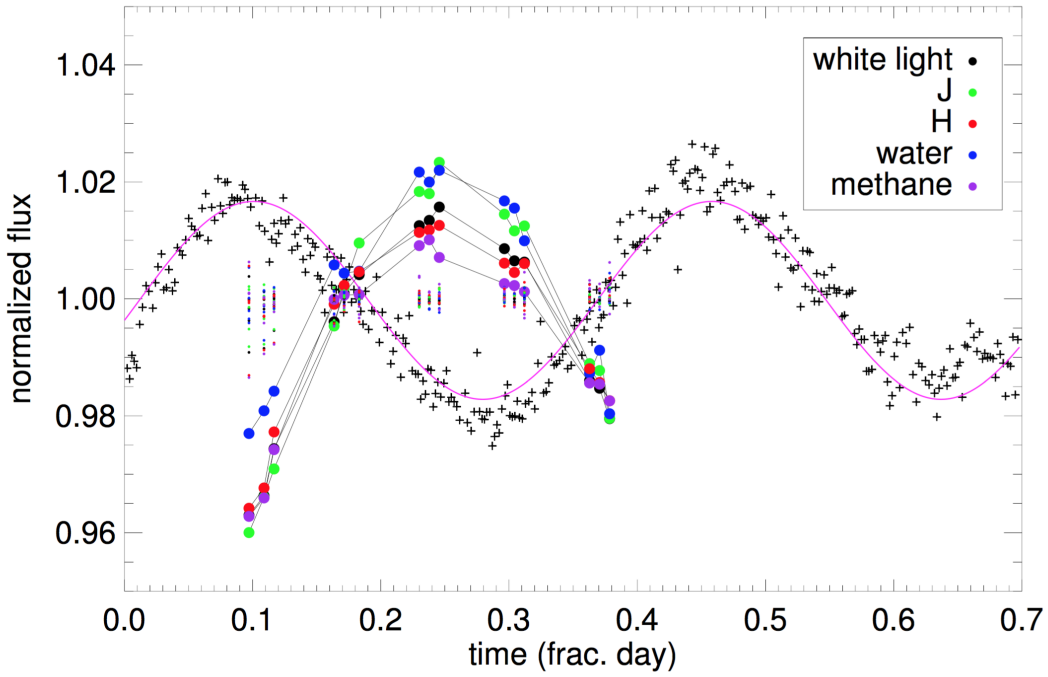

Figure 2.6 *Spitzer* (crosses) and *HST* (filled circles) corrected lightcurves for PSO 318.5–22. The least-squares best fit to the *Spitzer* lightcurve is shown as a solid purple line. *HST* lightcurves are shown binned over 5 spectral bandwidths: the full usable $1.07 - 1.67$ μm spectral bandwidth of the *HST* grism spectroscopy (white light, black circles), 2MASS J band (green circles), 2MASS H band (red circles), a band centred on the 1.4 μm water absorption feature (blue circles), and a band covering as much of the 1.6 μm methane absorption feature as falls in the *HST* G141 grism spectral bandwidth (purple circles). Small coloured points are the 6 background stars in the *HST* field after being detrended by the calibration curve; PSO 318.5–22 is clearly variable compared to the reference stars.

2.6.3 HST Data Reduction and Lightcurve Extraction

The data reduction and lightcurve extraction of the *HST* data is described in detail in Biller et al. (2018). The main points are described here. The spectra of PSO 318.5–22 and 6 background stars were extracted from the calibrated individual exposures obtained from the MAST archive. For each object on the detector, the aXe pipeline was used to extract slitless spectroscopy from each of the 9×278 grism exposures per orbit. The usable spectral bandwidth runs from $1.07-1.67$ μm, with a resolution of R = 130. The lightcurves were extracted from the spectra across a variety of spectral bandwidths. We integrated over the full $1.07-1.67$ μm spectral range to generate a "white-light" lightcurve. In order to compare with ground-based studies we also integrated over the standard 2MASS J and H bandpasses. We also consider variability in two spectral features; the $1.34-1.44$ μm region to capture variability in the 1.4 μm water absorption feature and from $1.60-1.67$ μm to capture variability in the 1.6 μm methane absorption feature.

As noted by previous studies (Buenzli et al., 2012; Apai et al., 2013; Buenzli et al., 2015b), WFC3 photometry displays a "ramp effect" - where the flux appears to increase with an exponential ramp at the beginning of each orbit. Since the ramp effect will affect all sources on the detector, a calibration curve can be created using well-behaved background stars. We median combine their normalised white-light lightcurves to produce a calibration curve. We then divide both target and background star lightcurves and spectra by the calibration curve to correct for the ramp effect as well as any other systematics which affect all objects on the detector. This is similar to the approach used for ground-based observations in Section 2.4.

2.6.4 Results

We present the corrected *Spitzer* and *HST* lightcurves of PSO 318.5–22 in Figure 2.6. The lightcurves have been binned to increase S/N ratio, resulting in a 2.5 minute cadence for *Spitzer* and a 14 minute cadence for *HST*. The small coloured points show the six detrended background stars observed with *HST*; PSO 318.5–22 is clearly variable compared to the reference stars. We observe a large phase shift between the near-IR *HST* and mid-IR *Spitzer* observations. This is discussed in Section 2.7.1.

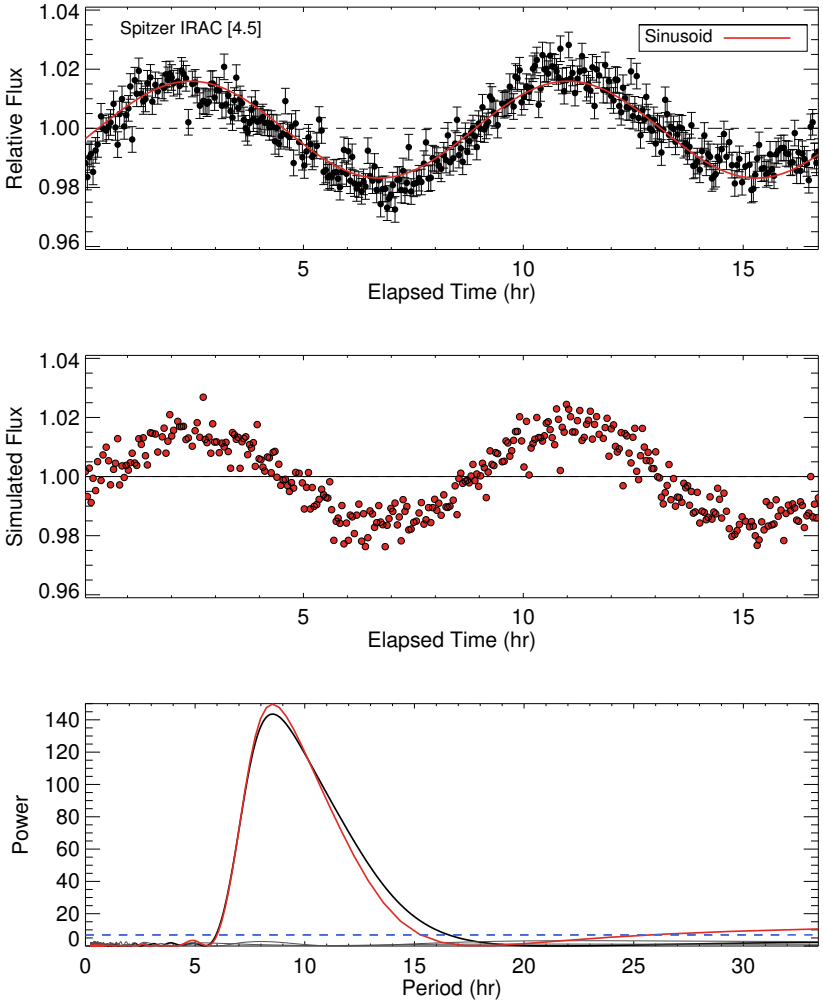

Figure 2.7 *Top panel: Spitzer* lightcurve of PSO 318.5–22. *Middle panel:* Best-fitting model obtained from Levenberg-Marquardt least-squares minimisation algorithm. *Bottom panel:* Periodogram of PSO 318.5–22 (black), best-fitting model (red) and reference stars (grey). The 1% false-alarm probability (FAP) is shown by the dotted blue line.

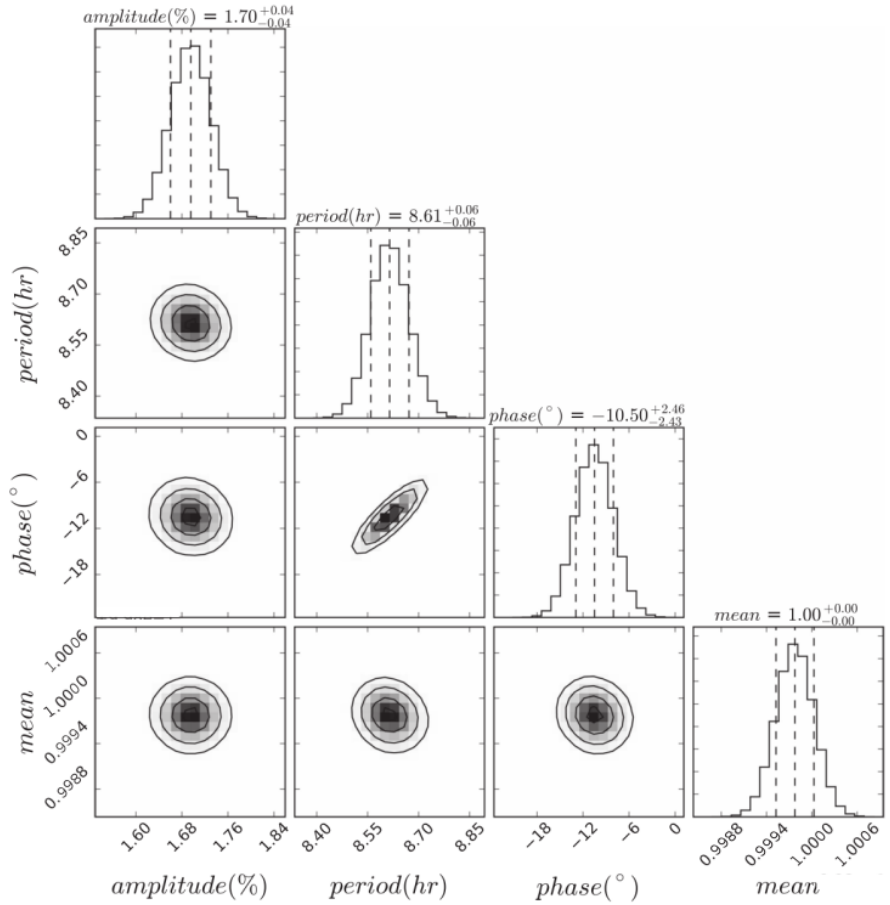

Figure 2.8 Posterior probability distributions of parameters from sinusoid MCMC fits to our *Spitzer* 4.6 μm lightcurve of PSO 318.5–22. The middle dashed line gives the median, and the two outer vertical dashed lines represent the 68% confidence interval. Contours show the 1, 1.5 and 2σ levels.

Period and Amplitude from the Spitzer Lightcurve

The unbinned *Spitzer* lightcurve (30 s cadence) along with the best fit sinusoid obtained from Levenberg-Marquardt least-squares minimisation algorithm is presented in the top panel of Figure 2.7. The middle panel shows the best fit model with Gaussian noise and visually provides a good match to the observed lightcurve. In the bottom panel we show our periodogram analysis of the target, the best fit model and reference stars in the field. A periodogram is a mathematical tool that is useful for searching for periodic signals in time-series data. The periodogram calculates the significance of frequencies in the data to identify any intrinsic signals. It is similar to the Fourier Transform, but is optimised for unevenly time-sampled data, and for different shapes in periodic signals (e.g. the Lomb-Scargle method; Scargle, 1982). The plot shows the Lomb-Scargle periodogram of the target, the best fit model and a number of reference stars in the field. The 1% false-alarm probability (FAP) is calculated from 1000 simulated lightcurves. These lightcurves are produced by randomly permuting the indices of reference star lightcurves (Radigan et al., 2014). This produces lightcurves with Gaussian-distributed noise. The 1% FAP is plotted in blue in each periodogram. The rotational period calculated from the Levenberg-Marquardt algorithm agrees well with the peak of the periodogram of PSO 318.5–22.

We additionally use the MCMC algorithm EMCEE (Foreman-Mackey et al., 2013) to fully explore the posterior probability distributions of our model parameters. We run an MCMC chain with 1000 walkers for 2000 steps. The first 100 steps of each chain are discarded as part of the "burn-in". Chains were checked by eye for convergence. Figure 2.8 shows the posterior distributions of the sinusoidal model parameters. We adopt the 50% quantile value as the best value for amplitude and period. Thus, we measure a period of 8.61 ± 0.06 for the rotational period of PSO 318.5–22. This is very similar to the rotational period of 8.45 ± 0.05 hr measured using NTT/SofI data in Section 2.5.

2.7 Discussion

2.7.1 Phase Shifts

We measure a dramatic phase offset of $\sim 200°$ between the *Spitzer* and *HST* lightcurves shown in Figure 2.6. Yang et al. (2016) report similar findings for four brown dwarfs observed simultaneously with *HST* and *Spitzer*, observing phase shifts between the mid-IR and near-IR for all four objects. Interestingly, the phase shifts for the objects 2M1507, 2M1821 and 2M2228 were measured to be $\sim 180°$, similar to the $\sim 200°$ we have measured for PSO 318.5–22. Observed phase shifts between the near-IR and mid-IR have generally been interpreted as different "top of atmosphere" locations at different wavelengths – near-IR wavelengths generally probe deep layers of the atmosphere while the mid-IR probes high altitudes (Buenzli et al., 2012; Biller et al., 2013; Yang et al., 2016). In other words, the "top of the atmosphere" inhomogeneity driving the near-IR variability is located at lower altitudes than the 'top of the atmosphere' inhomogeneity driving the mid-IR variability.

Phase shifts have also been reported within the near-IR wavelength range. Buenzli et al. (2012) report phase shifts between near-IR bands for the object 2M2228–43. Calculating the pressure probed by each wavelength band, they found that these phase shifts were correlated with the pressure probed by each band. For PSO 318.5–22, the near-IR bands agree in phase at the 2σ level, and the J-band is shifted relative to the other near-IR bands by $\sim 6°$ at the 1σ level. However, since we have monitored less than one rotational period with *HST* and have assumed a sinusoidal lightcurve shape, this phase shift is still within the errors expected from the sinusoidal model fitting. Additionally, our NTT/SofI followup observations presented in Section 2.5 showed no evidence of phase shifts between the J_S and K_S bands. Based on both sets of lightcurves, the observations are consistent with near-IR wavelengths probing similar heights in the atmosphere.

2.7.2 Amplitudes

The 7 hr *HST* lightcurve exhibits one clear extremum – a brightness maximum at orbit 3. The minimum brightness observed occurred in orbit 1, however this

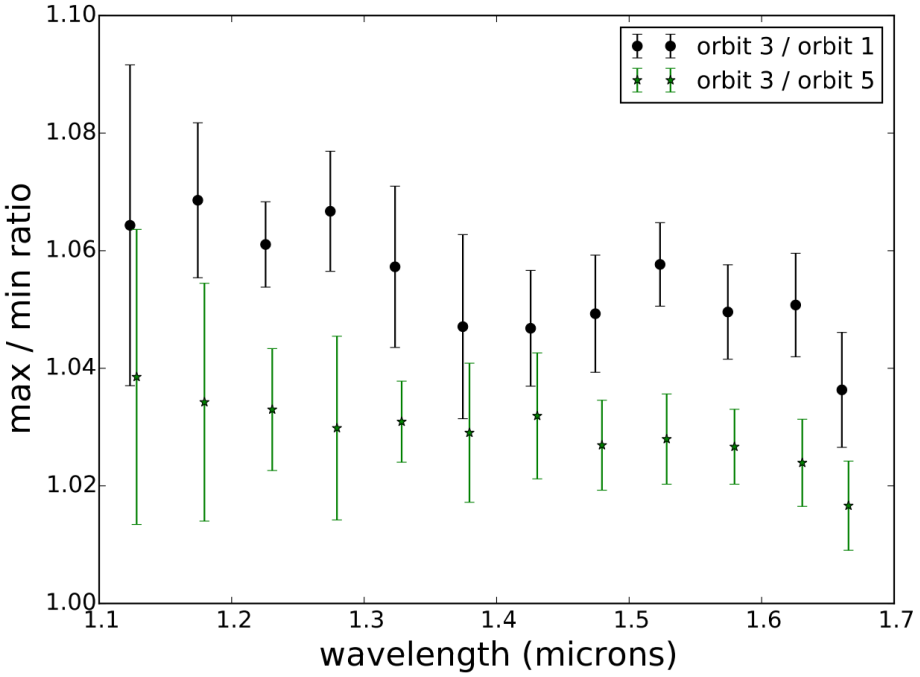

Figure 2.9 Ratio of minimum and maximum PSO 318.5–22 *HST* spectra binned by 0.05 μm. As our *HST* observations did not cover a full period, these are lower limits on the full amplitude.

orbit was most affected by the ramp effect. Orbit 5 is near a minimum and should not be as strongly affected by the ramp effect. The ratios of maximum and minimum flux (taking both orbits 1 and 5 as potential minima) are plotted as a function of wavelength in Figure 2.9. Both max/min ratios show a steady decrease with increasing wavelength. In addition to this monotonic decrease with wavelength, the ratios resulting from the division of orbit 3 by orbit 1 exhibits a slight dip at the 1.4 μm water absorption feature, indicating a possible suppression of variability in the water band. For the L/T transition objects SIMP 0136+09 and 2M2139+10, Apai et al. (2013) and Yang et al. (2016) found significantly smaller variability amplitudes in the water band than other near-IR wavelengths. Yang et al. (2015) monitored variability on two mid-L type objects and found a small but significant decrease in variability amplitude with increasing wavelength, with similar variability amplitudes observed in the water band. This variability was explained by the presence of spatially varying high-altitude haze layers above the condensate clouds. These haze layers exist at altitudes where the water opacity is negligible, and thus drives the observed variability. Our results appear to be a hybrid of these cases, with different behaviour observed in orbits 1 and 5.

The mid-IR *Spitzer* lightcurve follows the same trend of decreasing amplitude

with longer wavelength, with an amplitude of $\sim 3.4\%$ compared to the $4.4-5.8\%$ amplitudes observed in the near-IR. For field brown dwarfs, near-IR variability is generally found to have a significantly higher amplitude than the mid-IR variability. It is notable that the mid-IR amplitude for PSO 318.5–22 is so similar to its near-IR amplitude. In fact PSO 318.5–22 exhibits one of the highest mid-IR amplitudes that have been measured for a brown dwarf. Most brown dwarfs are found to vary in the mid-IR with an amplitude below $\sim 2\%$ (Metchev et al., 2015). This high-amplitude variability may be the effect of low surface gravity on the vertical structure of the atmosphere. Low surface gravity allows clouds to potentially extend to higher altitudes in the atmosphere compared to the higher mass brown dwarfs (Marley et al., 2012). In general, for brown dwarfs and free-floating planetary-mass objects, the photosphere probed by the mid-IR is at lower pressures and higher altitudes than the photosphere probed by the near-IR (Marley et al., 2012; Biller et al., 2013). Thus, the extension of clouds up to higher altitudes increases the chance of heterogeneous cloud opacity at the low pressures probed by mid-IR observations.

2.7.3 Rotation

Even if young, planetary-mass objects have significant top-of-atmosphere inhomogeneities, we will only be able to detect such features through variability monitoring if they have relatively fast rotation rates with periods < 20 hr. Since young brown dwarfs have not yet contracted to their final radii, we expect them to spin up over their first ~ 200 Myr. Thus, we expect the population of young brown dwarfs to rotate more slowly than the field population. Preliminarily however, the rotational periods of the planetary-mass objects are relatively fast. In Figure 2.10, we show the equatorial velocities of the free-floating and companion planetary-mass objects that are known to date, alongside the Solar System planets and the field dwarfs with measured periods compiled in Chapter 3 (Vos et al., 2017). The Solar System planets obey a strict relation between equatorial velocity and mass. PSO 318.5–22 has a remarkably similar rotational period to the exoplanet companions β Pic b and 2M1207b. These three planetary-mass objects are young ($\sim 10-20$ Myr) and have not contracted to their final radius. Once they have contracted to their final radii, we estimate that their equatorial velocities (Biller et al., 2015; Allers et al., 2016; Zhou et al., 2016; Snellen et al., 2014) will become consistent with the Solar System extrapolation (along with the 200 Myr old object SIMP 0136). With a rotational period of

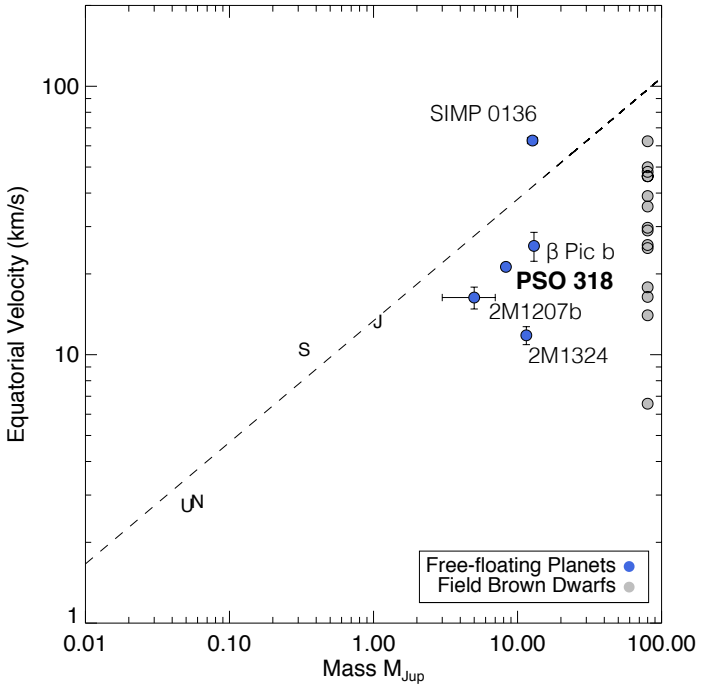

Figure 2.10 Mass plotted against equatorial velocity for the free-floating planets PSO 318.5–22, SIMP 0136, 2M1324 and the companion exoplanets 2M1207b and β Pic b.

13 ± 1 hr (Metchev et al., 2015), 2M1324 is a somewhat slower rotator, despite having a similar mass to the other objects (Gagné et al., 2018a). High-gravity, field dwarfs display a large range in equatorial velocities, with periods ranging from hours to days, even at young ages (Metchev et al., 2015; Scholz et al., 2015). Rotational braking due to star-disk interaction and accretion-driven winds is strongly mass dependent (Bouvier et al., 2014), becoming less efficient at substellar masses (Scholz et al., 2015). It is possible that the magnetic fields present in planetary-mass objects are not strong enough to effectively brake their rotation, which is consistent with the current deficit of slow rotating planetary-mass objects. However, statistics are still too sparse for a robust comparison to the field brown dwarf population. A larger sample of objects is needed to disentangle the effects of mass and age on the rotational properties of the planetary-mass objects.

2.8 Conclusions

In this chapter we have presented the first detection of photometric variability in a planetary-mass object, supplemented with subsequent ground-based and space-based followup observations and analysis. The amplitude of PSO 318.5–22 has been observed to change from epoch to epoch, with the J-band amplitude ranging from $\sim 2-10\%$. With a maximum measured amplitude of $10.0 \pm 1.3\%$, PSO 318.5–22 shows one of the highest variability amplitudes in an L dwarf to date. Along with the high-amplitude variability in the young, late-L object W0047 (Lew et al., 2016), this potentially suggests that there is a link between low gravity and high amplitude variability, as was tentatively found by Metchev et al. (2015). We obtained 3 consecutive nights of follow-up observations of PSO 318.5–22 with NTT/SofT in the J_S and K_S bands. We detected variability in all three epochs and measure an amplitude ratio, A_K/A_J, of 0.36 ± 0.25, similar to the amplitude ratios that have been observed for field brown dwarfs (Artigau et al., 2009; Radigan et al., 2012). We also find that the J_S and K_S lightcurves are in phase. The long baseline of these observations allow us to measure a rotational period of 8.45 ± 0.05 hr for PSO 318.5–22, which is comparable to the rotation rates of the field brown dwarfs, directly-imaged companions and the Solar System planets (Metchev et al., 2015; Snellen et al., 2014; Zhou et al., 2016).

We additionally present simultaneous *HST* and *Spitzer* monitoring of PSO 318.5–22. We measure an amplitude of $3.4 \pm 0.1\%$ in the *Spitzer* [4.5 μm] band, one of the highest mid-IR amplitudes measured to date. We measure a phase offset of $200-210^\circ$ between the near-IR and mid-IR lightcurves, suggesting the presence of varying longitudinal atmospheric structure at different depths in the atmosphere. We observe a decrease in variability amplitude as a function of increasing wavelength, as has been observed previously for field brown dwarfs (e.g. Apai et al., 2013; Radigan et al., 2014; Yang et al., 2016). We use the *Spitzer* lightcurve of PSO 318.5–22 to measure a rotational period of 8.61 ± 0.06 hr which is very similar to the rotational period measuring using the NTT/SofI data discussed above. In Chapter 5 we present the full survey for photometric variability in young, low-gravity exoplanet analogues.

Chapter 3

The Viewing Geometry of Brown Dwarfs Influences Their Observed Colours and Variability Amplitudes

3.1 Abstract

We study the full sample of known *Spitzer* [3.6 μm] and J-band variable brown dwarfs. We calculate the rotational velocities, $v \sin(i)$, of 16 brown dwarfs using archival Keck NIRSPEC data and compute the inclination angles of 19 variable brown dwarfs. The results obtained show that all objects in the sample with mid-IR variability detections are inclined at an angle $> 20°$, while all objects in the sample displaying J-band variability have an inclination angle $> 35°$. J-band variability appears to be more affected by inclination than *Spitzer* [3.6 μm] variability, and is strongly attenuated at lower inclinations. Since J-band observations probe deeper into the atmosphere than mid-IR observations, this effect may be due to the increased atmospheric path length of J-band flux at lower inclinations. We find a statistically significant correlation between the colour anomaly and inclination of our sample, where field objects viewed equator-on appear redder than objects viewed at lower inclinations. Considering the full sample of known variable L, T, and Y spectral type objects in the literature, we find that the variability properties of the two bands display notably different trends that are due to both intrinsic differences between bands and the sensitivity of ground-based versus space-based searches. However, in both bands we find that

variability amplitude may reach a maximum at $\sim 7-9$ hr periods. Finally, we find a strong correlation between colour anomaly and variability amplitude for both the J-band and mid-IR variability detections, where redder objects display higher variability amplitudes.

3.2 Introduction

Time-resolved photometric variability monitoring is a key probe of atmospheric structures in brown dwarf atmospheres, revealing a periodic modulation of the light curve as a feature rotates in and out of view. The combination of atmospheric inhomogeneities and rapid rotation has long motivated searches for photometric variability in brown dwarfs. The first unambiguous detections (Artigau et al., 2009; Radigan et al., 2012) were high-amplitude variable objects at the L/T transition. More recently, space- and ground-based surveys in the near-IR and mid-IR have revealed that variability is common across the full range of L and T spectral types (Buenzli et al., 2014; Radigan et al., 2014; Wilson et al., 2014; Metchev et al., 2015). In fact, Metchev et al. (2015) concluded from a *Spitzer* survey that most L and T spectral type brown dwarfs display low-level variability. To date, variability has been detected in ~ 30 brown dwarfs, with ~ 5 objects displaying high-amplitude variability ($> 5\%$). Of the highest variability brown dwarfs discovered thus far, we know that WISE 1049B is viewed roughly equator-on, with a viewing angle $i \geq 60°$ (Crossfield et al., 2014). For an equator-on object (with an inclination angle, $i \sim 90°$) we measure the full variability amplitude via photometric monitoring. In contrast, we measure lower variability amplitudes for low-inclination objects (Kostov & Apai, 2013). In this chapter, we aim to ascertain whether the range of observed amplitudes is due to properties intrinsic to each brown dwarf or whether it can be explained by consideration of their inclination angles.

A proper motion survey conducted by Kirkpatrick et al. (2010) led to the discovery of a number of L spectral type brown dwarfs that were redder than the median and L-type brown dwarfs that were bluer than the median. Their kinematics revealed that they are both drawn from a relatively old population. This led to the possibility that both of these phenomena occur in the same objects, and that viewing angle determines their spectral appearance. This idea that spectral appearance is influenced by inclination angle is again suggested by Metchev et al. (2015), who find a tentative correlation between near-IR colour and

high-amplitude variability. If the inclination angle affects the observed amplitude as well as the observed near-IR colour, then these two measurements will be related. The calculation of the inclination angle of brown dwarfs is critical in testing the relation between inclination and atmospheric appearance.

Attempts to model the cloud structure observed on variable brown dwarfs as patchy spots of thick and thin clouds have also been hindered by the unknown inclination of such objects. Walkowicz et al. (2013) performed extended numerical experiments to assess degeneracies in models of spotted light curves, and confirmed that in the absence of inclination constraints, spot latitudes cannot be determined, regardless of data quality. Apai et al. (2013) obtained high-precision *HST* near-infrared spectroscopy of the two highly variable L/T transition dwarfs 2M2139+02 and SIMP 0136. Surface brightness distributions were modeled using the inclination angle as an optimizable parameter, although the results are highly degenerate with respect to inclination, as multiple spot models with different inclinations fit the same light curve equally well. More recently, Karalidi et al. (2016) updated their *Aeolus* routine, a Markov chain Monte Carlo (MCMC) code that can map the top-of-the-atmosphere structure of an ultracool atmosphere, to fit for inclination as a free parameter and successfully retrieved an inclination of $69 \pm 8^{\circ}$ for WISE 1049B, in agreement with the earlier measurement by Crossfield et al. (2014). Constraining the inclination angles of variable brown dwarfs will allow us to model brown dwarf atmospheres in unprecedented detail.

In this chapter we study the effects of inclination angle on the observed properties of a sample of brown dwarfs for the first time. We measure the rotational velocity, $v \sin(i)$, of 16 variable brown dwarfs (11 of which have no previous measurement in the literature) using archival Keck data, and use estimates of radius to determine their inclination angles. We investigate the relationship between inclination angle, variability amplitude and colour anomaly. Furthermore, we investigate the entire list of known brown dwarf J-band, *Spitzer* [3.6 μm] and Kepler variability detections and explore the relations between variability amplitude, rotation period and colour anomaly. In Section 3.3 we discuss the sample of variable brown dwarfs. In Sections 3.4 – 3.5 we discuss the archival data and our methods in calculating inclinations. We discuss our results in Section 3.6.

3.3 The Sample

Our sample consists of all variable brown dwarfs in the L-T spectral range with published periods and high-dispersion NIRSPEC-7 data available in the Keck Archive, as well as three known variable brown dwarfs with measured periods and previously measured $v \sin(i)$ (WISE 1049B, DENIS 1058 and PSO-318). The full sample is shown in Table 3.1 and each object is described briefly below.

2MASS J0036159+182110 — The object 2M0036+18 is a magnetically active L3.5 dwarf. Variability was first detected by Berger et al. (2005) in the radio, with a period of ~ 3 hr. Harding et al. (2013) detected optical I-band variability, confirming the 3 hr period. 2M0036+18 was subsequently observed as part of the *Weather on Other Worlds* campaign by Metchev et al. (2015), who measured a period of 2.7 ± 0.3 hr in mid-IR wavelengths. Croll et al. (2016) measure an J-band amplitude of $1.22 \pm 0.04\%$. Blake et al. (2010) have previously measured a $v \sin(i)$ of 35.12 ± 0.57 km s^{-1} for this object.

WISE J004701.06+680352.1— This very red L6 dwarf was discovered by Gizis et al. (2012). Lew et al. (2016) detect J-band variability with an amplitude of 10% and a period of ~ 13 hr. They further proceed to measure a $v \sin(i) = 6.7^{+0.7}_{-1.4}$ km s^{-1} and constrain the inclination to $i = 33^{+5}_{-8}$ °. This $v \sin(i)$ differs from the previously measured value of 4.3 ± 2.2 km s^{-1} by Gizis et al. (2015). Gizis et al. (2015) assign an INT-G gravity classification to W0047.

2MASS J0103320+193536 — The L6 brown dwarf 2M0103+19 was first monitored by Enoch et al. (2003), who did not detect J-band variability. *Spitzer* observations later revealed mid-IR variability, with an amplitude of $0.47 \pm 0.05\%$ and a regular 2.7 hr period (Metchev et al., 2015). This object is given a β gravity classification by Faherty et al. (2012) and an INT-G classification by Allers & Liu (2013).

2MASS J01075233+0041561 — The L8 object 2M0107+00 was observed as part of the *Weather on Other Worlds* campaign by Metchev et al. (2015). This is a complex and irregular variable, with an unconstrained period of 5 hr and an amplitude of $1.27 \pm 0.12\%$.

SIMP J0136566+0933473 — The variability detection of the T1.5 dwarf SIMP 0136 by Artigau et al. (2009) was the first highly significant periodic variability detection in a brown dwarf. Long-term monitoring of SIMP 0136 revealed changes

in both amplitude and shape over multiple rotations (Metchev et al., 2013). Yang et al. (2016) constrain the period to 2.41±0.08 hr and measure a mid-IR amplitude of $1.5 \pm 0.2\%$.

SDSS J042348.57–041403.5AB — Enoch et al. (2003) reported tentative K_S variability in this T0 binary system. Clarke et al. (2008) monitored SDSS 0423–04 in the J-band and report low-level variability with a 2 hr period and a $0.8 \pm 0.8\%$ amplitude. Radigan et al. (2014) reobserved the binary, finding inconclusive evidence for its variability during a 3.6 hr observation.

WISE J104915.57–531906.1B — WISE 1049B (Luhman, 2014) is one component of a brown dwarf binary system with spectral types L9 and T0.5 for the A and B components respectively. Variability has been detected in both components (Biller et al., 2013; Buenzli et al., 2015a). A period of 4.87 ± 0.01 hr has been determined for the B component (Gillon et al., 2013), while a period has not been robustly observed for the A component (Buenzli et al., 2015a). Crossfield et al. (2014) report $v \sin(i) = 26.1 \pm 0.2$ km s^{-1}.

DENIS 1058.7–1548 — Both *Spitzer* monitoring and ground-based J-band photometry reveal variability in this L3 dwarf (Heinze et al., 2013). DENIS 1058 has a period of 4.3 ± 0.3 hr and amplitudes of $0.39 \pm 0.04\%$ and 0.843% in the mid-IR and J-band respectively. This object is one of five in the sample with both a J-band and mid-IR variability detection. DENIS 1058 also has a published $v \sin(i) = 37.5 \pm 2.5$ km s^{-1} (Basri et al., 2000).

2MASS J11263991–5003550 — 2M1126–50 (Folkes et al., 2007) is a peculiar L dwarf with $J - K_S$ colours that are unusually blue for its L4.5 optical or L6.5 IR spectral type. This target was found to be variable in the J-band with a peak-to-peak amplitude of $1.2 \pm 0.1\%$ and a period of ~ 4 hr (Radigan et al., 2014; Radigan, 2014). Metchev et al. (2015) later constrained the period to 3.2 ± 0.3 hr via their $0.21 \pm 0.04\%$ mid-IR variability detection.

2MASS J1507476–162738 — This L5 object is another irregular variable, showing lightcurve evolution during a 20 hr *Spitzer* observation reported by Metchev et al. (2015). The authors determine a period of 2.5 ± 0.1 hr and an amplitude of $0.57 \pm 0.04\%$ for this object. Previous $v \sin(i)$ measurements have ranged between $21 - 30$ km s^{-1} (Bailer-Jones, 2004; Reiners & Basri, 2008; Blake et al., 2010).

Table 3.1 Variable Brown Dwarfs with Known Periods and Archival Spectra.

Name	SpT	[3.6] Amp (%)	J Amp (%)	Kep Amp (%)	Period (hr)	$v\sin(i)$ (kms^{-1})	$(J-K_S)$	Refs
2M0036+18	L3.5	0.47 ± 0.05	1.22 ± 0.04	...	2.7 ± 0.3	35.12 ± 0.57	1.41	(1, 2, 3)
W0047	L6	...	10	...	13.2 ± 0.14	4.3 ± 2.2,$6.7^{+0.7}_{-1.4}$	2.55	(4, 5)
2M0103+19	L4	0.47 ± 0.05	...	...	2.7 ± 0.3	...	2.14	(1)
2M0107+00	L8	1.27 ± 0.13	...	...	5	...	2.11	(1)
SIMP 0136	T2.5	1.5 ± 0.2	5	...	2.414 ± 0.078	...	0.90	(6, 7)
SDSS0423-04	T0	...	0.8 ± 0.08	...	2 ± 0.4	...	1.54	(8)
WISE1049B*	T0.5	...	7	...	4.87 ± 0.01	26.1 ± 0.2	1.89	(9, 10, 11)
DENIS 1058*	L3	0.39 ± 0.04	0.843	...	4.3 ± 0.31	37.5 ± 2.5	1.62	(1, 12, 13)
2M1126-50	L4.5	0.21 ± 0.04	1.2 ± 0.1	...	3.2 ± 0.3	...	1.17	(1, 6)
2M1507-16	L5	0.57 ± 0.04	...	...	2.5 ± 0.1	21.27 ± 1.86	1.51	(1, 3)
2M1615+49	L4	0.9 ± 0.2	...	...	24	...	2.47	(1)
SIMP 1629	T2	...	4.3	...	> 7	...	1.25	(6)
2M1721+33	L3	0.33 ± 0.07	...	...	2.6 ± 0.1	...	1.14	(1)
2M1821+14	L4.5	0.54 ± 0.05	...	...	4.2 ± 0.1	28.85 ± 0.16	1.78	(1, 3)
2M1906+40	L1	...	...	1.5	8.9	11.2 ± 2.2	1.31	(14)
PSO-318*	L7.5	...	10 ± 1	...	7.5 ± 2.5	$17.5^{+2.3}_{-2.8}$	2.78	(15, 16)
2M2139+02	T1.5	11 ± 1	26	...	7.618 ± 0.178	...	1.68	(6, 7)
2M2148+40	L6	1.33 ± 0.07	...	...	19 ± 4	...	2.38	(1)
2M2208+29	L3	0.69 ± 0.07	...	...	3.5 ± 0.2	...	1.65	(1)

Note: Starred objects are those for which we have adopted $v\sin(i)$ values from the literature. $(J-K_S$ colours are $2MASS$.
References: — (1) Metchev et al. (2015), (2) Croll et al. (2016), (3) Blake et al. (2010), (4) Lew et al. (2016), (5) Gizis et al. (2015), (6) Radigan et al. (2014), (7) Yang et al. (2016), (8) Clarke et al. (2008), (9) Gillon et al. (2013), (10) Biller et al. (2013), (11) Crossfield et al. (2014), (12) Heinze et al. (2013), (13) Basri et al. (2000), (14) Gizis et al. (2013), (15) Biller et al. (2015), (16) Allers et al. (2016).

Table 3.2 Rotational Periods and Peak-to-peak Variability Amplitudes for J-band Variable Brown Dwarfs.

Name	SpT	Period (hr)	J-band Amp (%)	Ref
2M0036+18	L3.5	2.7 ± 0.3	1.22 ± 0.04	(1)
W0047	L6	13.2 ± 0.14	10 ± 0.5	(2)
SIMP 0136	T2.5	2.414 ± 0.078	5	(3, 4)
SDSS 0423-04	T0	2 ± 0.4	0.8 ± 0.08	(5)
2M0559	T4.5	10 ± 3	0.7 ± 0.5	(3)
SDSS 0758	T2	4.9 ± 0.2	4.8 ± 0.2	(3)
2M0817	T6.5	2.8 ± 0.2	0.6 ± 0.1	(3)
WISE 1049B	T0.5	4.87 ± 0.01	7 ± 0.5	(6, 7)
SDSS 1052	T0.5	3 ± 0.5	2.2 ± 0.5	(8)
DENIS 1058	L3	4.3 ± 0.31	0.843 ± 0.098	(9)
2M1126-50	L4.5	3.2 ± 0.3	1.2 ± 0.1	(3)
2M1207b	L5	10.7 ± 0.8	1.36 ± 0.23	(10)
SIMP 1629	T2	6.9 ± 2.4	4.3 ± 2.4	(3)
2M1828	T5.5	5.0 ± 0.6	0.9 ± 0.1	(3)
PSO-318	L7.5	7.5 ± 2.5	10 ± 1	(11, 12)
2M2139+02	T1.5	7.614 ± 0.178	26	(4, 13)
2M2228	T6	1.369 ± 0.032	1.6 ± 0.3	(3, 4)
2M2331	T5	2.9 ± 0.9	1.5 ± 0.2	(5)

References: — (1) Croll et al. (2016), (2) Lew et al. (2016), (3) Radigan et al. (2014), (4) Yang et al. (2016), (5) Clarke et al. (2008), (6) Gillon et al. (2013), (7) Biller et al. (2013), (8) Girardin et al. (2013), (9) Heinze et al. (2013), (10) Zhou et al. (2016), (11) Biller et al. (2015), (12) Allers et al. (2016), (13)Radigan et al. (2012).

2MASS J16154255+4953211 — Metchev et al. (2015) detect mid-IR variability in 2M1615+49, and infer a period of 24 hr and an amplitude of $0.9 \pm 0.2\%$ from the light curve. This object is classified as VL-G by Allers & Liu (2013) based on FeH and alkali absorption as well as H-band shape, but it lacks the deep VO absorption observed in other low-gravity brown dwarfs. Faherty et al. (2016) assign a γ gravity classification.

SIMP J16291841+0335380 — Radigan et al. (2014) detect J-band variability in this T2 dwarf, with an estimated peak-to-peak amplitude of $\sim 4.3\%$ and a period of ~ 6.9 hr. These estimates are uncertain as only the trough of the light curve was caught in the 4 hour observation.

2MASS J1721039+334415 — Mid-IR variability was detected in this L3 dwarf by Metchev et al. (2015), with an inferred period of 2.6 ± 0.1 hr and an amplitude

of $0.33 \pm 0.07\%$.

2MASS J18212815+1414010 — Metchev et al. (2015) detected mid-IR variability in this L4.5 dwarf, determining a period of 4.2 ± 0.1 hr and an amplitude of $0.54 \pm 0.05\%$. The red near-IR colours and silicate absorption of 2M1821+14 (Looper et al., 2008) indicate an extremely dusty atmosphere, but Allers & Liu (2013) and Gagné et al. (2015c) find no clear signs of low gravity. This object has a previously measured $v \sin(i) = 28.9$ km s^{-1} (Blake et al., 2010).

2MASS J1906485+4011068 — Gizis et al. (2013) detect optical variability in this L1 dwarf using *Kepler* data, finding a consistent rotation period of 8.9 hr with an amplitude of 1.5%. Gizis et al. (2013) also report $v \sin(i) = 11.2 \pm 2.2$ km s^{-1} and calculate the inclination, $i > 37°$. This is a magnetically active brown dwarf, so the observed variability may be due to magnetic phenomena such as starspots.

PSO J318.5 –22 — Biller et al. (2015) detect J-band variability in this extremely red planetary-mass object with amplitudes of $5 - 10\%$ during two consecutive nights of observations. PSO 318.5–22 has a period of 7.5 ± 2.5 hr (Biller et al., 2015; Allers et al., 2016). Allers et al. (2016) report a $v \sin(i) = 17.5^{+2.3}_{-2.8}$ km s^{-1} for this object. Liu et al. (2013) classifies PSO 318.5–22 as VL-G and Faherty et al. (2016) assign a γ classification.

2MASS J21392676+0220226 — 2M2139+02 is the most variable brown dwarf discovered to date; Radigan et al. (2012) detects variability with J-band amplitudes of up to 26% with a period of 7.721 ± 0.005 hr. More recently, Yang et al. (2016) monitored 2M2139+02 in eight separate *Spitzer* visits, finding a period of 7.614 ± 0.178 hr, with lower mid-IR amplitudes of $\sim 11\%$. 2M2139+02 is an extreme outlier, exhibiting the highest J-band and mid-IR variability amplitudes observed in any brown dwarf to date.

2MASS J21481628+4003593 — Metchev et al. (2015) report mid-IR variability in this L6 dwarf with a period of 19 ± 4 hr and an amplitude of $1.33 \pm 0.07\%$.

2MASS J2208136+292121 — Metchev et al. (2015) observed variability in this L3 brown dwarf. A period of 3.5 ± 0.2 hr and an amplitude of 0.62% were determined from the light curve. 2M2208+40 has been assigned γ and VL-G classifications (Cruz et al., 2009; Allers & Liu, 2013).

3.3.1 Low-Gravity Brown Dwarfs

As discussed in Section 3.3, the brown dwarfs 2M0103+19, 2M1615+49, 2M2208+29, PSO–318 and W0047 show signs of low gravity. Low gravity is indicative of both a lower mass and a larger radius, which in turn is suggestive of a young brown dwarf that has not yet contracted to reach its equilibrium radius. This subsample provides valuable information on the effects of gravity and youth on variability properties. Metchev et al. (2015) note a tentative correlation between low-gravity and high-amplitude mid-IR variability amplitudes. This correlation is further supported by a number of high-amplitude J-band detections in low-gravity objects (Biller et al., 2015; Lew et al., 2016). This is unexpected because atmospheric models typically require very thick clouds (Madhusudhan et al., 2011), and initial variability studies suggest that objects with patchy clouds in the process of breaking up tend to have the highest variability amplitudes (Radigan et al., 2014). Evidently, low-gravity objects can exhibit very different atmospheric properties to field brown dwarfs, and they are denoted by a black inset in all plots in this paper.

3.3.2 Sample Selection Biases

The sample described above is affected by a number of selection biases, arising from the sensitivity biases of variability monitoring observations.

Firstly, the rotational periods that have been measured for brown dwarfs likely does not capture the true distribution of periods. Variability monitoring is sensitive to shorter rotational periods since period measurements are limited by the observation duration. This bias is more apparent for objects whose rotational periods have been measured in the near-IR, since most of these observations are taken using ground-based telescopes. Mid-IR variability observations have primarily been taken using the *Spitzer Space Telescope*, which can carry out much longer observations, such as the ~ 20 hr observations published in Metchev et al. (2015). For this reason, most objects with measured periods > 10 hr have been measured in the mid-IR with *Spitzer*. Our sample of measured rotational periods are mainly in the range $0 - 5$ hr, however since these periods are the most accessible by variability monitoring, this feature may not be representative of the full sample of brown dwarfs. This rotational period bias also effects the measured amplitudes of our sample. For objects with long rotational periods, only

the higher variability amplitudes will be detected. Thus, we are likely missing variable objects with long rotation periods and low variability amplitudes.

Secondly, it is likely that the inclination angle of a variable object has an effect on whether the variability is detectable (Buenzli et al., 2014; Radigan et al., 2014). The true variability amplitude can be detected on an object that is viewed equator-on because atmospheric features will rotate in and out of view, causing variability in the lightcurve. In contrast, for a pole-on object, these features will remain in the observable hemisphere and the lightcurve does not display variability. Thus, variability monitoring is likely to be most sensitive to objects that are close to equator-on. The observed variability amplitude is attenuated as the inclination angle approaches 0° (pole-on). This effect is important to keep in mind as it could skew our inclination angle measurements towards 90°. We compare our measured inclination angles to the expected distribution for randomly oriented objects in Section 3.6.1, and find that our sample is consistent with the expected distribution of randomly oriented inclination angles.

3.4 Data and Observations

We obtained high-dispersion NIRSPEC spectra for our targets from the Keck Observatory Archive. NIRSPEC is a near-infrared echelle spectrograph on the Keck II 10 m telescope on Maunakea, Hawaii. The NIRSPEC detector is a 1024×1024 pixel ALADDIN InSb array. Observations were carried out using the NIRSPEC-7 ($1.839 - 2.630$ μm) passband in echelle mode using the 3-pixel slit ($0.432''$), an echelle angle of $62°.67 - 63°.00$ and a grating angle of $35°.46 - 35°.52$. Observations of targets were gathered in nod pairs, allowing for the removal of sky emission lines through the subtraction of two consecutive images. Arc lamps were observed for wavelength calibration. $5 - 10$ flat field and dark images were taken for each target to account for variations in sensitivity and dark current on the detector. Details of the observations are given in Table 3.4.

Table 3.3 Rotational Periods and Peak-to-peak Variability Amplitudes for *Spitzer* [3.6]μm Variable Brown Dwarfs.

Name	SpT	Period (hr)	[3.6] μm Amp (%)	Ref
2M0036+18	L3.5	2.7 ± 0.3	0.47 ± 0.05	(1)
2M0050	T7	1.55 ± 0.02	$< 0.59 \pm 0.50$	(1)
2M0103+19	L6	2.7 ± 0.1	0.56 ± 0.03	(1)
2M0107+00	L8	5 ± 10	1.27 ± 0.13	(1)
SIMP 0136	T2.5	2.414 ± 0.078	1.5 ± 0.2	(2)
2M0825	L7.5	7.6 ± 10	0.81 ± 0.08	(1)
WISE0855	Y1	10 ± 1	4.5 ± 0.5	(3)
SDSS1043	L9	3.8 ± 0.2	1.54 ± 0.15	(1)
DENIS 1058	L3	4.1 ± 0.2	0.39 ± 0.04	(1)
2M1126-50	L4.5	3.2 ± 0.3	0.21 ± 0.04	(1)
2M1324	T2.5	13 ± 1	3.05 ± 0.15	(1)
WISE1405	Y0.5	8.2 ± 0.3	3.6 ± 0.4	(4)
2M1507-16	L5	2.5 ± 0.1	0.53 ± 0.11	(1)
SDSS1511	T2	11 ± 2	0.67 ± 0.07	(1)
SDSS1516	T0.5	6.7 ± 10	2.4 ± 0.2	(1)
2M1615+49	L4	24 ± 10	0.9 ± 0.2	(1)
2M1632	L8	3.9 ± 0.2	0.42 ± 0.08	(1)
2M1721+33	L3	2.6 ± 0.1	0.33 ± 0.07	(1)
WISE1738	Y0	6.0 ± 0.1	3 ± 0.1	(5)
2M1753	L4	50 ± 10	0.25 ± 0.5	(1)
2M1821+14	L4.5	4.2 ± 0.1	0.54 ± 0.05	(1)
HNPegB	T2.5	18 ± 4	0.77 ± 0.15	(1)
2M2148+40	L6	19 ± 4	1.33 ± 0.07	(1)
2M2139+02	T1.5	7.618 ± 0.18	11 ± 1	(2)
2M2208+29	L3	3.5 ± 0.3	0.69 ± 0.07	(1, 2)
2M2228	T6	1.37 ± 0.01	4.6 ± 0.2	(1)

References: — (1) Metchev et al. (2015), (2) Yang et al. (2016), (3) Esplin et al. (2016), (4) Cushing et al. (2016), (5) Leggett et al. (2016).

Table 3.4 NIRPSEC-7 High-dispersion Observing Information. All data were taken from the Keck archive.

Name	UT Date	Slit Name	Echelle (deg)	Cross Disp (deg)	Exp Time (s)	Airmass	S/N	Prog ID
2M0036+18	2011 Sep 10	0.432×12	63.00	35.52	2×450	1.006	28	U049NS
W0047	2013 Sep 17	0.432×12	62.97	35.51	2×1200	1.507	24	U055NS
2M0103+19	2014 Jul 19	0.432×24	62.68	35.44	2×300	1.209	10	N160NS
2M0107+00	2011 Sep 07	0.432×12	63.00	35.46	2×1500	1.070	24	U049NS
SIMP1036	2011 Sep 10	0.432×12	63.00	35.52	2×600	1.061	17	U049NS
SDSS0423-04	2004 Mar 08	0.432×12	62.65	35.51	2×1200	1.342	21	C13NS
2M1126-50	2014 Jan 20	0.432×12	63.02	35.53	2×600	2.892	15	U055NS
2M1507-16	2011 Jun 10	0.432×12	63.00	35.53	2×600	1.288	19	U038NS
2M1615+49	2011 Sep 10	0.432×12	63.00	35.52	2×900	1.491	21	U049NS
SIMP 1629	2011 Sep 07	0.432×12	63.00	35.46	2×1200	1.119	24	U049NS
2M1721+33	2011 Sep 07	0.432×12	63.00	35.46	2×1000	1.254	27	U049NS
2M1821+14	2006 Jul 30	0.432×12	62.67	35.51	2×600	1.075	26	N050NS
2M1906+40	2011 Sep 10	0.432×12	63.00	35.52	2×120	1.631	10	U049NS
2M2139+02	2011 Sep 07	0.432×12	63.00	35.46	2×1200	1.048	23	U049NS
2M2148+40	2006 Dec 32	0.432×12	62.68	35.52	2×750	1.451	22	N044NS
2M2208+29	2011 Sep 10	0.432×12	63.00	35.52	2×1500	1.054	27	U049NS

3.5 Data Reduction Methods

Data were reduced using a modified version of the REDSPEC reduction package to spatially and spectrally rectify each exposure. The Keck/NIRSPEC Echelle Arc Lamp Tool was used to identify the wavelengths of lines in our arc lamp spectrum. We focus our analysis on order 33 since this part of the spectrum contains a good blend of sky lines and brown dwarf lines, allowing for an accurate fit. Order 33 is also commonly used in the literature for NIRSPEC high-dispersion N-7 spectra (Blake et al., 2010; Gizis et al., 2013). We additionally reduced orders 32 and 38, which also contain a sufficient amount of sky and brown dwarf lines, to check for consistency. After nod-subtracting pairs of exposures, we created a spatial profile that is the median intensity across all wavelengths at each position along the slit. To remove any residual sky emission lines from our nod-subtracted pairs we identified pixels in the spatial profile that did not contain significant source flux. We used Poisson statistics to determine the noise per pixel at each wavelength. We extracted the flux within an aperture in each nod-subtracted image to produce two spectra of our source. The extracted spectra were combined using a robust weighted mean with the XCOMBSPEC procedure from the Spextool package (Cushing et al., 2004).

3.5.1 Determining Rotational Velocities

We used the approach outlined in Allers et al. (2016) to determine the rotational velocities, $v \sin(i)$, of our objects. We employed forward modeling to simultaneously fit the wavelength solution of our spectrum, the rotational and radial velocities, the scaling of telluric line depths, and the FWHM of the instrumental line spread function (LSF). We used the BT-Settl model atmospheres (Allard et al., 2012) as the intrinsic spectrum for each of our objects. Further details can be found in Allers et al. (2016). In total, the forward model has nine free parameters: the $T_{\rm eff}$ and $\log(g)$ of the atmosphere model, the v_r and $v \sin(i)$ of the brown dwarf, τ for the telluric spectrum, the LSF FWHM, and the wavelengths of the first, middle, and last pixels. The forward model was compared to our observed spectrum, and the parameters used to create the forward model were adjusted to achieve the best fit.

To determine the best-fit parameters of our forward model as well as their

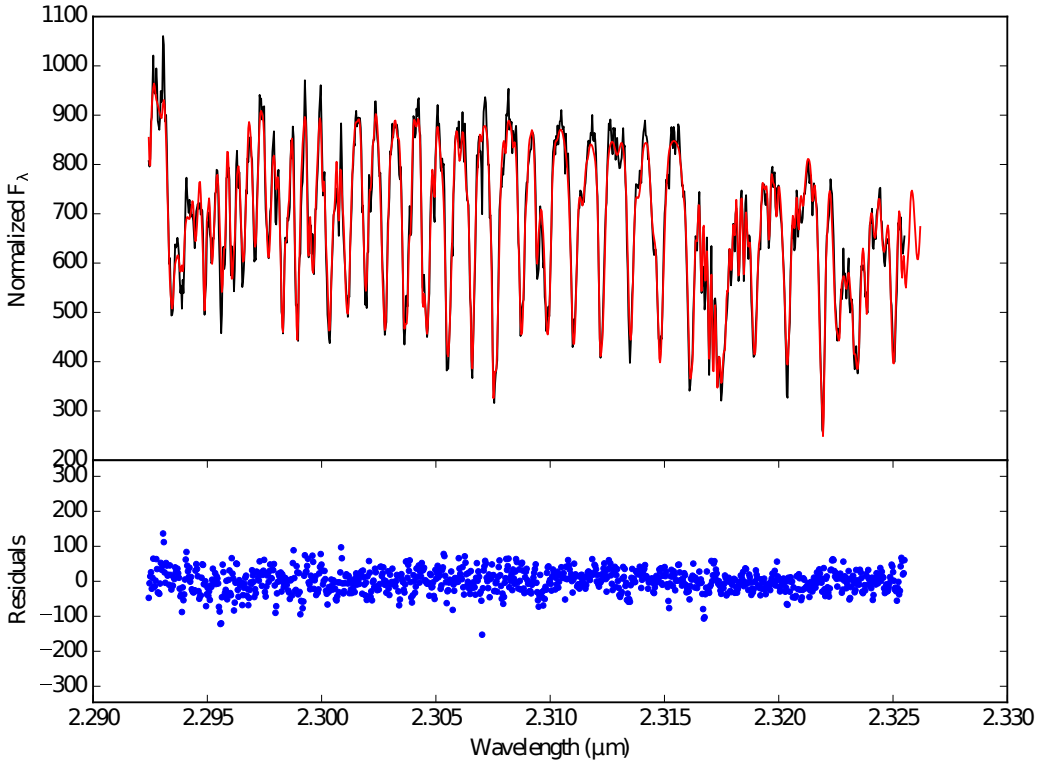

Figure 3.1 Observed spectrum of 2M1507–16 (black) compared to our forward model with best-fit parameters (red).

marginalised distributions we used an MCMC approach. This involves creating forward models that allow for a continuous distribution of $T_{\rm eff}$ and $\log(g)$ by linearly interpolating between atmosphere grid models. We employed the DREAM(ZS) algorithm (Ter Braak & Vrugt, 2008), which uses an adaptive stepper, updating model parameters based on chain histories. An example of our best-fit model for 2M1507–16 order 33 is shown in Figure 3.1. Table 3.5 shows the resulting rotational velocities, radial velocities, effective temperatures, and surface gravities calculated using order 33. We also find that orders 32 and 38 are consistent with the results obtained from order 33.

As discussed in Section 3.3, five of the objects in our sample have previous measurements of $v\sin(i)$. Our value of $35.91^{+0.8}_{-0.8}$ km s^{-1} for 2M0036+18 is consistent with the $v\sin(i)$ measured by Blake et al. (2010). Literature $v\sin(i)$ measurements for 2M1507-16 have ranged from 21−30 km s^{-1} (Bailer-Jones, 2004; Reiners & Basri, 2008; Blake et al., 2010) and we find that our measurement of $19.21^{+0.53}_{-0.53}$ km s^{-1} is consistent with the Blake et al. (2010) measurement. Our measurement of $30.61^{+0.69}_{-0.69}$ km s^{-1} for 2M1821+14 is slightly larger than the Blake et al. (2010) measurement of 28.9 ± 0.16 km s^{-1}, but is in agreement

within 2σ. Our $v\sin(i)$ measurement for 2M1906+40 is slightly larger than the Gizis et al. (2013) measurement, but is again consistent within 2σ. Finally, our measurement of $9.6^{+0.49}_{-0.49}$ km s^{-1} for W0047 is higher than both previous measurements by Gizis et al. (2015) and Lew et al. (2016). The model atmosphere for W0047 used by Gizis et al. (2015) has $T_{\rm eff} = 2300$ K and $\log(g) = 5.5$, while evolutionary models predict $T_{\rm eff} = 1270$ K and $\log(g) = 4.5$ (Gizis et al., 2015). Our model (with $T_{\rm eff} = 1670$ K and $\log(g) = 5.2$) is in better agreement with the evolutionary model results. With higher effective temperature and surface gravity, the atmospheric model used by Gizis et al. (2015) includes more pressure broadening, and thus results in a lower value of $v\sin(i)$. Lew et al. (2016) do not provide details on the atmospheric model used. Again, the consistency between orders 32, 33 and 38 further supports our results.

3.5.2 Calculating Inclination Angles

We assume that a brown dwarf rotates as a rigid sphere. However, this is not strictly true. The rotational period of Jupiter, as measured by magnetic fields originating in the core is $9^{\rm h}50^{\rm m}30^{\rm s}$, whereas the period measured using features rotating along the equator is $9^{\rm h}55^{\rm m}40^{\rm s}$, a difference of only 5 minutes. Since rotational periods as measured from photometric variability in general have much larger uncertainties, the rigid-body assumption is reasonable for our analysis. Thus, the equatorial rotation velocity, v, is given by $v = 2\pi R/P$, where R is the radius of the brown dwarf and P is its rotation period. With our measured values of $v\sin(i)$ in hand, an assumption of radius and a measurement of the rotation period allow us to determine the angle of inclination, i. Filippazzo et al. (2015) provide radius estimates from evolutionary models for eleven of nineteen of our targets (starred in Table 3.5). We use reasonable radius estimates for the remaining field brown dwarfs. At field brown dwarf ages, the radii are independent of mass due to electron degeneracy (Burrows et al., 2001) and approach the radius of Jupiter. Therefore, the field brown dwarf targets are assumed to have a radius of $0.8 - 1.2\ R_{Jup}$. 2M1615+49 is the only young brown dwarf with no radius estimate. Since it has not been associated with any moving group (Faherty et al., 2016), we have no age constraint on this object. We assume a radius of $1.1 - 1.7\ R_{Jup}$, similar to other VL-G objects in the sample.

Table 3.5 Rotational velocities, radial velocities, effective temperatures, and gravities calculated in this study.

Name	$v \sin(i)$ (km s^{-1})	RV (km s^{-1})	$T_{\rm eff}$ K	$\log(g)$ dex	Radius (R_{Jup})	Inclination (°)
2M0036+18	36.0 ± 0.2	20.9 ± 0.14	1909 ± 6	5.22 ± 0.02	$0.94 - 1.08$[a]	51 ± 9
W0047	9.8 ± 0.3	$-19.8^{+0.1}_{-0.2}$	1666 ± 2	$5.16^{+0.2}_{-0.3}$	$1.26 - 1.34$[a]	53 ± 3
2M0103+19	$40.0^{+3.7}_{-4.7}$	$12.4^{+3.8}_{-4.0}$	1880^{+200}_{-110}	$4.0^{+0.6}_{-0.4}$	$1.21 - 1.47$[a]	40 ± 8
2M0107+00	19.4 ± 0.8	8.2 ± 0.5	1450^{+70}_{-20}	$4.7^{+0.4}_{-0.1}$	$0.87 - 1.09$[a]	56 ± 17
SIMP 0136	$52.8^{+1.1}_{-1.0}$	12.3 ± 0.8	1290 ± 10	$5.45^{+0.03}_{-0.04}$	$0.8 - 1.2$	80 ± 12
SDSS 0423-04	68.0 ± 0.9	30.5 ± 0.6	1460 ± 10	$5.27^{+0.5}_{-0.04}$	$0.8 - 1.2$	79^{+11}_{-16}
WISE 1049B[b]	26.1 ± 0.2	...	...	...	$0.95 - 1.09$[a]	83^{+7}_{-8}
DENIS 1058[c]	37.5 ± 2.5	...	...	...	$0.93 - 1.07$[a]	90_{-2}
2M1126-50	$22.8^{+1.6}_{-2.4}$	49.3 ± 1.1	1270^{+60}_{-20}	$3.7^{+0.5}_{-0.1}$	$0.8 - 1.2$	35 ± 7
2M1507-16	19.1 ± 0.5	$-39.2^{+0.3}_{-0.4}$	1750 ± 6	5.45 ± 0.04	$0.9 - 1.08$[a]	23 ± 2
2M1615+49	$9.5^{+1.3}_{-1.2}$	-21.3 ± 0.5	1624^{+8}_{-48}	$4.53^{+0.08}_{-0.1}$	$1.1 - 1.4$	86^{+4}_{-10}
SIMP 1629	$19.7^{+0.7}_{-0.8}$	7.7 ± 0.5	1277 ± 7	5.29 ± 0.03	$0.8 - 1.2$	82^{+8}_{-13}
2M1721+33	21.5 ± 0.3	-102.8 ± 0.2	1656 ± 2	4.77 ± 0.02	$0.8 - 1.2$	27 ± 4
2M1821+14	30.7 ± 0.2	11.0 ± 0.1	1766 ± 1	4.89 ± 0.01	$0.8 - 1.2$	61 ± 17
2M1906+40	15.2 ± 0.5	$-22.8^{+0.3}_{-0.2}$	1999^{+3}_{-5}	5.30 ± 0.04	$0.8 - 1.2$	82^{+8}_{-12}
PSO-318[d]	$17.5^{+2.3}_{-2.8}$	$6.0^{+0.8}_{-1.1}$	1325^{+330}_{-12}	$3.7^{+1.1}_{0.1}$	$1.38 - 1.44$[a]	61 ± 17
2M2139+02	18.7 ± 0.3	-25.1 ± 0.3	1333 ± 5	5.37 ± 0.02	$0.8 - 1.12$[a]	90_{-1}
2M2148+40	$9.2^{+0.4}_{-0.3}$	-14.3 ± 0.1	1774 ± 1	$5.00^{0.01}_{-0.02}$	$0.89 - 1.09$[a]	88^{+2}_{-8}
2M2208+29	$40.6^{+1.3}_{-1.4}$	$-15.7^{+0.8}_{-0.9}$	1707^{+10}_{-9}	4.27 ± 0.11	$1.21 - 1.61$[a]	55 ± 10

Note: The results presented here are for order 33. The last two columns show our estimated radii and the resulting angle of inclination calculated for each object. [a] Radii are taken from Filippazzo et al. (2015)
[b] $v \sin(i)$ measurement taken from Crossfield et al. (2014)
[c] $v \sin(i)$ measurement taken from Basri et al. (2000)
[d] Measurements taken from Allers et al. (2016)

Monte Carlo analysis was used to determine the inclination, i, for each target, using uniformly distributed radii and Gaussian distributions for the $v \sin(i)$ and period values. The inclination and error were calculated as the mean and standard deviation of the resulting distribution of i. Table 3.5 shows the rotational velocities calculated for our sample, as well as the inclination angles determined based on our estimated radii. As stated earlier, we focus our analysis on order 33. However, using a weighted-average of $v \sin(i)$ values obtained from orders 32, 33 and 38 yields consistent inclination angles.

3.6 Results and Discussion

3.6.1 Effects of Inclination on Variability Amplitude

Figure 3.2 shows the variability amplitude plotted against the angle of inclination. We note a number of interesting trends in the J-band and *Spitzer* variable brown dwarfs.

Firstly, the highest amplitude J-band variable objects are either L/T transition brown dwarfs or young, low-gravity brown dwarfs. The highest *Spitzer* and J-band amplitudes are both for the L/T transition brown dwarf, 2M2139+02. The *Spitzer* amplitudes for young brown dwarfs are slightly enhanced, but only relative to their own spectral type and not the entire *Spitzer* sample.

Secondly, while it is clear that each brown dwarf has its own intrinsic amplitude, the inclination angle affects the observed amplitude for both bands. Figure 3.2 shows that there are no mid-IR variability detections at inclination angles $< 20°$ and no J-band detections at inclination angles $< 35°$. For a sample of objects with random orientation, the probability distribution of the inclination angles is $P(i) \sim \sin i$ (Jackson & Jeffries, 2010). Thus, the overall observed distribution is fairly consistent with the distribution expected for brown dwarfs that are randomly oriented in space (Figure 3.3). This means that although our sample is small, it is representative of the brown dwarf population with regard to inclination. Excluding the young objects, we find relatively low amplitudes at inclination angles $20 - 60°$. At inclinations close to $90°$ we observe the highest variability amplitudes in both bands. This makes sense as the brown dwarf is nearly equator-on, allowing us to observe the full variability amplitude. An atmospheric feature observed on a low-inclination object will appear smaller as a result of projection

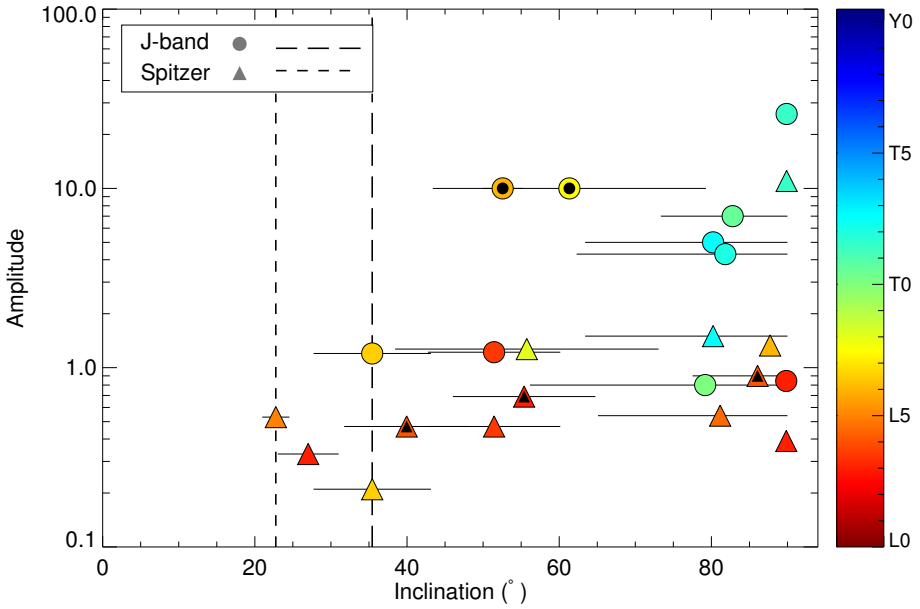

Figure 3.2 Variability amplitude plotted against inclination angle for our sample. Circles denote J-band detections, while triangles denote *Spitzer* 3.6 μm detections. The colour scale represents spectral type, and young objects are denoted by a black inset. Dashed lines represent the minimum inclination angle for each band.

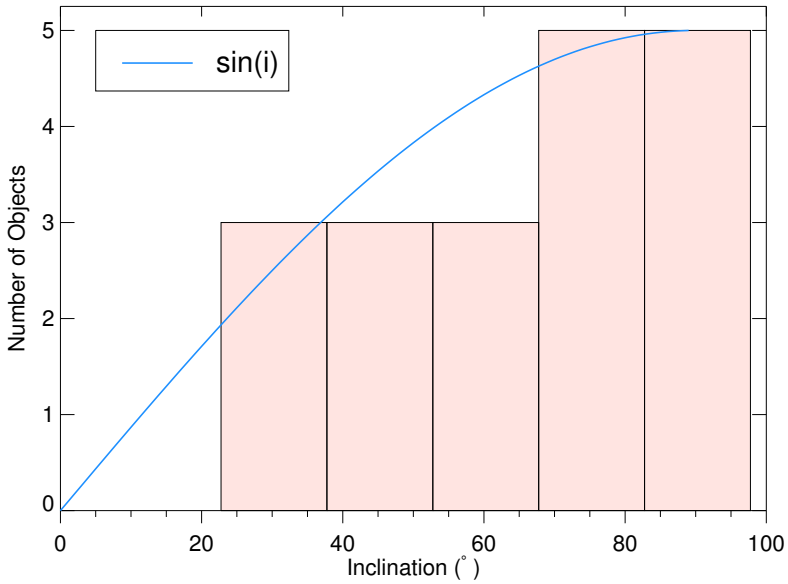

Figure 3.3 Histogram showing the distribution of inclination angles calculated for the our sample. The probability distribution of randomly oriented objects is $P(i) \sim \sin(i)$. This distribution fits the calculated distribution quite well

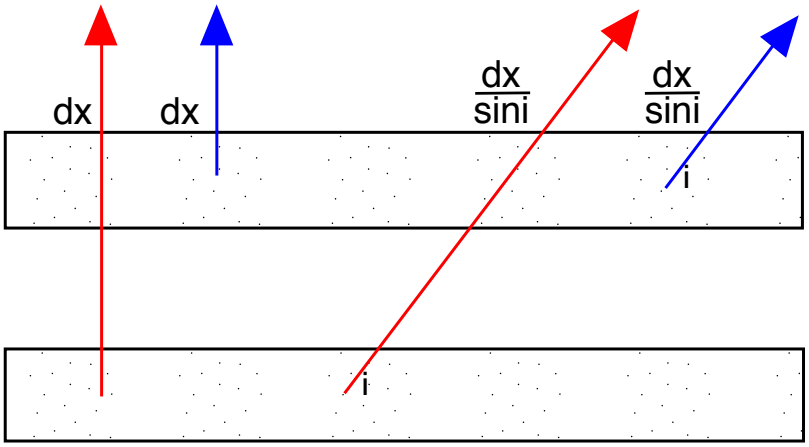

Figure 3.4 Inclination angle i affects the atmospheric path length travelled from flux originating from a certain depth. In this diagram, the bottom shaded area corresponds to the depth that most of the $J-$band flux originates from when an object is viewed equator-on. The top shaded area corresponds to the depth that most of the *Spitzer* 3.6 μm flux comes from for an equator-on object. At $i = 90°$, the flux is attenuated by κdx where κ is the attenuation coefficient and dx is the distance to the top of the atmosphere. At $i < 90°$ this flux is more strongly attenuated because the atmospheric path length is longer.

effects.

The J-band amplitudes appear to be more affected by inclination than the *Spitzer* amplitudes. The highest J-band variable objects appear at high inclinations, whereas a *Spitzer* brown dwarf viewed equator-on displays similar amplitudes to those observed at inclinations as low as $\sim 20°$. This may be explained by considering the pressures probed by each band. Biller et al. (2013), Buenzli et al. (2012), and Yang et al. (2016) determined the pressure level probed at optical depth $\tau = 2/3$ as a function of wavelength for various models, finding that the J-band probes a discrete range of pressures deep in the atmosphere. On the other hand, the *Spitzer* [3.6 μm] band probes a broader range of pressures that extend higher up in the photosphere. For the deep layers probed by the J-band, the flux will be strongly attenuated for the low-inclination objects due to an increased path length through the atmosphere. The effect is not observed as strongly for *Spitzer* detections because more of the flux originates from near the top of the photosphere. Thus, we see J-band amplitudes decrease strongly with decreasing inclination.

We used a toy model to investigate the effects of inclination on the observed

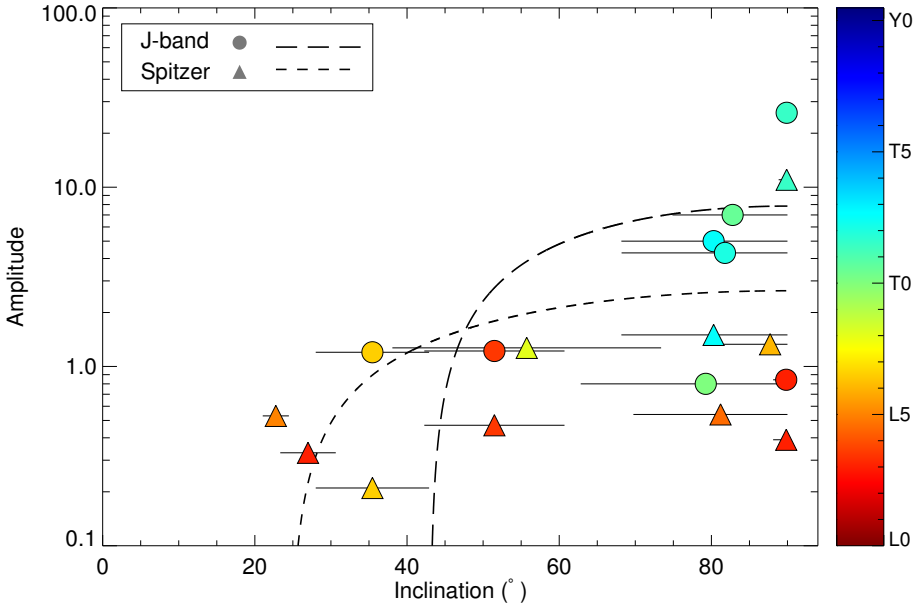

Figure 3.5 Variability amplitude plotted against inclination angle for *Spitzer* 3.6 μm (triangles) and J-band (circles) field objects in our sample. The colour scale represents spectral type, and young objects are denoted by a black inset. Best-fit functions of Equation 3.1 are plotted as grey dashed lines.

Table 3.6 Best-fit parameters for Equation 3.1. Best-fit functions for both bands are plotted in Figure 3.5.

	J-band	*Spitzer* [3.6 μm]
A_0	14.69 ± 0.11	3.20 ± 0.06
κdx	6.85 ± 0.07	0.56 ± 0.03

variability amplitude. Our model has two terms:

$$A = A_0 \sin i - \kappa \frac{\mathrm{dx}}{\sin i} \tag{3.1}$$

where A is the observed amplitude and A_0 is the amplitude that would be observed if there were no atmospheric attenuation of the flux. κ is the factor by which the flux is attenuated as it passes through the atmosphere, and $\frac{dx}{\sin i}$ is the atmospheric path length. The first term is a projection effect that causes the observed area of a spot to decrease as the brown dwarf approaches lower inclinations. The second term represents the attenuation of the flux as it passes through the brown dwarf atmosphere. Figure 3.4 shows that decreasing the inclination angle increases the atmospheric path length. From the models discussed above, we expect that the J-band path lengths are larger than the *Spitzer* path lengths. We fit the function for both bands, assuming that all objects have the same intrinsic amplitude. We considered only the field brown dwarfs since young objects likely have very different atmospheric structures. The best-fit parameters are shown in Table 3.6, with the functions plotted in Figure 3.5. The model fits the data reasonably well, displaying the earlier drop-off of the J-band amplitudes compared to the *Spitzer* amplitudes due to a much larger J-band $\kappa \mathrm{dx}/\sin(i)$ term. We estimate the brown dwarf atmospheric extinction as a power law: $\kappa \sim \lambda^{-\alpha}$, where $\alpha = 1.7$ (Bertoldi et al., 1999). While this is an empirical law based on extinction by the interstellar medium, dust grains found in the atmospheres of brown dwarfs may be similar in size and thus produce similar results (Looper et al., 2008; Marocco et al., 2014). Thus, by estimating the extinction coefficient, we can estimate the relative path lengths traveled by the flux in each band. We find that $\mathrm{dx}_{3.6\mu\mathrm{m}}/\mathrm{dx}_J = 0.40$. Yang et al. (2016) calculate the pressure levels probed at optical depth $\tau = 2/3$ as a function of wavelength for models with a range of spectral types. For all spectral types investigated, they find that the J-band probes a discrete range of pressures deep in the atmosphere, while the pressures probed by the *Spitzer* [3.6 μm] extend higher in the atmosphere. The relative pressures found in this study for L5, T2, and T6 brown dwarfs were $\mathrm{P}_{3.6\mu\mathrm{m}}/\mathrm{P}_J = 0.39, 0.05$ and 0.05, respectively. If we assume that the depth increases monotonically with pressure, then our value of $\mathrm{dx}_{3.6\mu\mathrm{m}}/\mathrm{dx}_J$ is consistent with that of the L5 brown dwarf computed by Yang et al. (2016). Of course this is a highly simplistic model with some limitations. Firstly, it does not take into account spectral types or different intrinsic variabilities. Secondly, since the majority of $J-$band variability detections are made from ground-based surveys, they are not sensitive to the lower amplitudes detected by *Spitzer* in the mid-IR. Thirdly, the model fits are strongly

influenced by the absence of detections at low amplitudes, but the reason may be the underlying inclination distribution and not that their variability amplitudes are below detection limits.

3.6.2 Relation between Period and Variability Amplitude

Figure 3.6 shows the variability amplitude plotted against rotation period for *Spitzer* and J-band variable L, T, and Y spectral type objects with published periods from the literature (shown in Tables 3.2 and 3.3). The mid-IR *Spitzer* detections are extremely robust because of the high photometric precision that is achievable from space. Additionally, these observations are typically longer than ground-based observations – for example, Metchev et al. (2015) employ $\sim$ 20 hr observations in their survey. This results in extremely accurate period measurements for *Spitzer*-monitored objects. In contrast, J-band detections come from a variety of ground-based and space-based *HST* surveys. The ground-based searches do not reach the same photometric precision as space-based searches and thus are limited to higher amplitudes. J-band monitoring observations are shorter than *Spitzer* observations and thus have larger period uncertainties. For both samples, we only take objects whose periods are constrained.

The J-band and *Spitzer* data display notably different period and variability amplitude properties. Ground-based J-band detections have lower photometric precision, so in general J-band detections are limited to larger amplitudes. It is clear that mid-IR variability is intrinsically lower than near-IR variability, as high-amplitude variability would certainly have been detected with *Spitzer*. Ground-based observations are only sensitive to shorter periods ($>$ 15 hr), so the longer period variable brown dwarfs have been detected with *Spitzer*.

Figure 3.7 shows the variability amplitude plotted against rotation period for all J-band variable objects with published periods (shown in Table 3.2). Measured periods are $<$ 15 hr, since most J-band detections are ground-based, and thus are sensitive to this range of periods. The highest amplitudes are L/T transition spectral types, as reported by Radigan et al. (2014). The young, low-gravity L-type objects W0047 and PSO-318 display higher variability amplitudes than other L dwarfs, supporting the tentative correlation between low-gravity and high-amplitude variability reported by Metchev et al. (2015). Additionally, for periods $\sim 7-9$ hr, there seems to be an overall increase in J-band variability amplitude with longer periods.

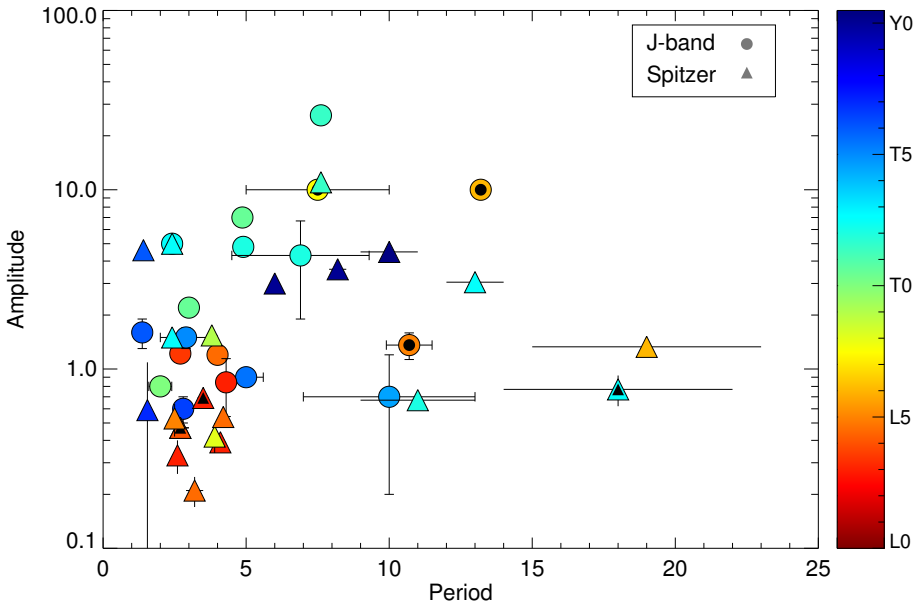

Figure 3.6 Variability amplitude plotted against period for *Spitzer* 3.6 μm (triangles) and J-band (circles) variability detections. The colour bar represents the spectral type of each object and young objects are denoted by a black inset. Objects with unconstrained periods were not included. Data and literature references are shown in Tables 3.2 and 3.3.

3.6.3 Spearman and Kendall Correlation Coefficients

We calculated the significance of possible correlations observed in our results by calculating Spearman's ρ and Kendall's τ correlation coefficients using IDLs R_CORRELATE.PRO. They are briefly described below.

Spearman's ρ Correlation Coefficient

Spearman's ρ-test is a non-parametric test that is based on the ranking of that data points rather than their values. If R_i is the rank of data point x_i, and S_i is the rank of y_i, the rank-order correlation coefficient is defined to be the linear correlation coefficient of the ranks:

$$\rho = \frac{\sum_i (R_i - \bar{R})(S_i - \bar{S})}{\sqrt{\sum_i (R_i - \bar{R})^2}\sqrt{\sum_i (S_i - \bar{S})^2}} \tag{3.2}$$

Spearman's ρ is distributed approximately as Student's distribution with $N - 2$ degrees of freedom. This approximation does not depend on the distribution of

the data (x, y); it is always the same approximation.

$$t = \rho\sqrt{\frac{N-2}{1-\rho^2}} \tag{3.3}$$

Using this distribution we can calculate the probability of obtaining a value $\geq \rho$ assuming that no correlation exists. This is known as the p-value (Press et al., 1987).

Kendall's τ Correlation Coefficient

Instead of using the numerical difference of ranks, Kendall's τ is a measure of correlation based on the relative ordering of the rank of each value in the dataset (Press et al., 1987). To define τ, we start with N data points (x_i, y_i), and consider all $\frac{1}{2}N(N-1)$ pairs of data points. A pair is *concordant* if the relative ordering of the ranks of (x_i, x_j) is the same as the relative ordering of the ranks of (y_i, y_j). A pair is *discordant* if the relative ordering of (x_i, x_j) differs from the ordering of the (y_i, y_j) ranks. When the relative (x_i, x_j) ranks are the same, we call the pair an "extra-y" pair. Similarly, when relative (x_i, x_j) ranks are the same, we get an "extra-x" pair. Kendall's τ is then calculated using the equation:

$$\tau = \frac{\mathrm{C} - \mathrm{D}}{\sqrt{\mathrm{C} + \mathrm{D} + \mathrm{extra}{-}y}\sqrt{\mathrm{C} + \mathrm{D} + \mathrm{extra}{-}x}} \tag{3.4}$$

where C and D are the number of concordant and discordant pairs, respectively. In the null hypothesis of no association between x and y, τ is normally distributed with zero-expectation value and a variance of

$$\mathrm{Var}(\tau) = \frac{N+10}{9N(N-1)} \tag{3.5}$$

As with the Spearman's ρ-test, we use this distribution to calculate the p-value of the null hypothesis. Although Spearman's rank correlation is a more widely used measure of rank correlation, Kendall's τ has slightly better statistical properties and the interpretation in terms of probabilities of observing the concordant and discordant pairs is more direct (Conover & Iman, 1980). Nonetheless, in most situations, the interpretations of both methods is very similar.

Calculating Spearman's ρ and Kendall's τ, we find that the relation between J-band variability amplitude and rotational period (for periods < 9 hr) is significant

with a p-value = 6.0% and 6.7% for the Spearman and Kendall tests respectively. In contrast, including all periods, the correlation between period and amplitude is not significant, with a p-value= 19 and 17% for the Spearman and Kendall tests. This tentative correlation between variability amplitude and rotation period for periods < 9 hr may be explained by consideration of the Rhines length (Rhines, 1970). Organised jet features in the atmospheres of the giant solar system planets generally scale in size with the Rhines length. This also represents the maximum attainable size that a coherent atmospheric structure can grow to before being destroyed by such zonal jets. The Rhines length is given by

$$L_{RH} \sim \sqrt{\frac{U}{2\Omega R \cos\phi}} \tag{3.6}$$

where U is the characteristic wind speed, R is the radius, $\Omega = 2\pi/P$, where P is the period, and ϕ is the latitude of the atmospheric feature. Assuming that the wind speeds and latitudes are the same then $L_{RH} \sim \sqrt{P}$. Thus we would expect the maximum atmospheric feature size to increase with longer rotational periods, explaining the increasing variability amplitude with period in Figure 3.7. Beyond periods of 9 hr, this correlation does not seem to hold. This suggests that for periods greater than $\sim 7 - 9$ hr, the Rhines length is no longer the dominant factor in controlling the size of atmospheric features.

Figure 3.8 shows the *Spitzer* amplitudes plotted against rotation periods for all *Spitzer* variable objects with published periods (presented in Table 3.3). *Spitzer* observations are in general longer than ground-based J-band observations (Metchev et al. (2015) employed $\sim$ 20 hr observations for their *Spitzer* survey) and are thus sensitive to longer periods. *Spitzer* light curves have much higher photometric precision than ground-based studies and thus are also sensitive to lower amplitudes. However, mid-IR variability is clearly intrinsically lower than the near-IR variability. In contrast to the J-band data, both statistical tests produce a p-value $\sim$ 80%, thus we find no correlation between variability amplitude and rotation period in this case. At longer periods, the observed variability amplitudes appear to decrease, but the sparse number of data points prevents us from confirming this. The highest variability amplitudes in the mid-IR case are detected in the late Ts and early Ys, in contrast to the J-band, where high amplitudes are detected in L/T transition objects. Again, the young L-type objects may have slightly enhanced amplitudes when compared to field L-type brown dwarfs (Metchev et al., 2015).

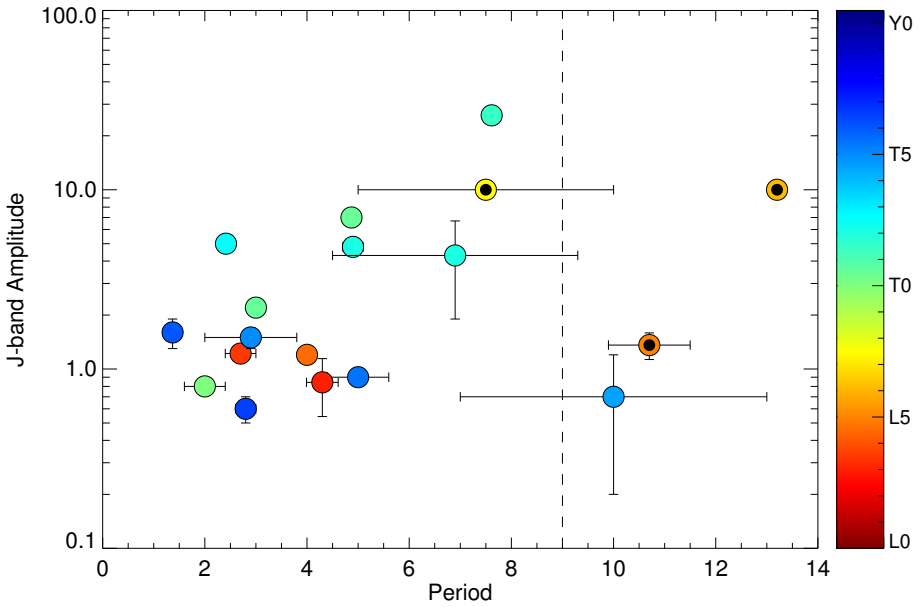

Figure 3.7 Variability amplitude plotted against period for J-band variability detections. The colour bar shows spectral type and young objects are denoted by a black inset. The dashed line shows the cut-off point of the period range for which the Rhines scale appears to have an effect on variability amplitude. For rotation periods < 9 hr, we find a tentative correlation between variability amplitude and period with a p-value $= 6.7\%$, using the Kendall's τ-test.

3.6.4 Investigating Colour Anomalies of the Sample

We define the colour anomaly of each object as the median 2MASS $J-K_S$ colour of objects of that spectral type and gravity class subtracted from the $J-K_S$ colour of the object. Objects with a positive colour anomaly appear redder than the median and objects with a negative colour anomaly appear bluer than the median. Median colours for L0 - T6 objects were taken from Schmidt et al. (2010). For 2M0050, the T7 object, we calculated the median of all IR T7 objects from DwarfArchives.org (20 objects) and found the median T7 ($J-K_S$) colour to be -0.04 ± 0.43. This is a much higher error than those in Schmidt et al. (2010) and was thus left out of the analysis. With no $J-K_S$ measurement of Y dwarfs, it was not possible to include WISE0855, WISE1405 and WISE1738. Liu et al. (2016) provides linear relations between spectral type and absolute magnitude for VL-G and INT-G brown dwarfs, and these were used to calculate the median colours for the low-gravity sample.

Figure 3.9 displays the colour anomaly of objects listed in Table 3.1 plotted

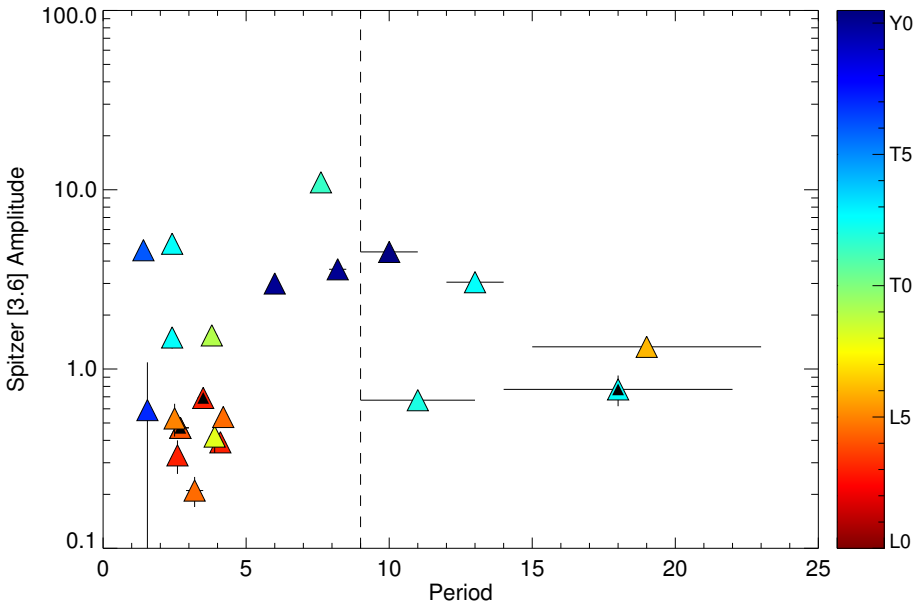

Figure 3.8 Variability amplitude plotted against period for *Spitzer* 3.6 μm variability detections. We do not find a significant correlation between variability amplitude and rotational period for periods < 9 hr in this case.

against their inclinations. We note a correlation between the $J - K_S$ colour anomaly and inclination, whereby objects viewed equator-on appear redder than objects viewed at lower inclinations.

Calculating Spearman's ρ and Kendall's τ coefficients, we find that the relation between colour anomaly and inclination is statistically significant with a p-values of 0.4% and 0.5% respectively. Objects we observe to be redder than the median are viewed equator-on, whereas objects appearing bluer than the median are viewed closer to pole-on. This result could be interpreted by the idea first proposed by Kirkpatrick et al. (2010), that viewing angle determines the spectral appearance of a brown dwarf. This could occur if clouds are not homogeneously distributed in latitude or if grain size and cloud thickness vary in latitude. Our results can be explained if thicker or large-grained clouds are situated at the equator, while thinner or small-grained clouds are situated at the poles.

Figures 3.10 and 3.11 show the variability amplitude plotted against the colour anomaly for J-band and *Spitzer* detections, respectively. Both plots exhibit a consistent trend, whereby field objects that are redder than the median display higher J-band and *Spitzer* variability amplitudes. The field objects with the

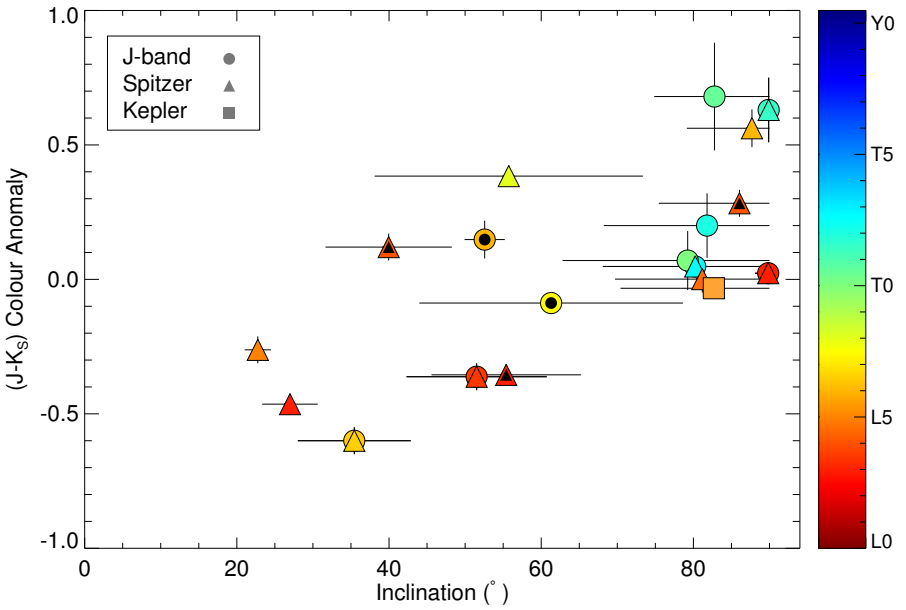

Figure 3.9 Colour anomaly plotted against inclination for the sample in Table 3.1. Young objects are denoted by a black inset.

highest observed variability amplitudes are those with the reddest $J - K_S$ colours of their spectral type. Using both correlation tests, we find that this correlation is significant at the 93% and 99% levels for the J-band and mid-IR detections, respectively. This relation may be explained by consideration of viewing angle. If redder brown dwarfs are viewed equator-on, and equator-on objects exhibit the highest amplitudes, then it follows that redder brown dwarfs should display the highest variability amplitudes. Similarly, bluer brown dwarfs are viewed close to pole-on, so the observed variability amplitude will be reduced because of the viewing angle.

We also see trends related to spectral type in both figures that could explain the observed relation. In the J-band case (Figure 3.10), the early- to mid-L spectral type field dwarfs display a blue anomaly, while the L/T transition field dwarfs display a red $(J - K_S)$ colour anomaly. The late-T type objects with detected variability display colours that are relatively close to the median. These trends are shown even more clearly for the *Spitzer* detections (Figure 3.11). The low-amplitude variability detections are observed in early-L type brown dwarfs displaying a blue anomaly. We observe higher amplitude variability in L/T transition objects that display a red anomaly. This trend could be explained by variability that is due to the breakup of silicate clouds. L-type brown dwarfs with thick silicate clouds generally appear red, while the relatively cloudless T

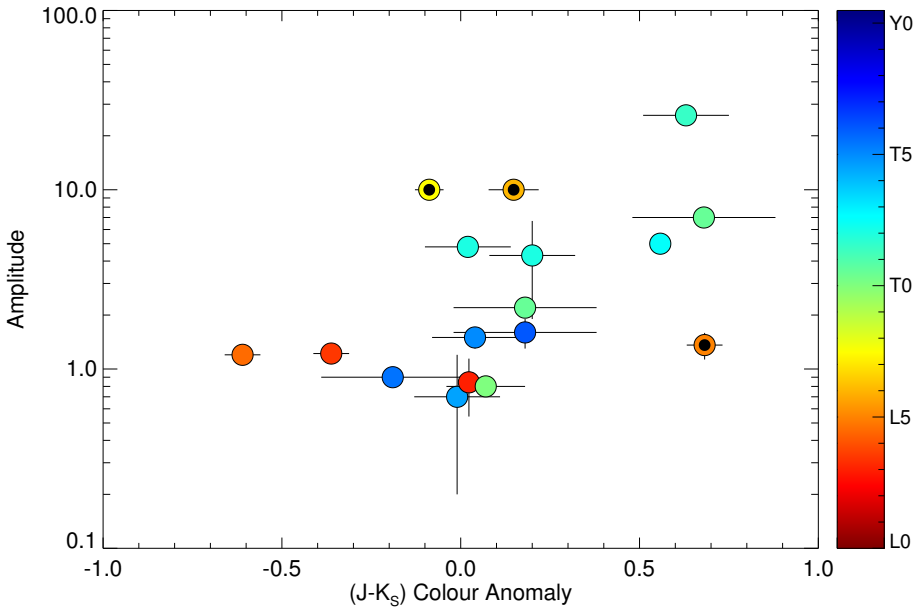

Figure 3.10 Amplitude plotted against colour anomaly for J-band variability detections.

dwarfs appear more blue. Thus, L dwarfs whose clouds have begun to break up will appear bluer than the median, and produce variability that is due to these patchy clouds. On the other hand, early-T dwarfs that still have clouds in their atmospheres will appear redder than the median, resulting in photometric variability as these clouds rotate in and out of view. While this simple idea is an attractive explanation, spectroscopic variability observations have shown that cloud evolution in L and T brown dwarf atmospheres is significantly more complex than simple formation of cloud holes (Buenzli et al., 2012, 2015b; Apai et al., 2013; Yang et al., 2016).

Furthermore, we see that surface gravity has an effect on this relation in both bands. For the $J-$band detections (Figure 3.10), the low-surface gravity objects do not seem to follow the trend in spectral type, and appear among the L/T transition field objects. It seems that low-surface gravity objects that are redder than the median appear variable, but with only three detections we cannot confirm this. In contrast, for the *Spitzer* detections, 2/3 of the low-surface gravity objects seem to follow the overall trend, with one object falling closer to the L/T transition field brown dwarfs. Variability surveys of young, low-surface gravity objects will clarify these possible deviations from the field brown dwarf population.

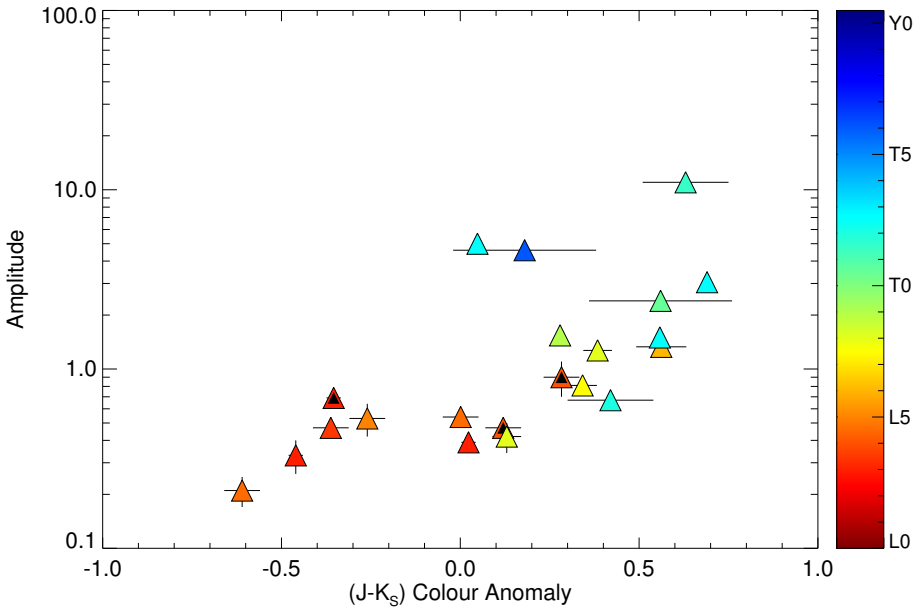

Figure 3.11 Variability amplitude plotted against colour anomaly for *Spitzer* variability detections.

Survival Analysis on Spitzer Amplitude - Color Anomaly Trend

The high precision of *Spitzer* data means that meaningful amplitude constraints can be placed on the variability amplitudes on non-detections in variability surveys (Metchev et al., 2015). These can be incorporated into our statistical results using survival analysis. Survival analysis comprises of a number of statistical analysis techniques designed to incorporate non-detections and/or upper/lower limits (Feigelson & Babu, 2013; Akritas & Siebert, 1996).

Metchev et al. (2015) provide upper limits on the variability amplitudes of non-detections from their survey, assuming fixed rotational periods of 10 hr. We plot these alongside the full sample of *Spitzer* detections in Figure 3.12. We perform the Spearman ρ test and the generalized Kendall's τ test of bivariate correlation incorporating the upper limit data using the IRAF STSDAS.ANALYSIS.STATISTICS package. Both tests result in a probability $> 99.99\%$ that a correlation is present. These results lend further evidence in favour of such a trend, and also suggest that the trend holds for all brown dwarfs, and is not just restricted to the population of variable brown dwarfs.

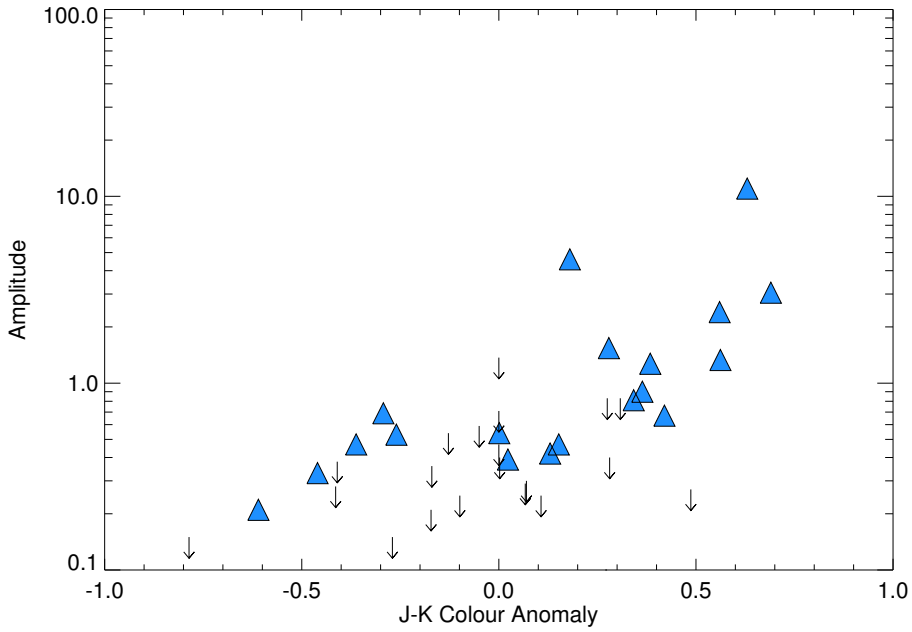

Figure 3.12 Variability amplitude plotted against colour anomaly for *Spitzer* detections (triangles) and amplitude upper limits for non-detections (downward arrows).

3.7 Summary and Conclusions

This chapter explores the effects of inclination angle on measured variability amplitudes and whether brown dwarfs display similar intrinsic amplitudes. We further proceeded to examine the relation between inclination angle and spectral appearance. We determined the inclination angle of 19 variable brown dwarfs using archival Keck NIRSPEC data and evolutionary model estimates on radius. We analyse the full sample of L, T and Y spectral type brown dwarfs with published J-band and *Spitzer* variability detections.

We conclude that brown dwarfs have different intrinsic amplitudes, dependent on properties such as spectral type, rotation period, and surface gravity. In this chapter we find evidence that the variability amplitude may increase with rotational period for periods $< 7 - 9$ hr. This result is significant at the 93% level for J-band detections, but is not significant for *Spitzer* detections. The inclination angle affects the observed amplitude through a projection effect as well as atmospheric attenuation. Our toy model suggests that J-band variability is more strongly affected by inclination than *Spitzer* variability. The reason may be that the J-band probes deeper levels in the atmosphere. The result is that

the flux coming from these deeper levels is more attenuated because the path lengths increase at lower inclinations. All brown dwarfs with mid-IR variability detections are inclined at an angle $> 20°$. In the near-IR, we find that all brown dwarfs with J-band variability detections are inclined at an angle $> 35°$.

We find a trend between the colour anomaly and inclination of our sample that is statistically significant at the 99% level. Field objects viewed equator-on appear redder than the median for their spectral type, whereas objects viewed at lower inclinations appear bluer. This supports the idea that our viewing angle influences the spectral and photometric appearance of a brown dwarf. These results can be explained if thicker or large-grained clouds are situated at the equator, with thinner or small-grained clouds at the poles. We also find a strong correlation between colour anomaly and both mid-IR and J-band variability, where redder objects have higher variability amplitudes. This again suggests that the spectral appearance of a brown dwarf is strongly affected by its inclination angle.

Chapter 4

Variability of the Lowest Mass Objects in the AB Doradus Moving Group

4.1 Abstract

We present the detection of [3.6 μm] photometric variability in two young, L/T transition brown dwarfs, WISE J004701.06+680352.1 (W0047) and 2MASS J2244316+204343 (2M2244) using the *Spitzer Space Telescope*. We find a period of 16.4 ± 0.2 hr and a peak-to-peak amplitude of $1.07 \pm 0.04\%$ for W0047, and a period of 11 ± 2 hr and amplitude of $0.8 \pm 0.2\%$ for 2M2244. Our measured period for W0047 is significantly longer than that measured previously during a shorter *HST* observation. We additionally detect significant J-band variability in 2M2244 using the Wide-Field Camera on UKIRT. We determine the radial and rotational velocities of both objects using Keck NIRSPEC data. We find a radial velocity of $-16.0^{+0.8}_{-0.9}$ km s^{-1} for 2M2244, and confirm it as a bona fide member of the AB Doradus moving group. We find rotational velocities of $v \sin i = 9.8 \pm 0.3$ km s^{-1}and $14.3^{+1.4}_{-1.5}$ km s^{-1} for W0047 and 2M2244, respectively. With inclination angles of $85^{+5\circ}_{-9}$ and $76^{+14\circ}_{-20}$, W0047 and 2M2244 are viewed roughly equator-on. Their remarkably similar colours, spectra and inclinations are consistent with the possibility that viewing angle may influence atmospheric appearance. We additionally present *Spitzer* [4.5 μm] monitoring of the young, T5.5 object SDSS111010+011613 (SDSS1110) where we detect no variability. For

periods < 18 hr, we place an upper limit of 1.25% on the peak-to-peak variability amplitude of SDSS1110.

4.2 Introduction

The growing number of young exoplanets that have been directly imaged in the infrared (Marois et al., 2008; Lagrange et al., 2010; Macintosh et al., 2015) have revealed some unexpected results. With comparable temperatures but lower masses, the young directly imaged planets were expected to share similar atmospheric properties to the well-studied population of brown dwarfs. However most young directly-imaged planets appear much redder in the near-IR than their higher mass field brown dwarf counterparts with similar spectral types. Fortunately, young brown dwarfs may still provide an excellent analogue to directly-imaged planets, and we now have a significant population of young brown dwarfs with colours and magnitudes similar to directly-imaged exoplanets, many of which have estimated masses in the planetary-mass regime (see the compilation of young, red M and L dwarfs made by Faherty et al. (2016), Liu et al. (2016) and references therein).

Three such objects are WISEP J004701+680352 (W0047), 2MASS J2244316+204343 (2M2244) and SDSS J111010+011613 (SDSS1110) (Gizis et al., 2012; Knapp et al., 2004; Gagné et al., 2015b). W0047 and SDSS1110 are kinematically confirmed members of the 150 Myr old AB Doradus moving group (Bell et al., 2015). 2M2244 is assigned a membership probability of 99.6% for AB Doradus based on its proper motion and distance (Gizis et al., 2015; Gagné et al., 2015b, 2014a; Liu et al., 2016), but a radial velocity measurement is necessary to confirm moving group membership. In this chapter we measure the radial velocity of 2M2244 (Section 4.3.2) and confirm it as a member of the AB Doradus moving group. W0047 is classified as an L7 INT-G brown dwarf and 2M2244 is classified as an L6 VL-G object (Gizis et al., 2015; Allers & Liu, 2013). W0047 and 2M2244 are a particularly interesting pair of young, low-gravity objects, with $0.65-2.5$ μm spectra that are remarkably similar (Gizis et al., 2015). There are no other free-floating L/T transition dwarfs known to be both coeval and spectrally similar that are bright enough for detailed characterisation (though see Best et al. (2015) for more candidates). SDSS1110 is a T5.5 $10-12$ $M_{\rm Jup}$ (Gagné et al., 2015b) object, and is one of very few young, age-calibrated T dwarfs known to date. W0047, 2M2244 and SDSS1110 are the lowest mass confirmed members of the

AB Doradus moving group (Liu et al., 2016), and can thus provide powerful insights into the atmospheres of the directly-imaged planets.

A key probe of brown dwarf atmospheres is time-resolved photometric monitoring, which is sensitive to the spatial distribution of surface inhomogeneities as objects rotate. Large-scale field brown dwarf surveys have revealed ubiquitous variability across the entire L-T spectral range (Buenzli et al., 2014; Radigan et al., 2014; Wilson et al., 2014; Metchev et al., 2015). Due to their lower gravity, young brown dwarfs exhibit atmospheric scale heights and time scales different from old field brown dwarfs (Freytag et al., 2010; Marley et al., 2010, 2012). Thus, studying their variability provides valuable information on atmospheric structure in brown dwarfs and exoplanet atmospheres as a function of surface gravity. Because of their more recent formation, young brown dwarfs and exoplanets have inflated radii compared to the field brown dwarfs. Hence, they are expected to rotate more slowly than their older counterparts due to conservation of angular momentum. However, the planetary mass objects β Pic b, PSO 318.5–22 and 2M1207b all have rotation periods of $6 - 11$ hr (Snellen et al., 2014; Biller et al., 2015; Allers et al., 2016; Zhou et al., 2016), similar to higher mass brown dwarfs (Zapatero Osorio et al., 2006).

To date, the observed variability has been interpreted as evidence for condensate clouds, which are required by the majority of brown dwarf and exoplanet models (Marley et al., 2010; Morley et al., 2014). Magnetic phenomena, such as starspots, have also been suggested as a driver of photometric variability. While some L-T type brown dwarfs have been found to possess strong magnetic fields (Pineda et al., 2016; Kao et al., 2016), Miles-Páez et al. (2017) report no correlation between magnetic activity and photometric variability in a sample of L0-T8 brown dwarfs. Recently, Tremblin et al. (2016) proposed cloud-free models, suggesting that the observed variability is due to differing CO abundances or temperature fluctuations. Further work is required to establish which scenario is appropriate for these objects.

W0047 and 2M2244 present a unique opportunity to explore the effects of both viewing angle and age on observed variability. For an equator-on object (with an inclination angle, $i \sim 90°$) we measure the full variability amplitude via photometric monitoring. In contrast, lower variability amplitudes are measured for objects that are close to pole-on (Chapter 3; Vos et al., 2017). Determining the variability amplitude and inclination angle of each object allows us to disentangle the effects of viewing angle on the observed variability.

Metchev et al. (2015) find evidence for higher variability amplitudes for young L3-L5.5 objects. This is unexpected because atmospheric models for young objects typically require very thick clouds (Madhusudhan et al., 2011) and variability studies have suggested that older objects with patchy coverage of thinner and thicker clouds tend to have the highest variability amplitudes (Apai et al., 2013; Buenzli et al., 2015b). 2M2244, W0047 and SDSS1110 provide three valuable data points to further explore this trend beyond the early L-type dwarfs.

Periodic variability has previously been detected in W0047 and 2M2244. Lew et al. (2016) report variability with a peak-to-peak J-band amplitude of 8% for W0047 during a 9 hr observation, determining a period of 13.2 ± 0.14 hr. Morales-Calderon et al. (2006) obtained *Spitzer* [4.5 μm] time-resolved photometry of 2M2244 and report variability with a period of 4.6 hr and a peak-to-peak amplitude of 8 mmag during a 5.7 hr observation. SDSS1110 has no previous variability detections in the literature. We have obtained *Spitzer* photometric monitoring for W0047, 2M2244 and SDSS1110 and J-band monitoring of 2M2244 taken with WFCAM at UKIRT, as well as high dispersion NIRSPEC spectra of W0047 and 2M2244. The spectrum of W0047 was first presented by Gizis et al. (2015), and we use the same data set in this paper. The chapter is organised as follows. In Section 4.3 we discuss the analysis and results of our Keck NIRSPEC high resolution spectra of 2M2244 and W0047. In Section 4.4 we present the lightcurves of our three targets 2M2244, W0047 and SDSS1110. In Section 4.5 we calculate the inclination angles of W0047 and 2M2244.

4.3 Keck NIRSPEC High Dispersion Spectroscopy

We obtained high dispersion NIRSPEC spectra for W0047 from the Keck Observatory Archive (Prog ID: U055NS, PI: Burgasser) and observed 2M2244 as part of a larger program (Prog ID: N160NS, PI: Allers). NIRSPEC is a near-infrared echelle spectrograph on the Keck II 10 m telescope on Mauna Kea, Hawaii. The NIRSPEC detector is a 1024×1024 pixel ALADDIN InSb array. Observations were carried out using the NIRSPEC-7 ($1.839 - 2.630$ μm) passband in echelle mode using the 3 pixel slit ($0.432''$), echelle angles of $62°.68 - 62°.97$, and grating angles of $35°.42 - 35°.51$. Observations of targets were gathered in nod pairs, allowing for the removal of sky emission lines through the subtraction of consecutive images. Arc lamps were observed for wavelength calibration. $5 - 10$ flat-field and dark images were taken for each target to account for variations in

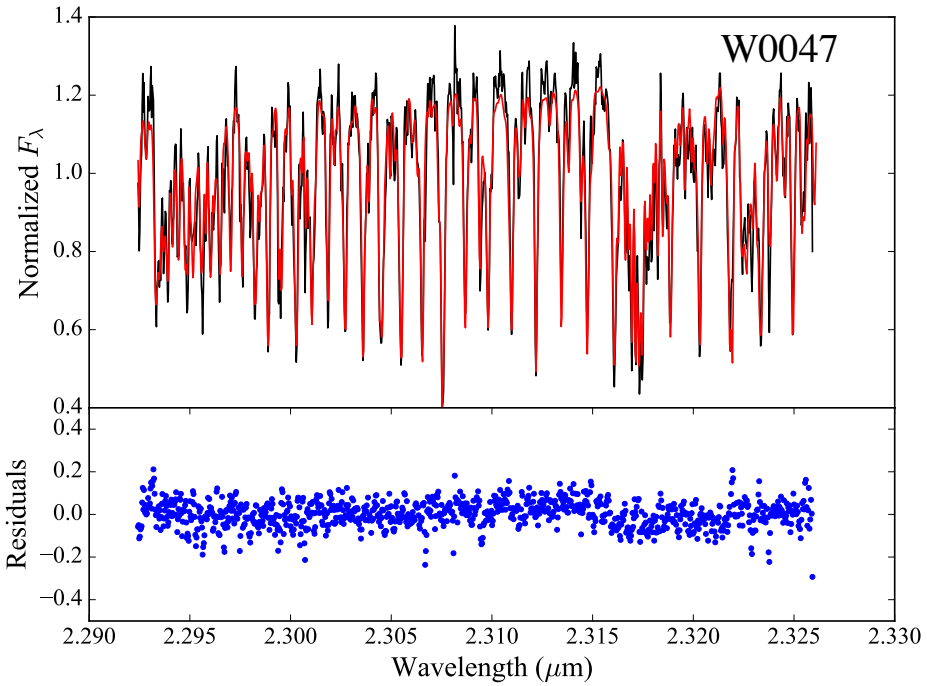

Figure 4.1 The observed spectrum of W0047 (black) compared to our best-fitting forward model (red). Residuals are plotted in the bottom panel.

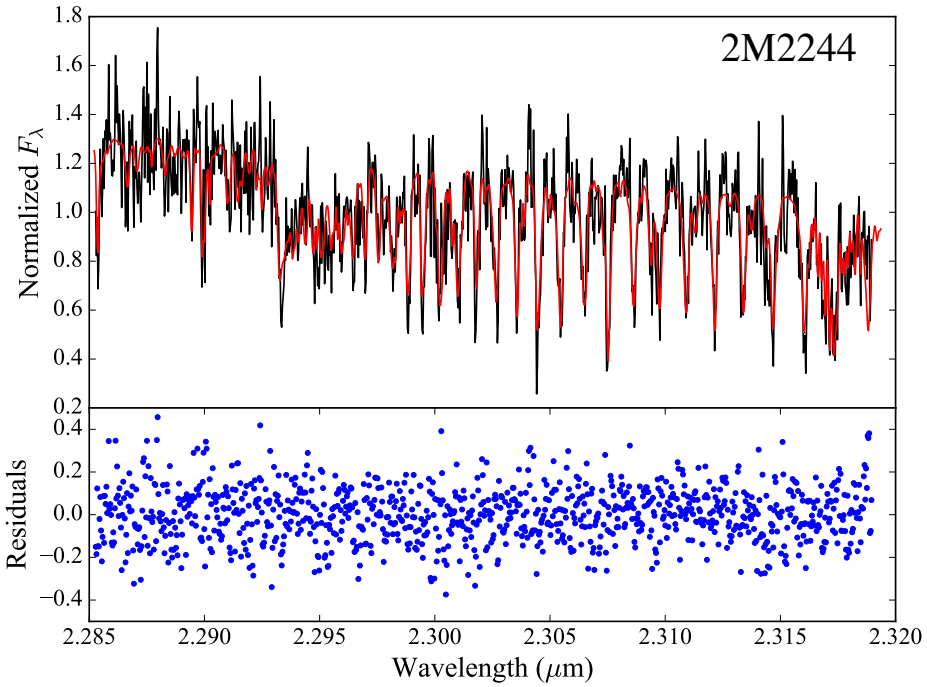

Figure 4.2 The observed and best-fitting forward model of 2M2244.

sensitivity and dark current on the detector. W0047 was observed on September 17 2013 with 2×1200 s exposures at an airmass of 1.5 and a mean DIMM seeing of 1.0″. 2M2244 was observed on July 6 2013 with 4×240 s exposures at an airmass of 1.0 and a mean DIMM seeing of 0.5″.

We focus our analysis on order 33 ($2.286 - 2.326$ μm) since this part of the spectrum contains a good blend of sky lines and brown dwarf lines, allowing for an accurate fit. This spectral region is rich in CO features, as well as H_2O and CH_4 features. These features are discussed in detail by Blake et al. (2010). Order 33 is also commonly used in the literature for NIRSPEC high dispersion N-7 spectra (Blake et al., 2010; Gizis et al., 2013). We additionally look at orders 32 ($2.364 - 2.398$ μm) (for W0047) and 38 ($1.987 - 2.016$ μm) (for both W0047 and 2M2244) to check for consistency. Data were reduced using a modified version of the REDSPEC reduction package to spatially and spectrally rectify each exposure. The NIRSPEC Echelle Arc Lamp Tool was used to identify the wavelengths of lines in our arc lamp spectrum. After nod-subtracting pairs of exposures, we create a spatial profile which is the median intensity across all wavelengths at each position along the slit. We use Poisson statistics to determine the noise per pixel at each wavelength. We extract the flux within an aperture in each nod-subtracted image to produce two spectra of our source. The extracted spectra are combined using a robust weighted mean with the XCOMBSPEC procedure from the Spextool package (Cushing et al., 2004).

4.3.1 Determining Radial and Rotational Velocities

We use the approach outlined in Allers et al. (2016) to determine the radial and rotational velocities of W0047 and 2M2244. We employ forward modelling to simultaneously fit the wavelength solution of our spectrum, the rotational and radial velocities, the scaling of telluric line depths, and the FWHM of the instrumental line spread function (LSF). We use the BT-Settl model atmospheres (Allard et al., 2012) as the intrinsic spectrum for each of our targets. In total, the forward model has nine free parameters: the $T_{\rm eff}$ and $\log(g)$ of the atmosphere model, the v_r and $v \sin i$ of the brown dwarf, τ for the telluric spectrum, the LSF FWHM, and the wavelengths of the first, middle and last pixels. The forward model is compared to our observed spectrum, and the parameters used to create the forward model are adjusted to achieve the best fit.

To determine the best-fitting parameters of our forward model as well as their

posterior distributions, we use a Markov Chain Monte Carlo (MCMC) approach. This involves creating forward models that allow for a continuous distribution of $T_{\rm eff}$ and $\log(g)$ by linearly interpolating between atmosphere grid models. We employ the DREAM(ZS) algorithm (Ter Braak & Vrugt, 2008), which uses an adaptive stepper, updating model parameters based on chain histories. To ensure that the median absolute residual of the fit agrees with the median uncertainty of our spectrum, we include a systematic uncertainty of 1.4% in the spectrum of W0047. We plot our spectra and best-fitting models along with the residuals in Figures 4.1 and 4.2. Final values for $v\sin(i)$ and radial velocities (RV) are shown in Table 4.2. Their 1σ uncertainties are determined from their marginalised distributions obtained from our MCMC method. Although we obtain values for $T_{\rm eff}$ and $\log(g)$, these derived values should be treated with caution since we are using a narrow wavelength range in K-band (Cushing et al., 2008). Furthermore, atmospheric models have been found to overpredict effective temperatures and underpredict radii for young, low-gravity L/T transition objects when fitting both the broad-band spectral morphology in low-resolution spectra or the depths of spectral lines in high-resolution spectra (e.g. Barman et al., 2011; Marley et al., 2012; Liu et al., 2013; Allers et al., 2016). These parameters are more reliably determined from evolutionary models, as is done in Section 4.3.3. The results for both 2M2244 and W0047 are consistent across orders 32, 33 and 38 at the 2σ level. The mean and standard deviation of the LSF FWHM is 0.08 ± 0.01 nm and 0.081 ± 0.002 nm for 2M2244 and W0047 respectively, resulting in a resolution $R = \lambda/\Delta\lambda \simeq 29000$ for both objects. The precision of our wavelength solution is determined to be 0.0025 nm and 0.0124 nm for 2M2244 and W0047.

Our $v\sin(i)$ measurement of 9.8 ± 0.3 km s^{-1} for W0047 is higher than both previous measurements by Gizis et al. (2015) (4.3 ± 2.2 km s^{-1}) and Lew et al. (2016) ($6.7^{+0.7}_{-1.4}$ km s^{-1}), despite all three measurements using the same data set. The model atmosphere for W0047 used by Gizis et al. (2015) has $T_{\rm eff} = 2300$ K and $\log(g) = 5.5$ while evolutionary models predict $T_{\rm eff} = 1270$ K and $\log(g) = 4.5$ (Gizis et al., 2015). Our model (with $T_{\rm eff} = 1670$ K and $\log(g) = 5.2$) is in better agreement with the evolutionary model. Higher effective temperature and surface gravity results in more pressure broadening, producing a lower value of $v\sin(i)$. Lew et al. (2016) do not provide details on the atmospheric model used. Again, the consistency betweens orders 32, 33 and 38 further supports our results.

Table 4.1 Physical properties of W0047 and 2M2244 from the Saumon & Marley (2008) $f_{sed} = 2$ evolutionary model.

	W0047	2M2244
$\log(L/L_\circ)$	-4.44 ± 0.04	-4.48 ± 0.02
Mass (M_{Jup})	$19.5^{+1.6}_{-1.7}$	$19.0^{+1.4}_{-1.5}$
$T_{\rm eff}$	1250^{+20}_{-30}	1230^{+16}_{-15}
Radius (R_{Jup})	1.28 ± 0.02	1.28 ± 0.02
$\log(g)$ (dex)	4.49 ± 0.05	$4.48^{+0.04}_{-0.05}$

4.3.2 2M2244+20 Membership in AB Doradus

A radial velocity measurement is required to confirm moving group membership. Using Bayesian analysis to assess the membership of >M5 brown dwarfs, Gagné et al. (2014b) find a 99.6% probability that 2M2244 is a member of the AB Doradus moving group, predicting a radial velocity of -15.5 ± 1.7 km s^{-1}. Our measured radial velocity of -16.0 ± 0.9 km s^{-1} is consistent with the predicted radial velocity. Including the measured radial velocity, along with parallax and proper motion measurements from Liu et al. (2016), and using the BANYAN II web tool (Gagné et al., 2014b; Malo et al., 2013), the probability of AB Doradus membership increases to 99.96%. Thus, our radial velocity measurement confirms 2M2244 as a member of the AB Doradus moving group.

4.3.3 The Physical Properties of W0047 and 2M2244

Filippazzo et al. (2015) provide radius, $\log(g)$, $T_{\rm eff}$ and mass estimates from evolutionary models for W0047 and 2M2244, however, the estimated age range used in this analysis of $50 - 110$ Myr for AB Doradus is systematically younger than current estimates. Barenfeld et al. (2013) place a strong lower limit of 110 Myr and Luhman et al. (2005) provides an upper limit of 150 Myr on the age of AB Doradus. Furthermore, Filippazzo et al. (2015) use a kinematic distance to determine the luminosity of 2M2244 while Liu et al. (2016) has since measured its parallax. We use measured parallaxes from Liu et al. (2016) to update the luminosities of 2M2244 and W0047. The errors on the updated luminosities are slightly overestimated, since the absolute flux and errors are not given in Filippazzo et al. (2015). For a uniformly-distributed age of $110 - 150$ Myr and normally-distributed luminosities, we determine the physical properties of

2M2244 and W0047 using model isochrones (final parameters shown in Table 4.1). W0047 and 2M2244 both exhibit extremely red $J-K$ colours, indicating a dusty atmosphere. Thus, we use the Saumon & Marley (2008) solar metallicity $f_{sed} = 2$ models. The older age of the AB Doradus moving group that is used in this analysis pushes both masses above the deuterium burning limit, and above the masses presented in Filippazzo et al. (2015). The revised radii are consistent with those reported by Filippazzo et al. (2015).

4.4 Spitzer and WFCAM Photometry

For our *Spitzer* observations of W0047, 2M2244 and SDSS1110 we followed standard observing practices for obtaining precise, stable, and nearly-photon limited performance. We employed "staring mode" AORs in which the object did not move on the chip throughout the entire observation, with a long exposure time (Metchev et al., 2015). W0047 and 2M2244 were observed for 18.7 hr and 8.8 hr on January 9 and September 15 2016 respectively, in the *Spitzer* [3.6 μm] band with an exposure time of 30 s and a pixel scale of 1.221″. SDSS1110 was observed for 9.0 hr on April 5 2016 in the *Spitzer* [4.5 μm] band with an exposure time of 100 s and a pixel scale of 1.231″. Additionally, we include *Spitzer* [4.5 μm] archival data of 2M2244 (Program ID: 20079, PI: Stauffer) published in Morales-Calderon et al. (2006) for re-analysis.

Photometry was obtained from the corrected Basic Calibrated Data images, provided by the Spitzer Science Center after processing through IRAC pipeline version 19.2.0. The centroids of the target and a number of reference stars are found using BOX_CENTROIDER.PRO. We perform aperture photometry on these centroids, using various aperture sizes and choosing the aperture size that produces lightcurves with the lowest RMS (radii of 3.0, 3.5 and 3.5 pixels for 2M2244, W0047 and SDSS1110 respectively). Outliers are identified and rejected from the raw light curves using a 6σ clip, removing $\sim 5-45$ points in each lightcurve.

The light curves are then corrected for intrapixel sensitivity variations, the so-called "pixel phase effect". This is the slight variation in flux depending on where a point source falls with respect to the centre of a pixel. The pixel phase response is modelled as a double-Gaussian – a summation of gaussians in the orthogonal pixel directions. We correct for the pixel phase effect using

the PIXEL_PHASE_CORRECT_GAUSS.PRO routine from the *Spitzer* IRAC website. The pixel phase corrected flux is then binned into $\sim$ 5 minute bins using a weighted average, followed by a final 3σ clip to produce the final lightcurves. The photometric noise of our normalised and corrected light curves is calculated following Radigan et al. (2014). While the standard deviation produces a measurement of noise for flat curves, in the case of variable lightcurves the standard deviation measures both noise and intrinsic variations. We therefore use the point-to-point noise to measure the photometric precision. This is the standard deviation of the lightcurve subtracted from a shifted version of itself, divided by $\sqrt{2}$. This measure of photometric noise is not sensitive to low frequency trends and thus provides a better estimate of the noise for variable lightcurves.

We also include an observation of 2M2244 taken with the infrared Wide-Field Camera (WFCAM; Casali et al., 2007) on July 21 2016 UT as part of a larger survey for variability on free-floating low-mass objects. This is a wide-field imager on the 3.8 m UK Infrared Telescope on Mauna Kea, with a pixel scale of $0.4''$. The observation was carried out with the J-band filter with a seeing of $\sim 1.1''$ during the 4 hr sequence. The target was observed using an ABBA nod pattern, with three exposures of 40 s at each position. The frames were reduced using the WFCAM reduction pipeline (Irwin et al., 2004; Hodgkin et al., 2009) by the Cambridge Astronomical Survey Unit. Aperture photometry is performed on the target as well as on a large number of reference stars in the field using an aperture size of 3.5 pixels. Raw light curves obtained from aperture photometry display brightness fluctuations due to changes in seeing, airmass and residual instrumental effects. To a very good approximation these changes are common to all stars in the field of view and can be removed via division of a calibration curve calculated from a set of iteratively chosen, well-behaved reference stars (Radigan et al., 2012). For each star a calibration curve is created by median combining all other reference stars (excluding that of the target and of the star itself). The standard deviation and linear slope for each light curve are calculated and stars with a standard deviation or slope 1.2 times greater than that of the target are discarded. This process is iterated a number of times, until a set of well-behaved reference stars is chosen. Reference stars are also examined by eye to check for any residual trends. Final detrended lightcurves are obtained by dividing the raw curve for each star by its calibration curve.

4.4.1 Identification of Variables

We plot the periodogram of the target as well as a number of reference stars in the field to identify periodic variability in our targets. For each periodogram, the 1% false-alarm probability (FAP) is calculated from 1000 simulated lightcurves. These lightcurves are produced by randomly permuting the indices of reference star lightcurves (Radigan et al., 2014). This produces lightcurves with Gaussian-distributed noise. The 1% FAP is plotted in blue in each periodogram. The rotational periods and peak-to-peak variability amplitudes of targets showing periodic variability are determined by fitting an appropriate function to the data using MPFIT.PRO. This is an implementation of the Levenberg-Marquardt least-squares minimisation algorithm which calculates the best-fitting periods and variability amplitudes with their 1σ uncertainties. Finding that the least-squares method can be sensitive to initial parameter guesses, we also use the MCMC algorithm EMCEE (Foreman-Mackey et al., 2013) to fully explore the posterior probability distributions of our model parameters.

Aperiodic or stochastic variations are not easily detectable from Lomb-Scargle periodograms so we additionally check for stochastic variability by comparing the photometric standard deviation of our target with the mean standard deviation of comparison stars of similar brightness. If the standard deviation of the target is considerably larger than the mean standard deviation of the comparison stars this suggests stochastic variability in the target.

4.4.2 W0047

The lightcurve of W0047 (Figure 4.3) appears sinusoidal over an entire period. The periodogram displays a strong peak at $\sim$ 16 hr that is well above the 1% FAP value. The least-squares best-fitting sinusoidal function gives a period of 16.3 ± 0.3 hr and an amplitude of $1.08 \pm 0.04\%$. We also use the EMCEE package (Foreman-Mackey et al., 2013) to obtain the full posterior probability distribution for each parameter of the sinusoidal model. We use 1000 walkers with 7500 steps (after discarding the initial burn-in sample) in the four-dimensional parameter space to model the lightcurve. Figure 4.4 shows the posterior probability distributions of the amplitude, period, phase and constant parameters of the fit. Each parameter is well constrained, and the MCMC method gives a period of 16.4 ± 0.2 hr and a peak-to-peak amplitude of $1.07 \pm 0.04\%$.

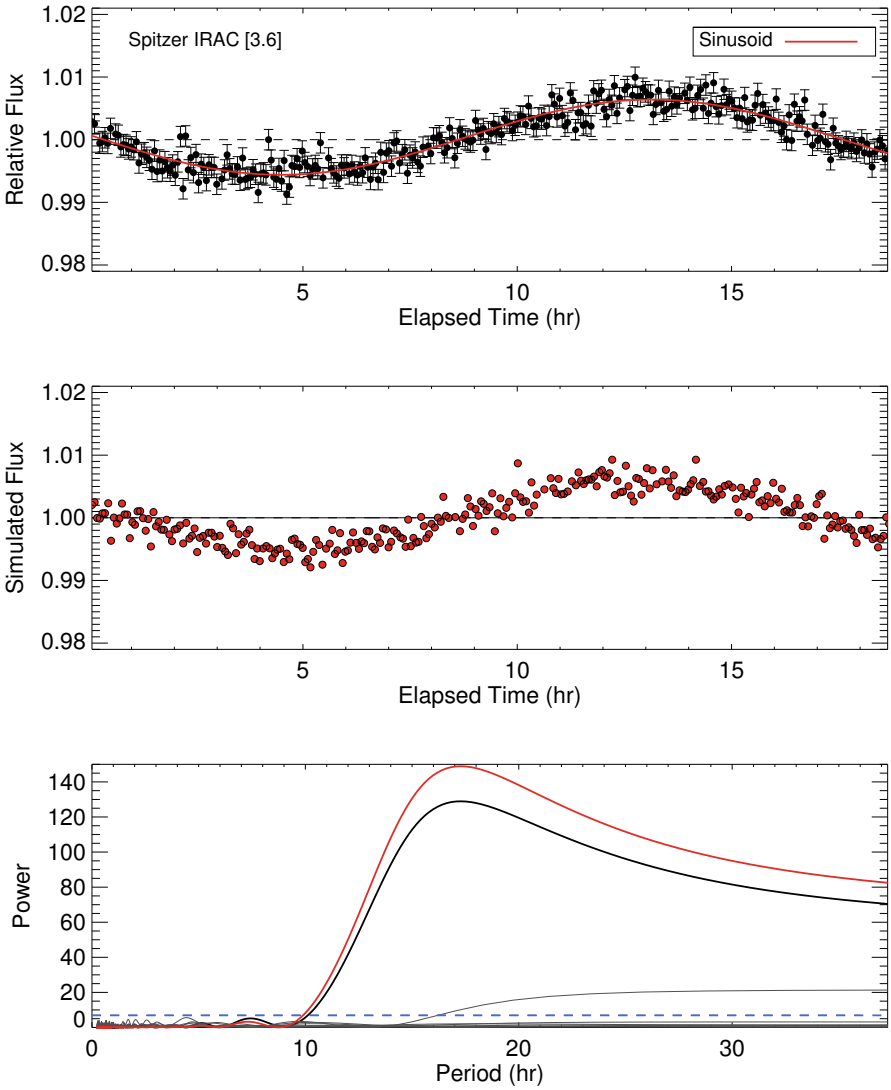

Figure 4.3 Top panel shows the normalised, pixel phase corrected lightcurve of W0047 with best-fitting sinusoidal function overplotted in red. The best-fitting function gives a period of 16.3 ± 0.2 hr and an amplitude of $1.08 \pm 0.04\%$. The middle panel shows the best-fitting function injected into a simulated lightcurve. The bottom panel shows the periodogram of the target and the simulated curve, as well as the periodogram of several reference stars in the field. The blue dashed line shows the 1% false-alarm probability.

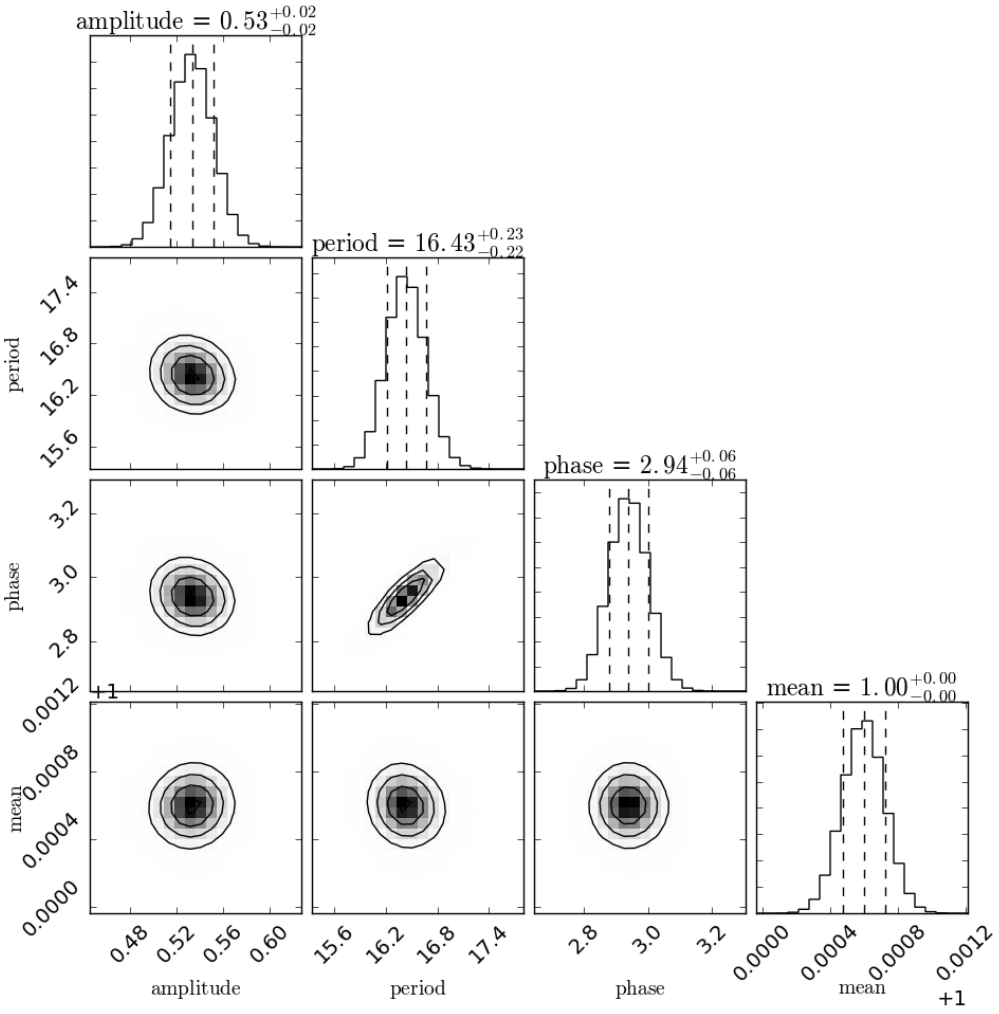

Figure 4.4 Posterior distributions of parameters of the *Spitzer* lightcurve of W0047 (shown in Figure 4.3) The middle dashed line is the median, the two outer vertical dashed lines represent the 68% confidence interval. The contours show the 1σ, 1.5σ and 2σ levels.

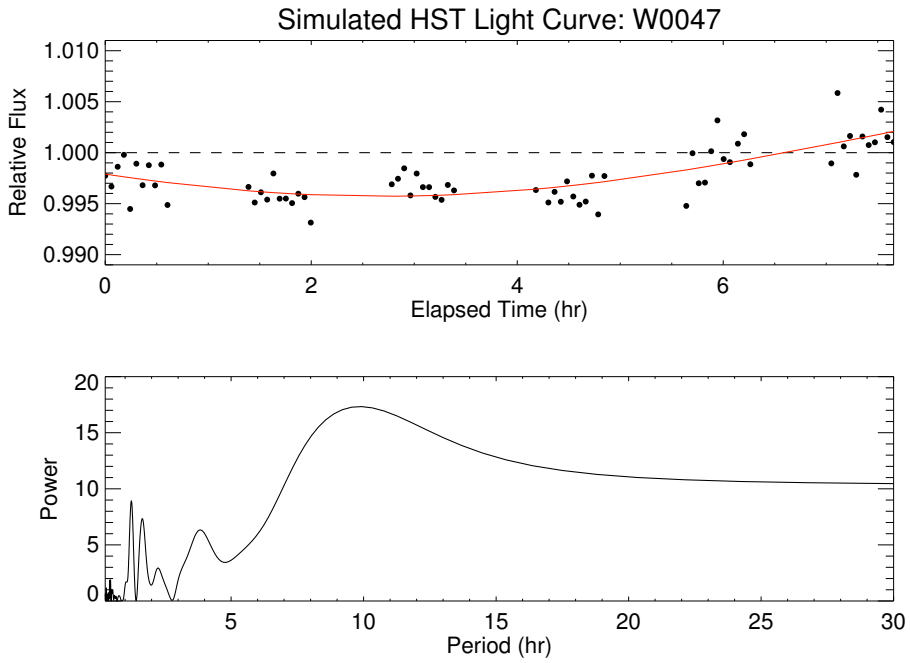

Figure 4.5 *Top panel:* Simulated *HST* lightcurve of W0047 based on observations in Lew et al. (2016). A least-squares fit to the data is shown in red. This fit favours a rotational period of $\sim$ 19.6 hr, but is sensitive to the initial guess. *Bottom panel:* Periodogram of simulated lightcurve of W0047.

Assuming rigid rotation, we use our measured $v \sin(i)$ and a radius estimate of 1.28 ± 0.02 $R_{\rm Jup}$ to place an upper limit of $16.3^{+0.8}_{-1.4}$ hr on the rotational period of W0047. We can therefore discount the possibility of a double-peaked lightcurve with a longer rotational period.

The measured period is significantly longer than the previously measured 13.2 ± 0.14 hr (Lew et al., 2016), however this initial period was determined from a 8.6 hr observation that did not cover a full rotation. To investigate whether or not the lightcurve shape has evolved since the initial *HST*observation, we restrict our data to match the lightcurve from Lew et al. (2016). The *HST* data was obtained during six orbits. Eleven images were obtained in each orbit, each with an exposure time of 201.4 s. We show our "simulated" *HST* data in the top panel of Figure 4.5, along with a least-squares fit to the curve. The least-squares fit shown here gives a rotational period of $\sim$ 19.6 hr, however this is very sensitive to the "first guess". The bottom panel shows a broad periodogram with a peak at $\sim$ 10 hr. We use MCMC to get a more robust measurement of the sinusoidal fit parameters and their errors. Figure 4.6 shows the posterior probability distributions of the amplitude, period, phase and constant parameters of the

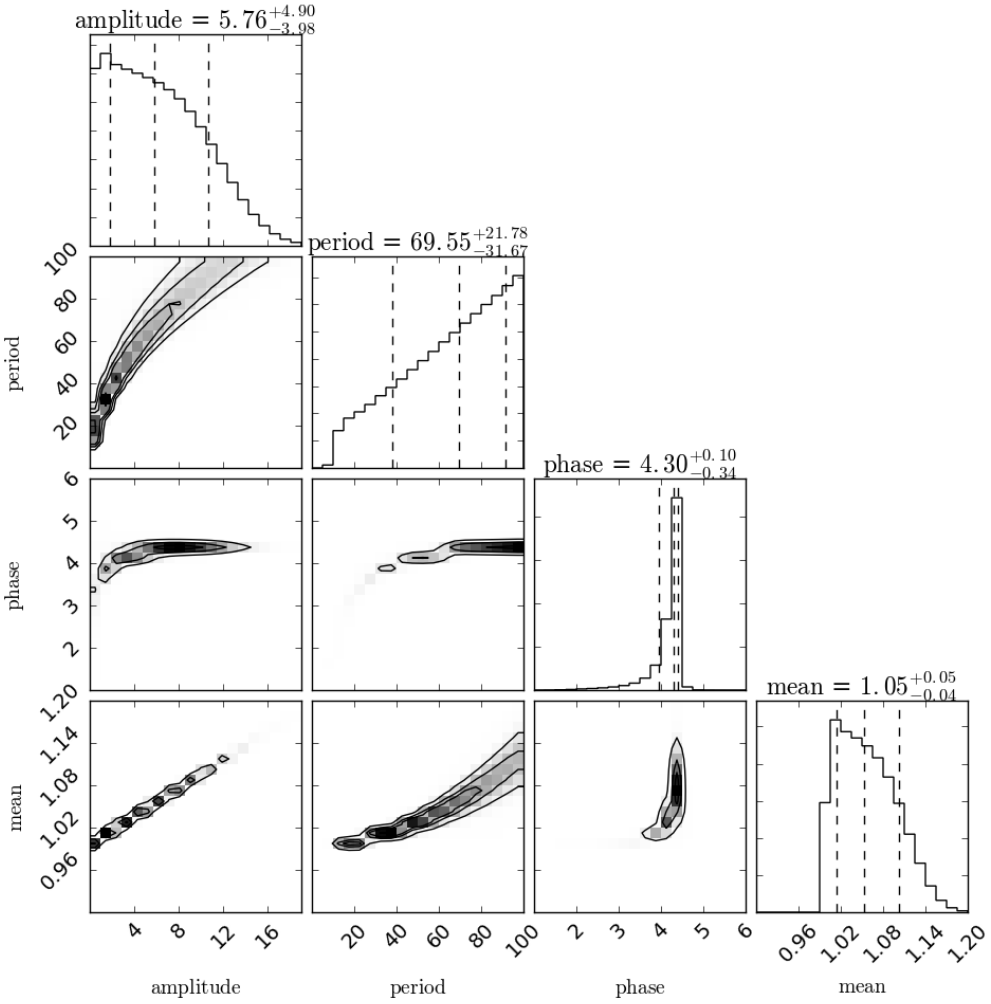

Figure 4.6 Posterior distributions of parameters of the simulated *HST* lightcurve of W0047 (shown in Figure 4.5) The middle dashed line is the median, the two outer vertical dashed lines represent the 68% confidence interval. The contours show the 1σ, 1.5σ and 2σ levels. The variability amplitude, rotational period and mean flux are not constrained by the simulated data.

fit. The amplitude, period and mean of the fit do not converge, so we are unable to provide an estimate on the rotational period using this simulated dataset. The disagreement between these measurements suggests that the variability may not be accurately described as a sinusoid. However it is possible that the higher variability amplitude in the near-IR ($\sim 8\%$) may have enabled the determination of period by Lew et al. (2016).

With a peak-to-peak amplitude of $1.07 \pm 0.04\%$, this is among the highest *Spitzer* [3.6 μm] variability amplitudes detected. Metchev et al. (2015) notes a tentative correlation between low-gravity and high amplitude variability among a sample of eight L3-L5.5 dwarfs. The variability detection measured here adds to a growing number of young, L objects that display high amplitude variability, suggesting that this correlation may extend into the late-L spectral types (Metchev et al., 2015; Biller et al., 2015; Lew et al., 2016).

4.4.3 2M2244

Spitzer [3.6 μm] Monitoring

In contrast to W0047, the *Spitzer* [3.6 μm] lightcurve of 2M2244 does not appear sinusoidal (Figure 4.7). The photometric noise of 2M2244 is similar to the noise measured in comparison stars of similar brightness in the field. Thus we do not detect any stochastic or aperiodic variability for 2M2244. Morales-Calderon et al. (2006) report a sinusoidal light curve period of 4.6 hr for this object; however the latest observations look very different. The periodogram shows a small peak at ~ 4 hr that is approximately at the 1% FAP level which roughly coincides with the 4.6 hr period determined by Morales-Calderon et al. (2006). We also identify a broad peak at ~ 9.6 hr that is highly significant. The light curve does not exhibit a sinusoidal shape, so we consider a two-term truncated Fourier series, which is an appropriate model for more complex lightcurves (Heinze et al., 2013; Yang et al., 2016). This model describes a scenario in which two atmospheric features are located on either hemisphere of the brown dwarf, each causing changes in brightness as they rotate in and out of view. The two-term Fourier series is given by:

$$F(t) = a_0 + \sum_{n=1}^{2} A_i \sin\left(\frac{2\pi t}{P/i}\right) + B_i \cos\left(\frac{2\pi t}{P/i}\right) \tag{4.1}$$

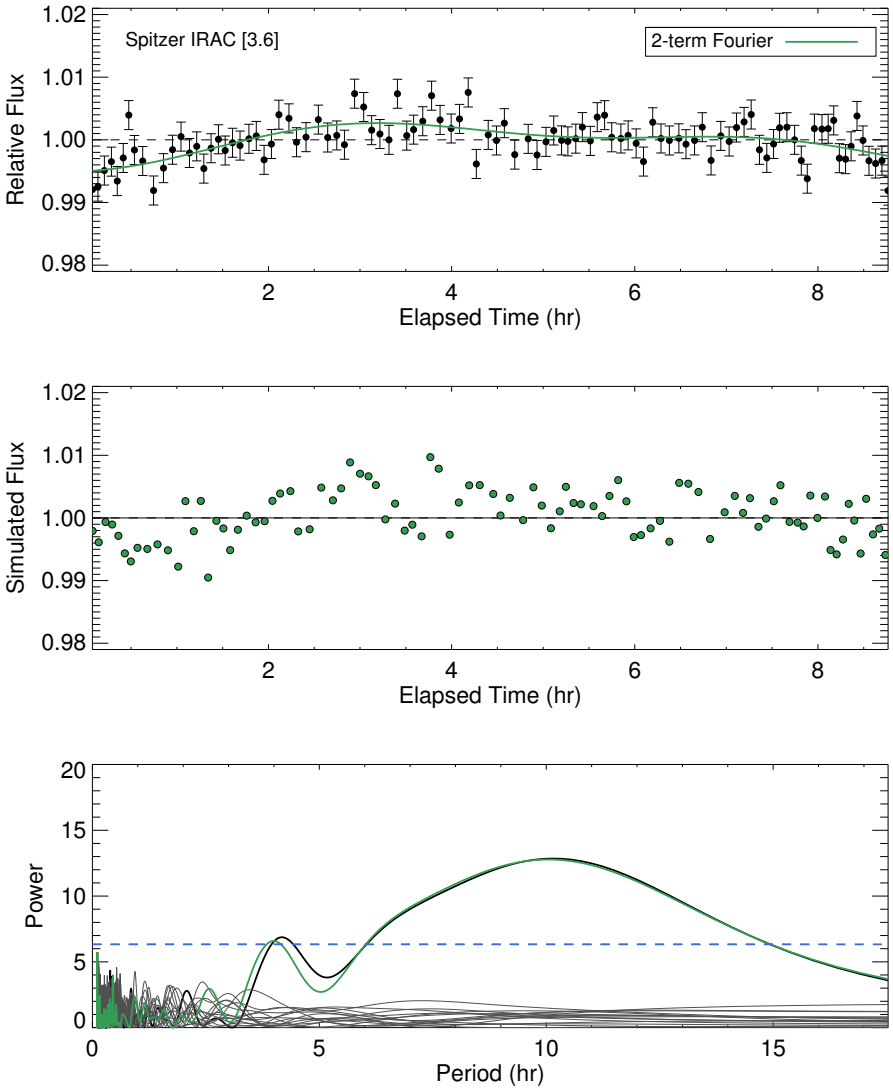

Figure 4.7 Same as Figure 4.3, but for 2M2244 data taken on Sep 15 2016. Here we consider a two-term Fourier series to model the variability. The Fourier function gives a period of 10 ± 2.4 hr with a peak to trough amplitude of $0.8 \pm 0.2\%$. The bottom panel shows that the Fourier-term fit matches the target periodogram well, reproducing both the minor smaller peak at ~ 4 hr and the large peak at ~ 10 hr.

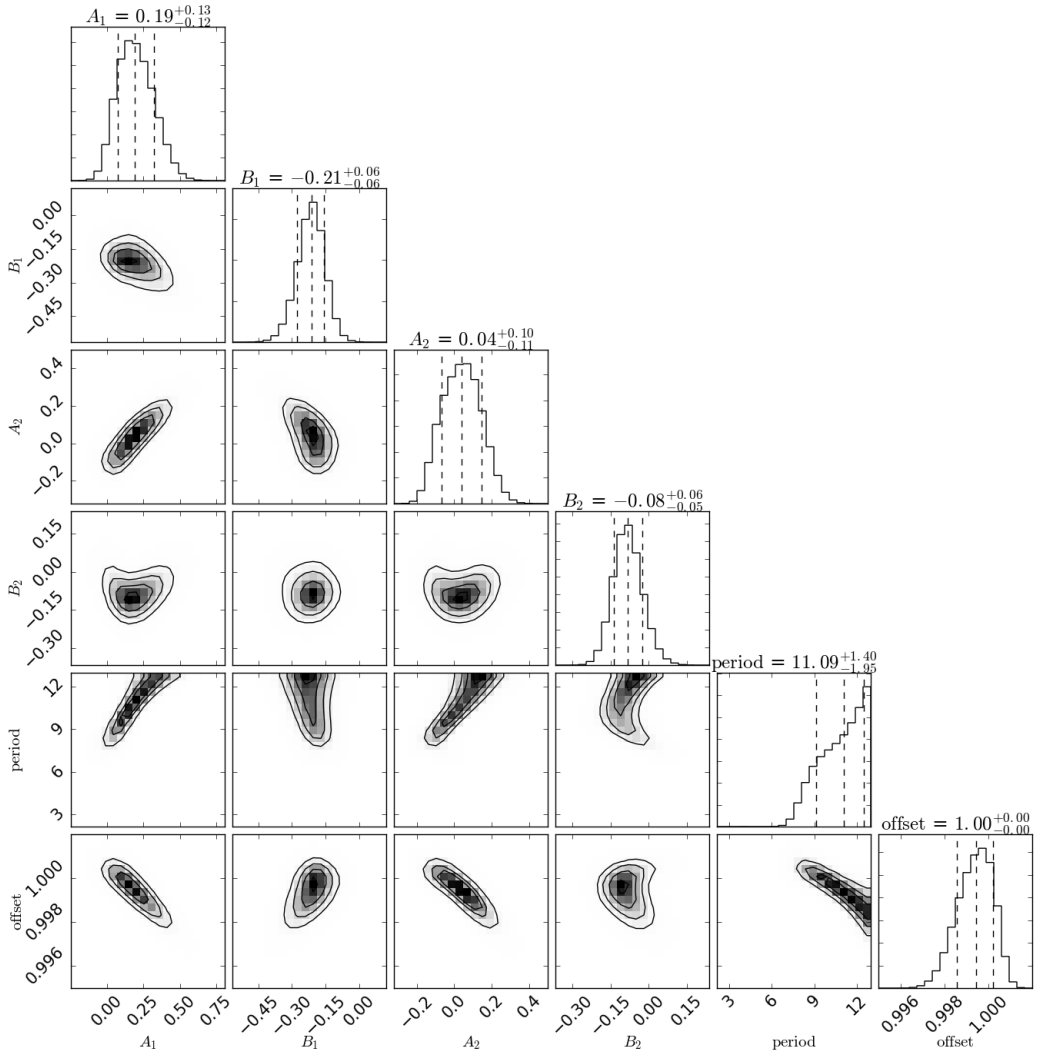

Figure 4.8 Posterior distributions of parameters of the Fourier model fit to the *Spitzer* lightcurve of 2M2244 (shown in Figure 4.7). The middle dashed line is the median, the two outer vertical dashed lines represent the 68% confidence interval. We have placed an upper limit on the period of 13 hr using our radius estimate from Table 4.1 and $v \sin(i)$ measurement from Table 4.2 . The contours show the 1σ, 1.5σ and 2σ levels.

The least-squares fit requires a "first guess" for the parameters, which we set to the peak of the periodogram for the period and one for all other parameters. The least-squares best-fitting Fourier series model gives a period of 10.0 ± 2.4 hr. We inject this function into simulated lightcurves and reference stars to compute their periodograms. As seen in the bottom panel of Figure 4.7, the two-term Fourier signal produces a periodogram shape very similar to that of 2M2244, with a strong peak at ~ 10 hr and a smaller peak at ~ 4 hr.

After experimentation with different starting parameters for the least-squares fit, we find that the results are not consistent across different initial guesses for the model parameters. Using the Morales-Calderon et al. (2006) measurement of 4.6 hr as an initial guess on the period of 2M2244, the best-fitting solution gives a period of ~ 4 hr. In contrast, using the peak of our periodogram (~ 10 hr) as an initial guess on the period, we obtain a best-fitting period of 10 hr for the Fourier model. In fact, any initial guess > 5 hr yields a best-fitting period of 10 hr. It is clear that the least-squares fitting procedure cannot locate global minima, and is over-dependent on initial guesses. Hence, we use the EMCEE algorithm (Foreman-Mackey et al., 2013) to explore the posterior distribution of the model parameters using the two-term Fourier model. We use 1000 walkers with 7500 steps (after discarding the initial burn-in sample) to model the lightcurve. Our measured $v \sin(i)$ value of $14.3^{+1.3}_{-1.5}$ km s^{-1} and estimated radius of 1.28 ± 0.02 $R_{\rm Jup}$ allow us to place an upper limit of $11.1^{+1.9}_{-1.2}$ hr on the period of 2M2244, hence we use an upper limit of 13 hr as a prior in our MCMC analysis. The posterior distributions of the parameters for the Fourier model are shown in Figure 4.8. This model favours a period of $11.1^{+1.4}_{-2.0}$ hr and this value is insensitive to the initial parameter guesses.

If we do not place an upper limit on the rotational period of 2M2244, our MCMC analysis favours a period of $14.0^{+3.5}_{-3.8}$ hr. We have explained above that this period would be unphysical based on our measured $v \sin(i)$ and estimated radius, however it is worth exploring what values of $v \sin(i)$ and radius would permit a rotational period of $14.0^{+3.5}_{-3.8}$ hr. First, we fix the inclination angle to 90° and calculate the radius that could allow such a rotation period. This is done using a Monte Carlo simulation. We plot the resulting radius distribution (pink) in Figure 4.12 alongside the estimated radius from Filippazzo et al. (2015) (blue). Since we have assumed an inclination of 90°, the hypothetical radius distribution represents the lowest possible radius implied by this longer rotational period. For lower inclination angles, a larger radius would be necessary. For this scenario, the 1σ

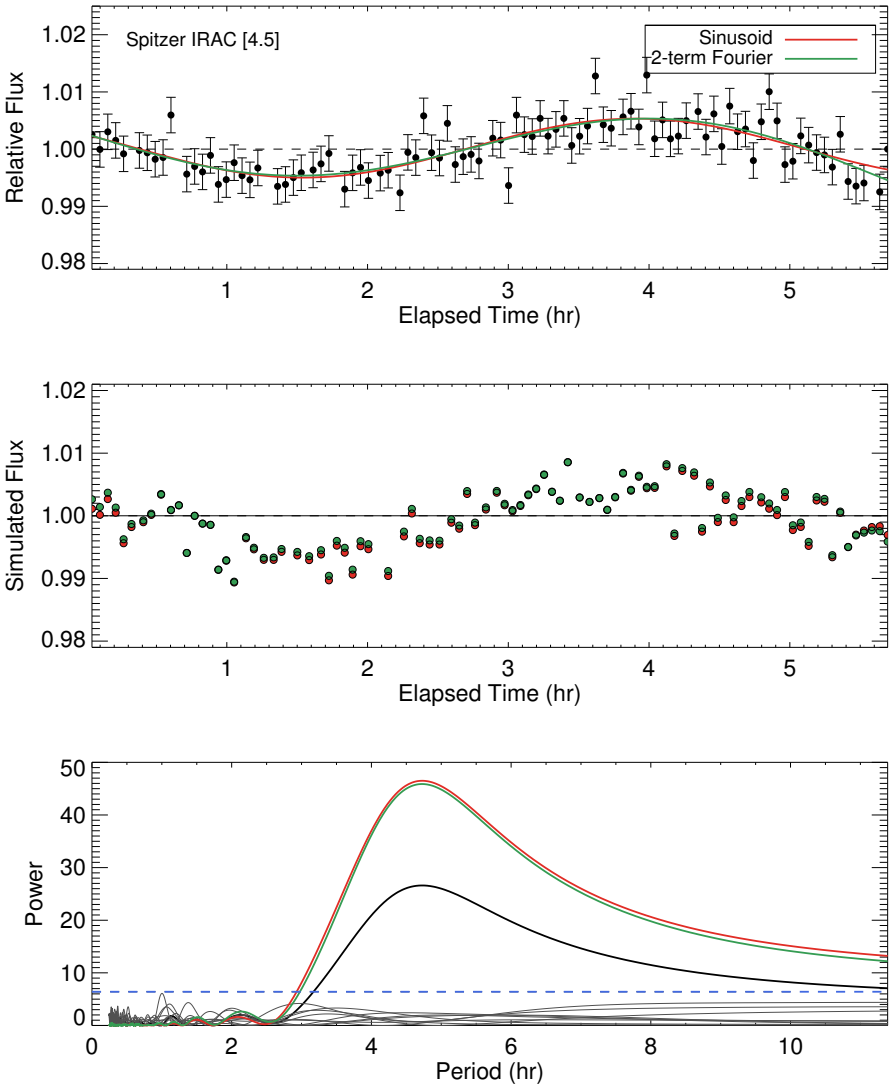

Figure 4.9 Same as Figure 4.3, but for the Morales-Calderon et al. (2006) [4.5 μm] observation of 2M2244, taken on November 27 2005. The best-fitting sinusoid function gives a period of 4.6 ± 0.2 hr while the double-peaked Fourier function gives a period of 10 ± 3 hr. Injecting both functions into simulated lightcurves and reference stars gives a periodogram shape similar to the observed lightcurve's periodogram. The functions are indistinguishable from each other over this observation.

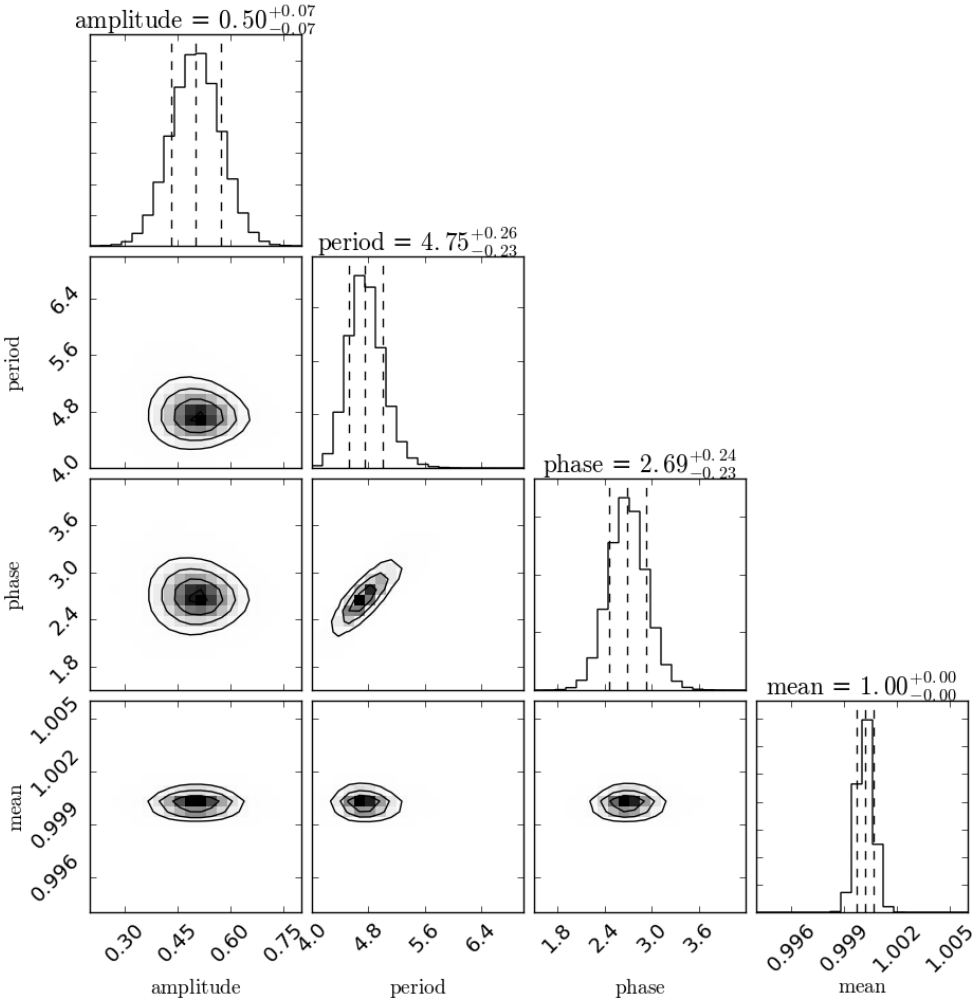

Figure 4.10 Posterior distributions of parameters of the sinusoid fit to the Morales-Calderon et al. (2006) *Spitzer* lightcurve of 2M2244 (shown in Figure 4.9) The middle dashed line is the median, the two outer vertical dashed lines represent the 68% confidence interval. We have placed an upper limit on the period of 13 hr using our radius estimate from Table 4.1 and $v \sin i$ measurement from Table 4.2. The contours show the 1σ, 1.5σ and 2σ levels.

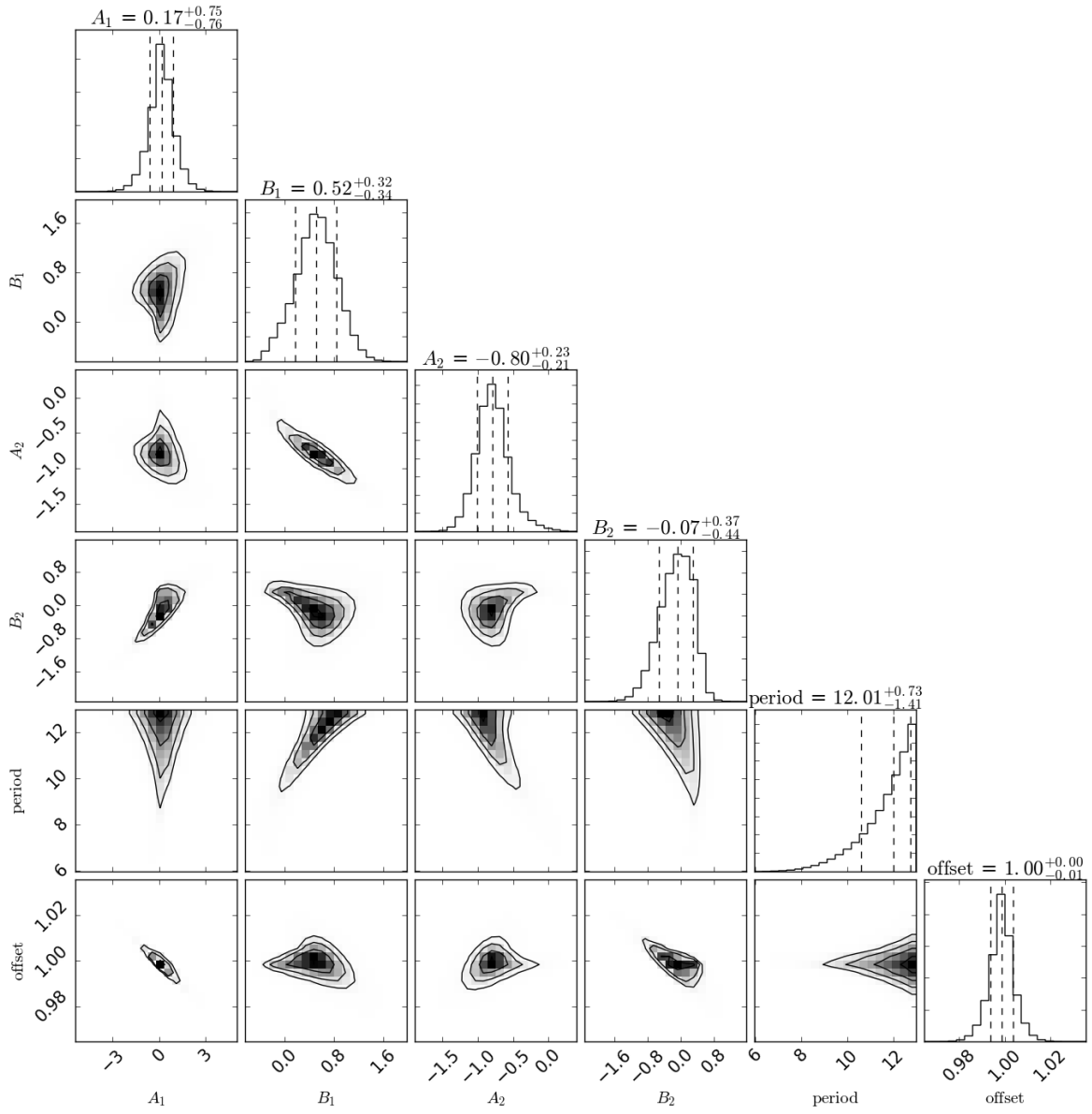

Figure 4.11 Posterior distributions of parameters of the Fourier model fit to the Morales-Calderon et al. (2006) *Spitzer* lightcurve of 2M2244 (shown in Figure 4.9) The middle dashed line is the median, the two outer vertical dashed lines represent the 68% confidence interval. We have placed an upper limit on the period of 13 hr using our radius estimate from Table 4.1 and $v \sin(i)$ measurement from Table 4.2. The contours show the 1σ, 1.5σ and 2σ levels.

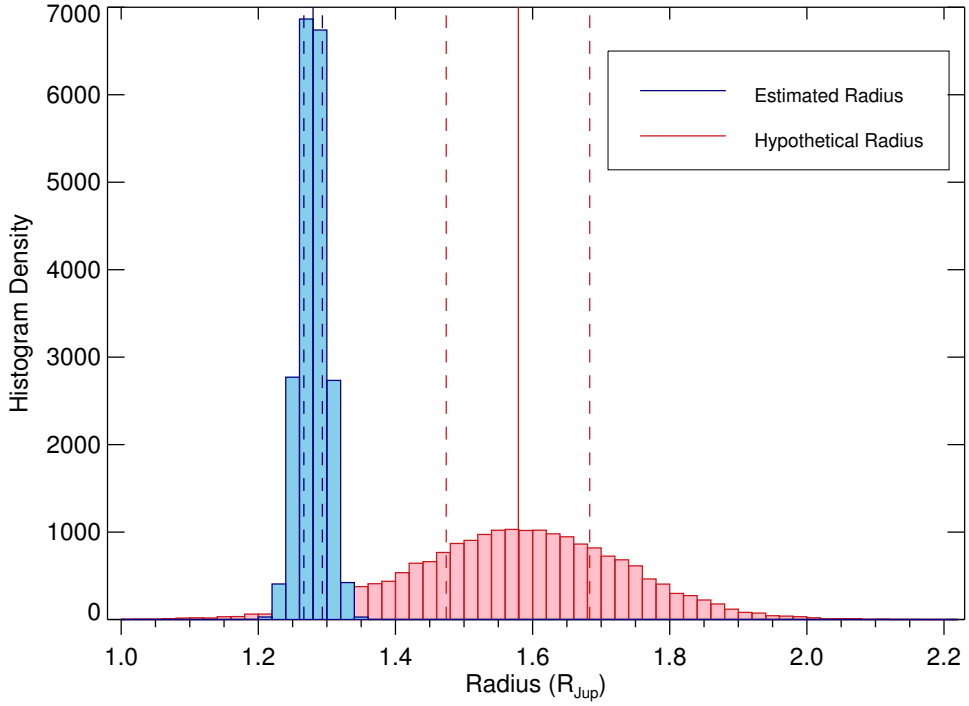

Figure 4.12 Radius distributions for 2M2244 from our evolutionary models (blue) and calculated assuming a rotational period of $13.9^{+3.5}_{-3.8}$ hr and an inclination angle of 90° (pink). The solid line shows the median radius value and the dashed lines show the 25% and 75% percentiles.

range on the radius would be $1.47 - 1.68$ R_{Jup}, which is much larger than the radii of brown dwarfs at the age of AB Doradus (Filippazzo et al., 2015), and several σ away from our radius estimate of 1.28 ± 0.02 $M_{\rm Jup}$. Second, we find the $v \sin(i)$ value that would allow a rotational period of $14.0^{+3.5}_{-3.8}$ hr. We show our measured $v \sin(i)$ value and this hypothetical value in Figure 4.13. Again, since this calculation assumes an inclination angle of 90°, the $v \sin(i)$ distribution represents an upper limit of possible values. A lower inclination angle would result in a lower $v \sin(i)$ value. A longer rotational period implies a smaller $v \sin(i)$ of $11.50^{+0.11}_{-0.13}$ km s^{-1}, and that our $v \sin(i)$ measurement is too large by at least 1.9 σ (depending on the inclination angle). Alternatively, a longer rotational period would be reasonable if we had both underestimated our radius and overestimated $v \sin(i)$. The scenario would require that both the radius and $v \sin i$ differ by at least 1 σ from our estimated values. While these scenarios are certainly possible, we conclude that they are unlikely since they both require a large systematic error on our estimated radius and/or $v \sin(i)$.

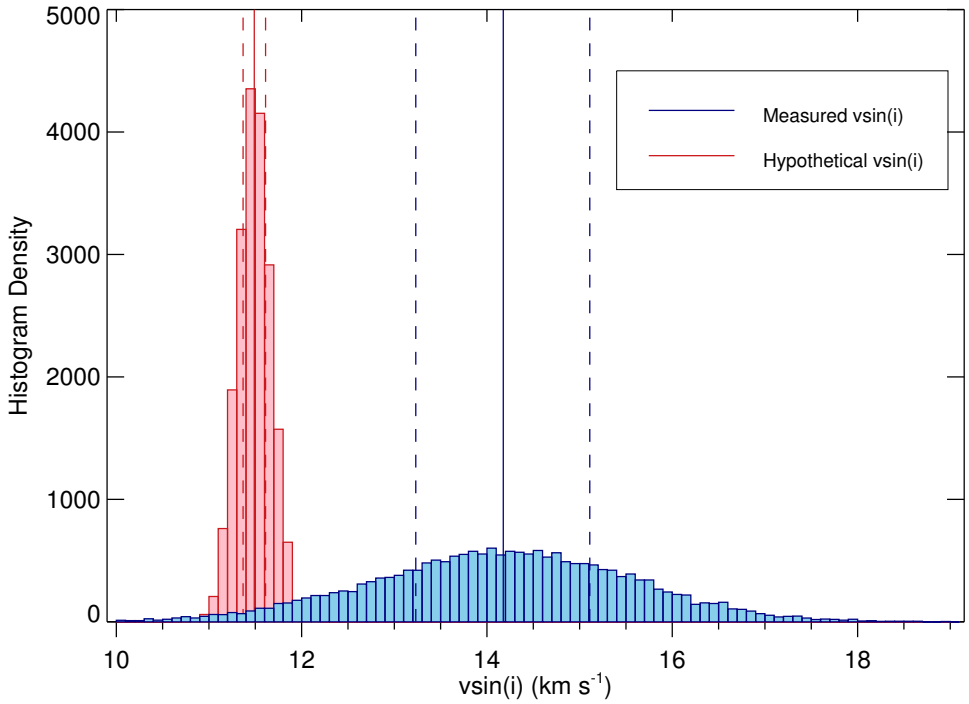

Figure 4.13 Measured $v \sin(i)$ distribution for 2M2244 (blue) and a $v \sin(i)$ distribution calculated assuming a rotational period of $14.0^{+3.5}_{-3.8}$ hr and an inclination angle of 90° (pink). The solid line shows the median $v \sin(i)$ value and the dashed lines show the 25% and 75% percentiles.

Spitzer [4.5 μm] Monitoring

The rotational period suggested by our *Spitzer* [3.6 μm] data is inconsistent with that of Morales-Calderon et al. (2006) who find a period of 4.6 hr during a $\sim$ 6 hr observation in the *Spitzer* [4.5 μm] band. We downloaded these data from the Spitzer Heritage Archive. The reduced lightcurve and periodogram are shown in Figure 4.9. The periodogram peaks at 4.6 hr, as reported by Morales-Calderon et al. (2006). The curve appears sinusoidal over the observation period but we investigate the possibility of a double-peaked lightcurve. Fitting a pure sinusoid to the data gives a period of 4.6 ± 0.2 hr while fitting a two-term truncated Fourier series gives a period of 10 ± 3 hr; however the functions are indistinguishable from each other over this observation. Injecting the 4.6 hr sinusoid fit and the 10 hr truncated Fourier fit into simulated lightcurves and reference stars produces the same periodogram shape as the target, seen in the bottom panel of Figure 4.9. We use the MCMC method to explore the parameter posterior distributions for both the sinusoid model and the Fourier model. Again we use an upper limit of 13 hr as a prior on the period. The posteriors are shown in Figures 4.10 and 4.11. Again, both models fit the light curve well, with the sinusoidal model giving a period of $4.8^{+0.3}_{-0.2}$ hr and the Fourier series model giving a period of $12.01^{+0.7}_{-1.4}$ hr. Thus, we conclude that the original observation is too short to rule out a double-peaked lightcurve with the $\sim$ 11 hr period of the *Spitzer* [3.6 μm] data set, and from this data set either scenario is possible.

UKIRT WFCAM Monitoring

The UKIRT/WFCAM photometry of 2M2244 is shown in Figure 4.14. In this 4 hr J-band observation we see evidence of significant ($\sim$ 4%) variability. The periodogram shows a highly significant peak that favours periodicities > 5.5 hr. This observation is too short to accurately measure the rotational period, but it is consistent with an $\sim$ 11 hr period. Since we have not covered a full rotational period of 2M2244 we cannot measure the full $J-$band variability amplitude, but can set a lower limit of $\sim$ 4%.

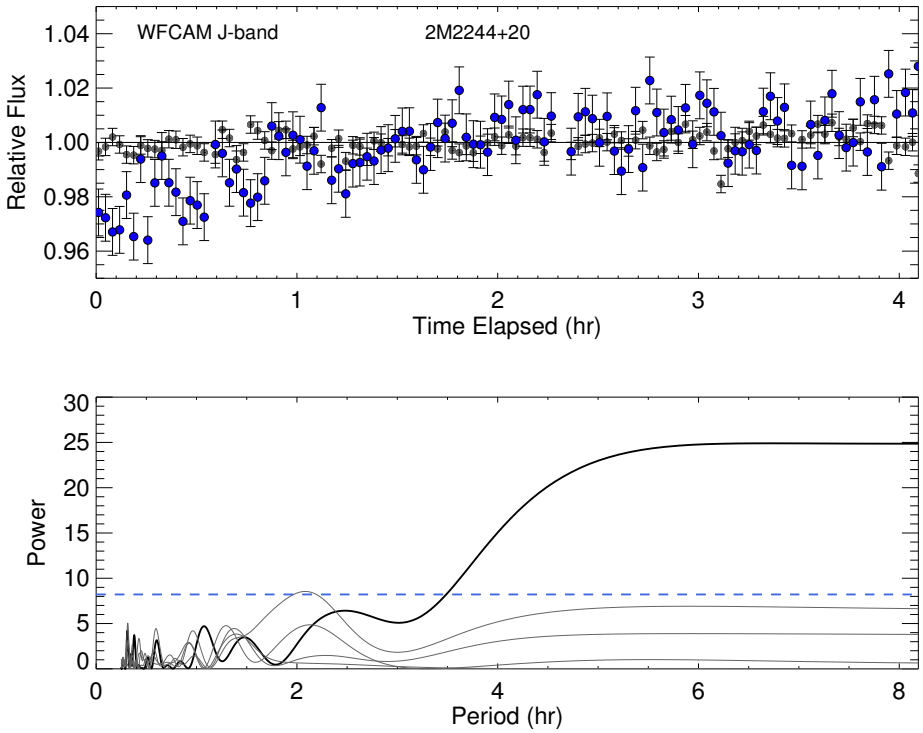

Figure 4.14 *Upper panel:* UKIRT WFCAM photometry of 2M2244+20 taken on 2016-06-21. 2M2244+20 is shown in blue with a reference star shown in grey. *Lower panel:* Periodogram of 2M2244+20 as well as the periodograms of reference stars in the field. In this observation 2M2244+20 shows trends with periodicities < 5.5 hr.

The Rotational Period of 2M2244

Considering all three epochs of data for 2M2244, we favour a longer period of 11 ± 2 hr. We conclude that the initial *Spitzer* [4.5 μm] monitoring observation by Morales-Calderon et al. (2006) is too short to completely rule out a longer period. The light curve is most likely double-peaked in this epoch, due to two different atmospheric structures in either hemisphere. We see a very different shape in the September 2016 *Spitzer* [3.6 μm] light curve. This is plausibly due to evolution of the cloud structure in the $\sim$ 10 years between epochs. This could also be due to the fact that we are probing different pressure levels in each *Spitzer* band, however recent studies have found [3.6 μm] and [4.5 μm] light curves to have similar shape and phase (Metchev et al., 2015; Cushing et al., 2016). A recent paper by Apai et al. (2017) suggests another possible explanation for evolving lightcurves such as that observed for 2M2244. In this paper the variability of three brown dwarfs is modeled by longitudinal bands with sinusoidal surface brightness modulations and an elliptical spot. When two bands have slightly different periods due to differing velocities or directions, they interfere to produce beat patterns. These beat patterns produce high amplitude variability when the waves are in phase and produce double-peaked variability when the phase shift between the waves is close to 90°. This model can explain light curves that are sometimes single-peaked and other times double-peaked as well as providing an explanation for the shape of the periodogram in the bottom panel of Figure 4.7, where the higher frequency peak at $\sim$ 5 hr may be explained by a beat pattern with wavenumber $k = 2$.

Both our periodogram and MCMC analysis of the new [3.6 μm] data set point to a period of $\sim$ 11.0 hr. This period is also consistent with our UKIRT WFCAM J-band observation. As we still have not covered a full period for 2M2244 we combine the periods obtained from our MCMC Fourier models (shown in Figure 4.8 and 4.11) to make a conservative estimate of 11 ± 2 hr for 2M2244.

The observed peak-to-peak amplitude of $0.8 \pm 0.2\%$ for the more recent *Spitzer* [3.6 μm] is comparable to the $1.0 \pm 0.1\%$ modulation observed in the original *Spitzer* [4.5 μm] epoch of Morales-Calderon et al. (2006). The amplitude ratio, $A[4.5]/A[3.6]$ of $1.25 \pm 0.2\%$ is similar to the amplitude ratios found by Metchev et al. (2015).

4.4.4 SDSS1110

The light curve of SDSS1110 (top panel of Figure 4.15) does not display any obvious trends, and our periodogram analysis (middle panel) confirms this. To determine the sensitivity of our observation, we inject simulated sinusoidal curves into random permutations of our SDSS1110 lightcurve. The simulated sine curves have peak-to-peak amplitudes ranging from $0.4 - 1.6\%$ and periods of $2 - 18$ hr, with randomly assigned phase shifts. Each simulated lightcurve is put through our periodogram analysis, which allows us to produce a sensitivity plot, shown in the bottom panel of Figure 4.15. The blue region corresponds to periods and amplitudes detected with a FAP $< 1\%$, the white region corresponds to those detected with $1\% <$ FAP $< 5\%$, and the orange region corresponds to those with FAP $> 5\%$. For periods < 18 hr, an upper limit of 1.25% is placed on the variability amplitude of SDSS1110. Considering only periods < 10 hr, as done by Metchev et al. (2015), we place an upper limit of 0.9% on the variability amplitude. However, since we expect that young brown dwarfs will rotate more slowly due to conservation of angular momentum, the limit based on periods < 18 hr is more robust.

The photometric noise measured for SDSS1110 is comparable to the noise measured for comparison stars of similar brightness, and thus we do not find evidence for stochastic or aperiodic variability. We additionally check the periodogram of the unbinned lightcurve to search for evidence of very short period ($<$ 1 hr) deuterium pulsations proposed by Palla & Baraffe (2005). The periodogram does not display significant peaks at these short periods. A photometric variability survey of late-M brown dwarfs with $T_{\rm eff} > 2400$ K and ages of $1 - 10$ Myr concluded that pulsations cannot grow to observable amplitudes in these objects (Cody & Hillenbrand, 2014). The absence of short period pulsations detected in the light curve of SDSS1110 suggests that this conclusion may extend to even cooler ($T_{\rm eff} \sim 900 - 1300$ K) brown dwarfs, however a larger sample will be needed to robustly explore this possibility. Deuterium pulsations are not expected to occur in objects with masses over the deuterium burning limit at the age of AB Doradus so would not be expected to occur in W0047 and 2M2244.

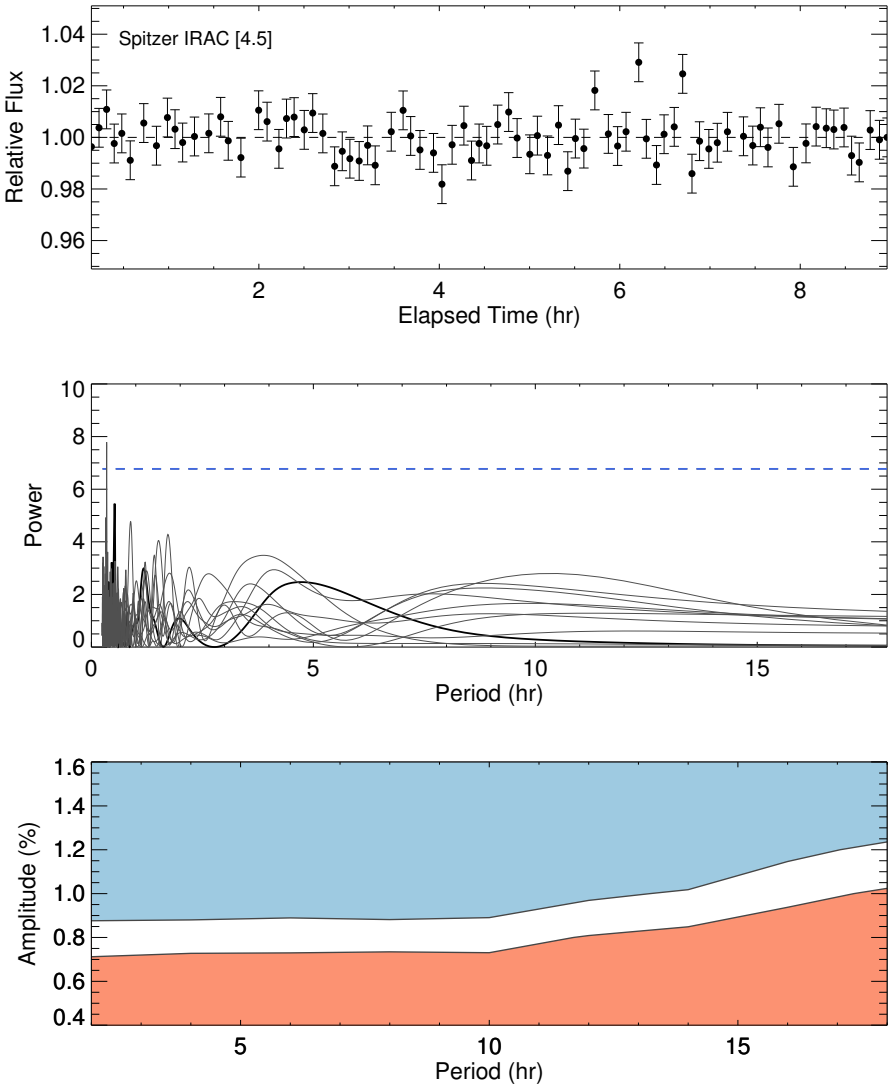

Figure 4.15 The top panel shows the normalised, pixel phase corrected lightcurve of SDSS1110. The middle panel shows the periodogram of SDSS1110 (thick black line) as well as the periodograms of several other reference stars in the field. The 1% FAP value is plotted in blue. The bottom panel shows the sensitivity of the observation as a function of amplitude and period. The blue area represents amplitudes detectable by the pipeline as a function of period (FAP $< 1\%$), the white area shows amplitudes marginally detectable ($1\% <$ FAP $< 5\%$), and the orange area shows amplitudes not detectable (FAP $> 5\%$). For periods < 18 hr, we place an upper limit of 1.25% on the variability amplitude of SDSS1110.

Table 4.2 Calculated rotational velocities, radial velocities, periods, [3.6 μm] peak-to-peak variability amplitudes and inclination angles for W0047 and 2M2244.

Parameter	W0047	2M2244
$v \sin(i)$ (km s^{-1})	9.8 ± 0.3	$14.3^{+1.3}_{-1.5}$
RV (km s^{-1})	$-19.8^{+0.1}_{-0.2}$	$-16.0^{+0.8}_{-0.9}$
P (hr)	16.4 ± 0.2	11.0 ± 2.0
[3.6 μm] Amp (%)	1.07 ± 0.04	0.8 ± 0.2
R (R_{Jup})	1.3 ± 0.04	1.29 ± 0.03
i	$85^{+5\circ}_{-9}$	$76^{+14\circ}_{-20}$

4.5 The Inclination Angles of W0047 and 2M2244

With measured values for $v \sin(i)$ and the rotation period, P, in hand, an assumption of radius allows us to determine the angle of inclination, i, if we assume that the brown dwarf rotates as a rigid sphere. However, this is not strictly true. The rotational period of Jupiter, as measured by magnetic fields originating in the core ($9^{\rm h}55^{\rm m}40^{\rm s}$) is 5 minutes slower than the period measured using features rotating along the equator ($9^{\rm h}50^{\rm m}30^{\rm s}$) (Cox, 2002). Since rotational periods that are measured from photometric variability monitoring typically have much larger uncertainties, the rigid body assumption is reasonable for our analysis. Thus, the equatorial rotation velocity, v, is given by $v = 2\pi R/P$, where R is the radius of the brown dwarf and P is its rotation period. We use the radii calculated from evolutionary models in Section 4.3.3.

Monte Carlo analysis was used to determine the inclination, i, for each target, using the posterior $v \sin(i)$ distributions obtained from our MCMC analysis. For the period and radius we draw samples from a Gaussian distributed sample with a width given by the reported errors. The radius estimates, rotational and radial velocities, periods, and resulting inclinations are shown in Table 4.2.

We find an inclination angle of $85^{+5\circ}_{-9}$ for W0047, so this object is viewed nearly equator-on. This inclination is significantly larger than the $33^{+5\circ}_{-8}$ calculated by Lew et al. (2016). This is as a result of both our longer period and larger $v \sin(i)$ measurement. The inclination angle of 2M2244 is found to be $76^{+14\circ}_{-20}$, which is similar to that of W0047. Considering their remarkably similar colours, spectra and inclination angles, the results are consistent with the idea that atmospheric appearance is influenced by viewing angle rather than rotation period

or variability properties. Figure 4.16 shows $(J-K_S)_{2\mathrm{MASS}}$ colour anomaly plotted against the inclination angle for variable brown dwarfs with our results for W0047 and 2M2244 overplotted (Chapter 3; Vos et al., 2017). The colour anomaly of each object is defined as the median $(J-K_S)_{2\mathrm{MASS}}$ colour for the spectral type and gravity flag of that object subtracted from its $(J-K_S)_{2\mathrm{MASS}}$ colour. Thus, positive and negative values of colour anomaly refer to objects that are redder and bluer than the corresponding median colour for their spectral types and gravity flags. Median colours for L0 - T6 field objects and their uncertainties were taken from Schmidt et al. (2010). Liu et al. (2016) provide linear relations between spectral type and absolute magnitude for VL-G and INT-G brown dwarfs, and these were used to calculate the median colours for the intermediate and low-gravity objects. Since W0047 and 2M2244 have nearly identical spectra (Gizis et al., 2015), we treat them both as L7 INT-G objects, and apply the same colour anomaly correction to both. The error bars for these objects are simply the J and K_S magnitude uncertainties combined. Our estimate of the median colour of low-gravity objects is limited by the low number of such objects known. As more of these objects are discovered this median colour will become more accurate. In Chapter 3 (Vos et al., 2017), we find that the correlation between near-infrared colour anomaly and inclination angle of field brown dwarfs is statistically significant at the 99% level. Variable brown dwarfs viewed equator-on appear redder than the median while objects closer to pole-on are bluer than the median. This figure is updated in Figure 4.16. W0047, 2M2244 and the low-gravity objects 2M0103+19, 2M1615+49, PSO-318 and 2M2208+29 may follow this trend, although more inclination data for young dwarfs are needed to fully explore this possibility. This relation between colour anomaly and inclination may be explained if clouds are inhomogeneously distributed in latitude or if grain size and cloud thickness vary in latitude. If thicker or large-grained clouds are situated predominantly at the equator, while thinner or small-grained clouds are situated at the poles then we would expect to observe objects with $i \sim 90^\circ$ to be redder than the median and objects with lower inclination angles to be bluer than the median. The addition of more inclination data for brown dwarfs is likely to reveal the physical origin of the correlation seen in Figure 4.16.

In Chapter 3 (Vos et al., 2017), we also find a relation between the colour anomaly of an object and its variability amplitude, where objects that are redder than the median for their spectral type and gravity class tend to have higher variability amplitudes. Figure 4.17 shows an updated version of this plot, showing that W0047 and 2M2244 are also consistent with this trend.

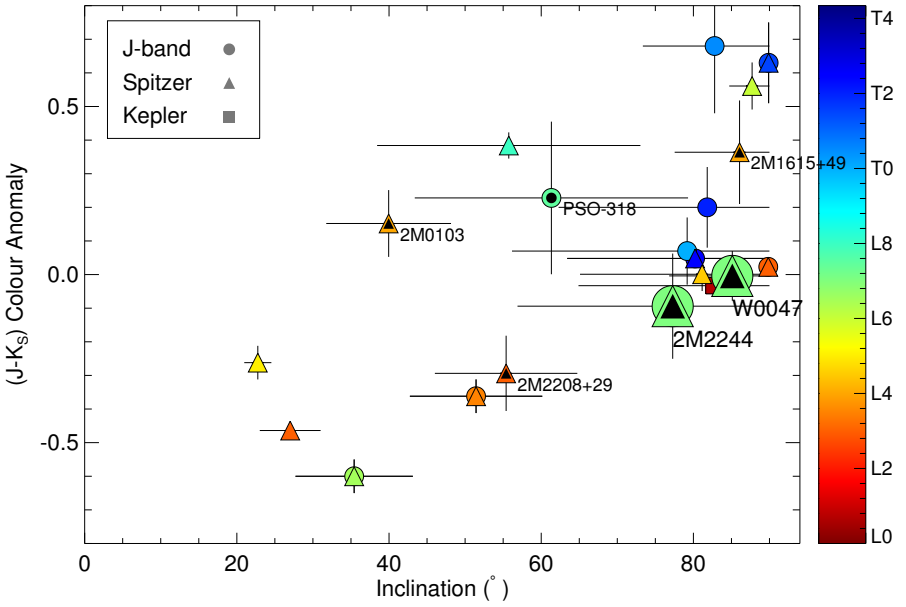

Figure 4.16 $(J-K_S)_{\rm 2MASS}$ colour anomaly plotted against the inclination angle for variable brown dwarfs. Black insets denote low-gravity brown dwarfs. In addition to 2M2244 and W0047, the low-gravity variable objects shown in this plot are 2M0103+19 (L4), 2M1615+49 (L4), PSO-318 (L7.5) and 2M2208+29 (L3). Inclination data for 2M2244 and W0047 are calculated in this chapter, inclination data for other objects are from Chapter 3 (Vos et al., 2017).

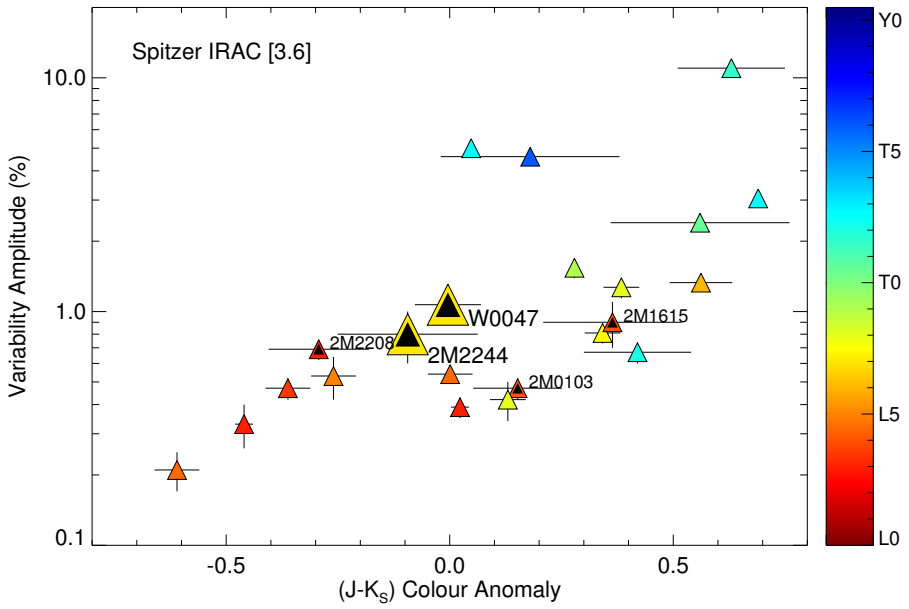

Figure 4.17 *Spitzer* [3.6 μm] variability amplitude plotted against $(J - K_S)_{\rm 2MASS}$ colour anomaly for variable brown dwarfs. Data for 2M2244 and W0047 are presented in this chapter, inclination data for other objects are from Chapter 3 (Vos et al., 2017).

4.6 Conclusions

We have obtained *Spitzer* [3.6 μm] photometric monitoring for two young free-floating objects, W0047, 2M2244 and *Spitzer* [4.5 μm] monitoring of SDSS1110 as well as J-band monitoring of 2M2244. Additionally, we obtain NIRSPEC N-7 spectra of W0047 and 2M2244. We detect variability in the two late-L, low mass dwarfs W0047 and 2M2244. MCMC analysis of the *Spitzer* [3.6 μm] lightcurve of 2M2244 gives a period of 11 ± 2 hr and a peak to trough amplitude of $0.8 \pm 0.2\%$. We detect significant ($\sim$ 3%) J-band variability in 2M2244. We find a period of 16.4 ± 0.2 hr for W0047 and an amplitude of $1.07 \pm 0.04\%$. Variability is not observed in the T5.5 object SDSS1110 during an 8.5 hr observation. For periods < 18 hr, we place an upper limit of 1.25% on the variability amplitude of SDSS1110.

With a peak to trough amplitude of $1.07 \pm 0.04\%$ for W0047, this is among the highest *Spitzer* [3.6 μm] variability amplitudes detected. This variability detection adds to a growing number of young, L-type objects that display high amplitude variability, suggesting that this correlation may extend into the late-L

spectral types (Metchev et al., 2015; Biller et al., 2015; Lew et al., 2016).

The rotational velocities, $v \sin(i)$, of both variable objects W0047 and 2M2244 are determined using NIRSPEC-7 high dispersion spectra, finding $v \sin(i) = 14.3^{+1.3}_{-1.5}$ km s^{-1} for 2M2244 and $v \sin(i) = 9.8 \pm 0.3$ km s^{-1} for W0047. Assuming rigid sphere rotation and using expected radii from evolutionary models, we find that both objects are close to equator-on, with inclination angles of $85^{+5\circ}_{-9}$ and $76^{+14\circ}_{-21}$ for W0047 and 2M2244 respectively. Their remarkably similar colours, spectral appearance and inclination angles are consistent with the possibility that viewing angle shapes the observed spectrum of a brown dwarf or giant exoplanet.

Chapter 5

The First Search for Weather Patterns in Exoplanet Analogues

5.1 Abstract

In this chapter we report the results of a J-band survey for photometric variability in a sample of young, low-gravity objects using the New Technology Telescope (NTT) and the United Kingdom InfraRed Telescope (UKIRT). Surface gravity is a key parameter in the atmospheric properties of brown dwarfs and this is the first large survey that aims to test the gravity dependence of variability properties. We do a full analysis of the spectral signatures of youth and assess the group membership probability of each target using the Convergent Point, BANYAN I, BANYAN Σ and LACEwING tools (Rodriguez et al., 2013; Malo et al., 2013; Gagné et al., 2015c; Riedel et al., 2017). This results in a 30 object sample of young low-gravity brown dwarfs. We find an overall variability occurrence rate of 20%, which is consistent with the 16% variability fraction reported by Radigan et al. (2014) for the higher mass, field brown dwarfs. However, since we are lacking in objects with spectral types later than L9, we focus our statistical analysis on the L0-L8.5 objects. We find that the variability occurrence rate of L0-L8.5 low-gravity brown dwarfs in this survey is 30^{+16}_{-8}%. We reanalyse the results of Radigan (2014) and find that the field dwarfs with spectral types L0-L8.5 have a variability occurrence rate of 11^{+13}_{-4}%, lower than the young population of exoplanet analogues. This is the first quantitative indication that the low-gravity objects are more likely to be variable than the field dwarf population.

5.2 Introduction

Time-resolved photometric variability monitoring is a key probe of cloud properties in brown dwarf atmospheres, as it is sensitive to the spatial distribution of condensates as a brown dwarf rotates. Photometric variability has been well-studied in field L and T spectral type dwarfs, but the variability properties of the population of younger, low-gravity objects are less understood.

Radigan et al. (2014) reported the results of a large, ground-based search for J-band variability in L and T dwarfs, finding that 9 out of 57 (16%) objects showed significant variability above photometric noise. Furthermore, the authors report enhanced variability frequency and amplitudes at the L/T transition, supporting the hypothesis that cloud holes contribute to the abrupt decline in condensate opacity and J-band brightening observed at the L/T transition. A similar ground-based variability survey, the *Brown Dwarf Atmospheric Monitoring* (BAM) survey, was reported by Wilson et al. (2014), who monitored 69 brown dwarfs spanning L0 to T8. Significant variability was reported in 14 of 69 objects (20%), with no evidence for an enhancement in frequency or amplitude across the L/T transition. However, Radigan (2014) carried out a reanalysis of the the 13 highly variable objects reported by Wilson et al. (2014) and found significant variability in only 4 from 13. Combining the revised BAM survey with the Radigan et al. (2014) survey, Radigan (2014) found that 24^{+11}_{-9}% of objects in the L9-T3.5 range exhibit J-band variability, in contrast to $2.9^{+4.1}_{-2.1}$% of L0-L8.5 brown dwarfs and $3.2^{+4.4}_{-2.3}$% of T4-T9.5 brown dwarfs. (Radigan, 2014).

A 22 target *HST* grism spectroscopy survey at wavelengths of $1.1 - 1.7$ μm was presented by Buenzli et al. (2014), attaining point-to-point precision of $0.1-0.2$% during ~ 40 min observations. Low-level (~ 1%) variability trends were detected in 6 brown dwarfs (27%), with no evidence for enhanced frequency across the L/T transition, suggesting that low-level heterogeneities are a frequent characteristic of brown dwarf atmospheres across the entire L-T spectral range. Metchev et al. (2015) reported results from a *Spitzer* program to search for photometric variability in a larger sample of 44 L3-T8 dwarfs at 3.6 μm and 4.5 μm, reaching $0.2-0.4$% precision. Metchev et al. (2015) reach a similar conclusion, finding that photometric variability is common among L and T dwarfs. The survey included eight low or intermediate gravity brown dwarfs to probe the effects of low surface gravity on the variability properties of brown dwarfs. A tentative correlation was found between low-gravity and high amplitude variability, however a larger

sample is necessary to confirm this potential relation (Metchev et al., 2015).

For the majority of directly-imaged exoplanets, the contrast between host star and planet make it difficult to obtain sufficiently high S/N photometry to allow detailed studies of their variability, thus only a handful are amenable to variability studies. In fact, Apai et al. (2016) explored the rotational variability of the HR8799 planets, reaching a photometric precision of $\sim$ 10%, thus insufficient to detect variability on levels of a few percent. However, young brown dwarfs provide an excellent analogue to directly-imaged exoplanets. Recently, a handful of young brown dwarfs with colours and magnitudes similar to directly-imaged planets have been discovered (see compilation of young objects made by Faherty et al., 2016; Liu et al., 2016). The atmospheres of these young brown dwarfs can provide insight into the atmospheres of directly-imaged planets. Like their higher-mass brown dwarf counterparts (Zapatero Osorio et al., 2006), young companion exoplanets and free-floating objects appear to be fast rotators with measured rotational periods of $\sim 7 - 11$ hours (Snellen et al., 2014; Biller et al., 2015; Allers et al., 2016; Zhou et al., 2016). This makes them excellent targets for photometric variability monitoring.

Variability has now been detected in a small sample of low-gravity objects. As part of this survey, variability was detected in the planetary-mass object PSO J318.5338–22.8603 (PSO 318.5–22) (Chapter 2; Biller et al., 2015). With a variability amplitude of $7 - 10$%, PSO 318.5–22 displays a very high variability amplitude compared to most objects in the field population. This was swiftly followed by a variability detection in the 3 $M_{\rm Jup}$ companion 2MASSW J1207334–393254 (2M1207b), which displayed $\sim$ 1.36% variability in the F125W filter during a 9 hr observation with *HST* (Zhou et al., 2016). The 19 $M_{\rm Jup}$ object WISEP J004701.06+680352.1 (W0047) was found to exhibit $\sim$ 8% variability during a 9 hr *HST* observation (Lew et al., 2016). In Chapter 4 (Vos et al., 2018), we reported results from a *Spitzer* program to monitor variability on the intermediate gravity late-L dwarfs W0047 and 2MASS J2244316+204343 (2M2244) and the planetary-mass T5.5 object SDSS 111010+011613 (SDSS1110). W0047 and 2M2244 were both found to be variable in the mid-IR, with fairly high amplitudes compared to the sample of higher-mass field dwarfs that have been studied. There has also been tentative evidence that the low-gravity T dwarfs exhibit higher variability amplitudes compared to field objects. Gagné et al. (2017) find that the highly variable object SIMP0136 is a likely member of the $\sim$ 200 Myr Carina-Near moving group. Gagné et al. (2018a) confirm the variable

object 2M1324 as a member of the AB Doradus moving group and estimate a mass of $11 - 12\ M_{\rm Jup}$. Naud et al. (2017) obtained three $5 - 6$ hr epochs of variability monitoring observations of the young T-type companion GU Psc b in AB Doradus. The authors detect marginal variability in one epoch but do not detect significant variability in the other two epochs. The high amplitudes observed in this small sample of low-gravity variable objects adds to the growing evidence that there is a link between low-gravity and high-amplitude variability.

Here we present the results of a large photometric monitoring survey of young, low-gravity L and T dwarfs, with the goal of investigating the gravity dependence of variability properties. Observations were carried out at the 3.6 m New Technology Telescope (NTT) and the 3.8 m UK InfraRed Telescope (UKIRT).

5.3 Sample Selection

From Autumn 2014 to Spring 2017 we observed a sample of 36 brown dwarfs that are candidate members of young moving groups in the literature and/or show signatures of youth in their spectra. Our survey targets are primarily sourced from the BANYAN catalogues (Gagné et al., 2014c, 2015c) and Best et al. (2015). We additionally include the wide companions HN Peg B and GU Psc b (Luhman et al., 2007; Naud et al., 2014). The full survey sample is show in Table 5.3. We consider the following young moving groups in this paper: TW Hydra (TWA, 10 ± 3 Myr; Bell et al., 2015), β Pictoris (β Pic, 22 ± 6 Myr; Shkolnik et al., 2017), Columba (Col, 42^{+6}_{-4} Myr; Bell et al., 2015), Tucana-Horologium (THA, 45 ± 4 Myr; Bell et al., 2015), Carina (Car, 45^{+11}_{-7} Myr; Bell et al., 2015) Argus (Arg, $30 - 50$ Myr; Torres et al., 2008), AB Doradus (AB Dor, $110 - 150$ Myr; Barenfeld et al., 2013; Luhman et al., 2007) and Carina-Near (CarN, 200 ± 50 Myr; Zuckerman et al., 2006). Our targets show signs of low-gravity in their spectra and/or are candidate members of nearby young moving groups. We reassess the evidence of low-gravity/youth for each object in Section 5.9.

To obtain high signal-to-noise (S/N) measurements that could be robustly compared to previous surveys (Radigan et al., 2014; Wilson et al., 2014), targets were limited to objects with magnitudes brighter than $J_{2MASS} = 17.0$ mag (apart from one target, GU Psc b). We observed our targets at airmasses < 1.5 to maximise the S/N.

The sample consists of spectral types L0 and later, as these are less likely to exhibit magnetic spot activity due to the increasingly neutral atmospheres present in objects with $T_{\rm eff}$ below $\sim$ 2100 K. Gelino et al. (2002) and Miles-Páez et al. (2017) find no correlation between magnetic activity (in the form of Hα emission) and photometric variability in a sample of L and T dwarfs. We attempt to cover the entire L-T spectral range uniformly, however few young T dwarfs sufficiently bright for ground-based IR photometric monitoring are known, preventing us from fully covering the T spectral type. Thus our sample is predominantly comprised of L-type objects.

There is only one known binary in our sample, 2MASS J03572695–4417305 (Bouy et al., 2003). The binary separation ($\approx 0.1''$) is less than the seeing so the photometry in this study records the combined flux from both components. The variability of one component in an unresolved binary will be diluted by flux from the non-variable component, making it more difficult to detect the variability. Alternatively, if both components of the binary are variable (as is the case for the Luhman 16AB binary system; Biller et al., 2013; Buenzli et al., 2015b), their differing variability amplitudes and rotational periods will be combined in the observed lightcurve, likely resulting in a rapidly evolving lightcurve.

5.4 Observations and Data Reduction

5.4.1 NTT SofI

The observations took place between October 2014 and March 2017 with the SofI (Son of Isaac) instrument, mounted on the 3.6 m New Technology Telescope (NTT) at La Silla Observatory. Observations were carried out in large field imaging mode, which has a pixel scale of $0.288''$ and a $4.92' \times 4.92'$ field of view. Targets were observed using the J_S band ($1.16 - 1.32$ μm). The J_S filter was chosen as it avoids contamination from the water band at 1.4 μm. Two targets were observed each night, alternating between nods in an ABBA pattern, with 3 exposures at each position. At each nod we ensured the target was accurately placed on the same original pixel in order to preserve photometric precision. $2 - 5$ hr observations were obtained for each target. The flux of the target was kept below 10,000 ADU to prevent any non-linearity effects.

The data reduction steps are outlined in the SofI manual, and an IRAF pipeline

was provided by ESO. We processed our images using both the standard IRAF routine as well as an IDL version. Here we detail our data reduction process.

Inter-quadrant Row Crosstalk

The SofI detector suffers from inter-quadrant row crosstalk, where a bright target imaged in one quadrant can cause a faint glow in equivalent rows of the other quadrants. The intensity of the crosstalk feature scales with the total intensity along a given row by an empirically determined value of 1.4×10^{-5} and can be removed easily.

Flat-fielding

The shade pattern on the array is a function of the incident flux, so the method of creating flat-fields by subtracting lamp-off from lamp-on dome flats leaves a residual shade pattern across the centre of the array. For this reason "special" dome flats are taken using standard frames along with frames in which the array is partially obscured to estimate the illumination dependent shade pattern of the array. The shade pattern can be removed as described by the ESO documentation.

Illumination Correction

Illumination correction removes the difference between the illumination pattern of the dome flat screen and the sky. This correction is determined from a grid of 16 observations of a standard star across the field of view. The illumination correction is created by fitting a 2D surface to the fluxes of the star after flat-fielding.

Table 5.1 Observing log

Target	Telescope	Filter	**Date**	Δt (hr)	FWHM ($''$)
2M0001+15	UKIRT	J	2016-10-12	3.75	1.01
2M0045+16	NTT	J_S	2014-11-11	4.05	1.30
2M0045+16	NTT	J_S	2015-08-17	3.36	0.56
2M0045+16	UKIRT	J	2016-11-13	4.36	0.94
2M0103+19	NTT	J_S	2014-11-03	5.28	0.40
GU Psc b	NTT	J_S	2014-10-11	3.46	0.83
2M0117–34	NTT	J_S	2014-11-08	4.44	0.44
2M0117–34	NTT	J_S	2016-10-18	1.92	2.26
2M0234–64	NTT	J_S	2014-11-10	5.59	0.63
2M0303–73	NTT	J_S	2014-11-09	5.50	0.49
2M0310–27	NTT	J_S	2014-11-08	3.00	0.46
2M0323–46	NTT	J_S	2014-11-07	5.32	1.07
2M0326–21	NTT	J_S	2014-11-04	4.68	0.51
2M0342–68	NTT	J_S	2014-11-03	2.88	0.44
PSO 057+15	UKIRT	J	2016-12-23	3.59	1.26
2M0355+11	NTT	J_S	2014-10-07	4.73	0.83
2M0357-44	NTT	J_S	2014-10-10	4.13	1.10
2M0418–45	NTT	J_S	2017-03-14	2.11	0.68
2M0421–63	NTT	J_S	2014-10-08	5.50	1.01
PSO071.8–12	NTT	J_S	2017-10-18	3.31	1.71
PSO071.8–12	UKIRT	J	2017-12-08	4.29	1.16
2M0501–00	NTT	J_S	2014-11-11	4.03	1.06
2M0501–00	NTT	J_S	2015-08-16	2.01	2.39
2M0501–00	NTT	J_S	2016-10-19	4.99	1.49
2M0501–00	NTT	J_S	2017-03-12	1.85	0.43
2M0512–27	NTT	J_S	2017-03-13	3.00	0.40
2M0518–27	NTT	J_S	2014-11-05	3.98	1.52
2M0536–19	NTT	J_S	2014-10-11	2.88	0.90
SDSS1110+01	NTT	J_S	2017-03-12	5.40	0.37
2M1207–39	NTT	J_S	2017-03-13	4.49	0.34
2M1256–27	NTT	J_S	2017-03-14	2.54	0.40
2M1425–36	NTT	J_S	2015-08-17	2.52	0.42
2M1425–36	NTT	J_S	2017-03-14	4.10	0.39
2M1615+49	UKIRT	J	2016-07-10	4.33	1.14
W1741	NTT	J_S	2014-10-11	2.37	0.67
PSO 272.4–04	NTT	J_S	2017-03-12	2.28	0.34
2M2002–05	UKIRT	J	2016-07-09	4.37	1.22

Table 5.1 – continued from previous page

Target	Telescope	Filter	Date	Δt (hr)	FWHM ($''$)
2M2011–05	NTT	J_S	2015-08-15	3.43	0.48
SIMP J2154	NTT	J_S	2014-11-07	3.44	1.12
HN Peg B	NTT	J_S	2014-10-08	3.88	1.17
HN Peg B	NTT	J_S	2015-08-17	1.42	0.58
HN Peg B	UKIRT	J	2016-07-11	4.97	1.00
HN Peg B	UKIRT	J	2016-07-13	5.01	1.00
PSO J318–22	NTT	J_S	2014-10-09	5.13	0.48
PSO J318–22	NTT	J_S	2014-11-09	2.83	0.42
PSO J318–22	NTT	K_S	2014-11-10	3.10	0.52
PSO J318–22	NTT	J_S	2015-08-16	4.99	0.38
PSO J318–22	NTT	J_S	2016-08-09	9.12	1.26
PSO J318–22	NTT	K_S	2016-08-10	9.65	1.44
PSO J318–22	NTT	J_S	2016-08-11	10.46	1.37
PSO J318–22	NTT	K_S	2016-08-11	9.84	1.22
2M2244+20	UKIRT	J	2016-07-21	4.10	1.13
2M2322–61	NTT	J_S	2014-10-10	4.37	1.28

Sky Subtraction

The sky subtraction of images obtained with SofI serves to remove the dark current as well as the illumination-dependent shade pattern. Sky frames are created by median combining normalised frames of different nods which are closest in time. These are then re-scaled to the science frame before being subtracted from the science frame.

Aperture Photometry

The positions of the target star as well as a set of reference stars in the field of view were found in each frame using IDL FIND.PRO followed by GCNTRD.PRO to measure the centroids. Aperture photometry was performed on the target as well as the set of reference stars. Fixed apertures of sizes similar to the median FWHM of all stars on the chip were used. The final aperture was chosen to minimise the photometric noise.

For a non-variable lightcurve, the standard deviation provides a good estimate of the noise, however for a variable lightcurve, the standard deviation measures both noise and intrinsic variations. We estimate the typical photometric error for each lightcurve, $\sigma_{\rm pt}$, using a method described by Radigan et al. (2014). This is the standard deviation of the lightcurve subtracted from a shifted version of itself, $f_{i+1} - f_i$, divided by $\sqrt{2}$. This quantity is sensitive to high frequency noise in the data and is insensitive to the low frequency trends we expect from variable brown dwarfs. Thus it provides a more accurate estimate of the photometric noise for variable lightcurves.

5.4.2 UKIRT WFCAM

Observations of 8 targets were taken with the infrared Wide-Field Camera (WFCAM; Casali et al., 2007). WFCAM is a wide-field imager on the 3.8 m UK Infrared Telescope on Mauna Kea, with a pixel scale of $0.4''$. The observations were carried out in the J-band. Each target was observed using an ABBA nod pattern, as before. Frames were reduced using the WFCAM reduction pipeline (Irwin et al., 2008; Hodgkin et al., 2009) by the Cambridge Astronomy Survey Unit. The pipeline reduction steps include linearity correction, dark correction, flat-fielding, gain-correction, decurtaining, defringing, sky subtraction and crosstalk removal (Irwin et al., 2004). We performed aperture photometry on the target and reference stars in the field of similar brightness, using a range of aperture sizes similar to the median FWHM of all stars in the field.

5.4.3 Lightcurve Analysis

The raw light curves obtained from aperture photometry display fluctuations in brightness due to changing atmospheric transparency, airmass and residual instrumental effects. To a very good approximation these changes are common to all stars in the field of view and can be removed via division of a calibration curve calculated from a set of iteratively chosen, well-behaved reference stars (Radigan et al., 2012). Firstly, reference stars with peak flux values below 10 or greater than 10,000 ADU were discarded. Different nods were normalised via division by their median flux before being combined to give a relative flux light curve. For each star a calibration curve was created by median combining all other reference stars (excluding that of the target and star in question). The

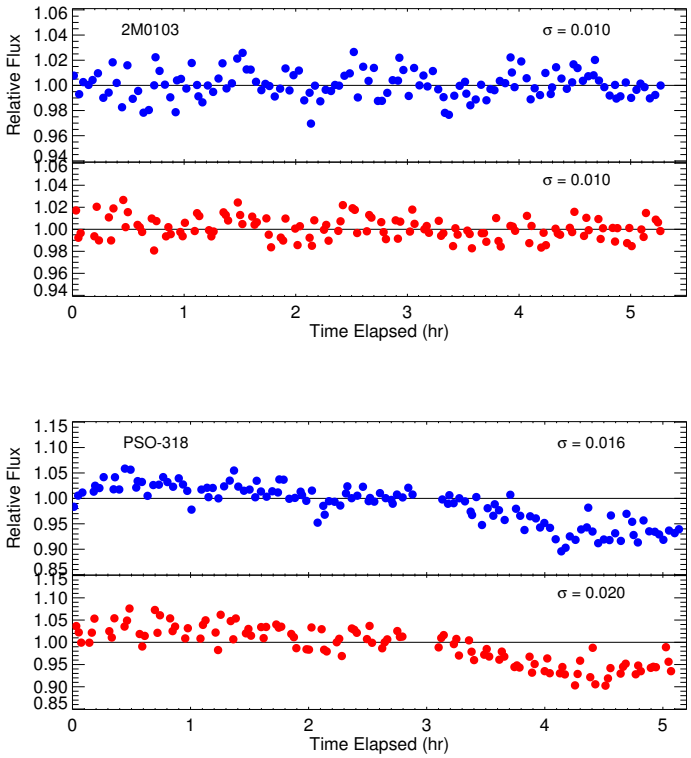

Figure 5.1 Lightcurves of 2M0103 and PSO-318 reduced and analysed using two methods. The blue points show the lightcurve obtained from the method described in Section 5.4.1 and the red points show the lightcurve obtained from the independent reduction described in Section 5.4.4. Both lightcurves are binned by a factor of 2. The same lightcurve shape and a similar photometric error σ is recovered for each observation.

standard deviation and linear slope for each light curve was calculated and stars with a standard deviation or slope $\sim 1.5-3$ times greater than that of the target were discarded. This process was iterated a number of times, until a set of well-behaved reference stars was chosen. Final detrended lightcurves were obtained by dividing the raw curve for each star by its calibration curve. Lightcurves shown in this paper have been binned by a factor of $1-3$.

5.4.4 Independent Reduction of NTT/SofI Data

We additionally present the results of an independent data reduction process outlined in the MSc thesis of Simon Eriksson and supervisor Markus Janson (Eriksson, 2016). 20 of the 21 targets observed with the NTT in 2014 were independently reduced and analysed. A further 10 observations from 2015-2017,

mainly follow-ups, were investigated in late 2017 in the same way. Overall, 24 out of 30 NTT targets underwent reduction, with the remaining 6 representing single nights. The reduction steps previously outlined in Section 5.4.1 were performed, with the addition of a dark subtraction. The SofI pipeline provided by ESO was used for dark, flat-field and crosstalk corrections as well as sky subtraction. The process resulted in combined images of two different nods closest in time, and subsequent photometry was obtained using PHOT in IRAF. Errors were estimated from PHOT output together with a polynomial fitting to the light curves. Both methods identified the same variable targets.

In Figure 5.1 we compare the lightcurves of two objects in our survey that were analysed using both reductions – the non-variable object 2M0103 (although Metchev et al. (2015) report low-amplitude mid-IR variability in this object) and the variable object PSO 318.5–22. The blue points show the lightcurve obtained from the method described in Section 5.4.1 and the red points show the lightcurve obtained from the independent reduction described above. Both methods produce the same lightcurve shape and a similar photometric error σ. Since the results were consistent between reductions, for the rest of the paper we present lightcurves obtained using the method described in Sections 5.4.1 and 5.4.3.

5.4.5 Identification of Variables

Variable targets were identified using the periodogram analysis outlined in Vos et al. (2018). The periodograms of each target and its respective reference stars are plotted to identify periodic variability. For each observation, the 1% false-alarm probability (FAP) is calculated from 1000 simulated light curves. These light curves are produced by randomly permuting the indices of the reference star lightcurves (Radigan et al., 2014). This method assumes Gaussian-distributed noise in the reference stars, however to assess the significance of residual correlated noise in the reference star lightcurves we measure the β factor of every light curve, which is the peak periodogram power of each reference star divided by the 1% FAP power (Radigan et al., 2014). Figure 5.2 shows the β factor of reference stars and targets for NTT (top) and UKIRT (bottom) observations. We display these separately as each instrument has unique systematics. For reference stars exhibiting Gaussian-distributed noise, we would expect that 1% of reference star peak powers would fall above a β factor $= 1$, however for both samples more

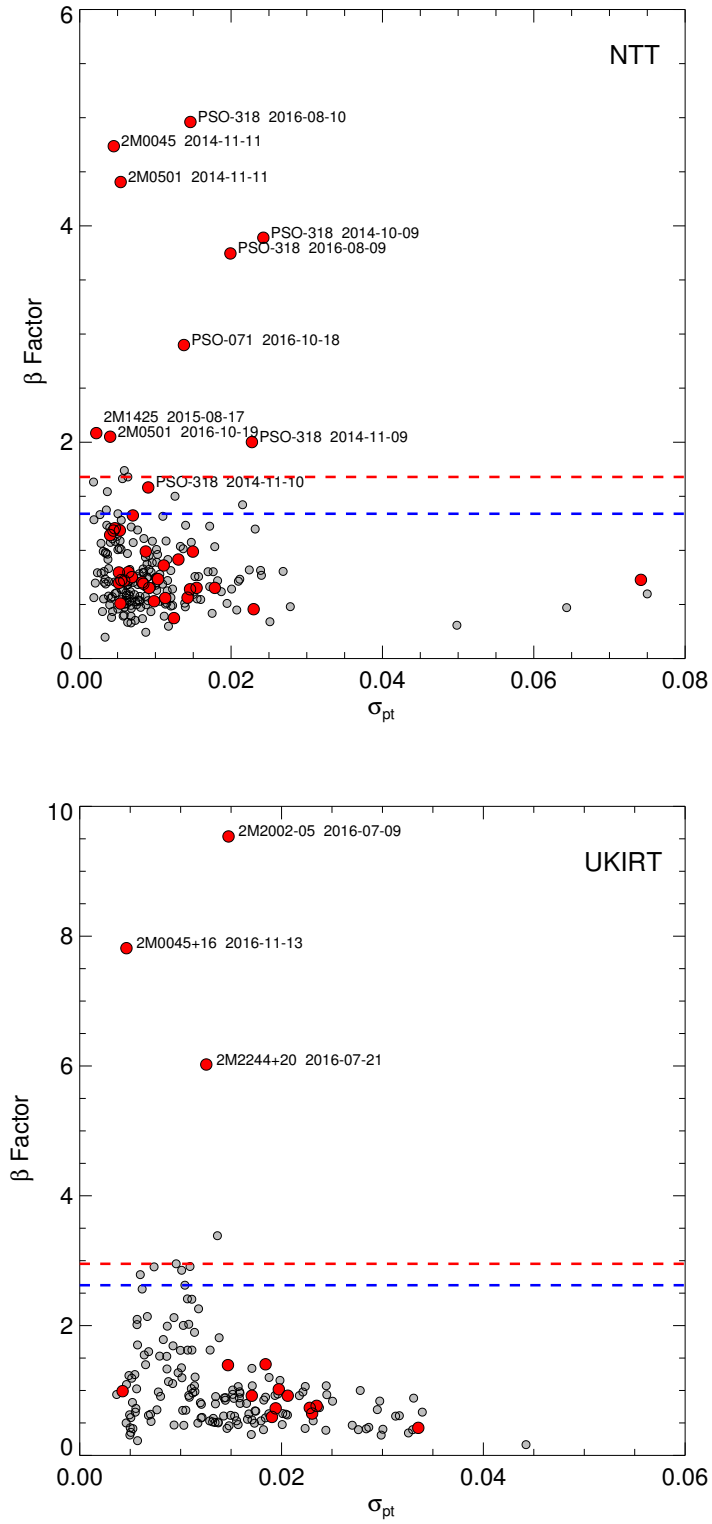

Figure 5.2 β factor plotted against the photometric error, $\sigma_{\rm pt}$ for reference stars (grey circles) and targets (red circles) for the NTT (top) and UKIRT (bottom) samples. The β factor is defined as the periodogram peak power of each reference star divided by 99% significance as calculated from our simulations. The updated, empirical 99% and 95% significance thresholds are shown by the red and blue dashed lines respectively.

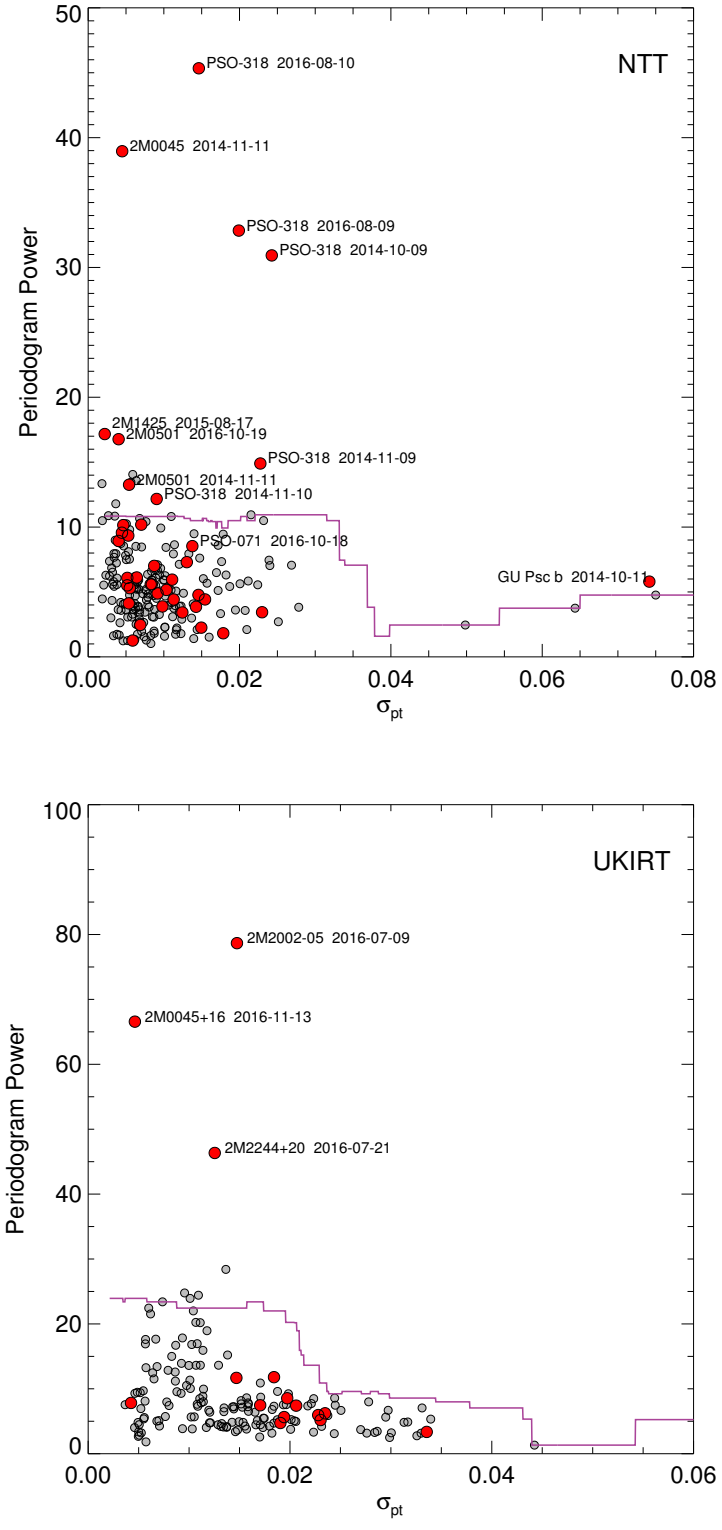

Figure 5.3 Maximum periodogram power plotted against the photometric error, $\sigma_{\rm pt}$, for reference stars (grey circles) and targets (red circles) for the NTT (top) and UKIRT (bottom) samples. The $\sigma_{\rm pt}$-dependent 95% significance is shown by the purple line.

than 1% of reference star peak powers fall above $\beta = 1$, and this is likely due to residual correlated noise in the lightcurves. To account for this excess noise, we find the empirical 1% FAP by finding the β factor above which 1% of reference star peak powers fall. Blue and red dashed lines indicate the new, empirical 95% and 99% significance thresholds. This increases the significance thresholds by a factor of 1.7 and 3.4 for the NTT and UKIRT samples respectively.

We additionally explore an alternative method for identifying significantly variable objects, following a method described in Heinze et al. (2015) in a survey for optical variability in T-type brown dwarfs. In this study, the authors find a weak dependence of their variability metric on the RMS of each target. We can also see this in Figure 5.2, where reference stars with a higher photometric error tend to have lower β factors. We thus investigate the dependence of the periodogram power on $\sigma_{\rm pt}$. We can expect some dependence because if two lightcurves vary with the same amplitude but different noise levels, the lightcurve with lower photometric error produces a periodogram with a higher power. Thus we take this into account in our significance threshold criteria. We show the peak periodogram power of targets and reference stars in Figure 5.3. We calculate a σ-dependent 95% threshold using a sliding box as described in Heinze et al. (2015). The box width was chosen such that > 50 reference star points were available to calculate the 95% threshold up to 0.02 $\sigma_{\rm pt}$ and 0.03 $\sigma_{\rm pt}$ for the NTT and UKIRT data respectively. We find that a box width of 0.02 $\sigma_{\rm pt}$ is suitable for both. We show the noise-dependent significance threshold by the purple line in Figure 5.3. Both methods identify the same variable objects with the exception of PSO 071.8–12 and GU Psc b. PSO 071.8–12 is identified as variable in the β factor method but is identified as non-variable in the noise-dependent periodogram power method. We count this object as variable since the lightcurve shows high-amplitude modulation. It is likely that the periodogram power is low because PSO 071.8–12 has a rotational period that is significantly longer than the observation duration. GU Psc b is identified as variable in the noise-dependent method shown in Figure 5.3. With a magnitude of $J = 18.12$, GU Psc b is at least an order of magnitude fainter than the other targets in our survey and as such, has a much higher photometric error than the other survey targets. Additionally, we have very few reference stars at $\sigma_{\rm pt} > 0.03$, so calculating a 95% threshold at values greater than this is not valid. Thus, we have detected variability in thirteen epochs of observations, finding seven variable objects in the survey. We show the lightcurves of each variable object and three reference stars in Figure 5.5.

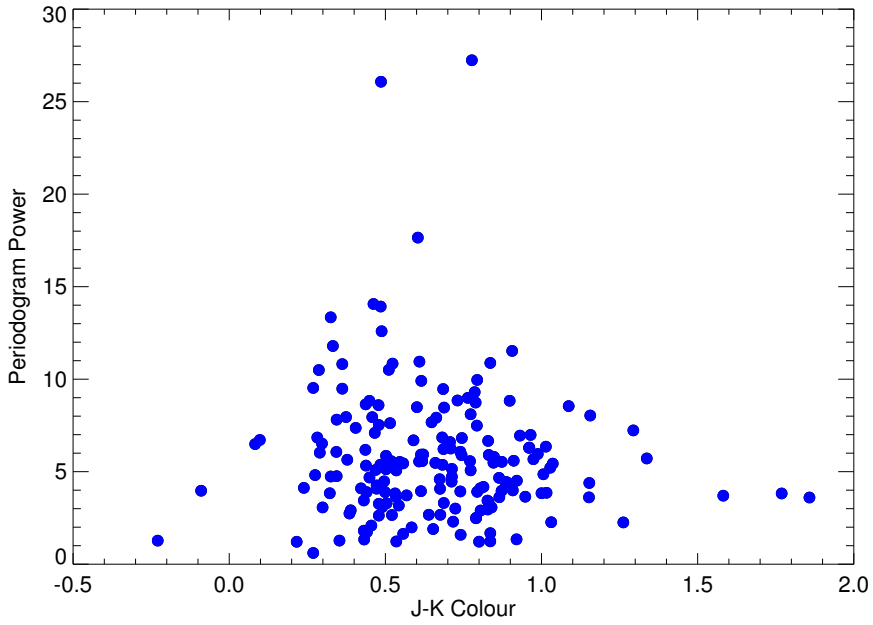

Figure 5.4 Maximum periodogram power plotted against] colour for reference stars in the NTT sample. There is no correlation observed between colour and periodogram power.

5.5 Possible Systematics

The majority of objects in our survey have very red $J - K_S$ colours. Since in general our reference stars are relatively bluer, lightcurve trends could be introduced as a result of differing atmospheric extinctions. To explore this possibility we examined the colours of all reference stars in the NTT/SofI survey, and searched for correlations between $J - K_S$ colour and maximum periodogram power (Figure 5.4). Within the range of reference star colours, we see no relation between colour and power, and thus conclude that colour differences do not affect lightcurve trends in this range. Since past studies have found that red brown dwarfs may be more likely to be variable (Metchev et al., 2015), this experiment cannot be robustly carried out on the targets. However, it is worth noting that there are both detections and non-detections across the full ~ 2.5 mag range of target colours.

Additionally, to check that our detrending algorithm has performed effectively, we have checked by eye that each variable lightcurve is not correlated with seeing, airmass and $x - y$ pixel position. Thus, we conclude that the trends observed in this survey are not likely to be caused by the systematics considered here.

5.6 Sensitivity to Variability Signals

To determine the sensitivity of each individual observation to variability signals, we inject simulated sinusoidal curves into random permutations of each target lightcurve. For targets found to be variable in the survey we divide the lightcurve by a polynomial fit to the lightcurve before injecting the simulated sinusoidal signals. The 1000 simulated sine curves have peak-to-peak amplitudes of 0.5−10% and periods of $1.5 - 20$ hr, with randomly assigned phase shifts. Each simulated lightcurve is put through our periodogram analysis, which allows us to produce a sensitivity plot, showing the percentage of recovered signals as a function of amplitude and period. Sensitivity plots for all light curves are shown in the bottom panel of Figures 5.6 – 5.16 for variable objects and Appendix A.3 for non-variables in the survey.

5.7 Significant Detections of Variability

We detect significant variability in seven objects in the survey. We present the light curves of these variable objects along with their reference stars in Figure 5.5. We show their periodograms and sensitivity plots in Figures 5.6 – 5.16. We discuss the first epoch variability detection of each object below.

2MASS J00452143+1634446 — Gagné et al. (2014c) classify the L2 object 2M0045+16 as a very low gravity brown dwarf, with Hα emission and unusually red colours. It has been identified as a bona fide member of the Argus association (30−50 Myr), giving it an estimated mass of 14.7 ± 0.3 $M_{\rm Jup}$ (Gagné et al., 2015c), however recent work by Bell et al. (2015) has called into question the validity of the Argus association. We observed 2M0045+16 on Nov 11 2014 using NTT SofI. We detect highly significant variability in this object at this epoch. The lightcurve of 2M0045+16 and the reference stars used for detrending are shown in Figure 5.5 and the periodogram and sensitivity plots are shown in Figure 5.6. A lack of stars in the field resulted in only 3 references stars suitable for detrending the lightcurve. We fit a sinusoid to the lightcurve using a Levenberg-Marquardt least-squares algorithm to estimate the amplitude of the modulation in the first epoch. This gives an amplitude of $1.0 \pm 0.1\%$ and a period 4.3 ± 0.3 hr. While it appears that we have covered a full rotational period, additional longer duration observations are necessary to rule out the possibility of a double-peaked lightcurve

with a longer rotational period (e.g. Chapter 4; Vos et al., 2018). We discuss followup observations of 2M0045+16 in Section 5.11.

PSO J071.8769 −12.2713 — PSO 071.8–12 was identified as a high-probability candidate member of β Pictoris by Best et al. (2015). Assuming membership of the β Pictoris moving group, it has an estimated mass of 6.1 ± 0.7 $M_{\rm Jup}$ (Best et al., 2015), making it the lowest mass object to date to exhibit photometric variability. The lightcurve shown in Figure 5.5 displays high-amplitude ($4.5 \pm 0.6\%$) variability. The periodogram shown in Figure 5.8 shows a highly significant ($> 99\%$) peak. Since we did not cover a full rotational period we can only estimate a period > 3 hr. We discuss subsequent follow-up observations of this object in Section 5.11.

2MASS J05012406−0010452 — Gagné et al. (2015c) categorise 2M0501–00 as L4γ, and an ambiguous candidate member of Columba or Carina (both moving groups are coeval at $20-40$ Myr). If 2M0501–00 is indeed a member of Columba or Carina it has an estimated mass of $10.2^{+0.8}_{-1.0}$ $M_{\rm Jup}$. We detect significant variability in 2M0501–00 on Nov 11 2014 with NTT SofI (shown in Figure 5.5). The periodogram shown in Figure 5.9 shows a highly significant peak at periods > 4 hr. A sinusoidal fit to the lightcurve gives a peak-to-peak amplitude of $2.0 \pm 0.1\%$ and a period of > 4 hr. Since we did not cover a full period of rotation in either epoch, our amplitude measurement is a lower limit and our period estimate is very uncertain. We obtained additional follow-up monitoring of 2M0501–00 and discuss these observations in Section 5.11.

2MASS J14252798−36502295.23 — 2M1425–36 is classified as a bona fide member of AB Doradus (Gagné et al., 2015c). Radigan et al. (2014) previously reported 2M1425–36 as a marginal variable, displaying low-level variability over a ~ 2.5 hr observation. We detect low-amplitude variability in the L3 object 2M1425–36 on Aug 17 2015. Figure 5.11 shows a highly significant periodogram peak at periods of ~ 3 hr. Using our least-squares algorithm we estimate a variability amplitude of $0.7 \pm 0.3\%$ for this epoch. We place a lower limit of 2.5 h on the rotational period since we did not cover a full period. We observed 2M1425–36 a second time in 2017 and discuss this observation in Section 5.11.

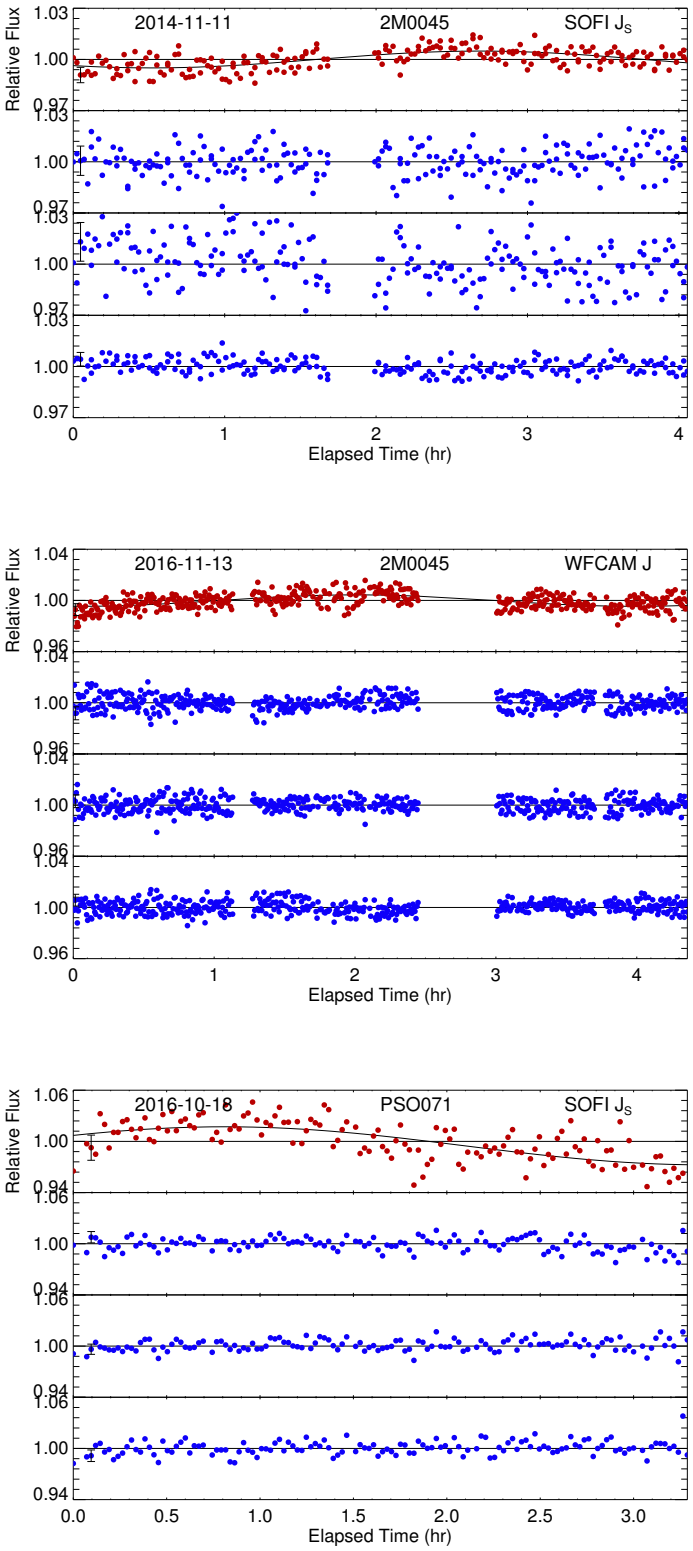

Figure 5.5 Lightcurves of variable targets (red) compared to a sample of reference stars in the field (blue).

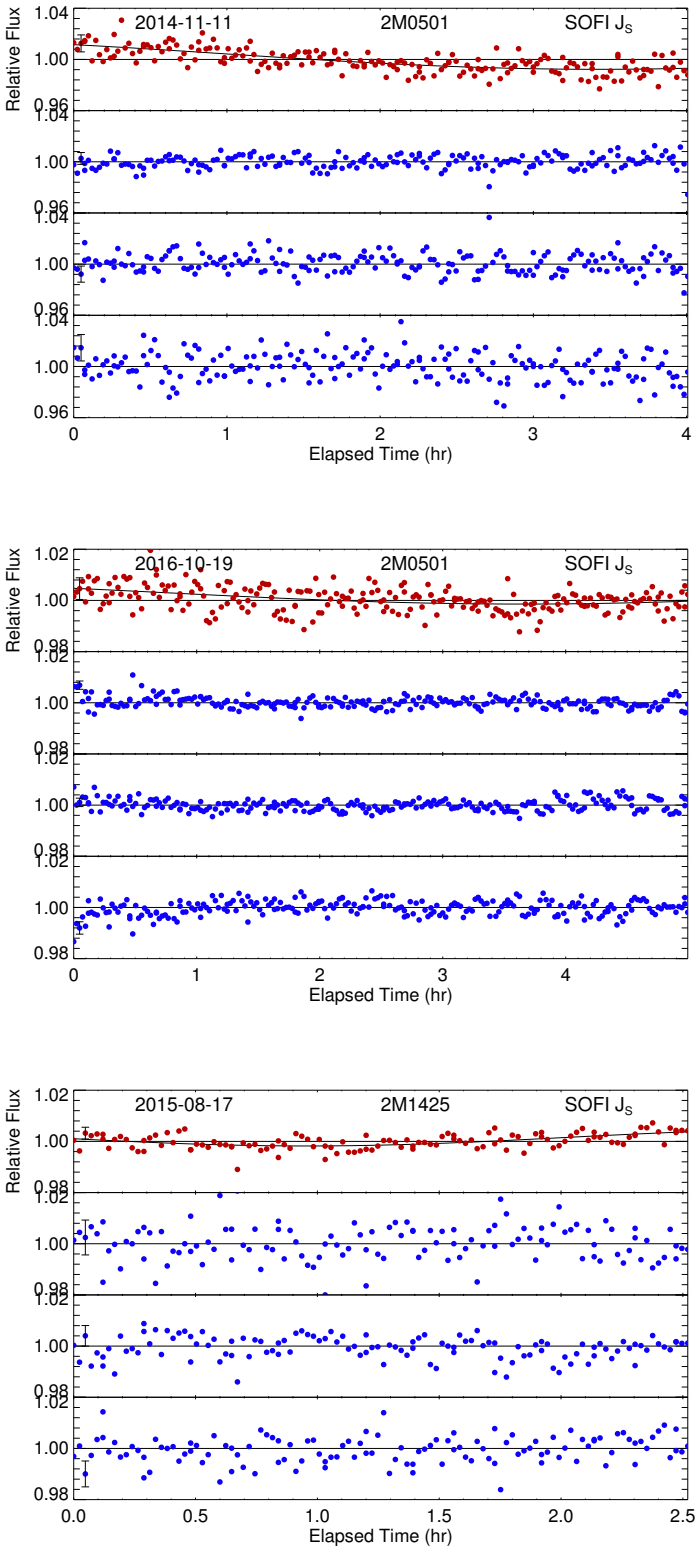

Figure 5.5 (Continued) Lightcurves of variable targets (red) compared to a sample of reference stars in the field (blue).

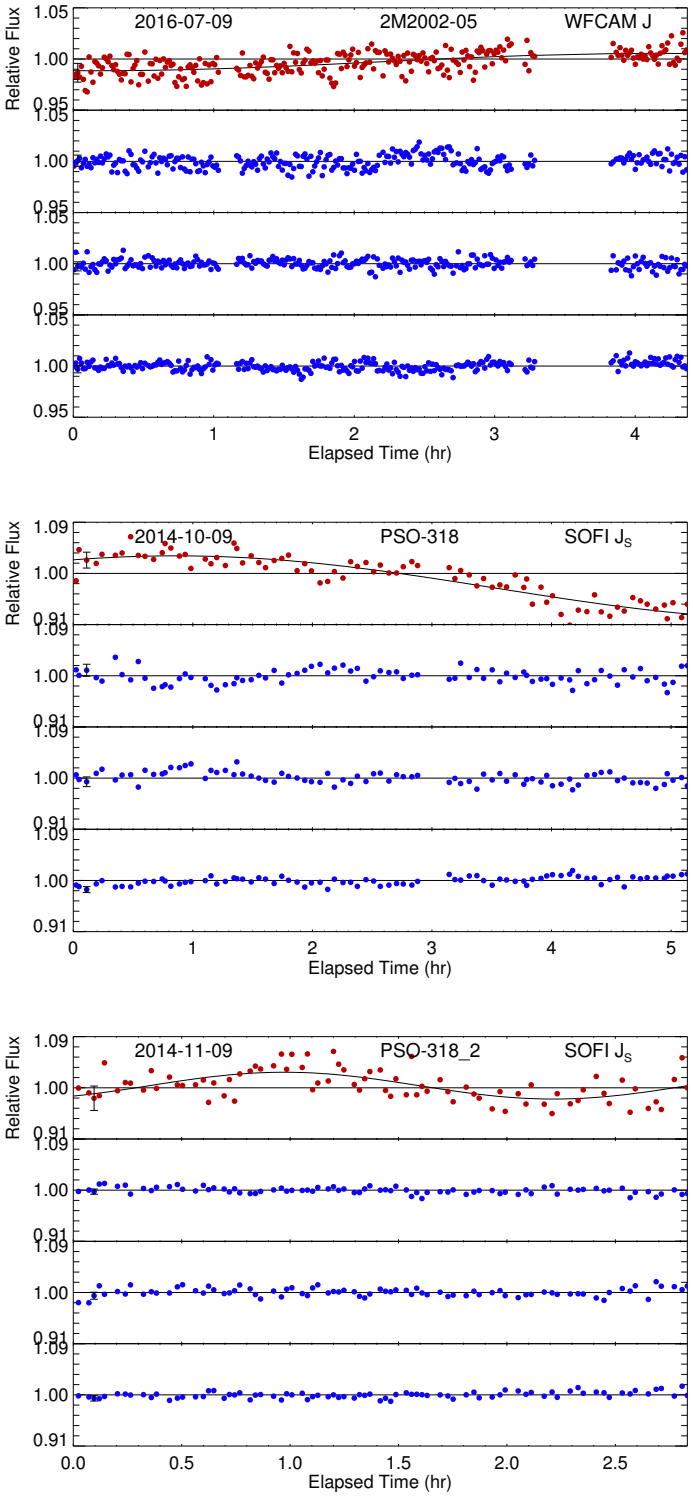

Figure 5.5 (Continued) Lightcurves of variable targets (red) compared to a sample of reference stars in the field (blue).

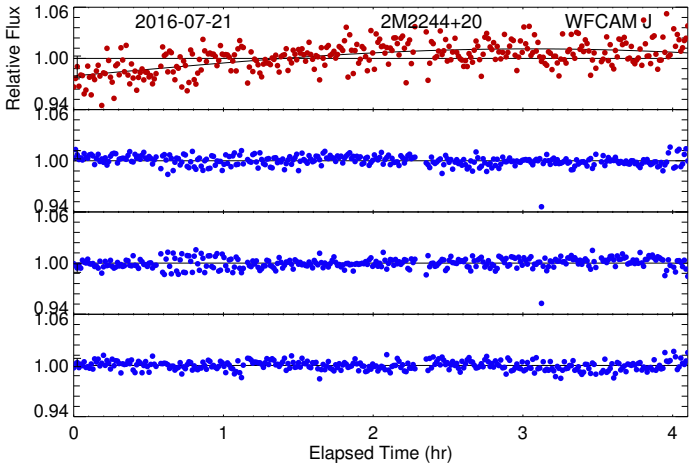

Figure 5.5 (Continued) Lightcurves of variable targets (red) compared to a sample of reference stars in the field (blue).

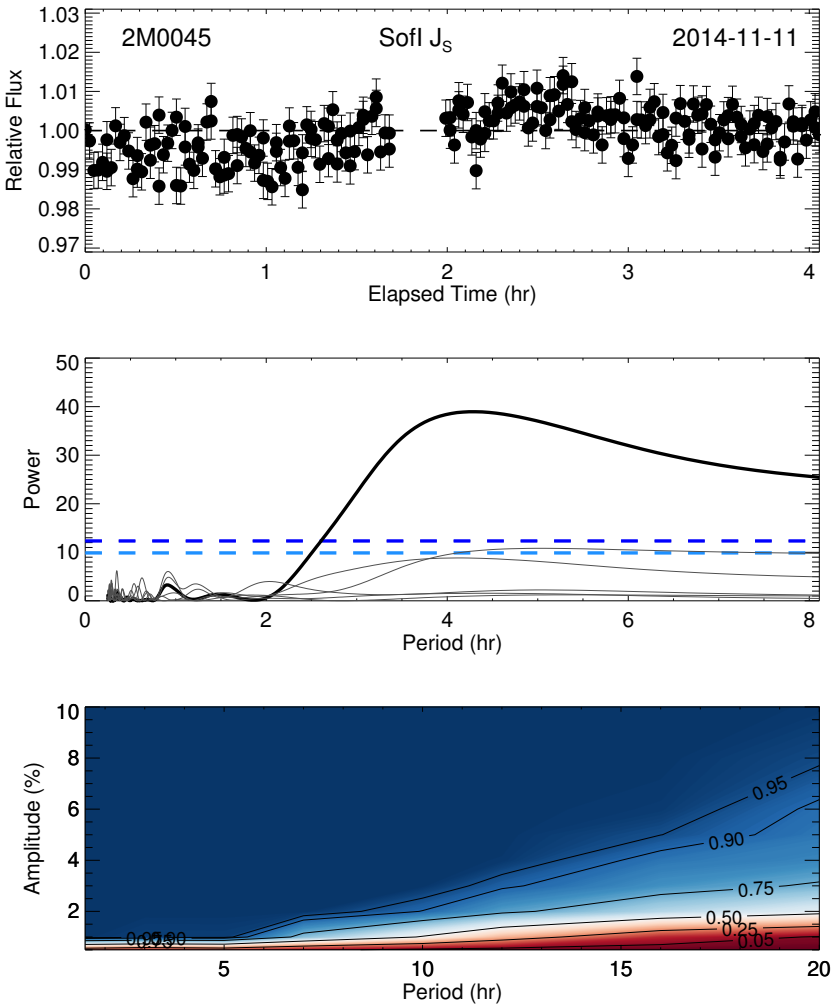

Figure 5.6 *Top panel:* Lightcurve of variable object 2M0045+16, observed on 2014-11-11. *Middle panel:* Periodogram of 2M0045+16 (black) and reference stars (grey). The 1% and 5% false-alarm probability thresholds are shown by the blue dashed lines. *Bottom panel:* Sensitivity plot showing the percentage of recovered signals as a function of amplitude and period.

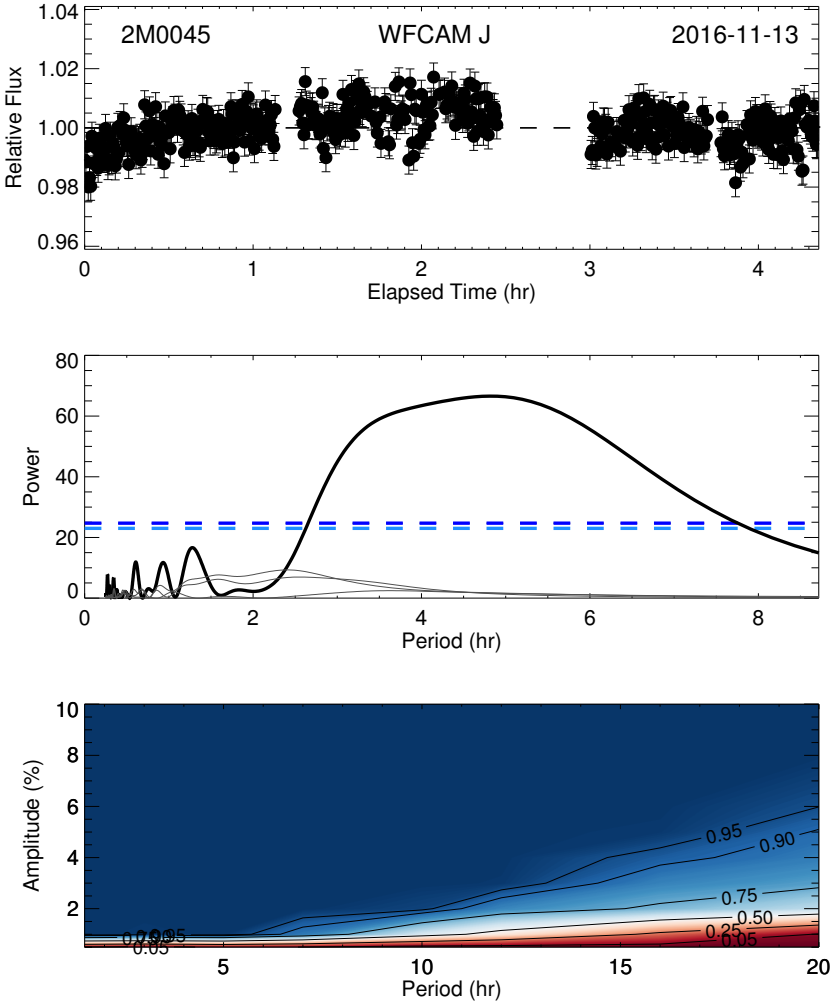

Figure 5.7 Same as Figure 5.6 but for the variable object 2M0045+16, observed on 2016-11-13.

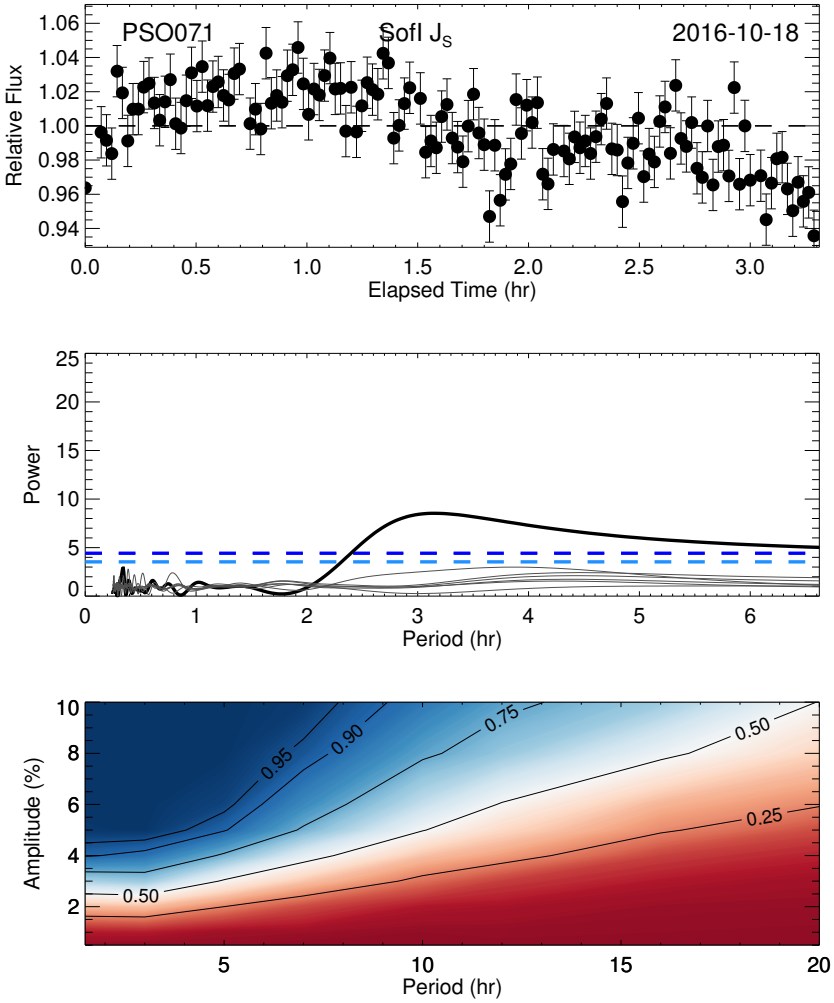

Figure 5.8 Same as Figure 5.6 but for the variable object PSO 071.8–12, observed on 2016-10-18.

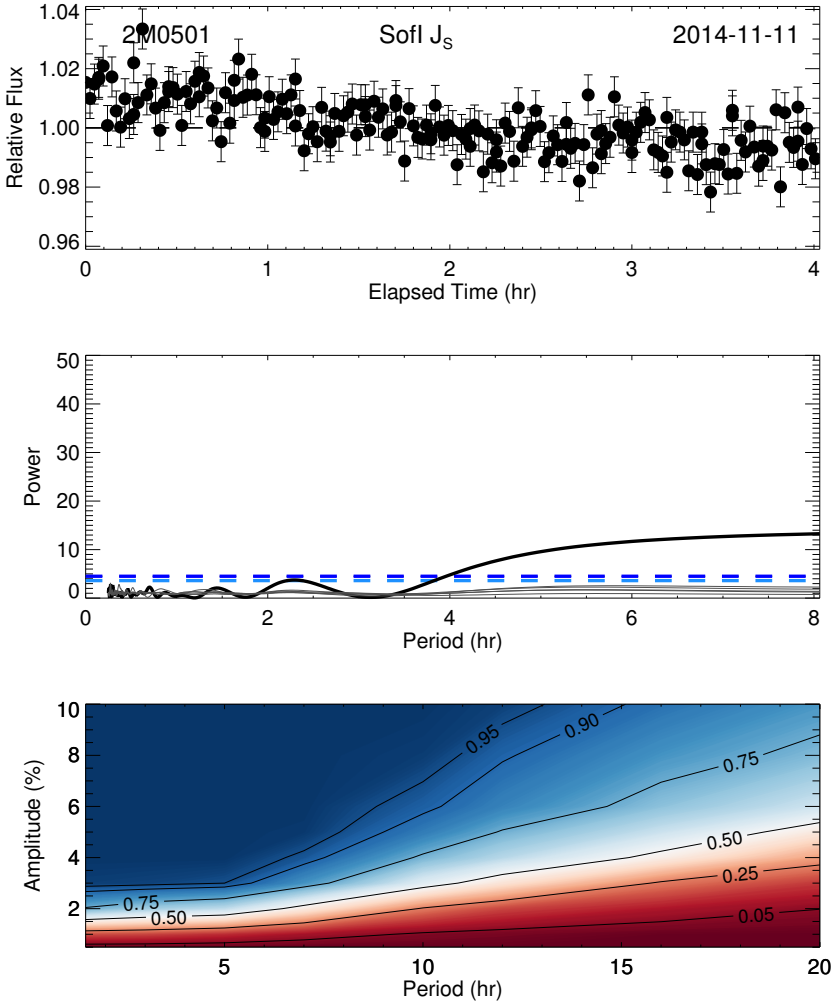

Figure 5.9 Same as Figure 5.6 but for the variable object 2M0501–00, observed on 2014-11-11.

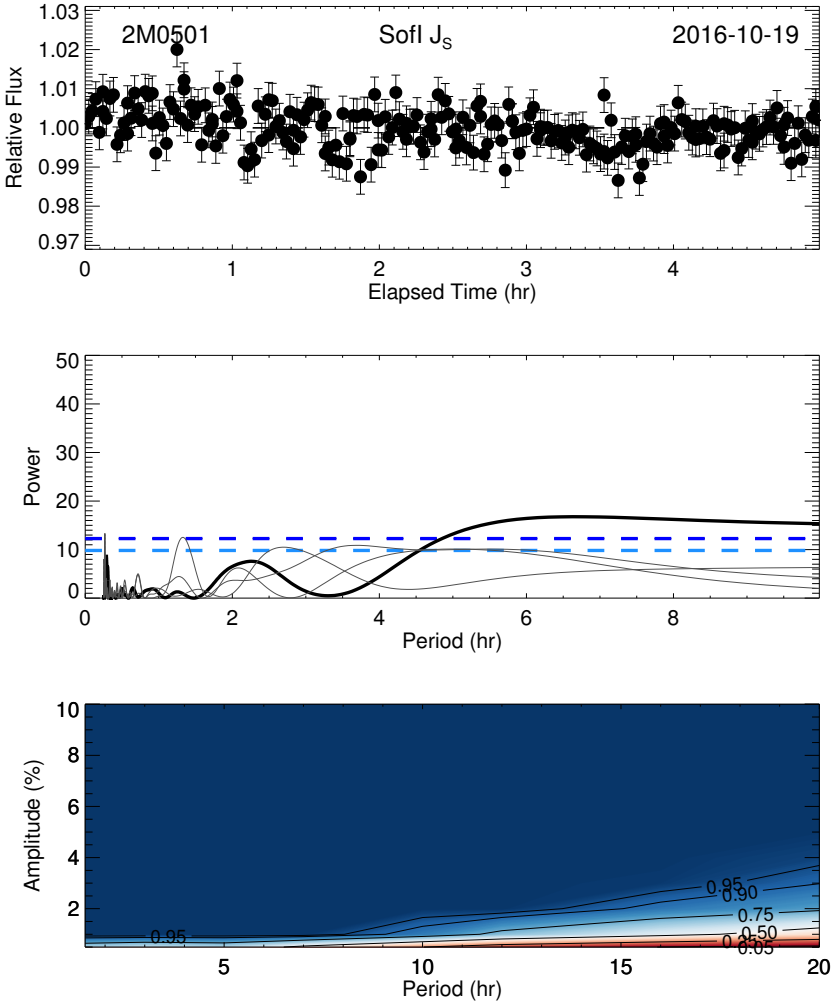

Figure 5.10 Same as Figure 5.6 but for the variable object 2M0501–00, observed on 2016-10-19.

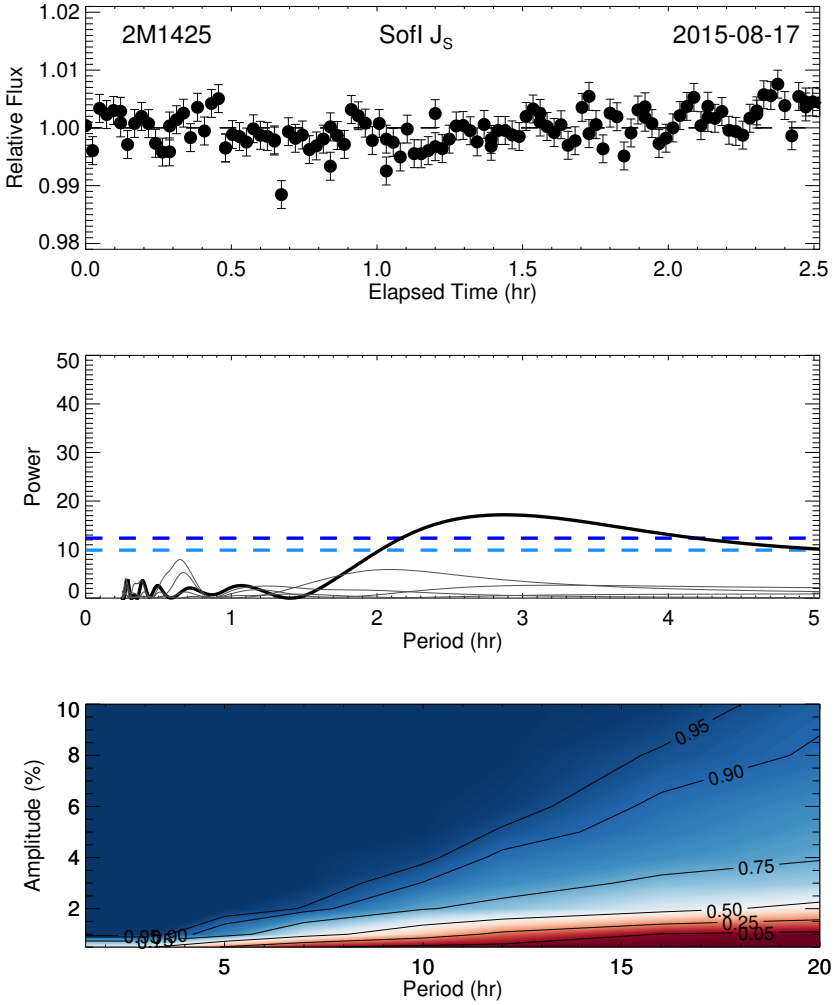

Figure 5.11 Same as Figure 5.6 but for the variable object 2M1425–36 observed on 2015-08-17.

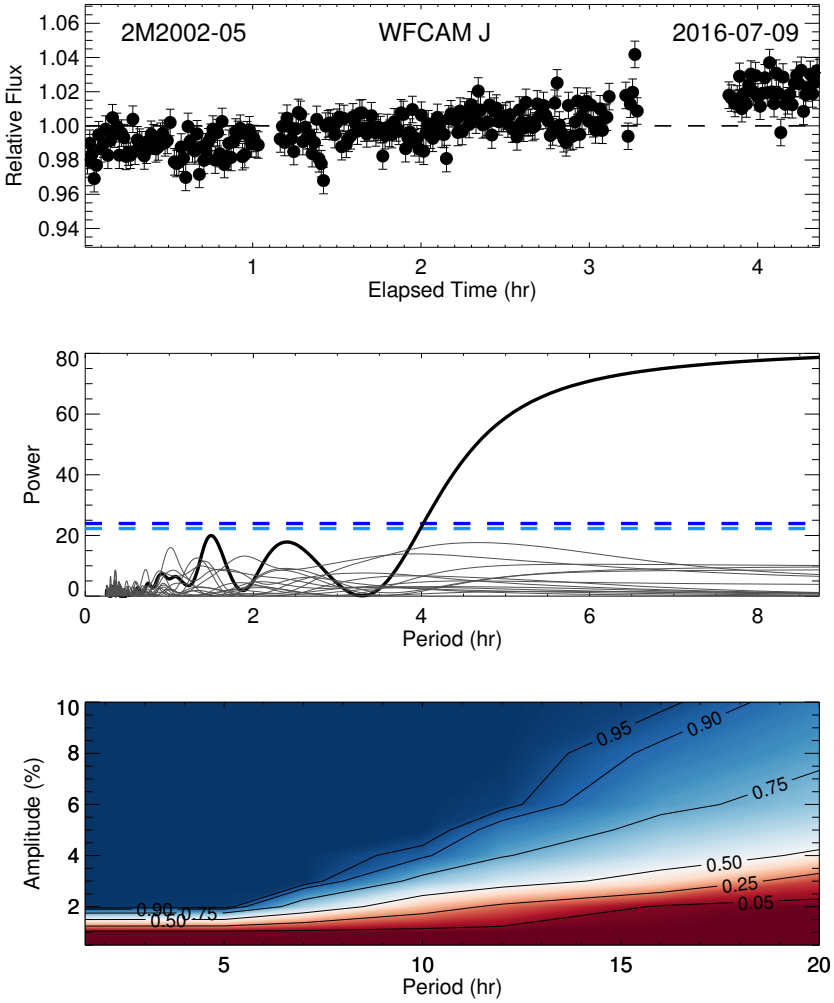

Figure 5.12 Same as Figure 5.6 but for the variable object 2M2002-05, observed on 2016-07-09.

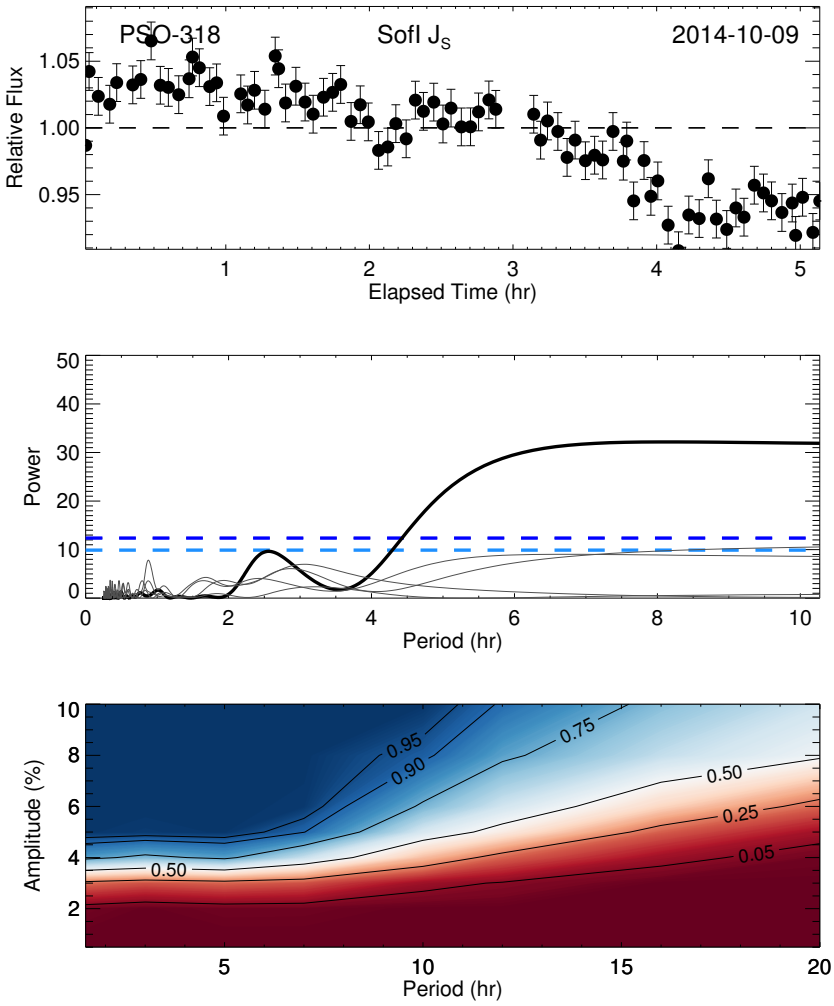

Figure 5.13 Same as Figure 5.6 but for the variable object PSO 318.5–22 observed on 2014-10-09.

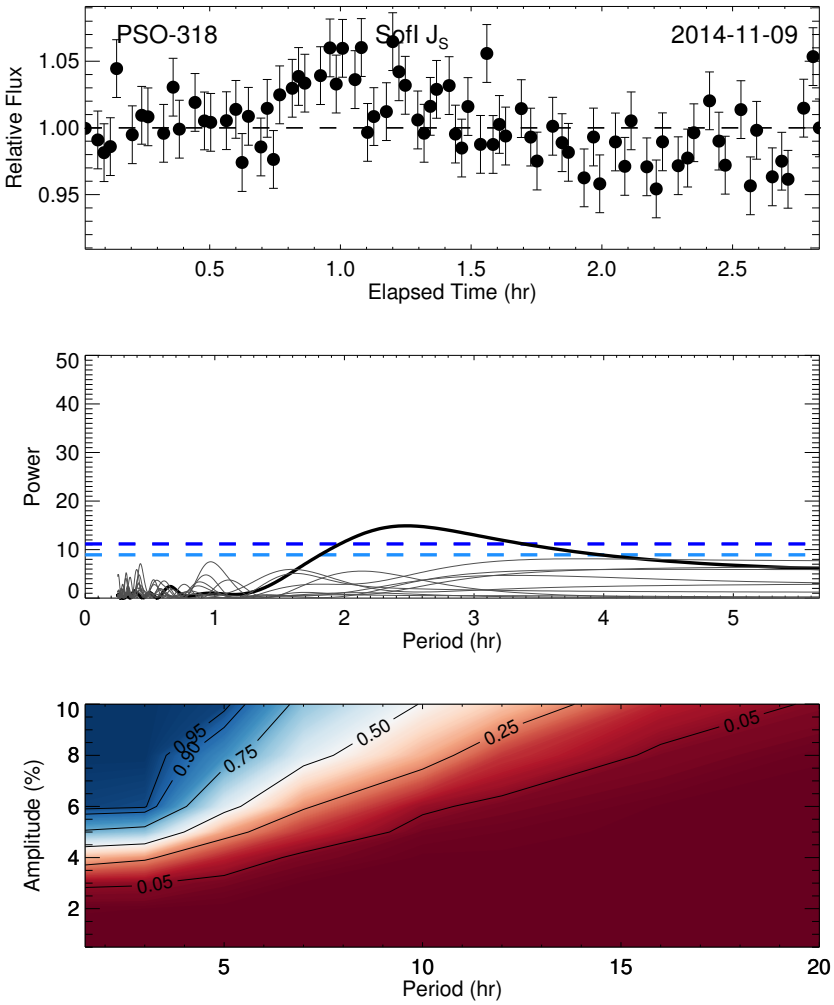

Figure 5.14 Same as Figure 5.6 but for the variable object PSO 318.5–22 observed on 2014-11-09.

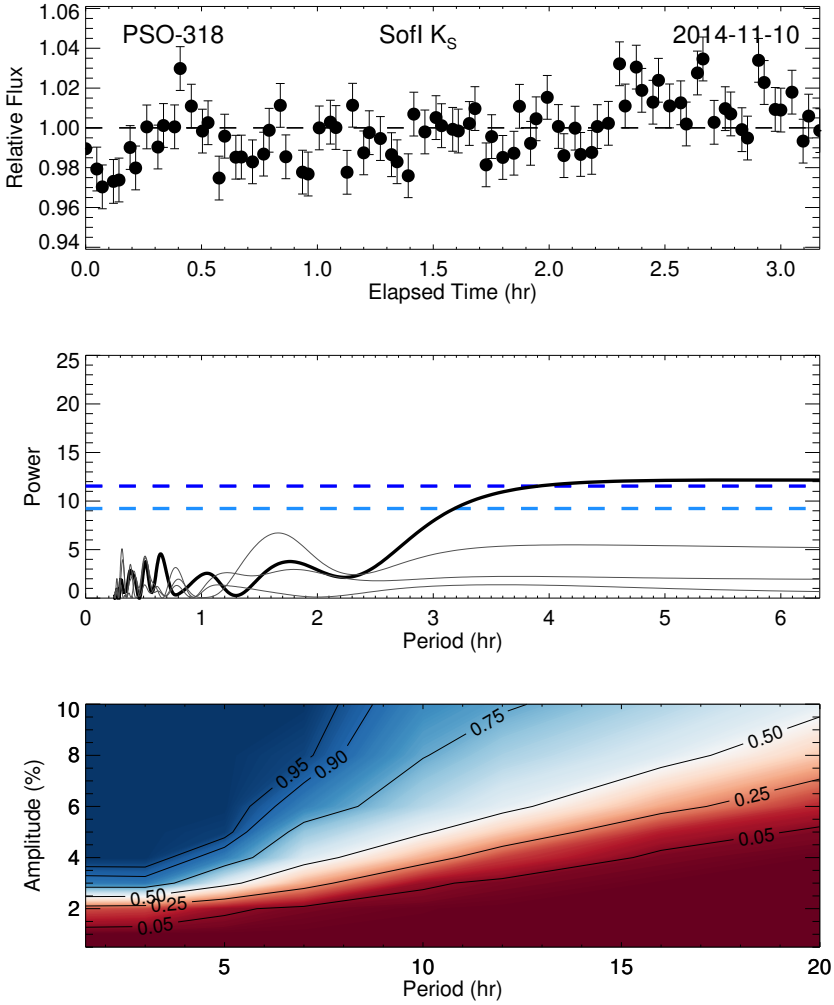

Figure 5.15 Same as Figure 5.6 but for the variable object PSO 318.5–22 observed on 2014-11-10.

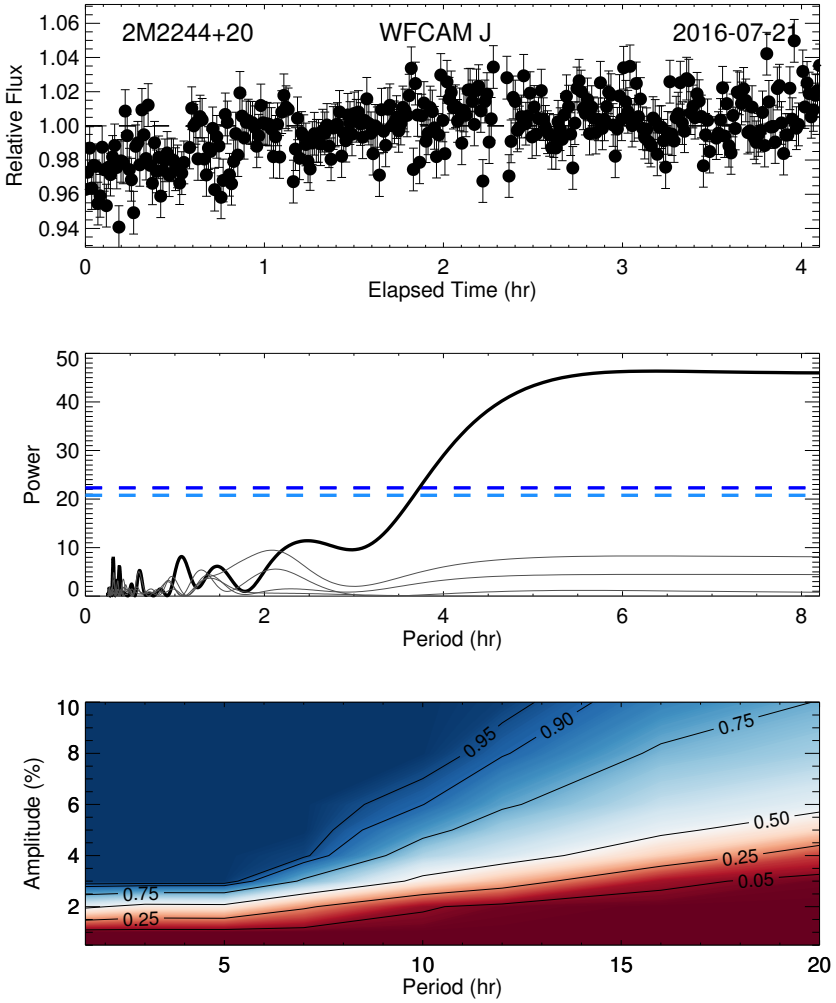

Figure 5.16 Same as Figure 5.6 but for the variable object 2M2244+20 observed on 2016-07-21.

Table 5.2 Measured first epoch variability amplitudes for variability detections.

Target	SpT	Amp (%)
2M0045+16	L2	1.0 ± 0.1
PSO 071.8–12	T2	4.5 ± 0.6
2M0501–00	L4	2 ± 1
2M1425–36	L4	0.7 ± 0.3
2M2002–05	L5-L7	1.7 ± 0.2
PSO 318.5–22	L7	10 ± 1.3
2M2244+20	L1	5.5 ± 0.6

2MASS J20025073−0521524 — 2M2002–05 is classified as a L5-L7 γ object by Gagné et al. (2015c), but has not been identified as a candidate of a young moving group (Faherty et al., 2016). Our UKIRT/WFCAM observation of this object taken on July 09 2016 shows significant variability. Fitting a sinusoid to the lightcurve we estimate an amplitude of $1.7 \pm 0.2\%$ and a period of 8 ± 2 hr, however these are very uncertain as we did not cover a full rotational period in this epoch.

PSO J318.5338−22.8603 — Allers et al. (2016) confirm the L7 PSO 318.5–22 as a member of the 23 ± 3 Myr (Mamajek & Bell, 2014) β Pictoris moving group. This implies a mass estimate of 8.3 ± 0.5 $M_{\rm Jup}$, placing PSO 318.5–22 clearly in the planetary-mass regime. The lightcurves of PSO 318.5–22 from 2014 are presented in Biller et al. (2015) and are also included in this paper in Figure 5.5. As discussed in Biller et al. (2015), we detect significant, high-amplitude variability in PSO 318.5–22 on October 9 2014. The periodogram in Figure 5.13 shows a highly significant peak for periods > 4.5 hr. A sinusoidal fit to the lightcurve gives a peak-to-peak amplitude of $10 \pm 1.3\%$ and a period of 10 ± 2 hr. We obtained two additional epochs of follow-up monitoring for PSO 318.5–22 as part of the variability survey and discuss these observations in Section 5.11.

2MASS J2244316+204343 — 2M2244+20 is a confirmed member of AB Doradus, with an estimated mass of ~ 19 $M_{\rm Jup}$ (Chapter 4; Vos et al., 2018). Morales-Calderon et al. (2006) and Vos et al. (2018) detect variability in the *Spitzer* 4.5 μm and 3.6 μm bands respectively. The J-band lightcurve obtained in this survey was initially presented in Chapter 4 (Vos et al., 2018), where we measured a period of 11 ± 2 hr for this object using *Spitzer* data. The UKIRT/WFCAM lightcurve obtained on July 21 2016 shows significant variability. The periodogram shown in Figure 5.16 shows a significant peak for periods > 4 hr. We set the period to 11 ± 2 hr (as measured in Chaper 4 in our least-squares sinusoidal fit and find an

amplitude of $5.5 \pm 0.6\%$ for this epoch.

5.8 Non-detections

We present light curves and reference star light curves of non-variables in Appendix A.1. Periodograms and sensitivity plots are shown in Appendix A.3. We discuss some of the noteworthy non-detections below.

2MASS J01033203+1935361 — 2M0103+19 has been assigned β and INT-G gravity classifications (Kirkpatrick et al., 2000; Faherty et al., 2012; Allers & Liu, 2013), however has not been assigned as a member of a young moving group. Metchev et al. (2015) obtained 21 hr of *Spitzer* monitoring, detecting variability in both the 3.6 μm and 4.5 μm bands. 2M0103+19 was observed to exhibit a regular periodic modulation with a period of 2.7 ± 0.1 hr. This short rotational period combined with variability amplitudes of $0.56 \pm 0.03\%$ and $0.98 \pm 0.09\%$ in the 3.6 μm and 4.5 μm bands respectively, would suggest that a J-band detection is likely for this object. Our observation taken on November 3 2014 shows no evidence of variability over a 5.3 hr observation. According to the sensitivity plot shown in Appendix A.3, we would have detected variability with an amplitude $> 2\%$ for a 2.7 hr period with a 90% probability.

GU Psc b — GU Psc b is a wide separation T3.5 planetary-mass companion to the young M3 star, a likely member of the AB Doradus moving group (Naud et al., 2014). Recently, Naud et al. (2017) reported results from a J-band search for variability in this object. Photometric variability with an amplitude of $4 \pm 1\%$ was marginally detected during one ~ 6 hr observation, with no significant variations observed at two additional epochs. The authors estimate a period > 6 hr as the lightcurve does not appear to repeat during this observation. With a magnitude of $J = 18.12$, GU Psc b is ~ 1 mag fainter than the other targets in our survey and we do not detect significant variability in its ~ 3.5 hr lightcurve. Looking at the sensitivity plot for GU Psc b shown in Figure A.3, we are not sensitive to variability with amplitudes $< 10\%$, and thus we cannot say whether the lightcurve has evolved from the variable epoch detected by Naud et al. (2017). While this remains a prime target for variability monitoring, long observations and high photometric precision will be needed to confirm and characterise its variability.

2MASS J16154255+4953211 — 2M1615+49 is identified as a young object by

Cruz et al. (2007); Kirkpatrick et al. (2008); Allers & Liu (2013), although it has not been identified as a member of a young moving group. Kirkpatrick et al. (2008) tentatively assign this object an age estimate of $\sim$ 100 Myr based on its optical spectrum. Metchev et al. (2015) obtained 21 hr of *Spitzer* 3.6 μm and 4.5 μm variability monitoring, finding significant variability in the 14 hr 3.6 μm sequence but not in the 7 hr 4.5 μm sequence. The authors estimate a period of $\sim$ 24 hr for 2M1615+49. We do not observe any significant variability in our UKIRT J-band observation of 2M1615+49 taken on Jul 10 2016. The sensitivity plot shown in Appendix A.3 indicates that we are not sensitive to periods longer than $\sim$ 10 hr, so it is unsurprising that we did not detect variability in this long-period variable.

HN Peg B — Discovered by Luhman et al. (2007), HN Peg B is a T2.5 dwarf companion to the 300 Myr old star HN Peg. Metchev et al. (2015) report significant variability in both the *Spitzer* 3.6 μm and 4.5 μm bands and estimate a period of $\sim$ 18 hr. We observed HN Peg B four times in total, twice with the NTT and with UKIRT, taking care to keep the primary HN Peg A off-frame. Although HN Peg A was kept off-frame for these observations, diffraction spikes still affected the quality of all of our observations. For our NTT data taken on October 8 2014 and August 7 2015, contaminated frames had to be removed from the lightcurve where the diffraction spikes coincided with the position of HN Peg B on the detector. For our UKIRT observations taken on July 11 2016 and July 13 2016 photometry from one nod position had to be removed from the data. Although the NTT lightcurves have lower $\sigma_{\rm pt}$, their short duration ($<$ 2.5 hr) means that they are insensitive to trends on timescales $>$ 5 hr. During two $\sim$ 5 hr observations with UKIRT, we do not detect any significant variability. Longer duration observations will be needed to characterise the variability of this young companion.

5.9 Assessing Evidence of Youth in the Sample

5.9.1 Analysing Sample Spectra

Our targets have been identified as potentially young in the literature, through indications of low-gravity in their spectra and/or identification as probable members of young moving groups (e.g. Cruz et al., 2009; Allers & Liu, 2013; Gagné et al., 2015c; Best et al., 2015). In this section, we consider gravity-sensitive features in the spectra of our targets. Cruz et al. (2009) present a spectral classification scheme for L0-L5 brown dwarfs that includes three gravity classes based on gravity sensitive features in their optical spectra. The three gravity subtypes α, β and γ, denote objects of normal gravity, intermediate gravity and very low gravity respectively. The δ suffix is used to designate objects with an even younger age (typically less than a few Myr) and lower surface gravity than those associated with the γ suffix (Kirkpatrick et al., 2006). Gagné et al. (2015c) use optically anchored IR spectral average templates for classifying the gravity subtype for L0-L9 dwarfs. This method assigns α, β and γ subtypes for each object. Allers & Liu (2013) present an index-based infrared gravity classification method that is based on FeH, VO, K I, Na I and H-band continuum shape in the IR. A score of 0 indicates that the feature is consistent with field gravity objects, 1 indicates intermediate gravity and 2 indicates very low gravity. A score of "n" is assigned if either the spectrum does not cover the wavelength range of the index or the feature is not gravity-sensitive at the object's spectral type. A score of "?" indicates that an index hints at low gravity, but the uncertainty in the calculated index is too large. The final gravity classification (FLD-G, INT-G, VL-G) is assigned based on the median of the individual gravity scores, ignoring "n" or "?" scores.

We present the spectral types, gravity subtypes and the specific signatures of low-gravity exhibited by each object in the sample in Table 5.3.

Table 5.3 Spectral Signatures of Youth in Sample

Name	SpT (Opt)	SpT (IR)	Grav Class	Grav Class Ref	AL13 Ind	AL13 Class	AL13 Ref	Signs of Youth[a]	Youth Ref
2MASS 00011217+1535355	...	L4	β	G15c	1211	INT-G	G15c	OTR	G15c
2MASS J00452143+1634446	L2	L2	β	G14	1221	VL-G	AL13	OITRH	G14
2MASS J01033203+1935361	L6	L6	β	G14	1n11	INT-G	AL13	OITR	G14
GU Psc b		T3.5	...	N14	...	...	...	RM	N14
2MASS J01174748-3403258	L2	L1	γ	G14	1121	INT-G	AL13	TRM	G14
2MASS J02340093-6442068	L0	L0	γ	G14	2211	VL-G	F16	OR	G14
2MASS J03032042-7312300	L2	...	γ	G14	...	...	...	OR	G14
2MASS J03101401-2756452		L5	γ	G14	...	...	...	RHL	G14
2MASS J03231002-4631237	L0	L0	γ	G14	2222	VL-G	F16	ORL	G14
2MASS J03264225-2102057	L5	L5	β/γ	G14, G15c	0n01	FLD-G	F16	RL	G14
2MASS J03421621-6817321	...	L0	γ	G14, G15c	...	...	...	R	G15c
PSO J057.2893+15.2433	...	L7	...	B15	...	...	...	R	B15
2MASS J03552337+1133437	L5	L3	γ	G14	2122	VL-G	G15c	OITRL	G14
2MASS J03572695-4417305	L0	M9+L1.5	β	G14	...	...		OR	G14
2MASS J04185879-4507413	...	L3	γ	G15c	2211	VL-G	G15c	OR	G15c
2MASS J04210718-6306022	L5	L5	γ	G14	0n11	INT-G	F16	OIRL	G14
PSO J071.8769-12.2713	...	T2	...	B15	...	...	...	...	...
2MASS J05012406-0010452	L4	L3	γ	G14	2112	VL-G	AL13	OTRL	G14
2MASS 05120636-2949540	L5	L5	β	G15c	1n01	INT-G	G15c	R	G15c
2MASS J05184616-2756457	L1	L1	γ	G15c	2222	VL-G	AL13	OITRU	G14
2MASS J05361998-1920396	L2	L2	γ	G14	2212	VL-G	AL13	OTR	G14
SDSS J111010.01+011613.1	...	T5.5		G15a	...	...	...	MR	G15a
2MASS J12074836-3900043	L0	L1	δ	G15c	2222	VL-G	G15c	OITR	G15c
2MASS J12563961-2718455	...	L4	β	G15c	2021	VL-G	G15c	TR	G15c

Table 5.3 – continued from previous page

Name	SpT (Opt)	SpT (IR)	Grav Class	Grav Class Ref	AL13 Ind	AL13 Class	AL13 Ref	Signs of Youth[a]	Youth Ref
2MASS 14252798-3650229	L3	L4	γ	G15c	11?1	INT-G	G15c	TR	G15c
2MASS J16154255+4953211	L4	L3	γ	G15c	2022	VL-G	AL13	OITRL	G14
WISE J174102.78-464225.5	...	L6-L8	γ	S14	...	...	...	ITRM	S14
PSO J272.4689-04.8036	...	T1	...	B15	...	...	...	...	...
2MASS J20025073-0521524	L5	L5-7	γ	G15c	–	–	F16	...	...
2MASS 20113196-5048112	...	L3	γ	G15c	2222	VL-G	G15c	OT	G15c
PSO J318.5338-22.8603	...	L7	γ	G15c	XXX2, 2X21	VL-G	L13	ITRM	G14
2MASS 21324036+1029494	...	L4	β	G15c	00?1	FLD-G	G15c	TR	G15c
HN Peg B		T2.5	...	L07	...	...	...	I	L07
SIMP J215434.5-105530.8	...	L4	β	G14	0n11	INT-G	G15c	ITR	G15c
2MASS J2244316+204343	L6.5	L6-L8	γ	G15c	2n21	VL-G	AL13	ITRLM	G14
2MASS J23225299-6151275	L0	L2	γ	G14	1221	VL-G	G15c	OR	G14

References: Allers & Liu (2013); Best et al. (2015); Faherty et al. (2016); Gagné et al. (2014c, 2015a,c); Liu et al. (2013); Naud et al. (2014); Luhman et al. (2007); Schneider et al. (2014)

[a] A capital letter means the object displays the associated sign of youth. O: lower-than normal equivalent width of atomic species in the optical spectrum, I: same but in the NIR spectrum, T: a triangular-shaped H-band continuum, R: redder-than-normal colors for given spectral type, U: over luminous, H: Hα emission, L: Li absorption, M: signs of low gravity from atmospheric models fitting.

5.9.2 Assessing Group Membership

Following a similar method to Faherty et al. (2016), we investigate the likelihood that each object in the survey is a member of a young moving group using four methods of assessing group membership using kinematic data; the convergent point analysis of Rodriguez et al. (2013), the BANYAN I tool of Malo et al. (2013), the BANYAN Σ method in Gagné et al. (2018b) and the LACEwING analysis of Riedel et al. (2017).

Convergent point analysis estimates the probability of membership using the perpendicular motion of the candidate member and the convergent point location of a given moving group, but does not take into account radial velocity or parallax. This method considers six potential moving groups: TWA, THA, β Pic, AB Dor, CarN and Col. BANYAN I uses a Bayesian statistical analysis to identify members of kinematic groups. BANYAN I minimally requires the position, proper motion, magnitude and colour of a star but radial velocity and distance measurements can be added. In addition to the groups considered by the convergent point analysis of Rodriguez et al. (2013), BANYAN I investigates membership in the Argus association. BANYAN Σ is a new Bayesian algorithm for identifying members of young moving groups that includes 27 young associations. This algorithm improves upon BANYAN I and II (Malo et al., 2013; Gagné et al., 2014c) by using analytical solutions when marginalising over radial velocity and distance, using multivariate Gaussian models for the young moving groups and removing several approximations in the calculation of Bayesian likelihood. BANYAN Σ does not include the Argus association in its analysis, as it is likely that this association suffers from a high level of contamination (Bell et al., 2015). Proper motions, radial velocities and parallaxes used in this analysis are shown in Table 5.4

The results of each membership tool should be evaluated differently. Malo et al. (2013) and Gagné et al. (2018b) use a threshold of 90% to confirm membership for the BANYAN I and Σ tools respectively. We use this threshold probability of 90% for the Convergent Point tool (Rodriguez et al., 2013). Riedel et al. (2017) find that a membership probability $> 66\%$ indicates a high membership likelihood using LACEwING.

Table 5.4 Kinematic Information of Variability Sample

Name	$\mu_\alpha \cos\delta$ (mas yr^{-1})	μ_δ (mas yr^{-1})	Ref	RV (km s^{-1})	Ref	π (mas)	Ref
2M0001+15	135.2 ± 10.7	-169.6 ± 13.7	F16	...	...	...	...
2M0045+16	355 ± 10	-40 ± 10	F16	3.16 ± 0.83	F16	65.9 ± 1.3	L16
2M0103+19	293.0 ± 4.6	27.7 ± 4.7	F12	...	...	46.9 ± 7.6	F12
GU Psc b	90 ± 6	-102 ± 6	N14	-1.6 ± 0.4	N14	...	...
2M0117–34	84 ± 15	-45 ± 8	F16	(3.96 ± 2.09)	F16	26.1 ± 1.9	L16
2M0234–64	88 ± 12	-15 ± 12	F16	11.762 ± 0.721	F16	(21 ± 5)	F16
2M0303–73	43 ± 12	3 ± 12	F16	...	...	...	...
2M0310–27	-119 ± 18	-47 ± 16	C08	...	...	...	..
2M0323–46	66 ± 8	1 ± 16	F16	13.001 ± 0.045	F16	(17 ± 3)	F16
2M0326–21	108 ± 14	-146 ± 15	F16	(22.91 ± 2.07)	F16	(41 ± 1)	F16
2M0342–68	65.3 ± 2.8	18.5 ± 9.1	F16	(13.87 ± 2.62)	F16	(21 ± 9)	F16
PSO 057.2+15	68 ± 11	-127 ± 12	B15	...	...	...	...
2M0355+11	225 ± 13.2	-630 ± 15	F16	11.92 ± 0.22	F16	109.5 ± 1.4	F16
2M0357–44	64 ± 13	-20 ± 19	F16	10.73 ± 4.6	F16	...	...
2M0418–45	53.3 ± 8.4	-8.2 ± 12.6	F16	...	...	...	...
2M0421–63	146 ± 8	191 ± 18	F16	14.7 ± 0.33	F16	...	...
PSO 071.8–12	20 ± 19	-89 ± 19	B15	...	...	...	...
2M0501–00	190.3 ± 9.5	-142.8 ± 12.5	F16	21.77 ± 0.66	F16	48.4 ± 1.4	F16
2M0512–29	-10 ± 13	80 ± 15	F16	...	...	...	...
2M0518–27	28.6 ± 4.2	-16 ± 4	F16	24.35 ± 0.19	F16	18.4 ± 1.1	F16
2M0536–19	24.6 ± 5.3	-30.6 ± 5	F16	22.065 ± 0.695	F16	21.1 ± 1.6	F16
SDSS 1110+0	-217.1 ± 0.7	-280.9 ± 0.6	G15a	7.5 ± 3.8	G15a	52.1 ± 1.2	D12
2M1207–39	-57.2 ± 7.9	-24.8 ± 10.5	F16	(9.48 ± 1.91)	F16	(15 ± 3)	F16
2M1256–27	-67.4 ± 10.2	-56.5 ± 12.7	F16	...	...	...	...

Table 5.4 – continued from previous page

Name	$\mu_\alpha \cos\delta$ (mas yr^{-1})	μ_δ (mas yr^{-1})	Ref	RV (km s^{-1})	Ref	π (mas)	Ref
2M1425–36	-284.89 ± 1.4	-463.08 ± 1	F16	5.37 ± 0.25	F16	86.45 ± 0.83	F16
2M1615+49	-80 ± 12	-18 ± 12	F16	-25.59 ± 3.18	F16	32 ± 1	L16
WISE 1741–46	-20.4 ± 9.2	-343 ± 13.7	F16	-5.7 ± 5.1	F16	...	...
PSO 272.4–04	-46 ± 4	-400 ± 13	B15	...	...	...	...
2M2002–05	-98 ± 5	-110 ± 8	F16	...	...	...	...
2M2011–50	21.3 ± 8.1	-71.3 ± 14.5	F16	...	...	...	...
PSO 318.5-22	137.3 ± 1.3	-138.7 ± 1.4	F16	-6.0 ± 0.95	A16	45.1 ± 1.7	L16
2M2132+10	107.8 ± 16.4	29.7 ± 18.1	F16	...	...	...	...
HN Peg B				...	...	...	...
SIMP 2154–10	175 ± 12	9 ± 12	F16	...	...	32.6 ± 1.0	L16
2M2244+20	252 ± 14	-214 ± 11	F16	-16.0 ± 0.85	V17	58.7 ± 1.0	L16
2M2322–61	62 ± 10	85 ± 9	F16	6.747 ± 0.75	F16	(22 ± 1)	F16

References: C08: Casewell et al. (2008) D12: Dupuy & Liu (2012) G15a: Gagné et al. (2015a) F12: Faherty et al. (2012) F16: Faherty et al. (2016) N14: Naud et al. (2014) V17: Vos et al. (2017)

Table 5.5 Moving Group Membership Probabilities

Name	Convergence[a]	P(%)	BANYAN I	P(%)	BANYAN Σ	P(%)	LACEwING	P(%)	Mem[b]	Decision[c]
2M0001+15	AB Dor	43.2	AB Dor	99.04	AB Dor	76.0	AB Dor	46	AM	Young
2M0045+16	CarN	74.2	Arg	99.97	CarN	89.0	Argus	99	AM	Young
2M0103+19	CarN	15.7	Old	96	Field	76.1	βPic	44	AM	Young
Gu Psc b	ABDor	99.5	ABDor	99.88	ABDor	89	ABDor	82	BM	Young
2M0117-34	THA	99.6	THA	92.4	THA	79.3	THA	51	AM	Young
2M0234-64	THA	79.5	THA	99.99	THA	96.3	THA	86	HLM	Young
2M0303-73	THA	97.6	Old	92.5	FLD	99.9	None	0	NM	Young
2M0310-27	CarN	99.9	Old	100	FLD	99.9	None	0	AM	Young
2M0323-46	THA	92.1	THA	99.97	THA	51.2	THA	41	AM	Young
2M0326-21	ABDor	65.8	ABDor	99.37	ABDor	91.9	AB Dor	55	AM	Young
2M0342-68	THA	98.3	THA	98.4	THA	67.7	None	0	AM	Young
PSO 057.2+15	ABDor	82.4	βPic	65.19	ABDor	67.2	None	0	AM	Uncertain
2M0355+11	ABDor	17.5	ABDor	99.99	ABDor	99.9	AB Dor	100	BM	Young
2M0357-44	THA	62.1	THA	53.07	Field, THA	66.6, 17.5	THA	39	AM	Young
2M0418-45	ABDor	91.5	ABDor	64	ABDor	41.9	AB Dor	24	AM	Young
2M0421-63	βPic, CarN	95.8, 95.9	βPic	92.8	CarN	93.8	CarN	38	AM	Young
PSO 071.8-12	ABDor	77.8	ABDor	62.7	ABDor	56.5	Col	32	AM	Uncertain
2M0501-00	THA	98.7	Old	99.86	Field	99.9	AB Dor	70	AM	Young
2M0512-29	CarN	5.5	Old	89.49	Field	99.9	None	0	NM	Young
2M0518-27	CarN	22.1	Col	86.5	βPic	62.7	Col	77	AM	Young
2M0536-19	βPic	77.5	βPic	57.28	βPic	81.1	Col	52	AM	Young
SDSS1110+01	ABDor	17.2	ABDor	99.91	ABDor	99.3	AB Dor	46	BM	Young
2M1207-39	βPic, TWA	100, 91.6	TWA	99.14	TWA	91.6	TWA	98	HLM	Young
2M1256-27	ABDor	75.8	TWA	99.14	Field	99.8	None	0	AM	Young

Table 5.5 – continued from previous page

Name	Convergence[a]	P(%)	BANYAN I	P(%)	BANYAN Σ	P(%)	LACEwING	P(%)	Mem[b]	Decision[c]
2M1425-36	ABDor	39.3	ABDor	99.98	ABDor	99.7	AB Dor	100	BM	Young
2M1615+49	ABDor	59.3	ABDor	95.12	ABDor	84.0	AB Dor	68	AM	Young
WISE 1741-46	βPic, ABDor	94.1, 91.8	βPic	99.88	ABDor, βPic	52.7, 45.9	AB Dor	71	AM	Young
PSO 272.4-04	TWA	61.8	ABDor	86.45	ABDor	89.0	AB Dor	29	AM	Uncertain
2M2002-05	None	0	Old	100	Field	99.9	None	0	NM	Young
2M2011-50 2	Col	96.5	THA	66.53	Field	72.2	None	0	AM	Young
PSO 318.5-22	βPic	98.9	βPic	99.99	βPic	99.6	β Pic	69	BM	Young
2M2132+10	CarN	92.8	Arg	53.44	Field	99.9	None	0	AM	Young
HN Peg B	...	...	...	...	...	...	...	...	...	Young
SIMP 2154-10	CarN	28.8	Old	89.97	CarN	71.4	None		AM	Young
2M2244+20	ABDor	68.9	AB Dor	99.99	ABDor	99.8	AB Dor	100	BM	Young
2M2322-61	THA	34.1	THA	99.78	THA	79.7	THA	97	AM	Young

Notes:

[a] Moving groups: AB Dor: AB Doradus, Arg: Argus, β Pic: β Pictoris, CarN: CarN, Col: Col, THA: Tucana-Horologium, TWA: TW Hydrae.

[b] BM: bona fide member, HLM: high-likelihood member, AM: ambiguous member, NM: non-member.

[c] Final decision based on spectral signatures of youth, membership probabilities and colour-magnitude diagrams. Young: Object is a high likelihood member of a young-moving group and/or has clear indications of youth in its IR and/or optical spectrum. Uncertain: This object does not have sufficient evidence of youth and is thus excluded from the final statistical sample.

We present the results of each method in Table 5.5. To assess the membership probability of each object based on the results of the kinematic analysis, we use the categories outlined in Faherty et al. (2016):

1. *Non-member* (NM): an object that is rejected from nearby associations due to its kinematics.

2. *Ambiguous member* (AM): an object requiring higher precision kinematics because it is classified as a candidate to more than one group or cannot be differentiated from field objects.

3. *High-likelihood member* (HLM): an object that does not have full kinematic information (proper motion, radial velocity and parallax) but is regarded as high confidence ($> 90\%$ for BANYAN I, BANYAN Σ and Convergent Point analysis, $> 66\%$ in LACEwING) in at least three out of four algorithms.

4. *Bona fide member* (BM): an object regarded as a high-likelihood member with full kinematic information.

Faherty et al. (2016) carried out this analysis on a larger sample of potential young objects, using convergent point analysis, BANYAN I, BANYAN II and LACEwING. Our results, which substitutes BANYAN Σ for BANYAN II, are mostly consistent with those found in Faherty et al. (2016) with a few exceptions. 2M0303–73 drops from an ambiguous member of Tucana-Horologium in Faherty et al. (2016) to a non-member in our analysis. 2M0045+16 had been previously identified as a bona fide member of Argus (Faherty et al., 2016), however given the uncertainty in the Argus group, Gagné et al. (2018b) excluded this group from the analysis. The convergent point method and LACEwING assign it to the Argus association while BANYAN I and Σ assign it to the Carina-Near association. The object 2M0117–34 drops from a high-likelihood member to an ambiguous member. Compared to analysis in Faherty et al. (2016), we include a parallax measurement from Liu et al. (2016) for this object. All moving group tools favour the Tucana-Horologium association, however BANYAN Σ and LACEwING probabilities are below 90% and 66% respectively. 2M0323–46, 2M0342–68 and 2M2322–61 all drop from a high-likelihood member to an ambiguous member due to lower membership probabilities calculated in BANYAN Σ compared to BANYAN II. 2M0326–21 is classified as an ambiguous member of AB Doradus because the Convergent Point tool and LACEwING predict membership probabilities of 66% and 55% respectively. As can be seen in Table 5.5, our sample is composed

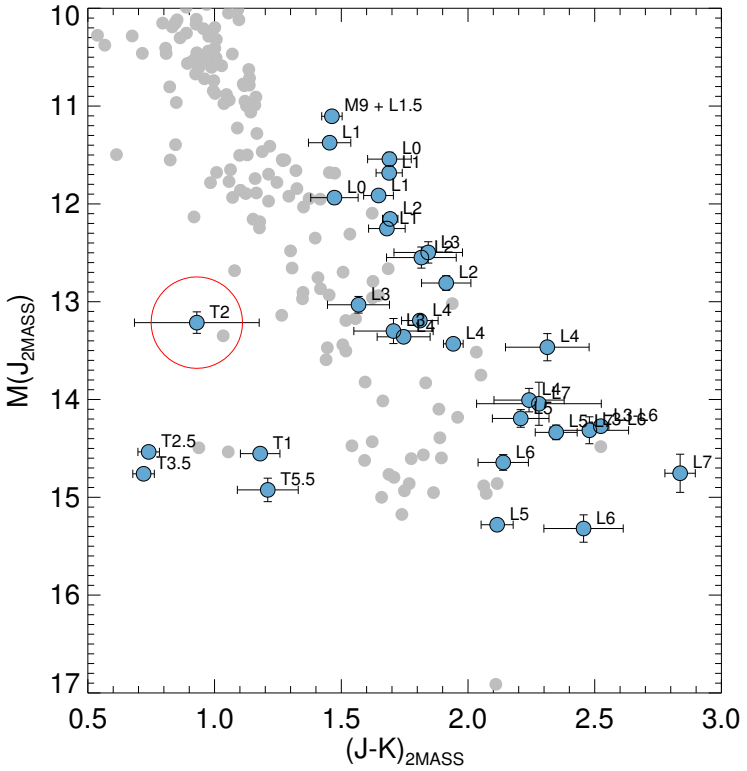

Figure 5.17 $J - K_S$ colour-magnitude diagram showing the field brown dwarf population (grey points) and our full sample of objects showing signs of low-gravity. Absolute magnitudes were calculated either using measured parallaxes or kinematic distances. From this analysis it is clear that the T2 object PSO 071.8-12 (shown in red circle) is an outlier in the sample. Assuming AB Doradus membership for PSO 071.8-12 results in magnitudes that are $\sim$ 1 mag brighter than other T dwarfs in the field and young populations.

of six bona fide members, two high-likelihood members, twenty-four ambiguous candidates and three non-members.

We additionally look at our sample on a colour-magnitude diagram to check that they follow the general trends seen in intermediate and low-gravity objects to date (Liu et al., 2016; Faherty et al., 2016). Many objects in the sample have measured parallaxes from Dupuy & Liu (2012); Faherty et al. (2012, 2016); Liu et al. (2016). When parallaxes were not available we used their estimated distance from kinematic group membership. We plot absolute magnitude against colour in Figures 5.17 and 5.18. Overall, the survey objects appear redder and more luminous than the field brown dwarf population, as seen in a larger sample of young objects by Liu et al. (2016). However the object PSO 071.8–12,

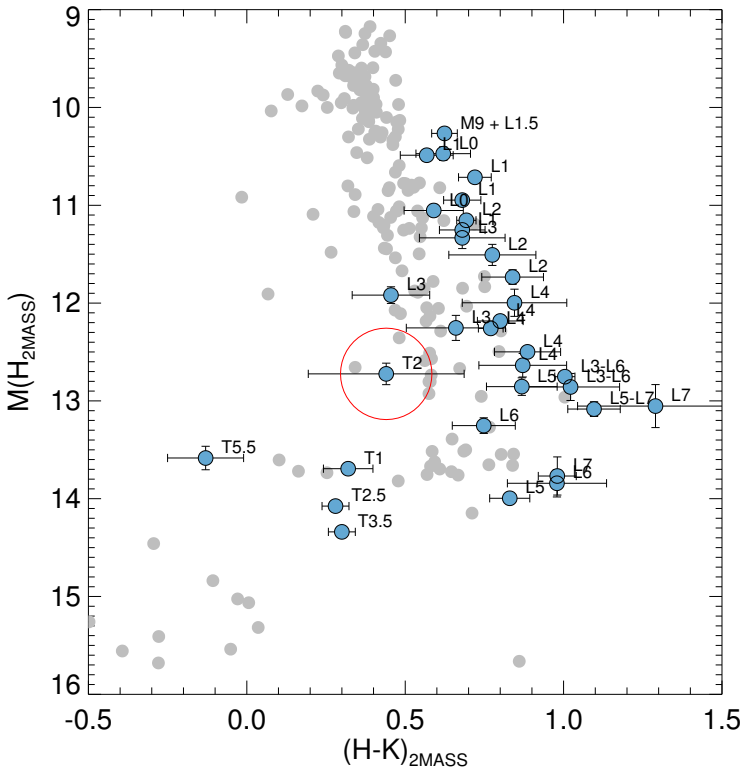

Figure 5.18 Same as Figure 5.17 but showing the $H - K_S$ colour-magnitude diagram. The T2 object PSO 071.8-12 appears as an outlier in the diagram.

shown by red circle in Figures 5.17 and 5.18, appears to be an outlier in this sequence. PSO 071.8–12 was discovered by Best et al. (2015), who find that it is a high probability candidate of β Pictoris using BANYAN II. However, our group membership assigns PSO 071.8–12 a moderate probability candidacy of the AB Doradus moving group, with very low probability candidacy to β Pictoris. The estimated kinematic distance of 45 ± 7 pc assuming AB Doradus membership results in an absolute magnitude that is $\sim$ 1 mag brighter than both T-type field brown dwarfs and T-type low-gravity objects. This over-luminosity could be explained is PSO 071.8–12 is a binary. If PSO 071.8–12 is not a binary then we estimate that PSO 071.8–12 must lie at a distance of $\sim 20 - 30$ pc, and thus is not a member of AB Doradus. Intriguingly, β Pic membership would imply a distance of 19 ± 4 pc according to BANYAN Σ, which would result in magnitudes consistent with other T dwarfs. More kinematic data and/or a high-resolution spectrum are needed to robustly assess the binarity and youth of PSO 071.8–12.

Combining the available kinematic information and spectral information for each target in the survey, we make a final call on whether the objects presented in Tables 5.3 and 5.5 are likely low-gravity. We exclude 3 objects from the original survey on the basis that there is insufficient evidence of youth. These objects are classified as 'Uncertain' in Table 5.5. We discuss the excluded objects below. The object PSO 057.2+15 is excluded from the survey. This L7 object appears redder than the field population (Best et al., 2015), but a high-resolution spectrum is not yet available for analysis of gravity sensitive features. The moving group tools suggest possible membership in AB Doradus or β Pictoris but are not consistent with each other. Updated kinematics and/or spectral analysis are needed to confirm the possible youth of this object. We thus exclude PSO 057.2+15 from the 'Young' sample. PSO 272.4–04 is a low-probability AB Doradus member using 3/4 membership tools. Since it has no available spectrum, its gravity sensitive features have not been analysed. We thus exclude it from the 'Young' sample. PSO 071.8–12 has uncertain status, as discussed above, and we thus exclude it from the final statistical analysis of the survey. We additionally exclude the binary 2M0357–44 from the final survey. Although 2M0357–44 is likely young (Cruz et al., 2009; Gagné et al., 2015b), we have a reduced likelihood of detecting variability in either component of the binary, since the non-variable component would effectively dilute the variability signal. 2M2322–61 and 2M0412–63 are also left out of the survey because they were observed during poor weather conditions which prohibited us from determining meaningful constraints on their variability properties. Their lightcurves are shown in Section A.2. In total we exclude 6

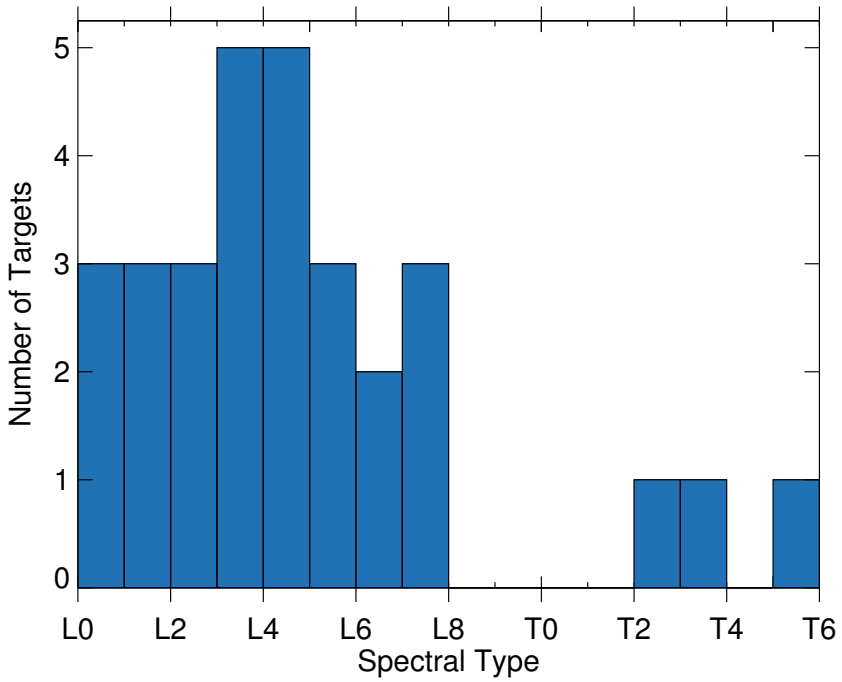

Figure 5.19 Histogram showing the distribution of spectral types in our final sample of 30 low-gravity brown dwarfs.

objects that we observed in our survey from the final sample of 30 young, low-gravity objects used in our analysis. We show the distribution of spectral types in our 30 object sample in Figure 5.19.

5.10 Variability Statistics

Figure 5.20 shows the spectral type of our sample plotted against the colour. Blue symbols correspond to variability detections, where the symbol size is proportional to the variability amplitude. Although many of our measured variability amplitudes are only a lower limit estimate, we see evidence for increasing J-band amplitude along the L sequence, something that is noted in Metchev et al. (2015) for mid-IR variability.

We find that 6/30 (20%) of objects in the full statistical sample exhibit significant variability, similar to the 9/57 (16%) reported by Radigan et al. (2014) for a similar high-gravity sample of field dwarfs. However, with only three young objects with spectral types >L8 included in our sample, we are lacking in L/T transition and T spectral type objects compared to the Radigan et al. (2014) and

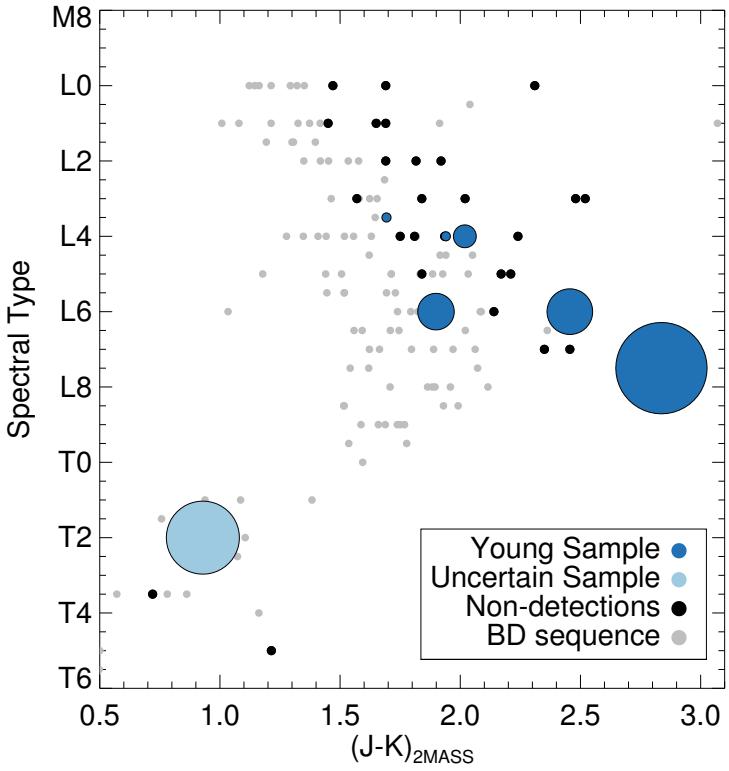

Figure 5.20 Spectral type of variable objects plotted against $(J-K)_{2\mathrm{MASS}}$ colour. Blue symbols represent young objects displaying significant photometric variability, where the radius is proportional to the variability amplitude. Dark blue symbols denote the objects that are highly likely to be young while light blue circles denote objects whose youth is more uncertain.

Radigan (2014) samples and thus we cannot obtain a robust comparison between the low-gravity and high-gravity populations as a function of spectral type. We thus consider objects with spectral types of L0-L8.5 in both samples. We find that 6/27 of L0-L8.5 low-gravity objects appear variable while Radigan (2014) report 2/34 variables in the field brown dwarf sample of L0-L8.5 objects

To calculate the overall variability occurrence rate of both samples, we use a modified version of the QMESS code (Bonavita et al., 2013, 2016) – a grid-based, non-Monte Carlo simulation code that uses direct-imaging sensitivity plots to estimate the frequency of giant planets. This code is based on the method described in Lafreniere et al. (2007) and estimates the fraction of planetary-mass objects that display variability using the sensitivity plots obtained for each observation and confirmed variability detections in the survey. For the Radigan (2014) sample, we use the average sensitivity plot from the Radigan et al. (2014) survey. This is reasonable since the reported photometric precision and observation lengths are comparable for both surveys (Radigan, 2014). We assume a flat prior on the variability occurrence rate and use uniformly distributed rotational periods of $1.5 - 20$ hr and variability amplitudes of $0.5 - 10\%$. The probability density function (PDF) of the variability occurrence rates for the 'Young' sample (Table 5.5) and field brown dwarf sample (Radigan, 2014) are plotted in Figures 5.21 and 5.22. For the low-gravity sample analysed in this work, we find a variability occurrence rate of $30^{+16}_{-8\%}$, which is higher than the rate of $11^{+13}_{-4}\%$ that we find for the Radigan (2014) survey. Thus we have found the first quantitative indication that the L-type low-gravity objects are more likely to be variable than the higher mass field dwarf counterparts.

We additionally employ a second method to analyse how statistically significant the correlation between low-gravity and frequent variability is. To do this we use a Bayesian framework to analyse the 2×2 contingency table shown in Table 5.6, following the method described by Biller et al. (2011) to determine the probability that the samples are drawn from different distributions. We denote y_1 as the number of young objects with detected variability and y_2 as the number of field objects with detected variability. We model the number of variable objects as a binomial function:

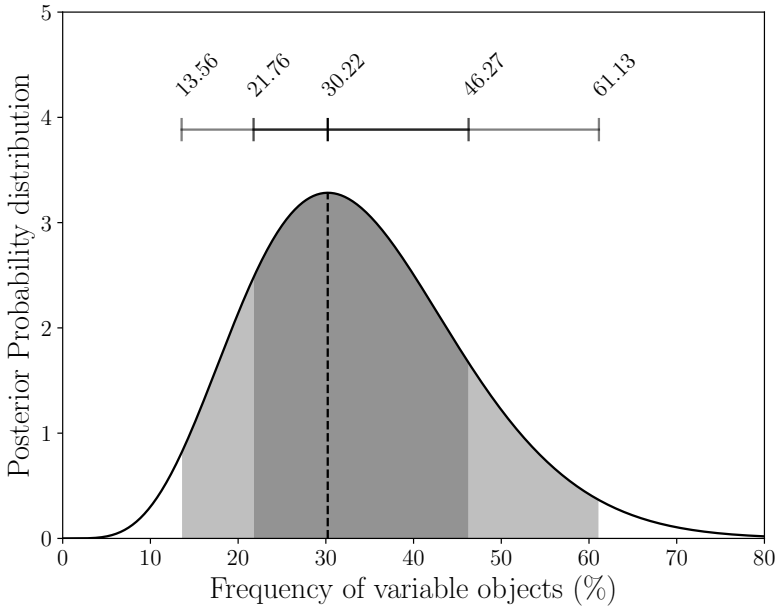

Figure 5.21 Probability distribution of the variability occurrence rate of young objects. The dark grey area shows the 1σ regions while the light grey area shows the 2σ region.

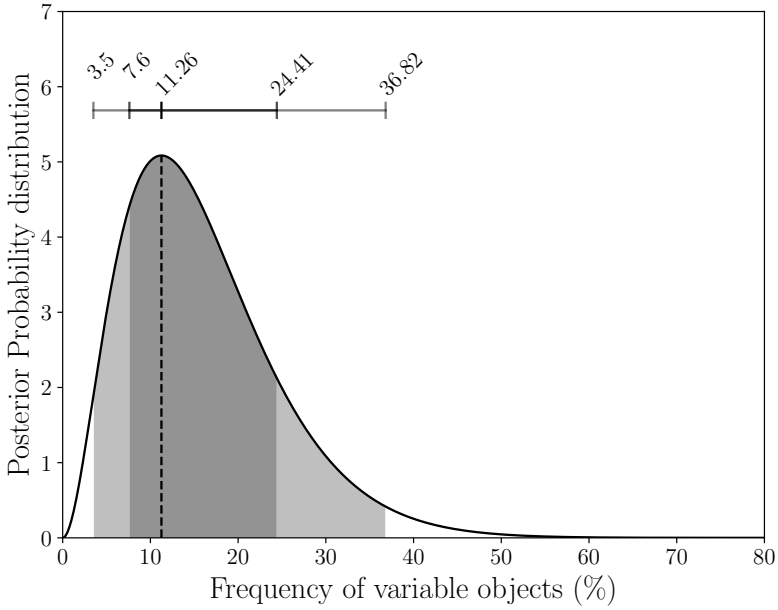

Figure 5.22 Probability distribution of the variability occurrence rate of the field brown dwarf population (Radigan, 2014). The dark grey area shows the 1σ regions while the light grey area shows the 2σ region.

Table 5.6 Contingency table showing the number of variability detections and non-detections in the Radigan (2014) survey (field objects) and this survey (low-gravity).

	Variable	Non-Variable
Field objects	2	32
Low-gravity	6	21

$$y_1 \sim \text{Binom}(n_1, \theta_1) \tag{5.1}$$
$$y_2 \sim \text{Binom}(n_2, \theta_2) \tag{5.2}$$

where n_1, n_2 are the total sample sizes and θ_1, θ_2 are the variability occurrence rates of the low-gravity and field objects respectively. We use uniform priors on the fraction of variable for each population:

$$\theta_1 \sim \text{Unif}(0, 1) = \text{Beta}(1, 1) \tag{5.3}$$
$$\theta_2 \sim \text{Unif}(0, 1) = \text{Beta}(1, 1) \tag{5.4}$$

Since the Beta distribution is a conjugate prior to the binomial distribution we can analytically compute the posteriors of the variability occurrence rate for each sample:

$$p(\theta_1|y_1, n_1) = \int_{-\infty}^{+\infty} \text{Beta}(\theta_1|y_1 + 1, n_1 - y_1 + 1) \tag{5.5}$$
$$p(\theta_2|y_2, n_2) = \int_{-\infty}^{+\infty} \text{Beta}(\theta_2|y_2 + 1, n_2 - y_2 + 1) \tag{5.6}$$

We plot the probability distributions of the variability occurrence rates in the left panel of Figure 5.23. We define the difference between the variability occurrence rates as $\delta = \theta_1 - \theta_2$. We then draw 50000 simulations from the joint posterior $p(\theta_1, \theta_2|y_1, n_1, y_2, n_2)$ and estimate the probability that $\delta > 0$ by the fraction of samples, m, where $\theta_1^m > \theta_2^m$. We plot the distribution δ in the right panel of Figure 5.23. We find a 98% probability that the variability occurrence rates of the field brown dwarf and low-gravity populations are drawn from different distributions. Thus, our survey strongly suggests that the low-gravity L-type objects appear more variable than their higher mass counterparts.

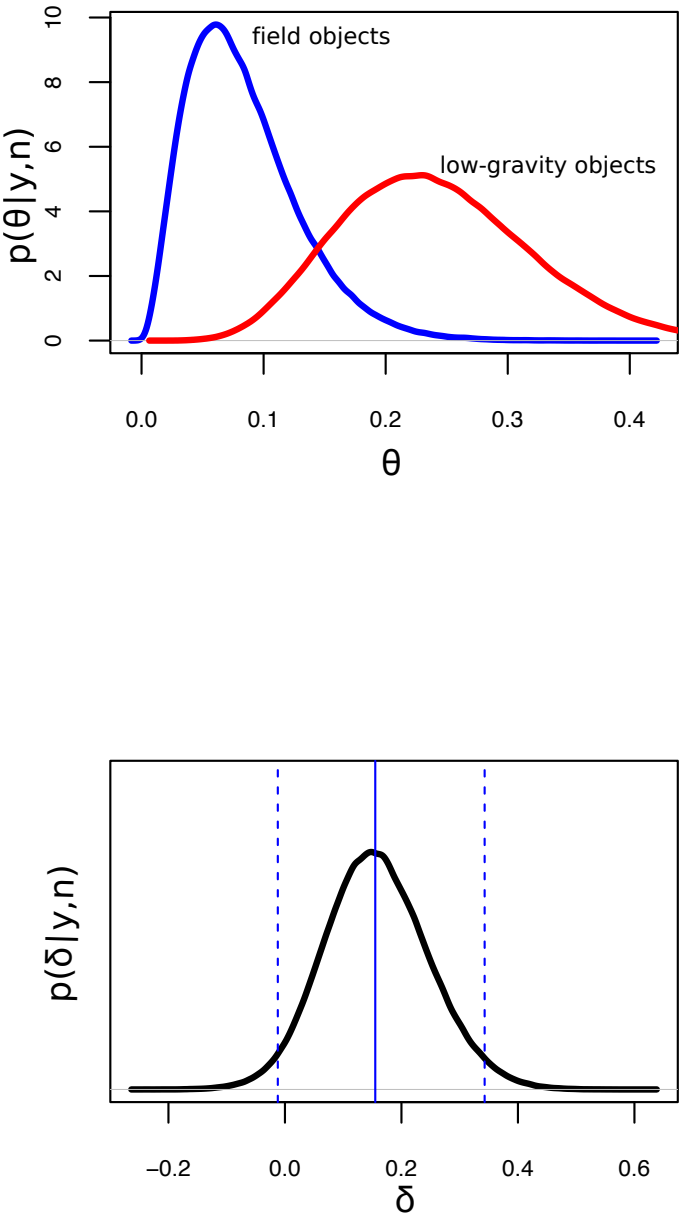

Figure 5.23 Top panel shows probability distributions for the variability occurrence rate of the field brown dwarf sample from Radigan et al. (2014)(blue) and our young sample (red), assuming binomial statistics and a uniform prior. The bottom panel shows the difference between these distributions. We find a 98% probability that the planetary-mass sample has a higher variability occurrence rate than the field brown dwarf sample.

Due to a low number of young T dwarfs in our sample, our survey cannot robustly determine the variability properties of low-gravity T-type objects. However there are a number of high-amplitude variability detections in young T dwarfs that suggest that this trend between low-gravity and high amplitude variability may extend into the T dwarfs. Metchev et al. (2015) report *Spitzer* 3.6 μm and 4.5 μm in the intermediate-gravity T2.5 companion HN Peg B, the only low-gravity T dwarf in the survey. The T2.5 known variable object SIMP 0136 was recently found to be a likely planetary-mass member of the Carina-Near moving group (Gagné et al., 2017). With its $1-6\%$ J-band variability, SIMP 0136 exhibits one of the highest variability amplitudes of the known variable T dwarfs. The T2 dwarf 2M1324+63 which exhibits high-amplitude variability in the optical and the mid-IR (Heinze et al., 2015; Apai et al., 2017), was found to be a planetary-mass member of the AB Doradus moving group (Gagné et al., 2018a). Finally, we report high-amplitude variability in PSO 071.8–22 in this survey. Although it does not have sufficient evidence of youth to be classed as 'Young' in our sample, additional kinematic information may confirm PSO 071.8–12 as a young object. As we identify more low-gravity T dwarfs it will become clearer whether the link between low-gravity and high-amplitude variability holds for cooler T-type objects.

5.11 Follow-up Observations of Variable Objects

When possible, we obtained follow-up observations of objects found to be variable in their first epoch. These observations were carried out so that we could confirm variability and also look for evolution in the lightcurves of our variable objects (Apai et al., 2017; Vos et al., 2018). We obtained follow-up observations of 2M0045+16, PSO 071.8–12, 2M0501–00, 2M1425–36 and PSO 318.5–22. We discuss each object below.

2M0045+16 — We observed 2M0045+16 on November 11 2014 and August 17 2015 with the NTT and November 13 2016 with UKIRT. 2M0045+16 was found to be variable in two out of three epochs - the NTT November 11 2014 and UKIRT November 13 2016 observation. As can be seen from Figures 5.6 and 5.7, both lightcurves exhibit a similar shape, with periodograms indicating a period of $\sim 3-6$ hr. We measure amplitudes of $1.0 \pm 0.1\%$ and $0.9 \pm 0.1\%$ for the 2014 and 2016 lightcurves respectively, thus we do not see any indication of lightcurve evolution in this case. The NTT August 17 2015 lightcurve shows a similar

trend, however the periodogram peak power does not fall above our significance threshold. According to the sensitivity plot of the August 17 2015 observation (shown in Appendix A.3), we can place an upper limit on the variability amplitude of this epoch of $\sim 2\%$ for a rotational period of $\sim 3-6$ hr. Thus, we did not reach the photometric precision necessary to robustly detect a 1% modulation in the lightcurve in this observation.

PSO 071.8–12 — We reobserved the variable object PSO 071.8–12 with UKIRT on December 8 2017. During this 4 hr observation we do not detect significant variability. The sensitivity plot shown in Appendix A.3 rules out significant variability $> 5\%$ for short periods, however we believe that PSO 071.8–12 has a somewhat longer period. For a rotational period of $5-8$ hr we place an upper limit of $6-8\%$ on the variability amplitude of PSO 071.8–12 in this epoch.

2M0501–00 — We observed 2M0501–00 a total of four times with the NTT. We detect significant variability on November 11 2014 and October 19 2016 and do not detect variability on August 16 2015 and March 12 2017. In the two variable epochs (Figures 5.9 and 5.10), which are separated by almost two years we observe a similar lightcurve shape - a slowly decreasing relative flux over the entire observation. Both periodograms favour a period > 5 hr and the Levenberg-Marquardt least-squares fits give amplitudes of $1-2\%$, although both the rotational period and variability amplitude are very uncertain since we did not observe a maximum or minimum in either lightcurve. We do not detect variability during two ~ 2 hr observations on August 16 2015 and March 12 2017 (shown in Appendix A.3). As these observations are shorter than the variable epochs, they are less sensitive to long period variability. The sensitivity plot from August 16 2015 shows that we are sensitive to amplitudes $> 6\%$ for a rotational period of 5 hr. The March 12 2017 lightcurve is noisier than the other epochs due to poor weather conditions, and the sensitivity plot shows that we are not sensitive to periods of ≥ 5 hr in this epoch. Thus, our observations do not show evidence for an evolving lightcurve in this case.

2M1425–36 — We obtained two epochs of variability monitoring of 2M1425–36 using the NTT. The initial observation on August 17 2015 shows a low-amplitude ($\sim 0.7\%$) trend with a period > 2.5 hr. Our second epoch observation, obtained using the NTT on March 14 2017 (shown in Appendix A.4) suffered from poor weather conditions, with the seeing ranging from $0.9-1.7''$. While the sensitivity plot suggests that we are sensitive to very low variability amplitudes, the periodograms of the reference stars display significant trends due to changing

weather conditions.

PSO 318.5–22 — As part of the initial survey observations, we obtained three epochs of NTT variability monitoring for the L7 object PSO 318.5–22. On October 9 2014 we observed significant J_S variability, with an amplitude of $10 \pm 1.3\%$, and a period > 5 hr (Figure 5.13). The J_S lightcurve obtained on November 9 2014 again shows similar variability, this time varying with an amplitude of $4.8 \pm 0.7\%$ over a ~ 3 hr observation (Figure 5.14). Finally, we observed PSO 318.5–22 in the K_S band on November 10 2014. Since PSO 318.5–22 is much brighter in K_S, we attain higher photometric precision in this band. The lightcurve shows a smooth upward trend with an amplitude of $2.2 \pm 0.6\%$ (Figure 5.15).

5.12 Conclusions

We report the first large survey for photometric variability in young low-gravity brown dwarfs with NTT/SofI and UKIRT/WFCAM. We monitored a total of 36 objects continuously for $\sim 2 - 6$ hr, detecting significant ($p > 99\%$) variability in seven objects. We assess the spectral indicators of youth and moving group membership of each object in the sample, finding that three objects have rather uncertain ages and are thus left out of the survey analysis. We also leave one unresolved binary out of the survey and lose two objects due to poor weather conditions. We detect variability in six objects that are likely to be young, four of which are new detections of variability.

In the 'Young' sample, we detect variability in 6/30 (20%) objects, which is consistent with the 16% variability fraction reported by Radigan et al. (2014) for the higher mass, field dwarfs. However, since we are lacking in objects with spectral types >L9 compared to earlier surveys of field L and T dwarf population, we focus our analysis on the L0-L8.5 objects in our sample. We find that the variability occurrence rate of L0-L8.5 objects in this survey is $30^{+16}_{-8}\%$, which is higher than the variability occurrence rate of $11^{+13}_{-4}\%$ that we find for the field brown dwarf population (Radigan, 2014). Thus we have found the first quantitative indication that the L-type low-gravity objects are more likely to be variable than the higher mass field dwarf counterparts.

Chapter 6

Conclusions

6.1 Summary

Photometric variability monitoring is a key probe of atmospheric features in brown dwarfs and giant exoplanets. The variability properties of an object can reveal the atmospheric structures present. This thesis explores photometric variability in substellar atmospheres, with a focus on the role of surface gravity in the variability properties of the exoplanet analogues.

6.1.1 Chapter 2

In Chapter 2 we present the detection of variability in the L7 planetary-mass object PSO 318.5–22, as well as subsequent multi-wavelength follow-up monitoring. This was the first detection of cloud-driven variability in a planetary-mass object. PSO 318.5–22 is a member of the $\sim$ 23 Myr β Pictoris moving group (Mamajek & Bell, 2014), with an estimated mass of 8.3 ± 0.5 $M_{\rm Jup}$ (Allers et al., 2016). It is one of the first free-floating objects with colours, magnitudes, spectrum, luminosity and mass that overlap the young dusty planets such as HR8799bcde and 2M1207–39b (Liu et al., 2013). In the initial discovery epochs, obtained with the SofI instrument at the NTT, PSO 318.5–22 exhibited J_S-band variability with an amplitude of $10 \pm 1.3\%$. This was the highest variability amplitude observed to date in an L-type object, and was the first indication that surface gravity may have an effect on the variability properties of L and T type

brown dwarfs and planetary-mass objects. Followup NTT/SofI monitoring in the J_S and K_S bands revealed lower amplitude variations: $2.4 \pm 0.2\%$ in J_S and 0.48 ± 0.08 in K_S. We find no evidence of phase shifts between the J_S and K_S lightcurves. The followup observations were taken over three consecutive nights, enabling us to measure a rotation period of 8.45 ± 0.05 hr for PSO 318.5–22.

Finally, we present simultaneous *HST* and *Spitzer* monitoring of PSO 318.5–22. Simultaneous multi-wavelength monitoring is a particularly powerful tool to understand the atmospheres of brown dwarfs and planetary-mass objects. Since different wavelengths probe different heights in the atmosphere (Marley et al., 2012), these observations can help to pinpoint the source of variability. Variability was detected in both near-IR and mid-IR bands with amplitudes of $4.4 - 5.8\%$ in the near-IR bands and $3.4 \pm 0.1\%$ in the *Spitzer* [4.5 μm] band. We measure a rotation period of 8.61 ± 0.06 hr for PSO 318.5–22 from the *Spitzer* observations, which covered more than two rotation periods. This period is consistent with the period derived from NTT/SofI data. We detect phase offsets of $200 - 210°$ between the near-IR and mid-IR bands, likely indicating the presence of varying longitudinal atmospheric structure at different depths in the atmosphere. The variability amplitude was found to decrease with increasing wavelength, a feature that has been observed previously in field brown dwarfs (Apai et al., 2013; Yang et al., 2016). The near-IR and mid-IR variability amplitudes observed in PSO 318.5–22 are considerably larger than the amplitudes measured for mid-L field brown dwarfs (Radigan et al., 2014; Metchev et al., 2015; Yang et al., 2015). PSO 318.5–22 shares many of its variability properties with the field brown dwarfs (e.g. phase shifts and amplitude ratios) suggesting that the variability mechanism is likely to be similar for both field brown dwarfs and free-floating planets, however the large variability amplitudes suggest that some of the variability properties are dependent on surface gravity. Overall, the results presented in Chapter 2 demonstrate the feasibility of a ground-based near-IR search for variability in low-gravity objects and provides some insight into the role of gravity in the variability properties of brown dwarfs and planetary-mass objects.

6.1.2 Chapter 3

In Chapter 3 we study the full sample of known *Spitzer* [3.6 μm] and J-band variable brown dwarfs in the literature. Additionally, we use new rotational velocities to measure the inclination of a sample of brown dwarfs for the first

time. We find that the viewing angle of a brown dwarf strongly affects the observed variability amplitudes through a projection effect as well as atmospheric attenuation. Our toy model suggests that J-band variability amplitudes are more strongly affected by the atmospheric attenuation than the mid-IR amplitudes, possibly due to the J-band probing deeper levels in the atmosphere than the mid-IR (Buenzli et al., 2014; Biller et al., 2013). We also find a trend between the colour anomaly and inclination angle of our sample that is statistically significant at the 99% level. Field objects viewed equator-on appear redder than the median for their spectral type, whereas objects viewed at lower inclinations appear bluer than the median. This result suggests that our viewing angle influences the spectral and photometric appearance of a brown dwarf. The relation between inclination and colour could be explained if thicker or large-grained clouds are situated at the equator, with thinner or small-grained clouds at the poles. This finding represents the first insights into the latitudinal variations in brown dwarf properties. Finally, we find a strong correlation between colour anomaly and both [3.6 μm] and J-band variability amplitude, where redder objects display higher variability amplitudes, again suggesting that the spectral appearance and variability amplitude of a brown dwarf are strongly affected by viewing angle. In this chapter we revealed important relations regarding colour, viewing angle and variability properties that will inform future variability searches on free-floating and companion exoplanets. The results from this chapter suggest that exoplanets viewed pole-on (such as the HR8799 planets Marois et al., 2010) are unlikely to display large-amplitude variability.

6.1.3 Chapter 4

In Chapter 4 we present *Spitzer* monitoring of W0047, 2M2244 and SDSS1110, the three lowest-mass members of the $110 - 150$ Myr old AB Doradus moving group. These three objects have estimated masses, radii and temperatures that overlap with the directly-imaged planets, and thus can provide insight into their atmospheres. W0047 and 2M2244 are a particularly interesting pair of late-L young, low-gravity objects, with $0.65 - 2.5$ μm spectra that are remarkably similar (Gizis et al., 2015). There are no other free-floating L/T transition dwarfs known to be both coeval and spectrally similar that are bright enough for detailed characterisation. SDSSS1110 is a T5.5 object, and is one of very few young, age-calibrated T dwarfs known to date. We detect significant *Spitzer* [3.6 μm] variability in W0047 and 2M2244. The lightcurve of W0047 appears sinusoidal

and we use MCMC analysis to measure a rotational period of 16.4 ± 0.2 hr and a variability amplitude of $1.07 \pm 0.04\%$. In contrast, the lightcurve of 2M2244 does not appear sinusoidal and looks very different to the *Spitzer* [4.5 μm] lightcurve presented by Morales-Calderon et al. (2006). We analyse both *Spitzer* lightcurves and a J-band lightcurve taken with UKIRT/WFCAM to estimate a period of 11 ± 2 hr for 2M2244. We measure a [3.6 μm] amplitude of $0.8 \pm 0.2\%$. We do not detect variability in the T5.5 object SDSS1110 during an 8.5 hr observation and place an upper limit of 1.25% on the variability amplitude for periods < 18 hr.

We additionally obtain NIRSPEC-7 high dispersion spectra of W0047 and 2M2244. We measure the radial velocity of 2M2244 for the first time and confirm it as a member of the AB Doradus moving group. We measure the $v \sin(i)$ of both W0047 and 2M2244. Assuming rigid sphere rotation and using expected radii from evolutionary models we find that both objects are close to equator-on, with inclination angles of $85^{+5\circ}_{-9}$ and $76^{+14\circ}_{-21}$ for W0047 and 2M2244 respectively. Their remarkably similar colours, spectral appearance and inclinations are consistent with the possibility that the viewing angle shapes the observed spectrum of a brown dwarf or giant exoplanet.

6.1.4 Chapter 5

Finally, Chapter 5 describes the first large survey for photometric variability in exoplanet analogues. Theory and observations have shown that gravity plays an important role in the atmospheric properties of L and T type objects. Directly-imaged planets and their free-floating analogues appear much redder in the near and mid-IR compared to their higher-mass field brown dwarf counterparts at similar $T_{\rm eff}$. Furthermore, the $T_{\rm eff}$ at which young exoplanets transition between spectral types is lower than for the field brown dwarf population (Barman et al., 2011). Surface gravity significantly affects the height at which cloud species form in the atmosphere (Marley et al., 2012), and thus it can be expected that surface gravity will have a significant effect on variability. Near-IR variability studies of high-gravity field brown dwarfs have shown that high-amplitude variable L dwarfs are rare, occurring in only $\sim 3\%$ of the population Radigan (2014). This is the first survey to assess the role of gravity in the variability properties of the low-gravity exoplanet analogues. The survey is composed of L and T type objects showing signs of low gravity and/or high-probability candidates of nearby young moving groups. We do a full analysis of the spectral signatures of youth

and assess the group membership probability of each target using the Convergent Point, BANYAN I, BANYAN Σ and LACEwING tools (Rodriguez et al., 2013; Malo et al., 2013; Gagné et al., 2015c; Riedel et al., 2017). This results in a 30 object sample of low-gravity exoplanet analogues. We find an overall variability fraction of 20%, which is consistent with the 16% variability fraction reported by Radigan et al. (2014) for the higher mass, field brown dwarfs. However, since we are lacking in objects with spectral types later than L9, we focus our statistical analysis on the L0-L8.5 objects. We find that the variability occurrence rate of L0-L8.5 exoplanet analogues in this survey is 30^{+16}_{-8}%. We reanalyse the results of Radigan (2014) and find that the field brown dwarfs with spectral types L0-L8.5 have a variability occurrence rate of 11^{+13}_{-4}%, which is lower than the young population of exoplanet analogues. This is the first quantitative indication that the young objects are more likely to be variable than their higher mass counterparts.

Furthermore, this survey has produced a sample of exoplanet analogues that display high amplitude near-IR variability, as such they are prime candidates for future follow-up monitoring. Multi-wavelength followup monitoring (e.g. the observations carried out for PSO 318.5–22 in Chapter 2) provide important information of the rotation rates, cloud particle size, vertical atmospheric structure and viewing angles of the object in question. These properties will provide crucial constraints for atmospheric and evolutionary models for both free-floating and companion exoplanets in the future.

6.2 Future Work

In particular, Chapters 2, 4 and 5 show the rapid advancement of our knowledge of variability in low-gravity objects over the past few years. From the first detection of variability in a planetary-mass object in Chapter 2 to the first large survey for variability in exoplanet analogues in Chapter 5, the work presented in this thesis has provided insight into the role of gravity in the variability properties of low-gravity brown dwarfs. In particular, this work acts as a pathfinder for future variability studies of exoplanet companions with the James Webb Space Telescope (*JWST*). *JWST* will enable us to search for variability in the directly-imaged planets for the first time and examine variability in the cold Y dwarfs. The variability monitoring observations have also yielded rotational periods of a number of young objects which will provide insight into the angular momentum

evolution of young brown dwarfs.

6.2.1 Variability Monitoring of Directly-Imaged Planets with JWST

The launch of *JWST* will allow us to move on from the free-floating planetary-mass objects and begin to study the variability properties of the directly-imaged exoplanet companions. While photometric variability has been detected in a small number of exoplanet companions at wide separations (Zhou et al., 2016; Naud et al., 2017), these objects likely have a different formation mechanism to the close-in exoplanets, which may affect their variability properties. *JWST* has an aperture and Strehl ratio on par with the Spectro-Polarimetric High-contrast Exoplanet REsearch instrument (SPHERE; Beuzit et al., 2008) at the Very Large Telescope (VLT), but is free of atmospheric aberrations. Combined with a suite of coronagraphs, *JWST* will enable the first detailed variability studies of exoplanet companions at separations $> 0.5''$ (Biller, 2017). The variability properties of the directly-imaged planets will be revealed by the unprecedented capabilities of *JWST*. In particular, the outer HR8799bcd planets (Marois et al., 2008) are prime targets for variability monitoring, as they have remarkably similar colours and spectra to the highly variable free-floating objects PSO 318.5–22 and W0047 (Bonnefoy et al., 2016). Currie et al. (2012) find that HR8799d is likely inclined $> 25°$ from face-on and the others may be on inclined orbits. While this geometry will attenuate any observed variability signal (as shown in Chapter 3), their spectral type and mass suggest that they will exhibit large variability amplitudes. The viewing geometry of the L1 exoplanet β Pic b is more favourable for variability detection, as it is inclined almost edge on (Wang et al., 2016). Although the L-type brown dwarfs are rarely variable (Radigan et al., 2014), it seems that the low-gravity L-type brown dwarfs are more likely to exhibit variability (e.g. Chapter 5), and thus β Pic b is also an excellent target for variability monitoring with *JWST*.

6.2.2 Probing Cooler Atmospheres with JWST

Y dwarfs are the coolest class of brown dwarfs known (Cushing et al., 2011; Kirkpatrick et al., 2012), with estimated temperatures < 500 K. At these low temperatures, their photosphere are composed of H_2, He, H_2S, CH_4, H_2O and NH_3

in the gas phase, and salt (KCl), sulfide (MnS, NA_2S and ZnS) and possible water ice condensates in the solid phase. These condensates tend to form clouds in the atmosphere (Morley et al., 2012). Like silicate clouds in the L and L/T transition brown dwarfs, these clouds are expected to produce a periodic modulation in the lightcurve of Y dwarfs as they rotate. To date, photometric variability has been detected in three Y dwarfs, WISE 1405+55 and WISE 0855–07 and WISE 1738+27 (Cushing et al., 2016; Esplin et al., 2016; Leggett et al., 2016). In all cases, the variability was detected in the mid-IR with *Spitzer*, and a tentative variability detection as ~ 1 μm was detected for WISE 1738+27.

The unprecedented sensitivity of *JWST* will enable us to search for variability in a larger sample of Y dwarfs. *JWST*/NIRcam will reveal near-IR variability in Y dwarfs for the first time, where high variability amplitudes have been predicted (Morley et al., 2014) and *JWST*/MIRI will enable us to monitor the faintest Y dwarfs, since they are brightest in the mid-IR. The variability properties of the cold Y dwarfs will shed light on what we can expect from directly-imaged planets with temperatures < 500 K.

6.2.3 Rotation Rates of Young Free-Floating Objects

A useful product of photometric variability monitoring is the measurement of rotation rates. Rotation periods and/or $v \sin(i)$ measurements have been measured for a large sample of brown dwarfs (e.g. Zapatero Osorio et al., 2006; Prato et al., 2015; Rice et al., 2010), however very little is known about rotation rates and angular momentum evolution in low-gravity objects.

Over their first $\sim$ 10 Myr, the rotation of brown dwarfs and planetary-mass objects is slowed by disk accretion and wind braking. This is opposed by contraction, which causes an object to spin up during the first $\sim$ 200 Myr (Bouvier et al., 2014; Batygin, 2018). Thus, it was expected that the young objects would rotate more slowly than their field brown dwarf counterparts. In recent years, we have discovered a sizable population of young brown dwarfs with relatively fast rotation periods of $2 - 11$ hr (Snellen et al., 2014; Zhou et al., 2016; Biller et al., 2018; Gagné et al., 2017). Rotational braking due to star-disk interaction and accretion driven winds is strongly mass-dependent (Bouvier et al., 2014), becoming less efficient at substellar masses (Scholz et al., 2015). It is possible that the magnetic fields present in low-gravity objects are not strong enough to effectively brake their rotation, which is consistent with the current deficit of

slowly rotating low-gravity objects. A larger sample of low-gravity objects with measured rotation periods will be necessary to investigate the angular momentum evolution of young, low-gravity brown dwarfs. Measuring the rotational periods of the variable, low-gravity objects reported in Chapter 5 will significantly add to the current sample.

Appendix A

Chapter 5 Appendix: Lightcurves and Sensitivity Plots for Non-Variable Objects

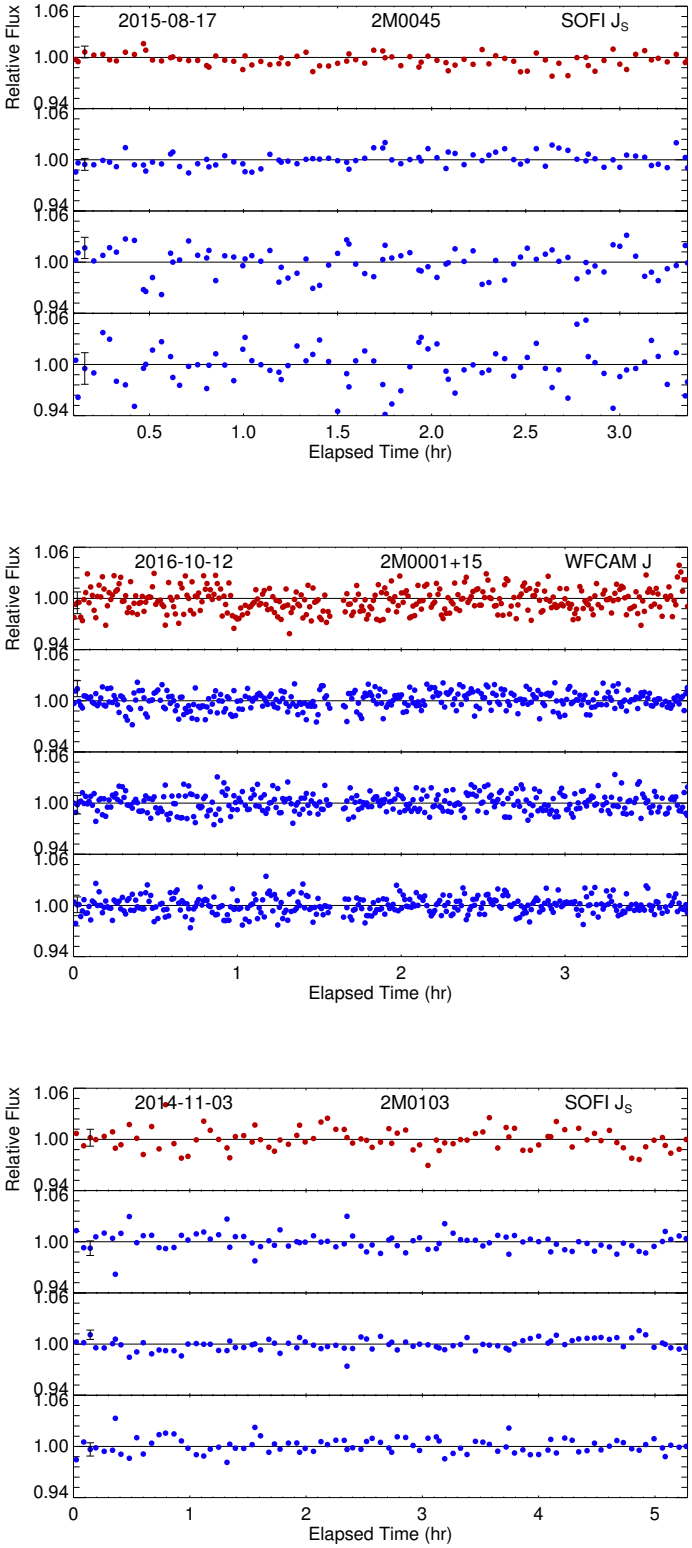

Figure A.1 Light curves of targets (red) and reference stars (blue) for non-detections in the survey.

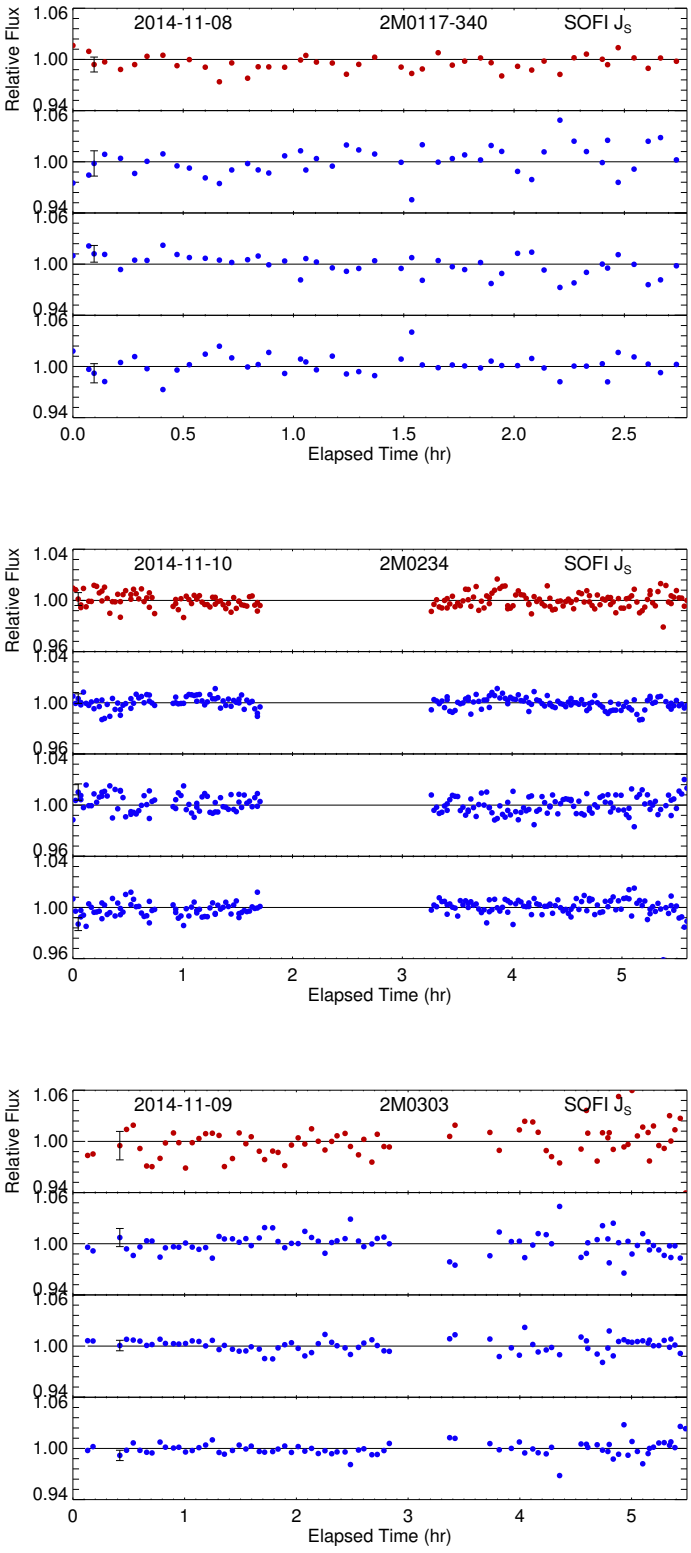

Figure A.1 Light curves of targets (red) and reference stars (blue) for non-detections in the survey.

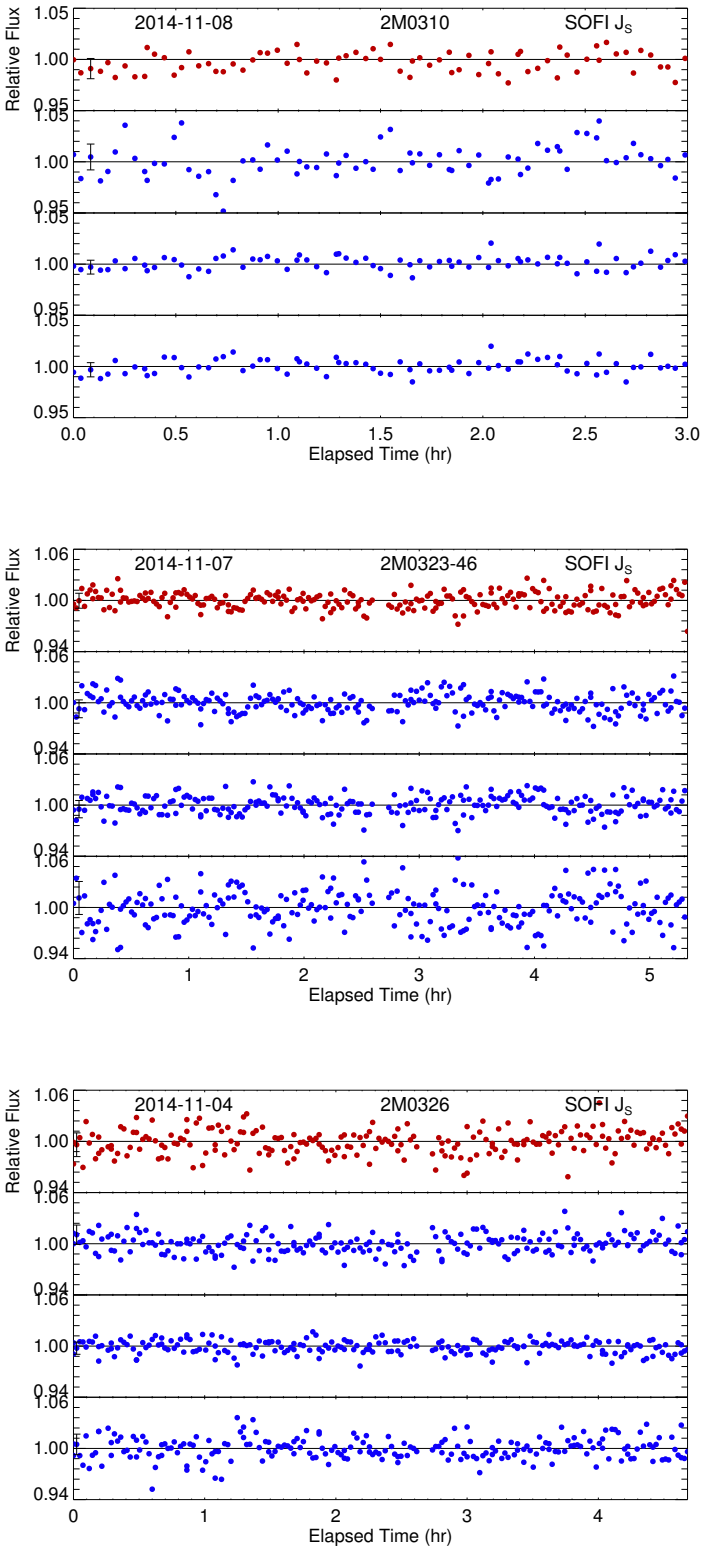

Figure A.1 Light curves of targets (red) and reference stars (blue) for non-detections in the survey.

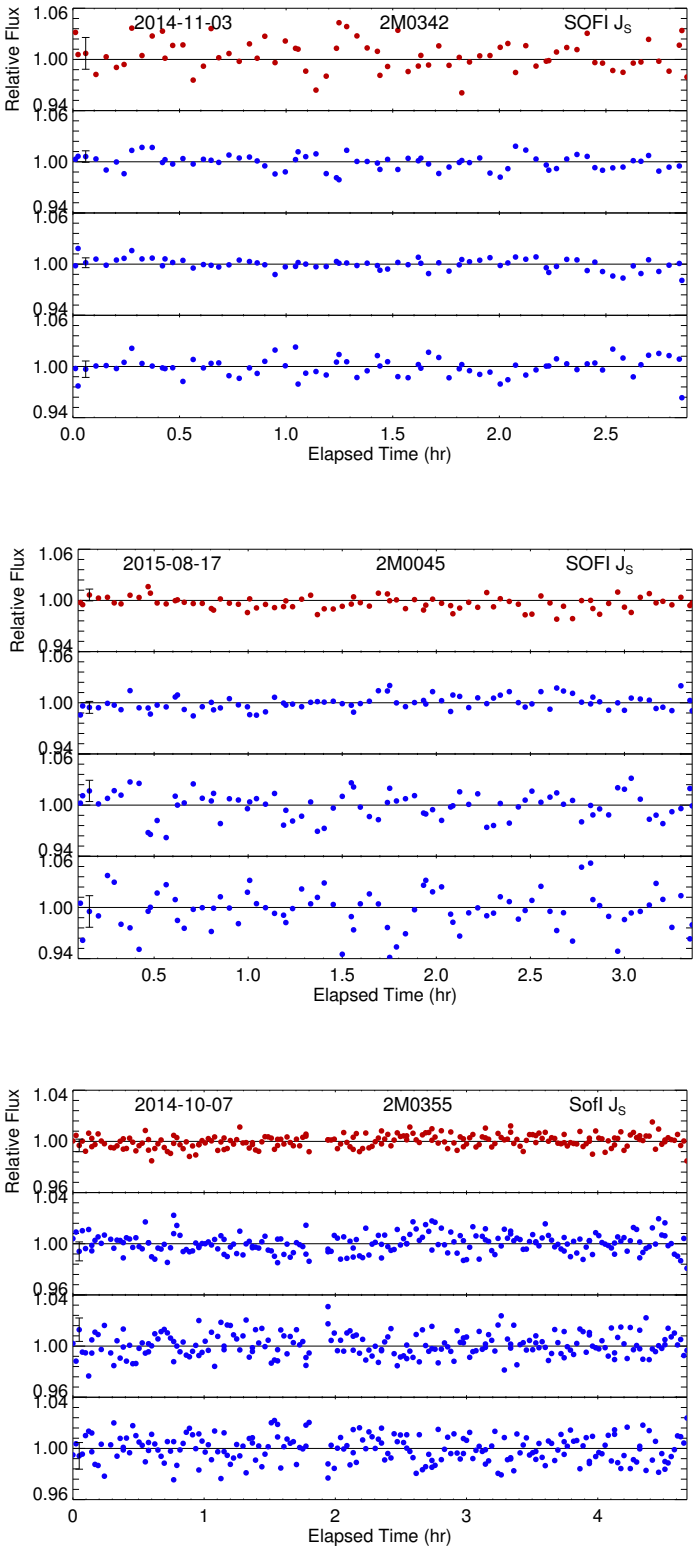

Figure A.1 Light curves of targets (red) and reference stars (blue) for non-detections in the survey.

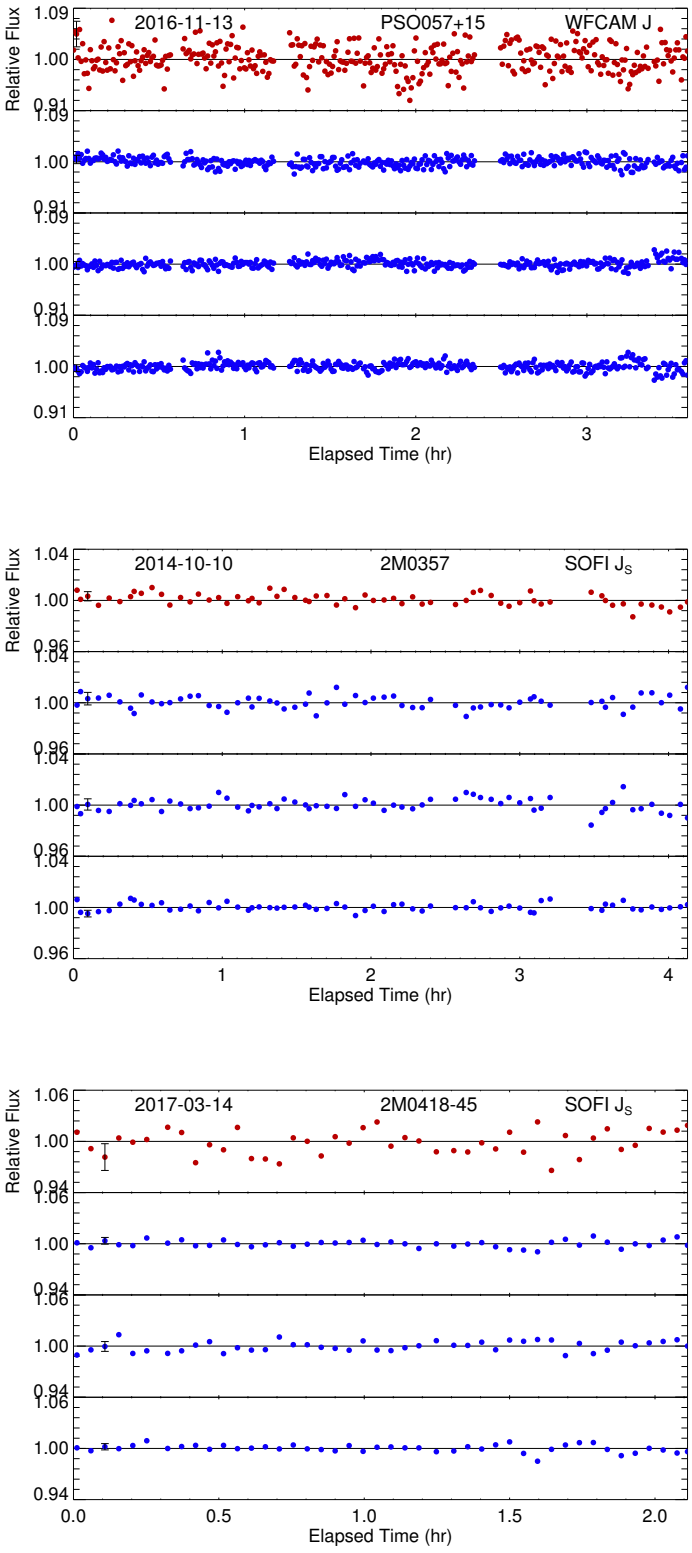

Figure A.1 Light curves of targets (red) and reference stars (blue) for non-detections in the survey.

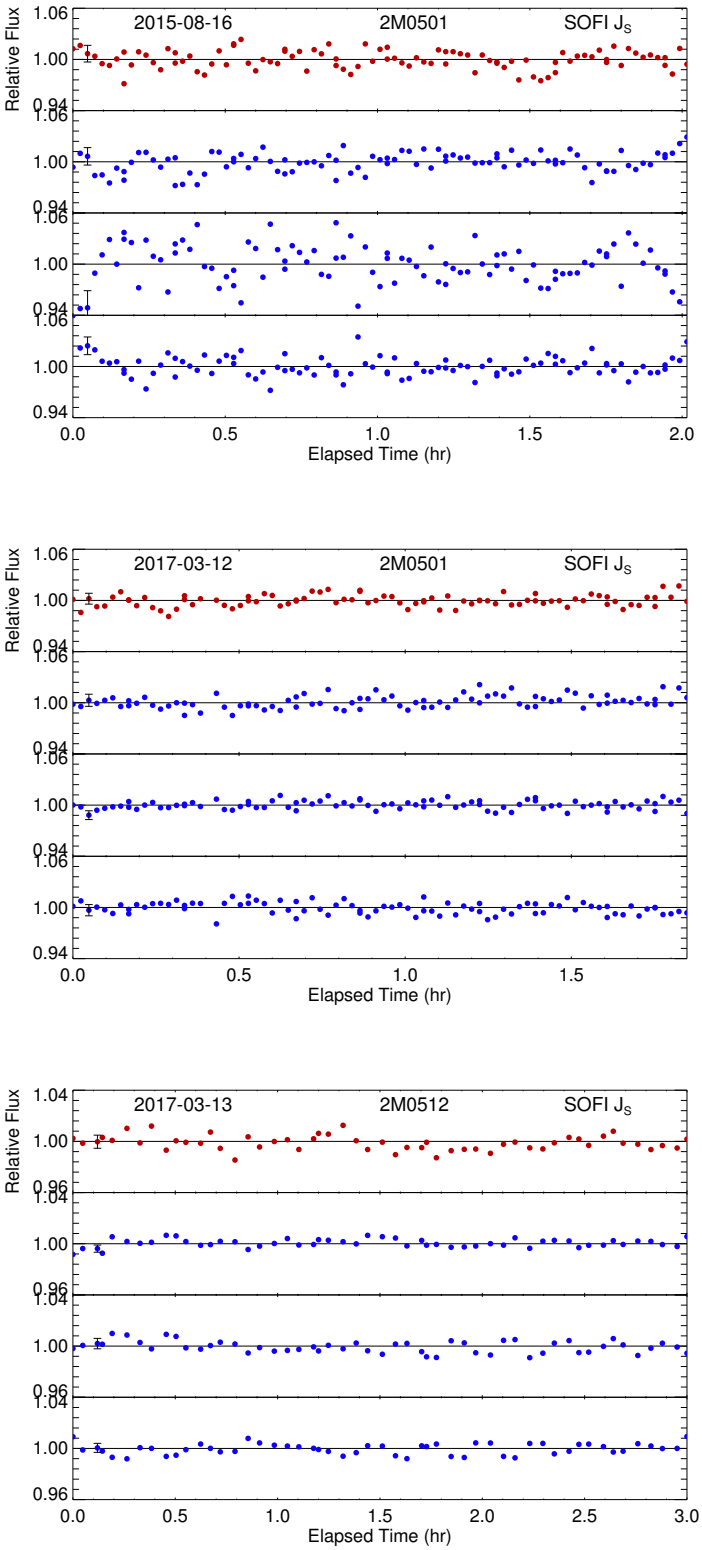

Figure A.1 Light curves of targets (red) and reference stars (blue) for non-detections in the survey.

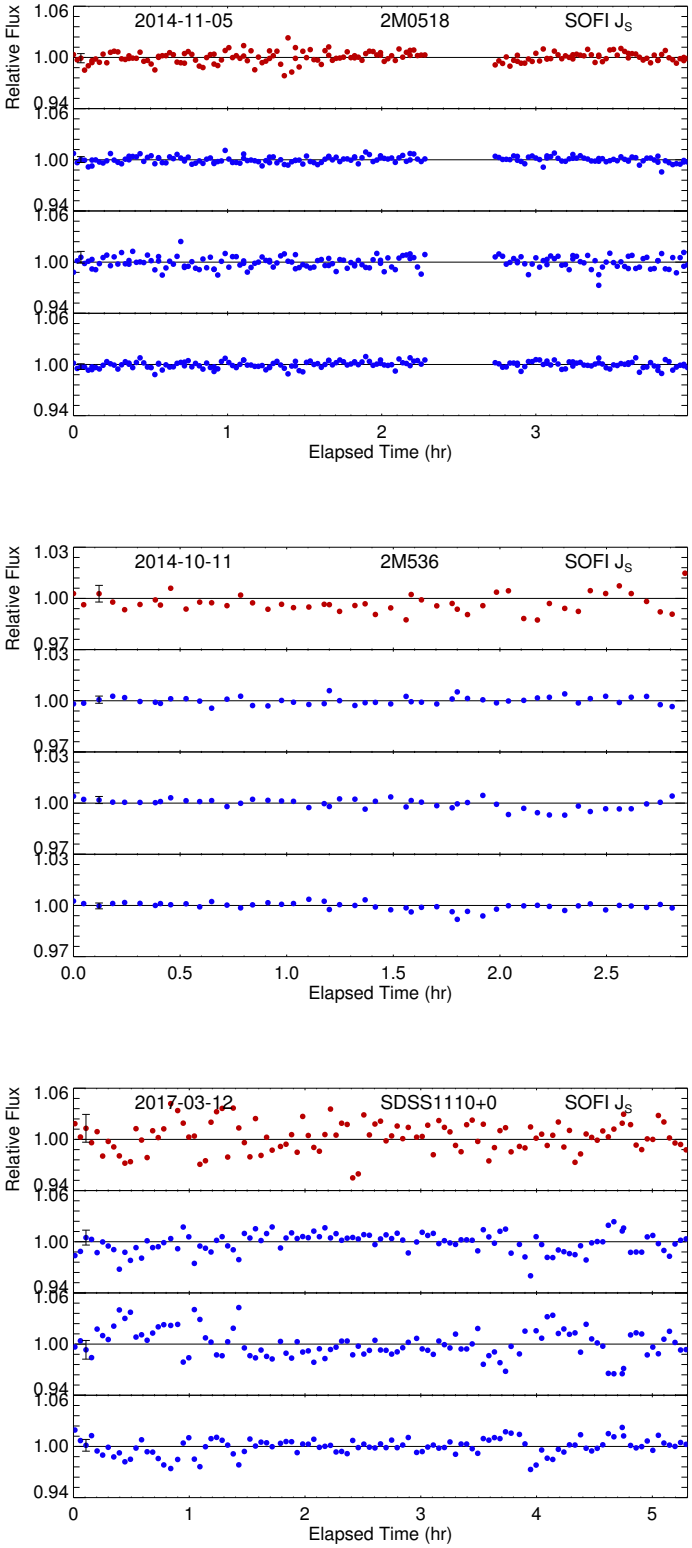

Figure A.1 Light curves of targets (red) and reference stars (blue) for non-detections in the survey.

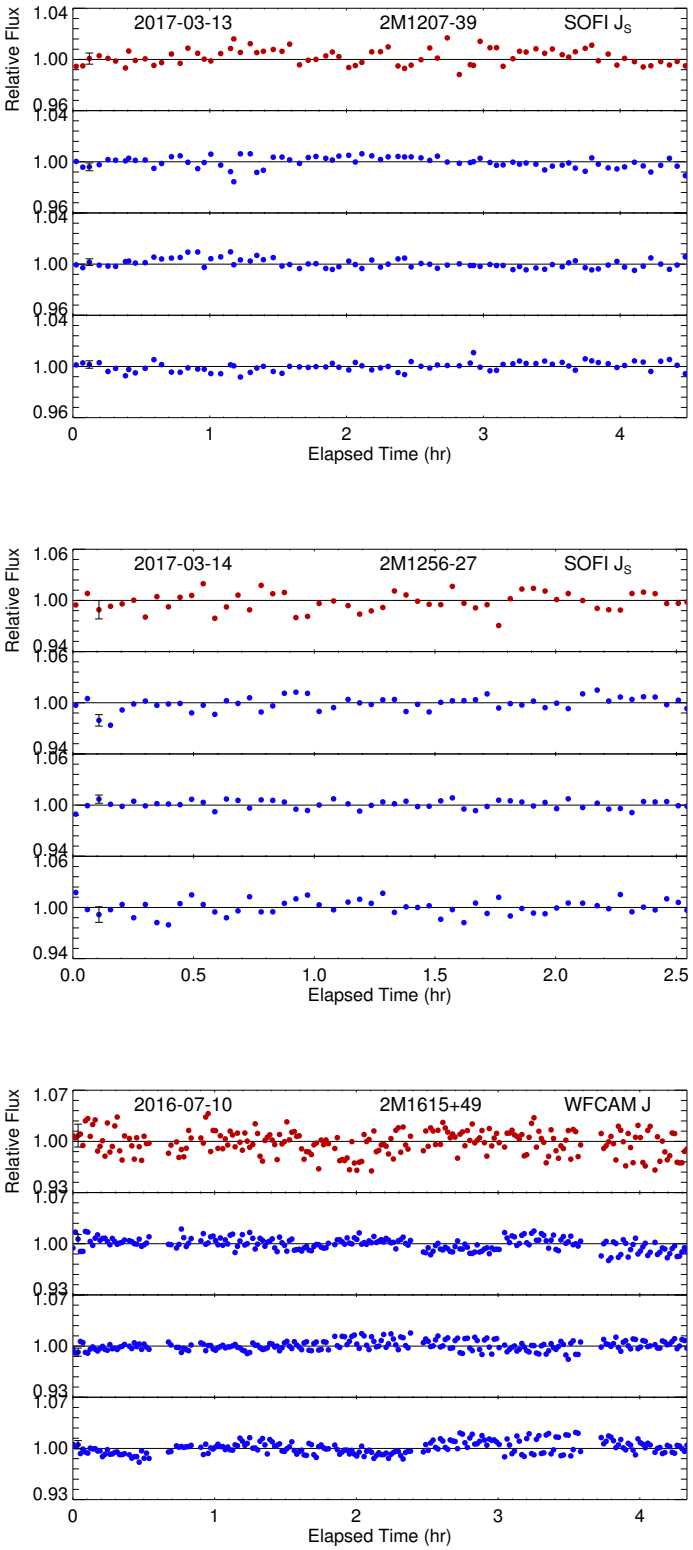

Figure A.1 Light curves of targets (red) and reference stars (blue) for non-detections in the survey.

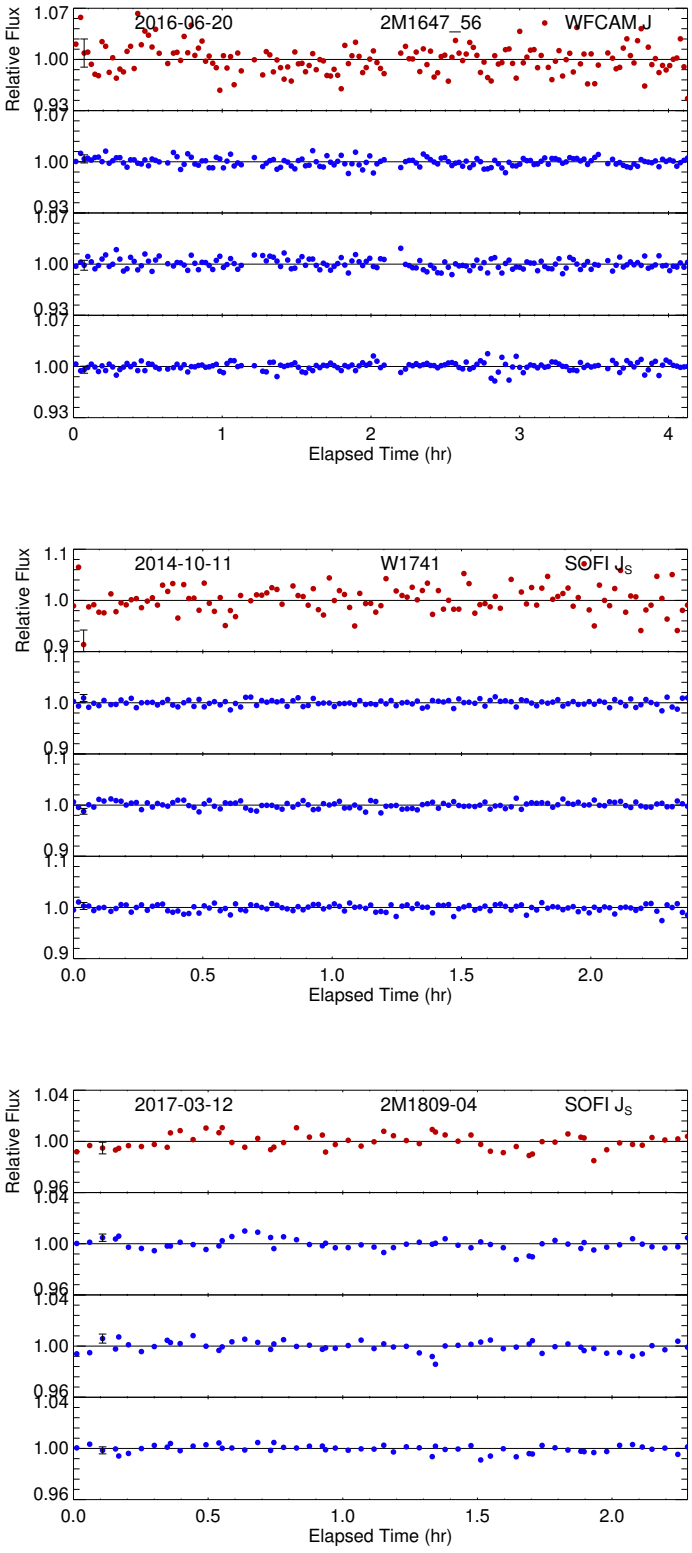

Figure A.1 Light curves of targets (red) and reference stars (blue) for non-detections in the survey.

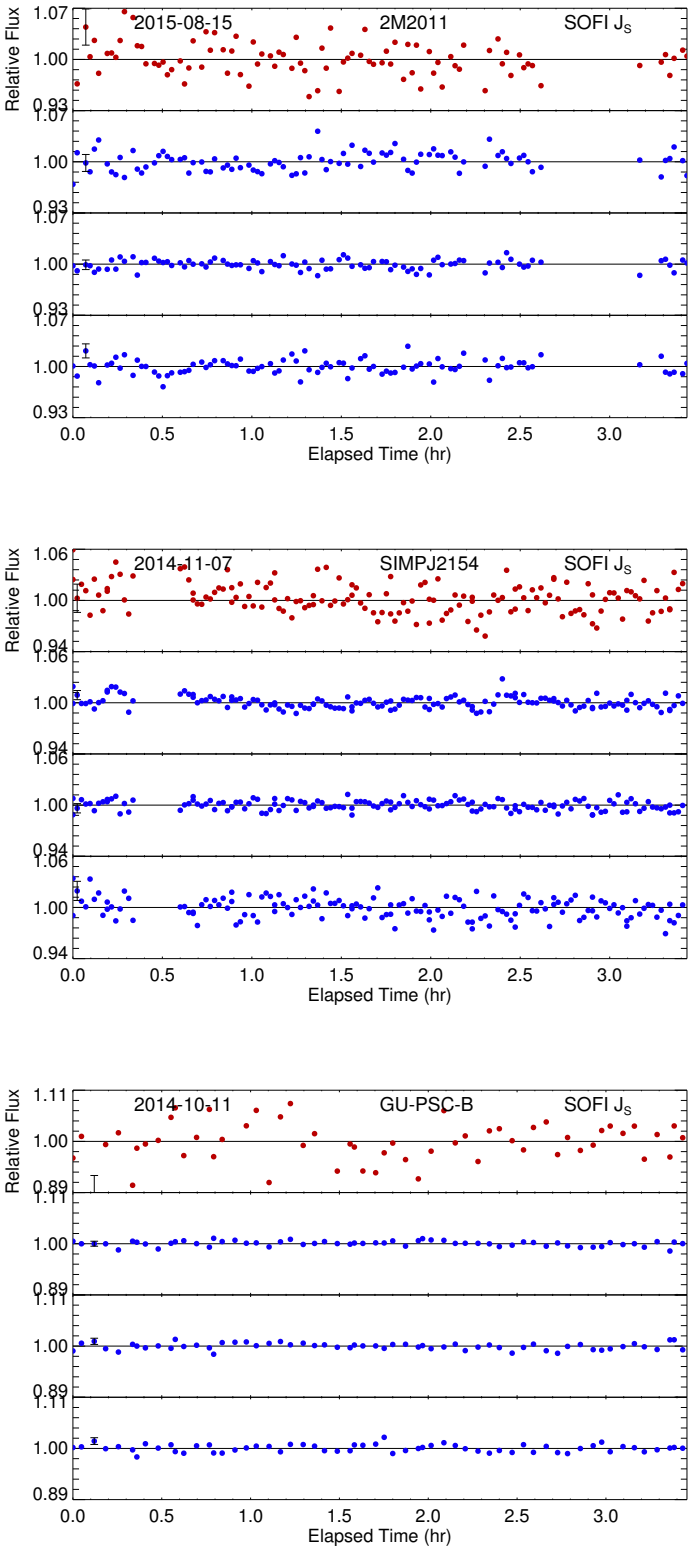

Figure A.1 Light curves of targets (red) and reference stars (blue) for non-detections in the survey.

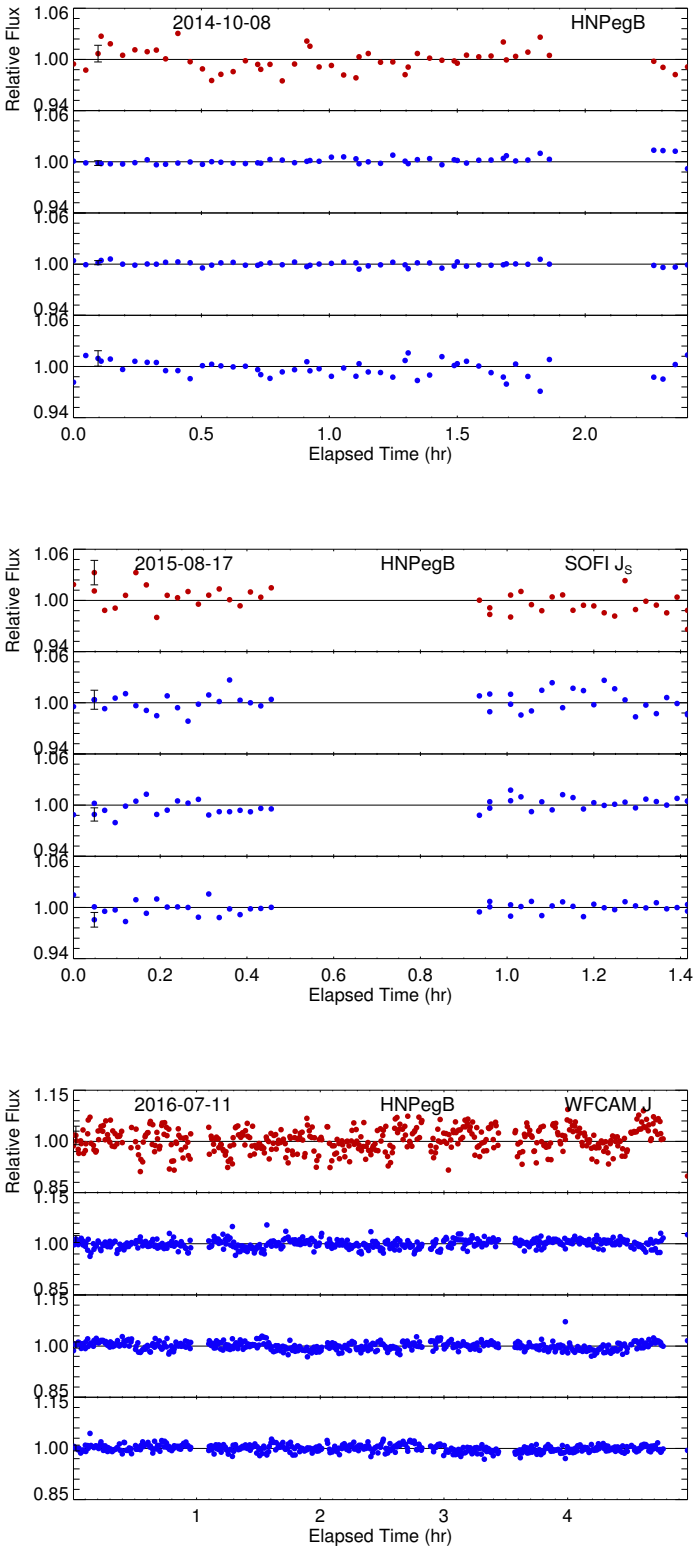

Figure A.1 Light curves of targets (red) and reference stars (blue) for non-detections in the survey.

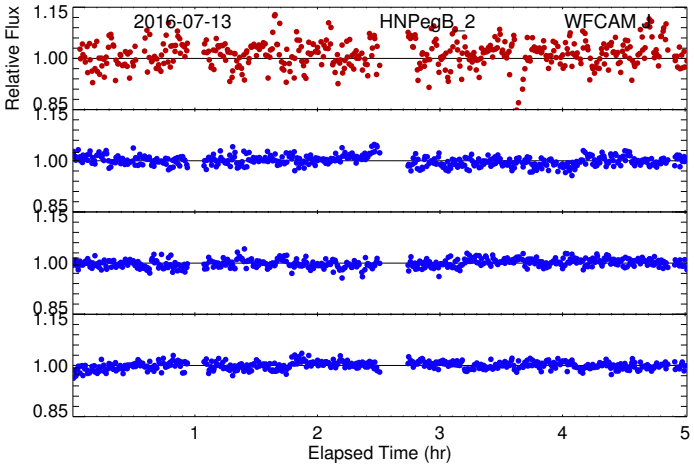

Figure A.1 Light curves of targets (red) and reference stars (blue) for non-detections in the survey.

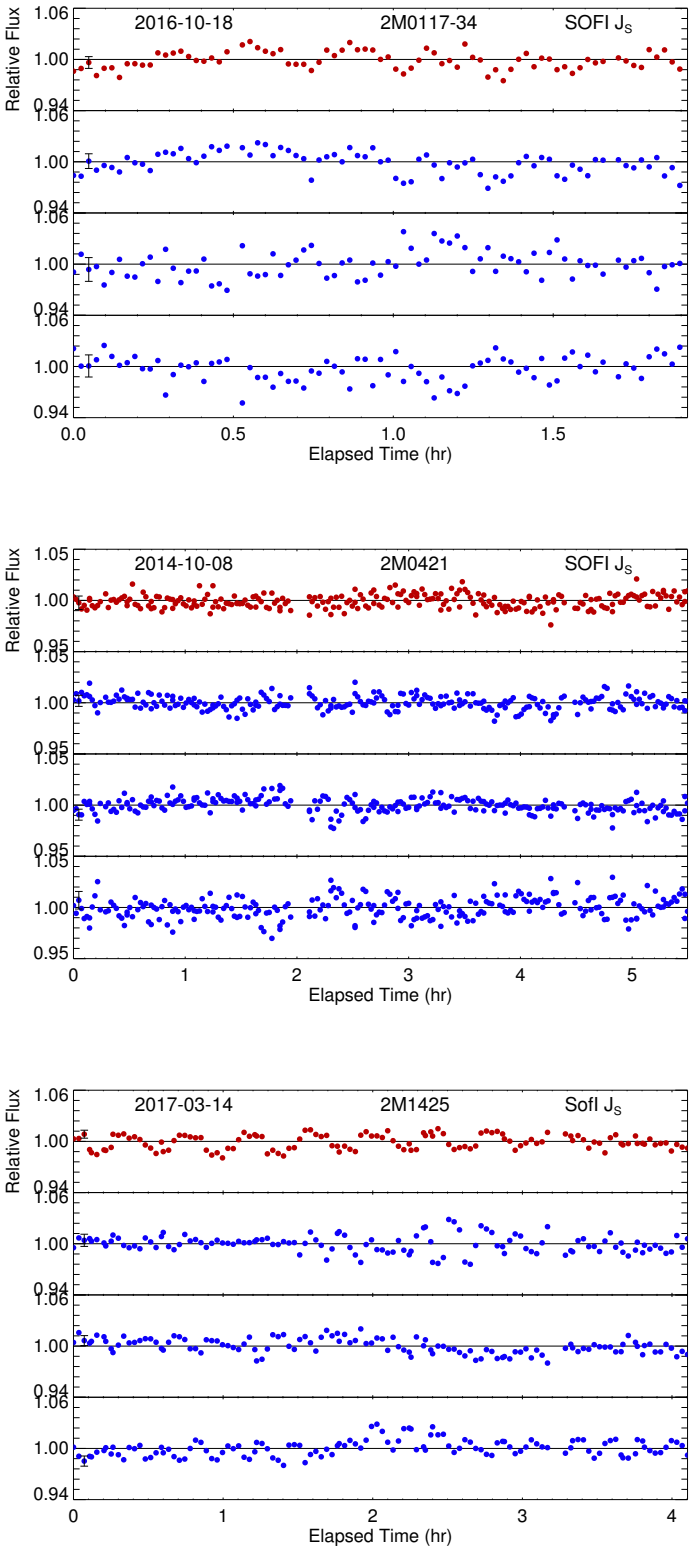

Figure A.2 Light curves of targets (red) and reference stars (blue) for bad quality observations.

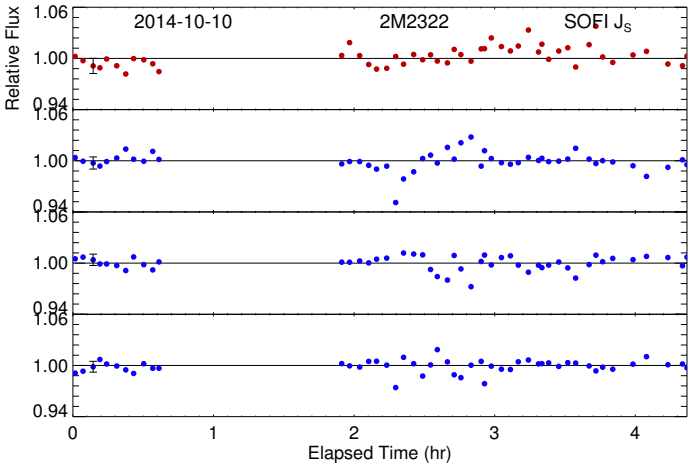

Figure A.2 Light curves of targets (red) and reference stars (blue) for bad quality observations.

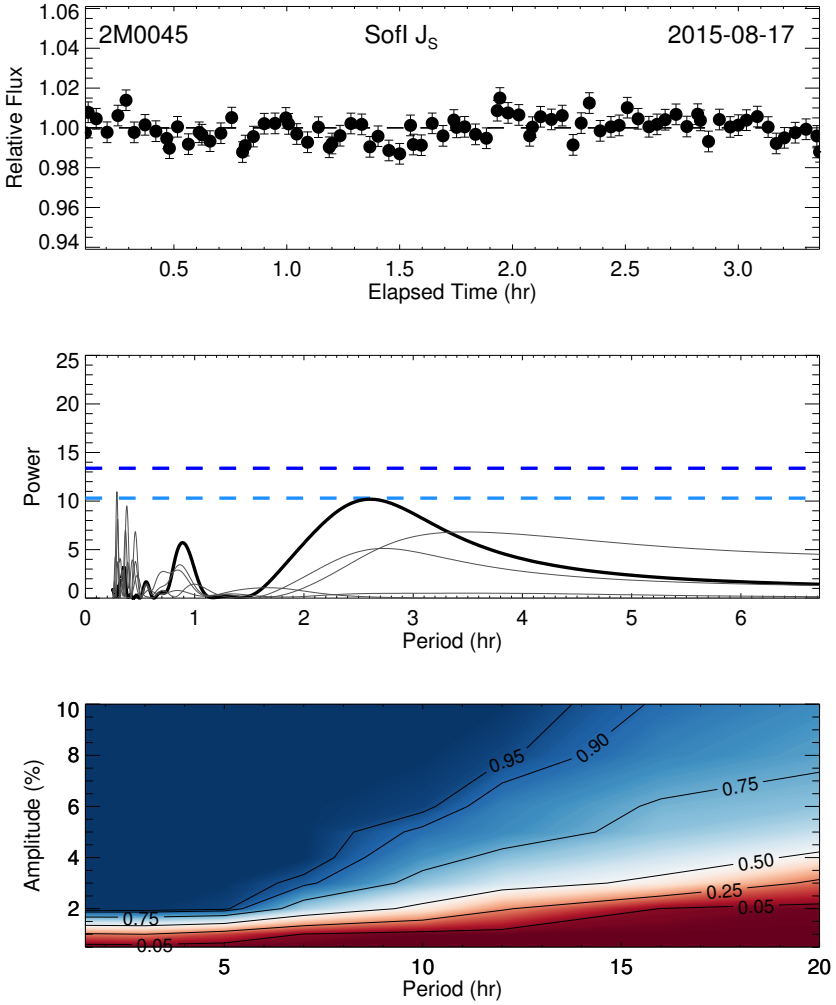

Figure A.3 Lightcurves, periodograms and sensitivity plots for non-variable objects.

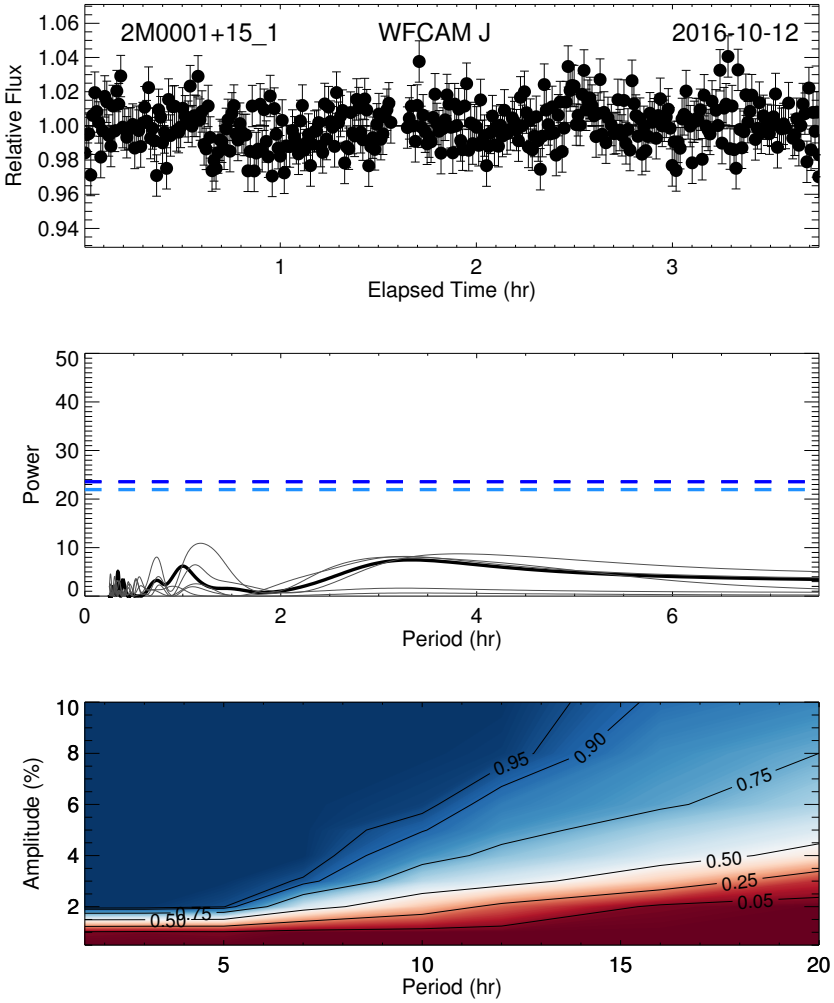

Figure A.3 Lightcurves, periodograms and sensitivity plots for non-variable objects.

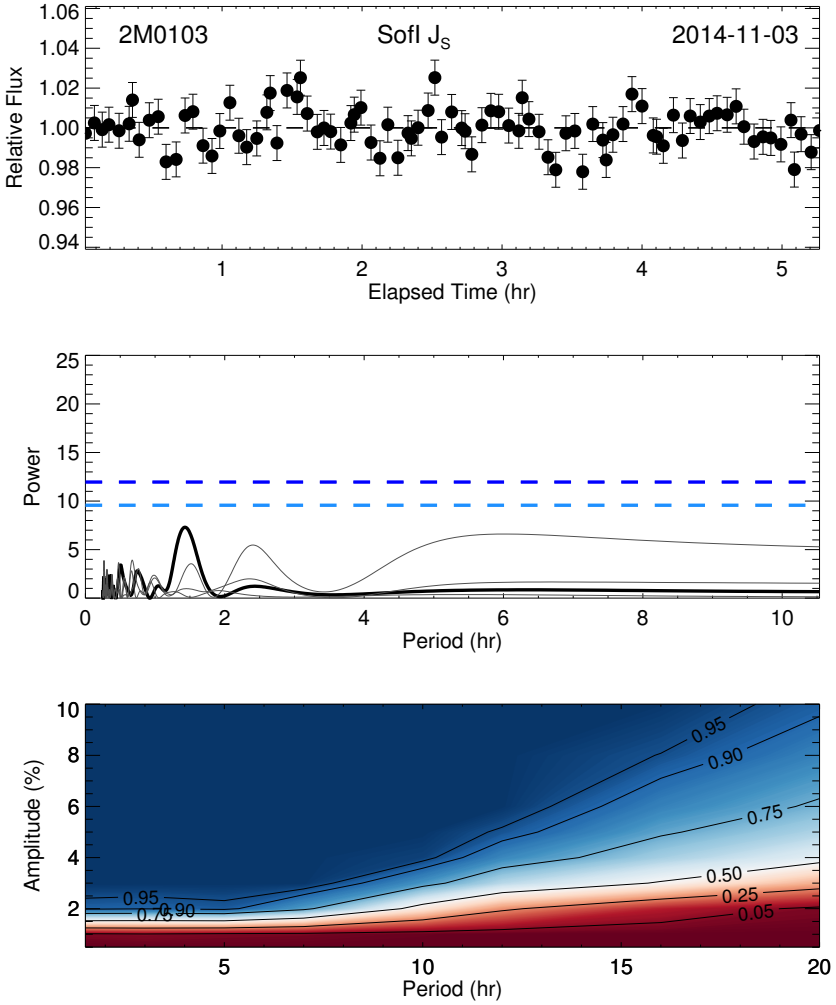

Figure A.3 Lightcurves, periodograms and sensitivity plots for non-variable objects.

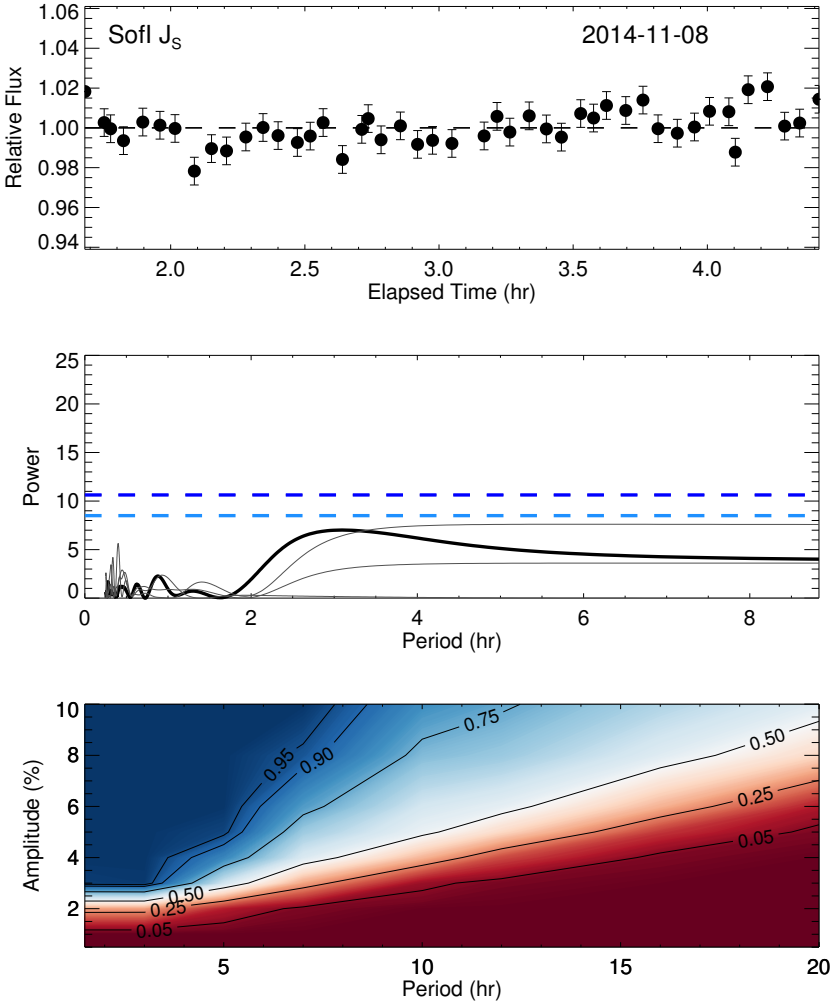

Figure A.3 Lightcurves, periodograms and sensitivity plots for non-variable objects.

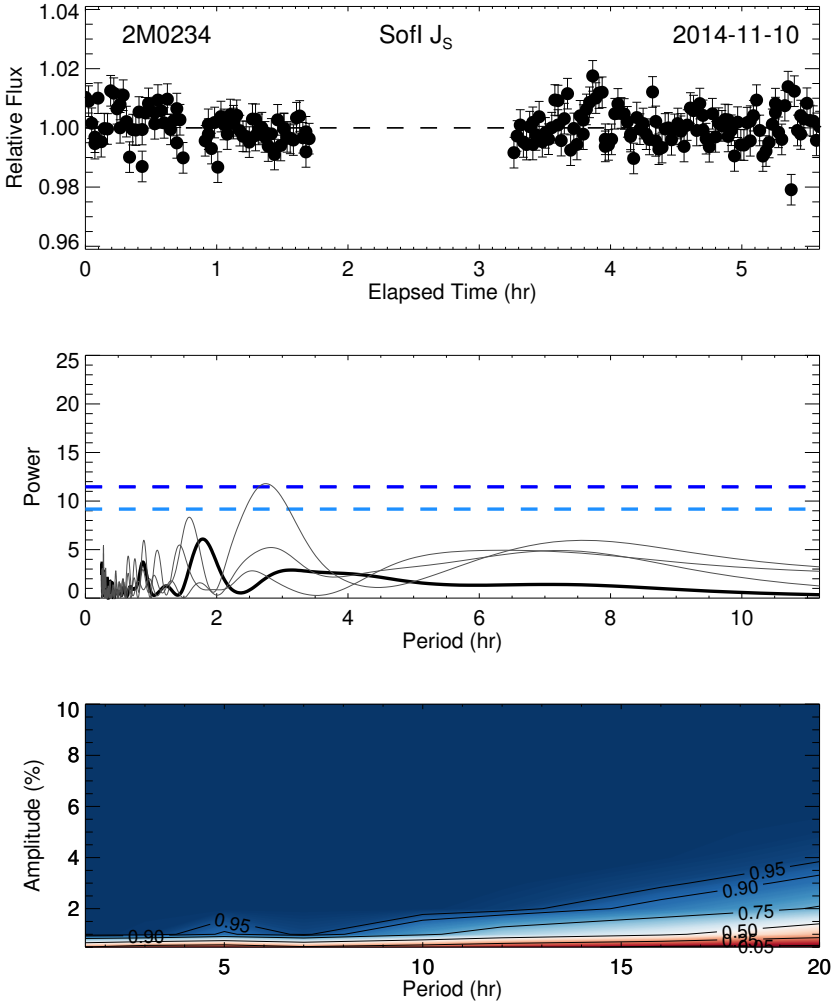

Figure A.3 Lightcurves, periodograms and sensitivity plots for non-variable objects.

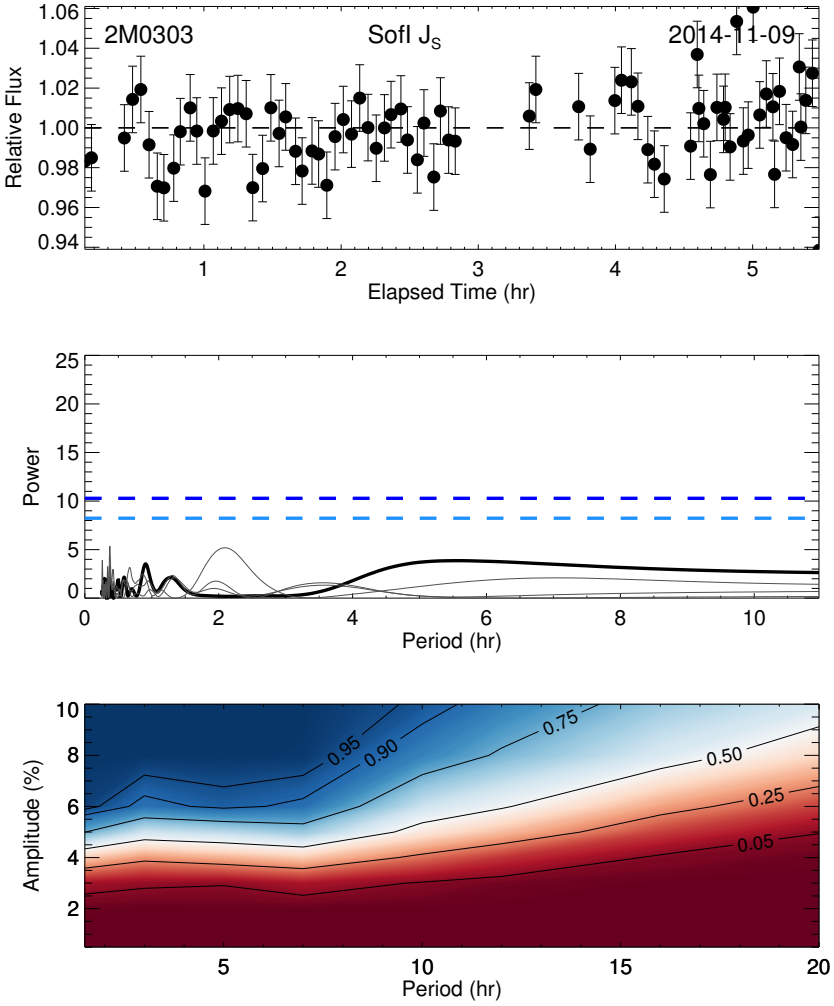

Figure A.3 Lightcurves, periodograms and sensitivity plots for non-variable objects.

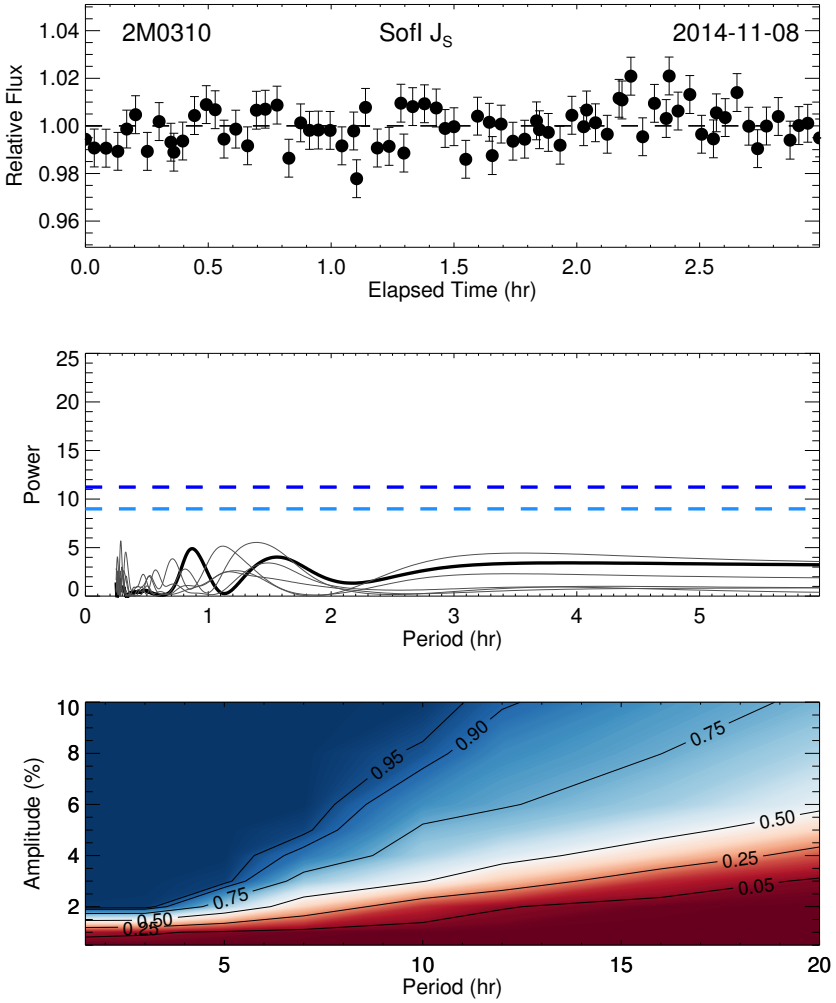

Figure A.3 Lightcurves, periodograms and sensitivity plots for non-variable objects.

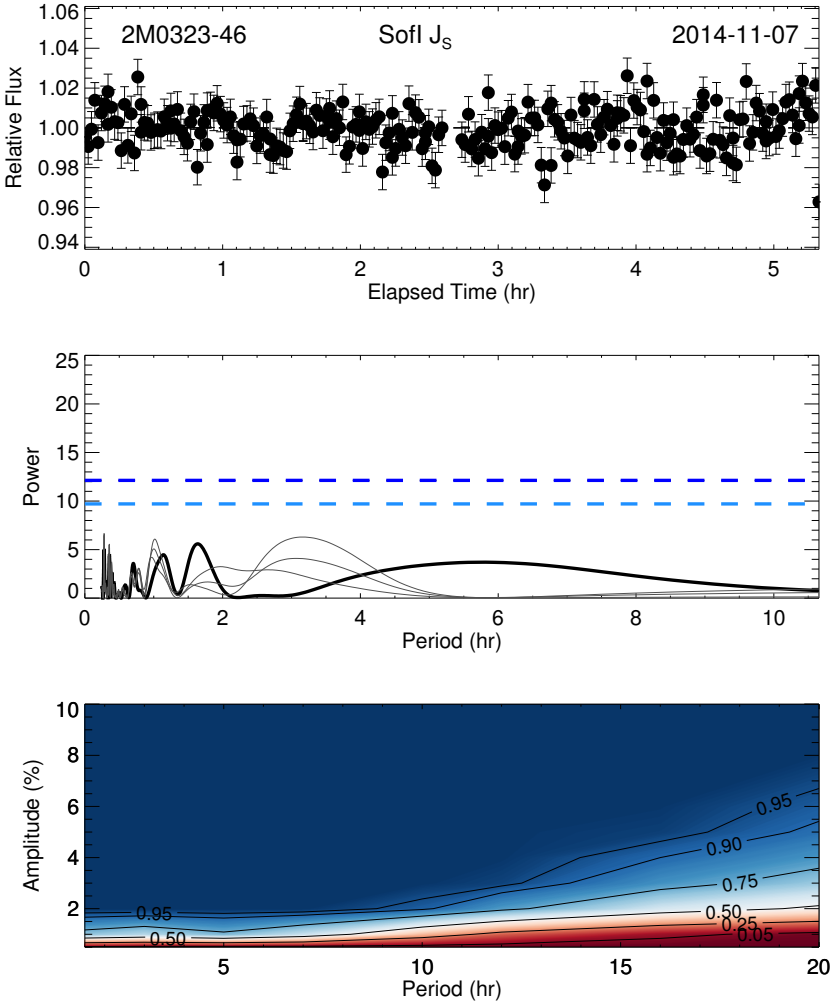

Figure A.3 Lightcurves, periodograms and sensitivity plots for non-variable objects

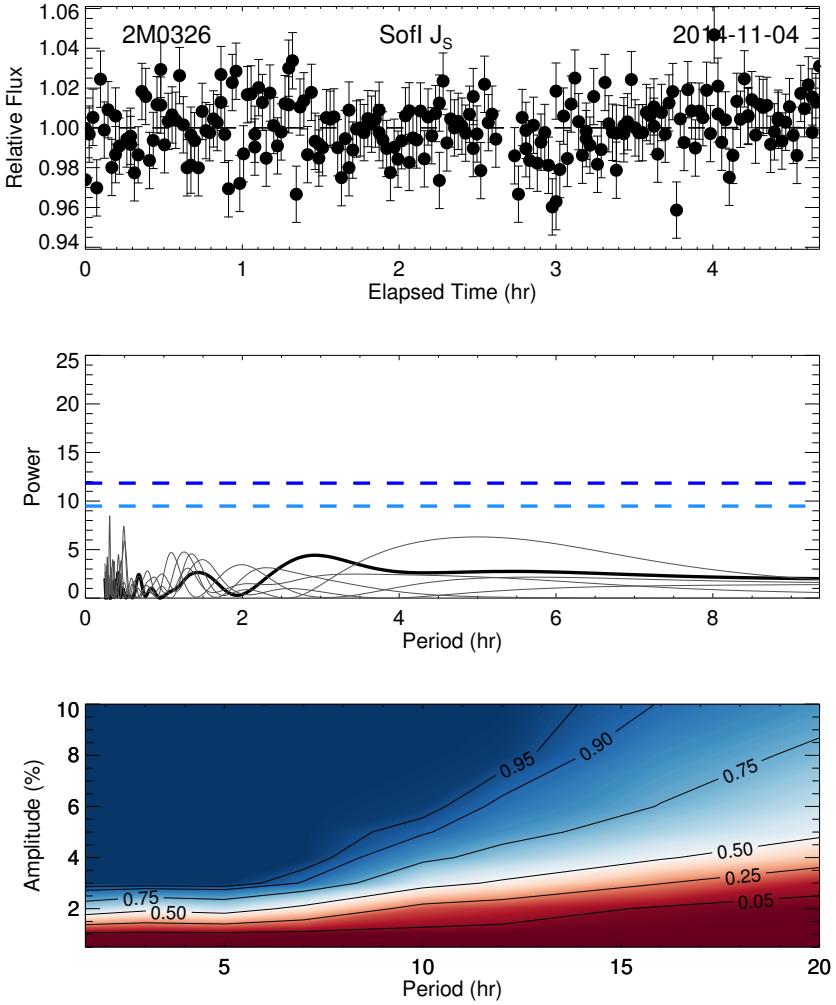

Figure A.3 Lightcurves, periodograms and sensitivity plots for non-variable objects.

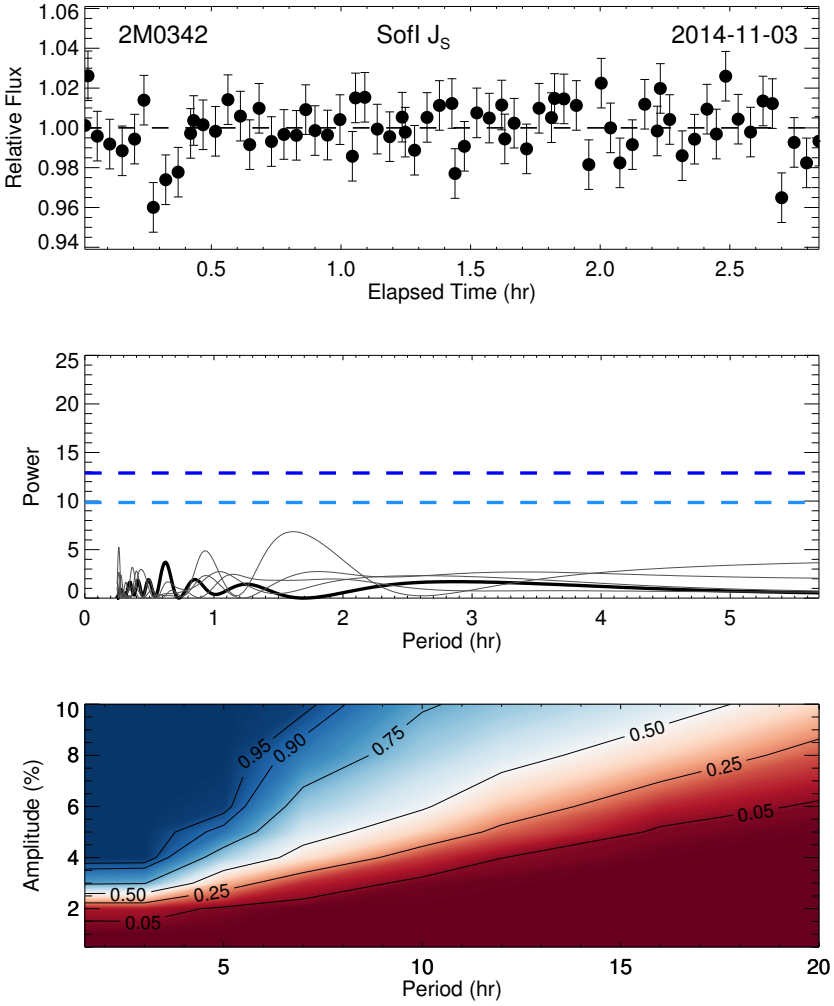

Figure A.3 Lightcurves, periodograms and sensitivity plots for non-variable objects.

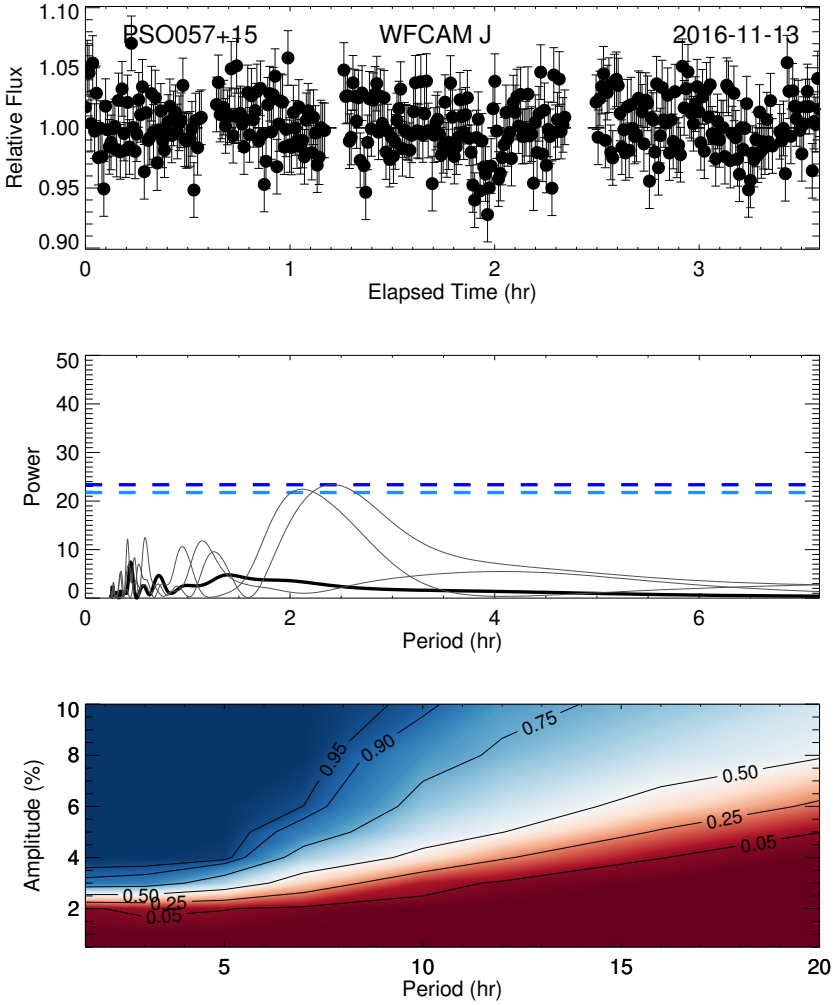

Figure A.3 Lightcurves, periodograms and sensitivity plots for non-variable objects.

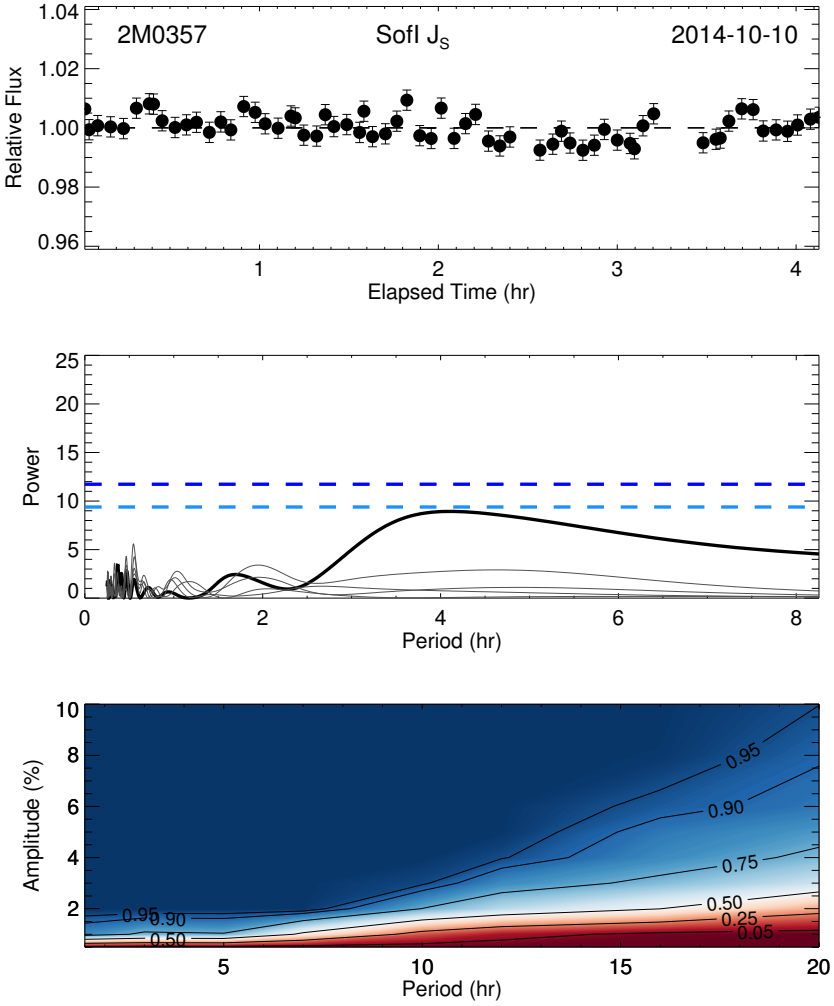

Figure A.3 Lightcurves, periodograms and sensitivity plots for non-variable objects.

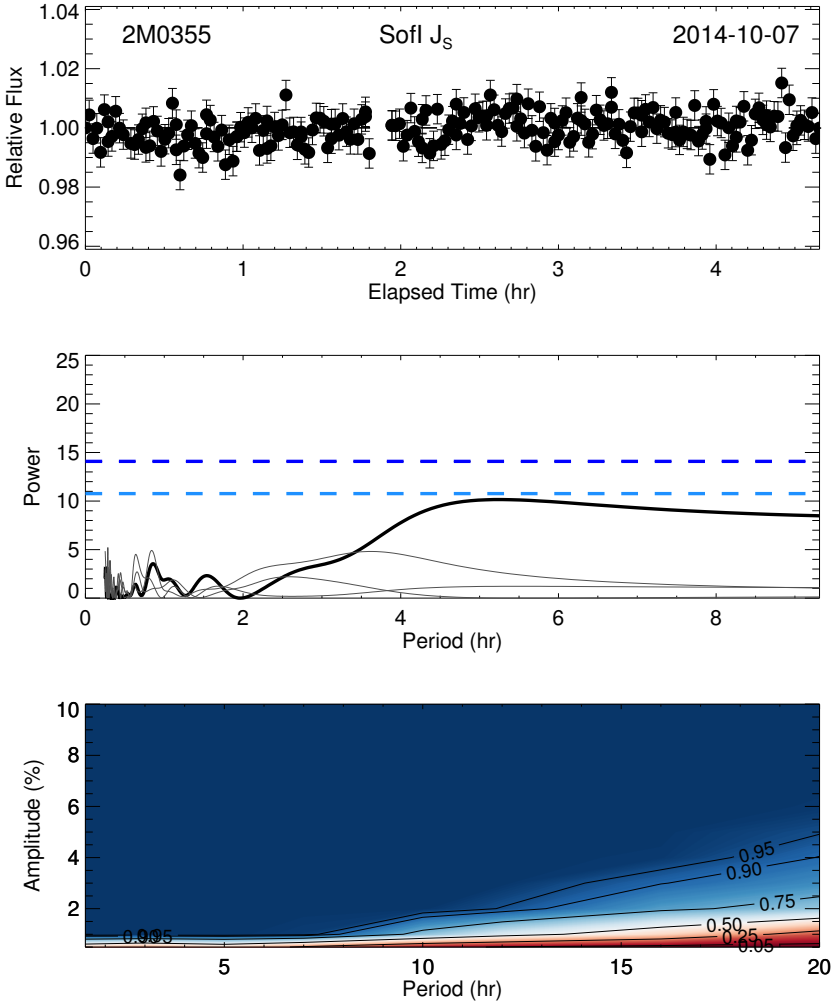

Figure A.3 Lightcurves, periodograms and sensitivity plots for non-variable objects.

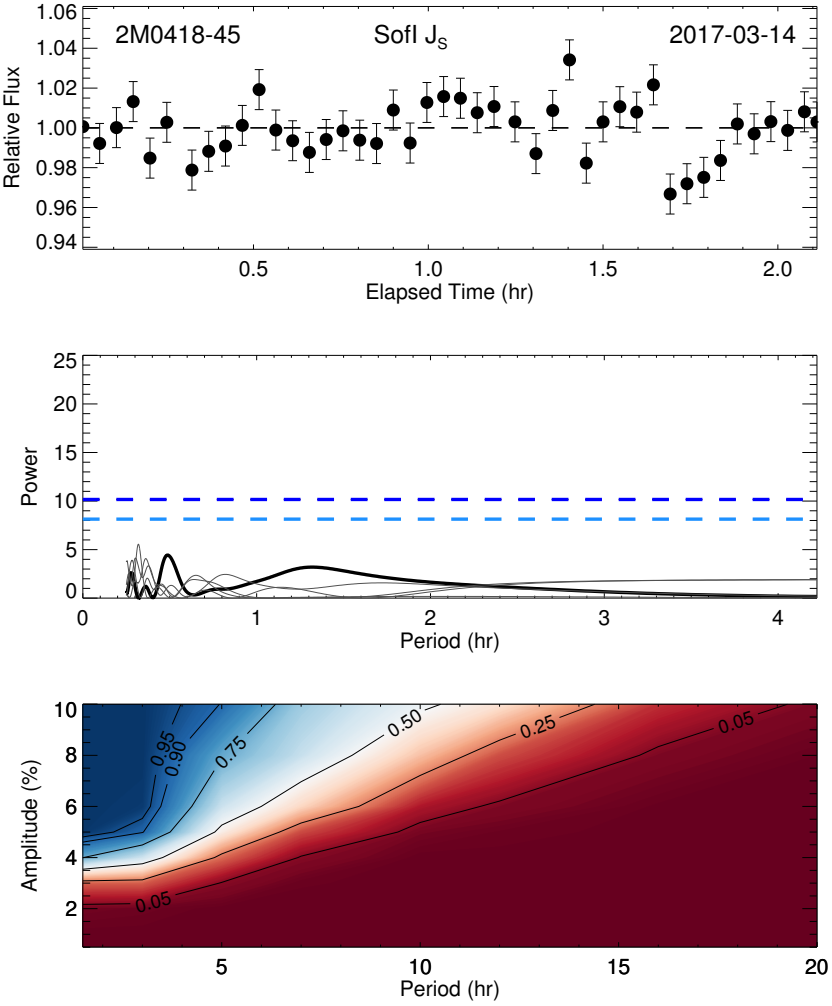

Figure A.3 Lightcurves, periodograms and sensitivity plots for non-variable objects.

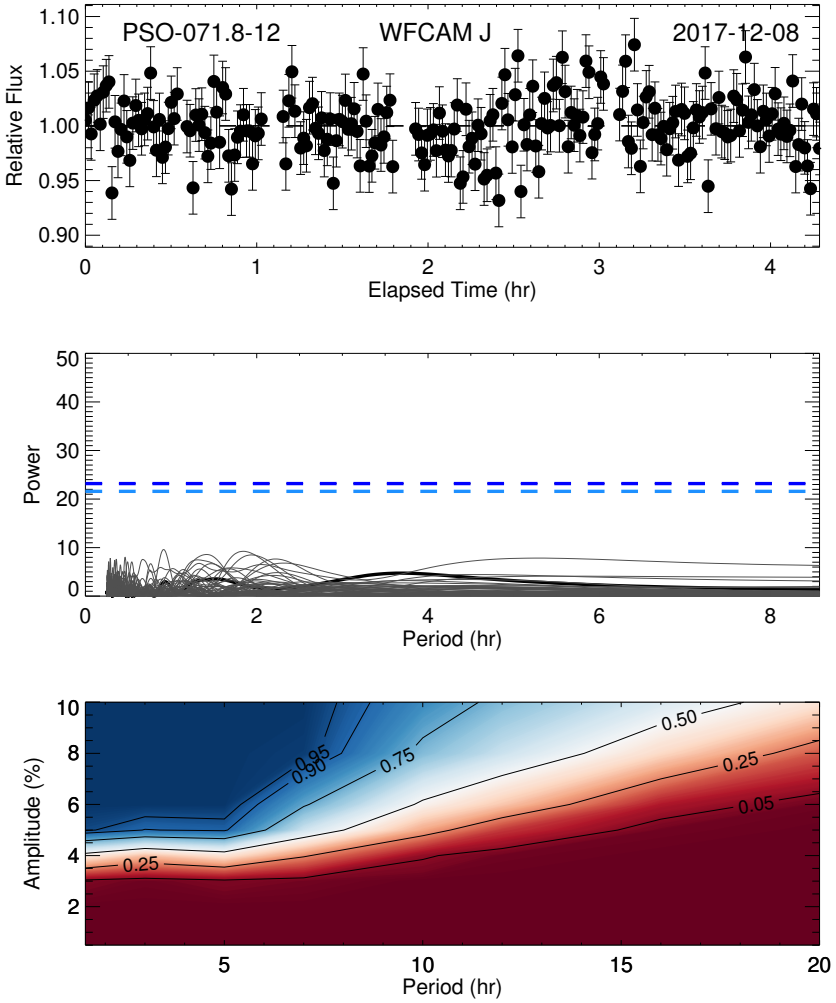

Figure A.3 Lightcurves, periodograms and sensitivity plots for non-variable objects.

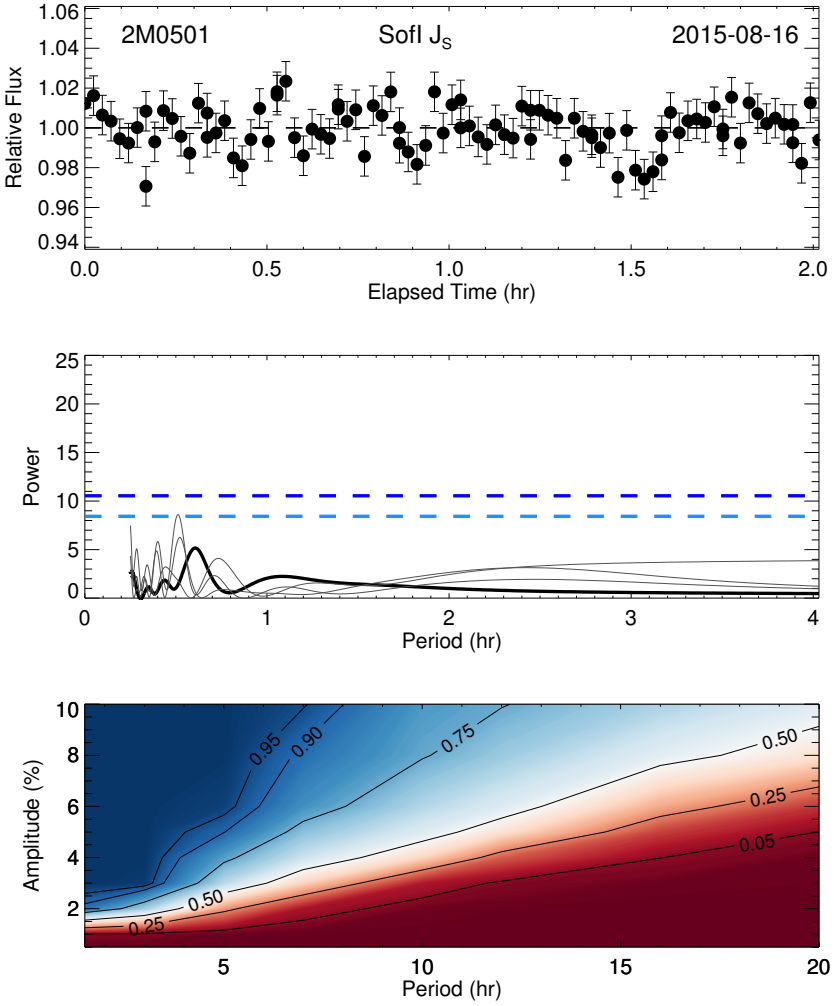

Figure A.3 Lightcurves, periodograms and sensitivity plots for non-variable objects.

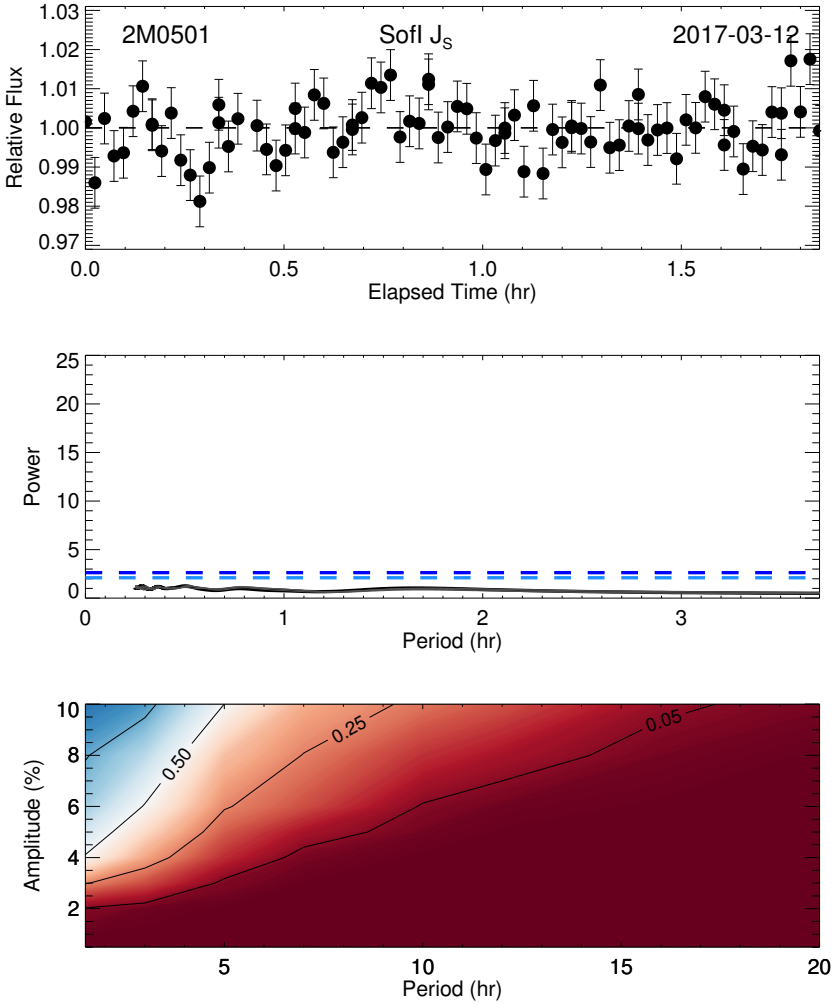

Figure A.3 Lightcurves, periodograms and sensitivity plots for non-variable objects.

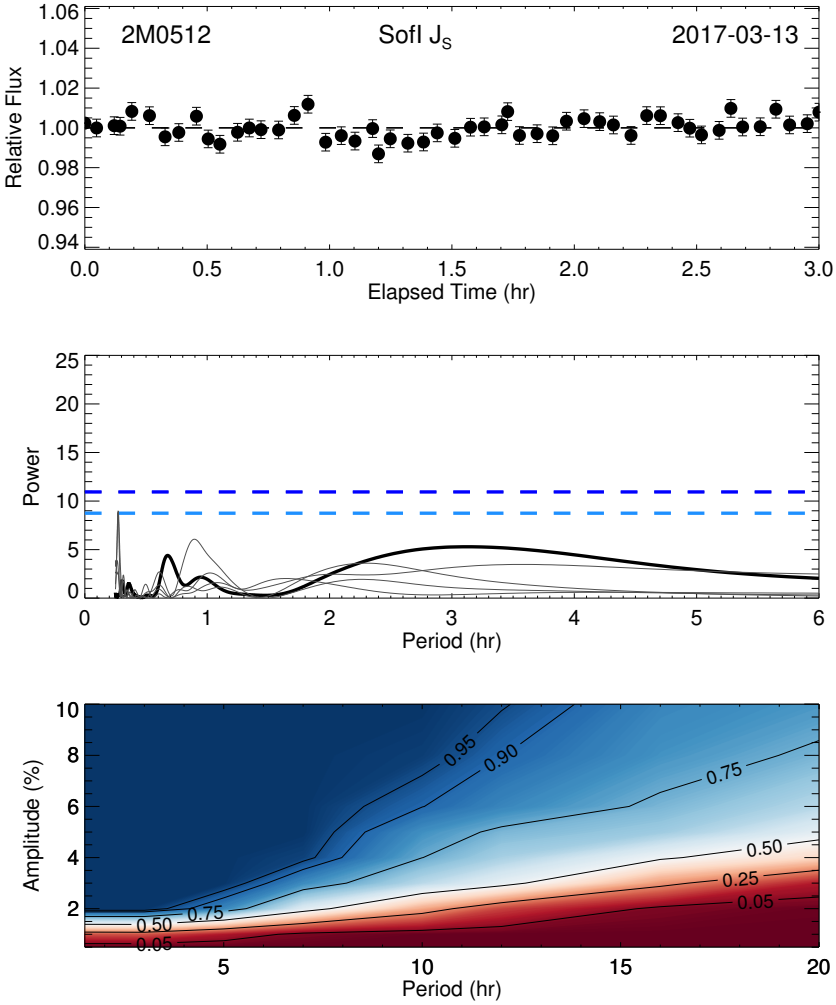

Figure A.3 Lightcurves, periodograms and sensitivity plots for non-variable objects.

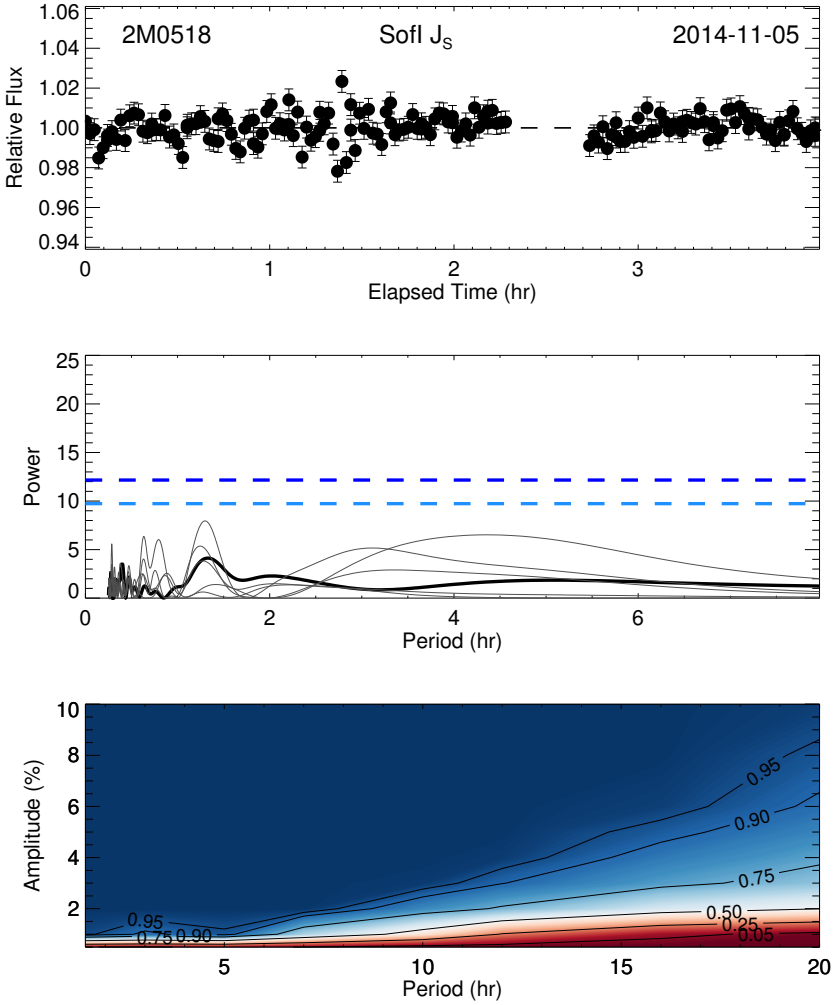

Figure A.3 Lightcurves, periodograms and sensitivity plots for non-variable objects.

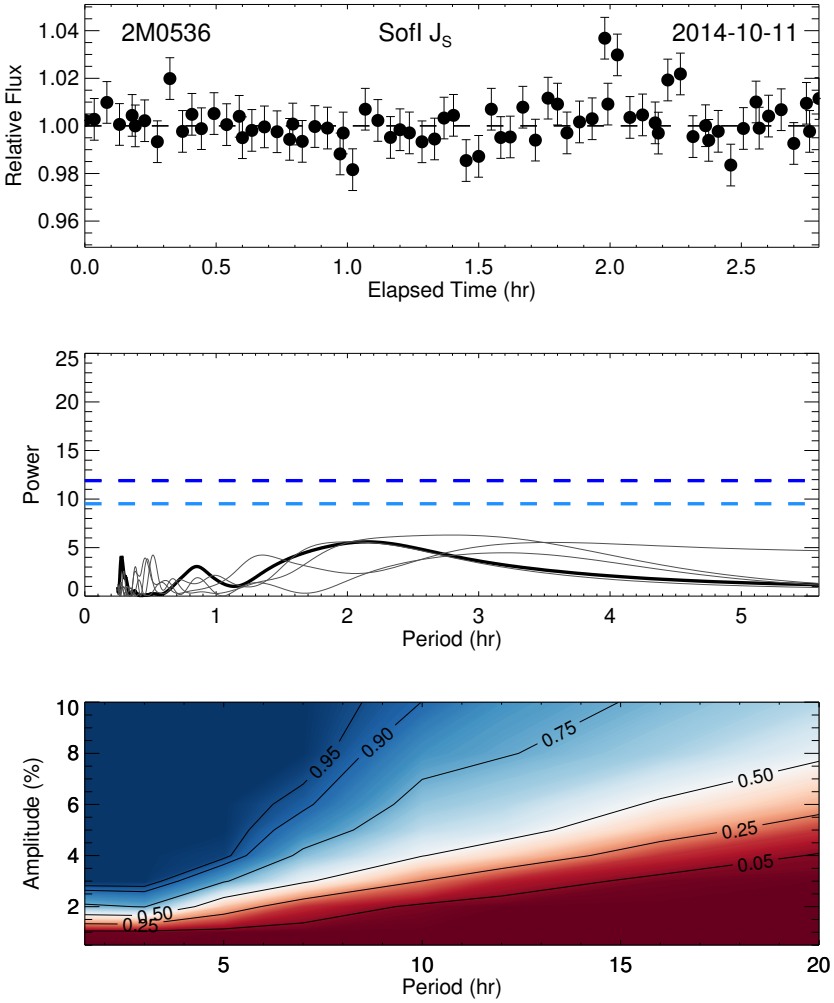

Figure A.3 Lightcurves, periodograms and sensitivity plots for non-variable objects.

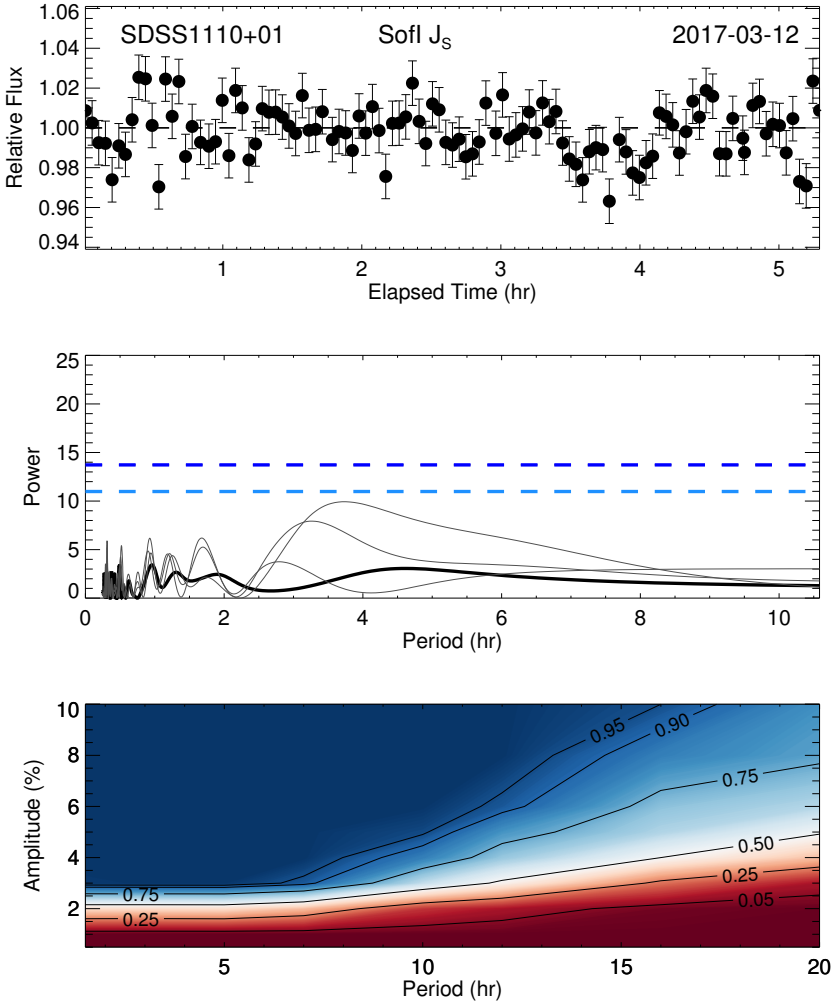

Figure A.3 Lightcurves, periodograms and sensitivity plots for non-variable objects.

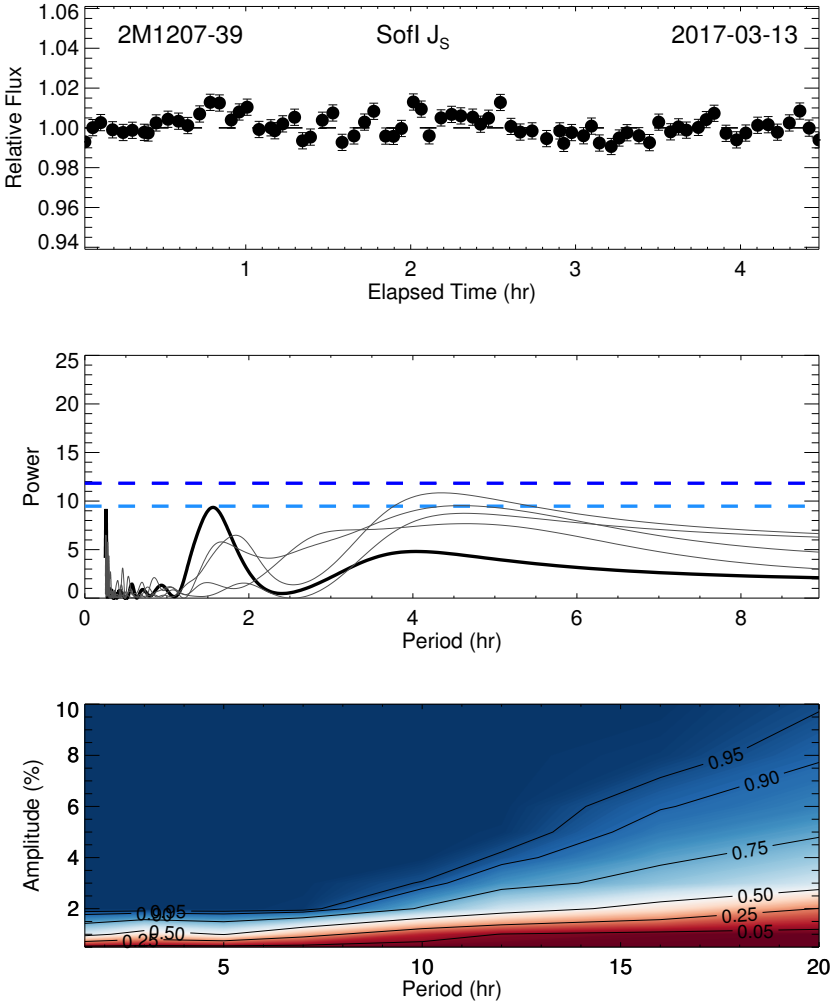

Figure A.3 Lightcurves, periodograms and sensitivity plots for non-variable objects.

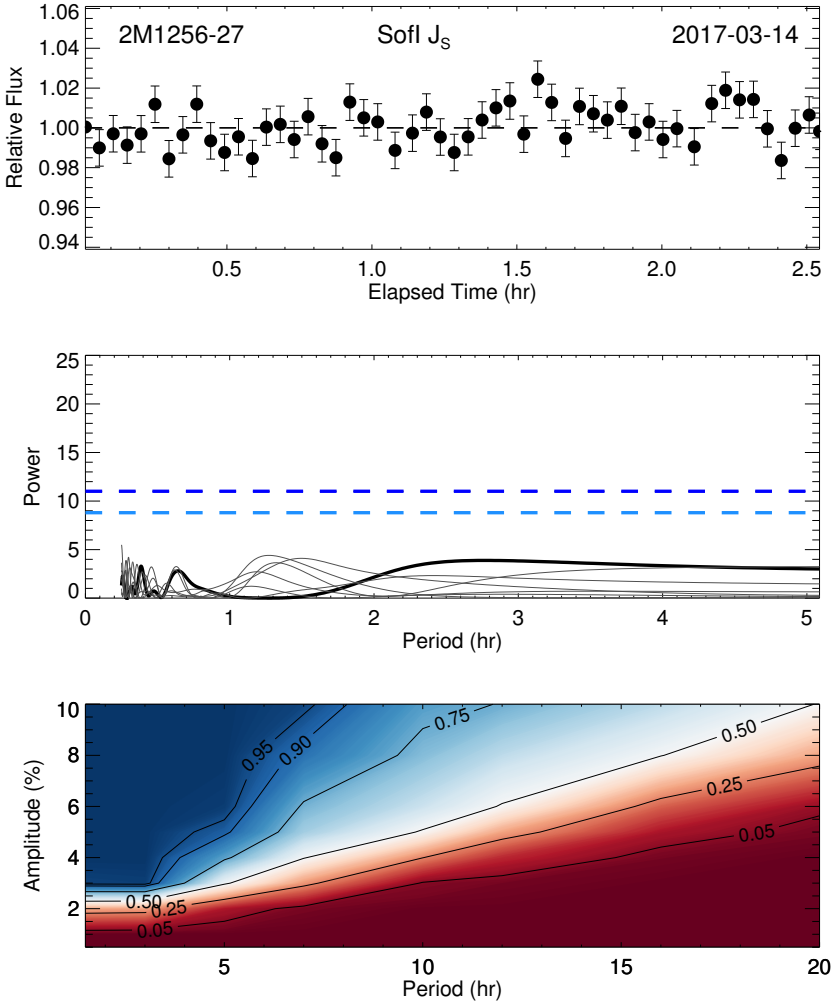

Figure A.3 Lightcurves, periodograms and sensitivity plots for non-variable objects.

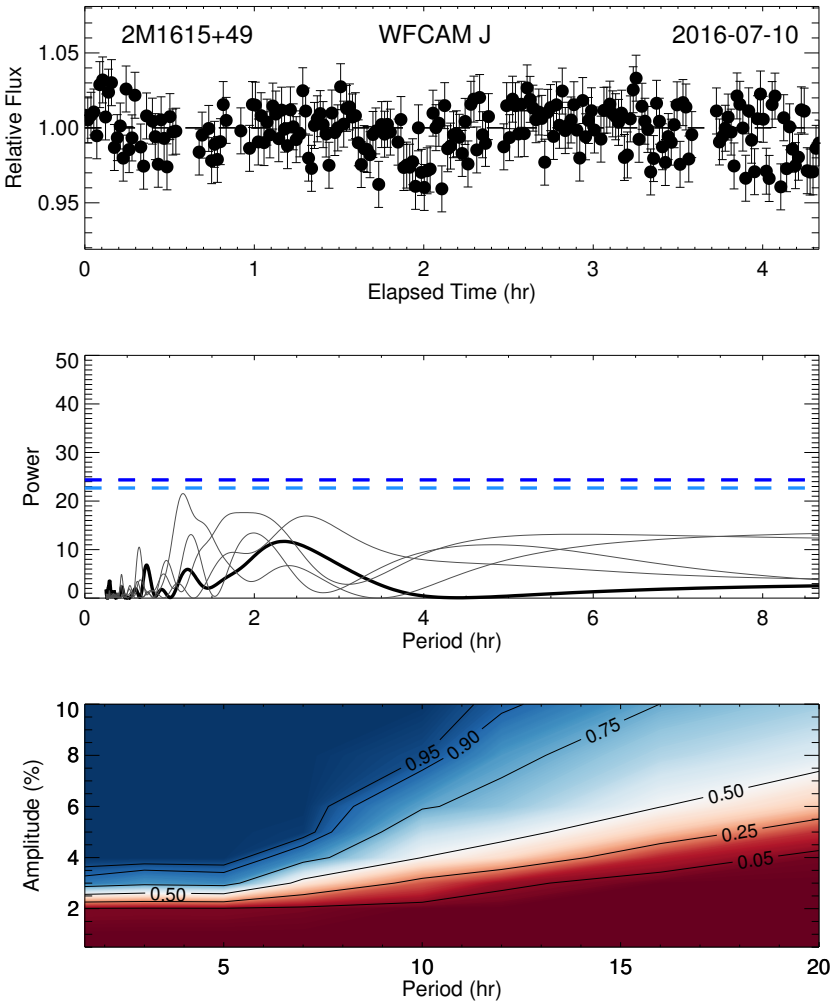

Figure A.3 Lightcurves, periodograms and sensitivity plots for non-variable objects.

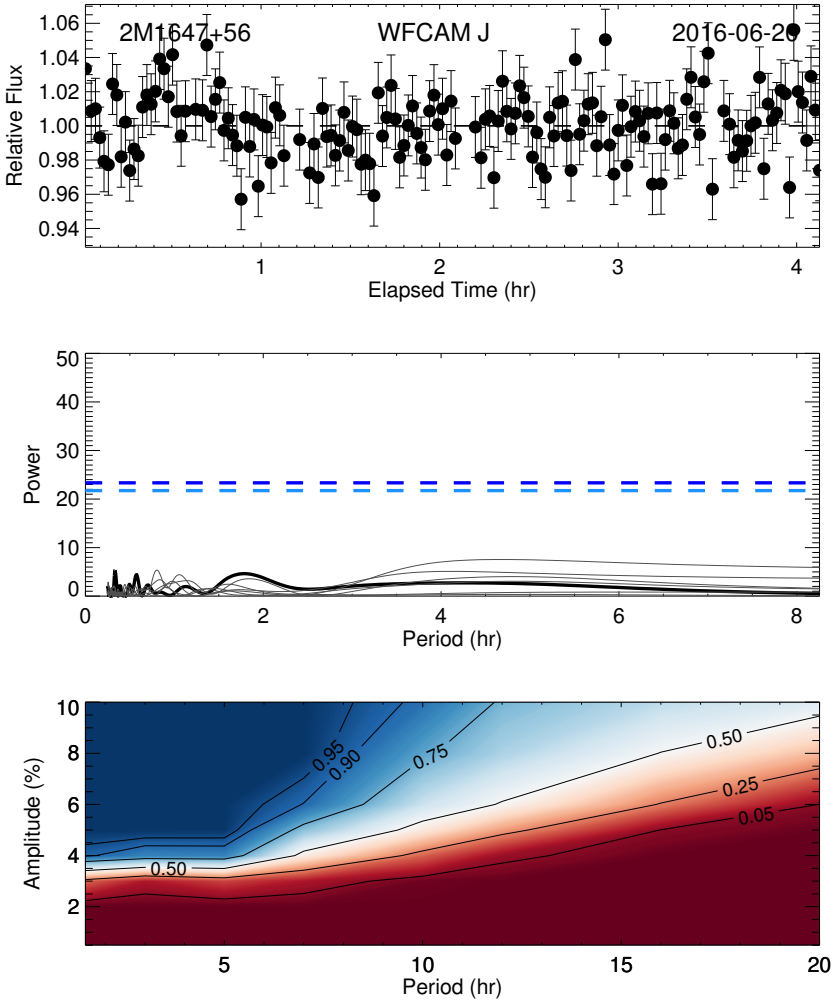

Figure A.3 Lightcurves, periodograms and sensitivity plots for non-variable objects.

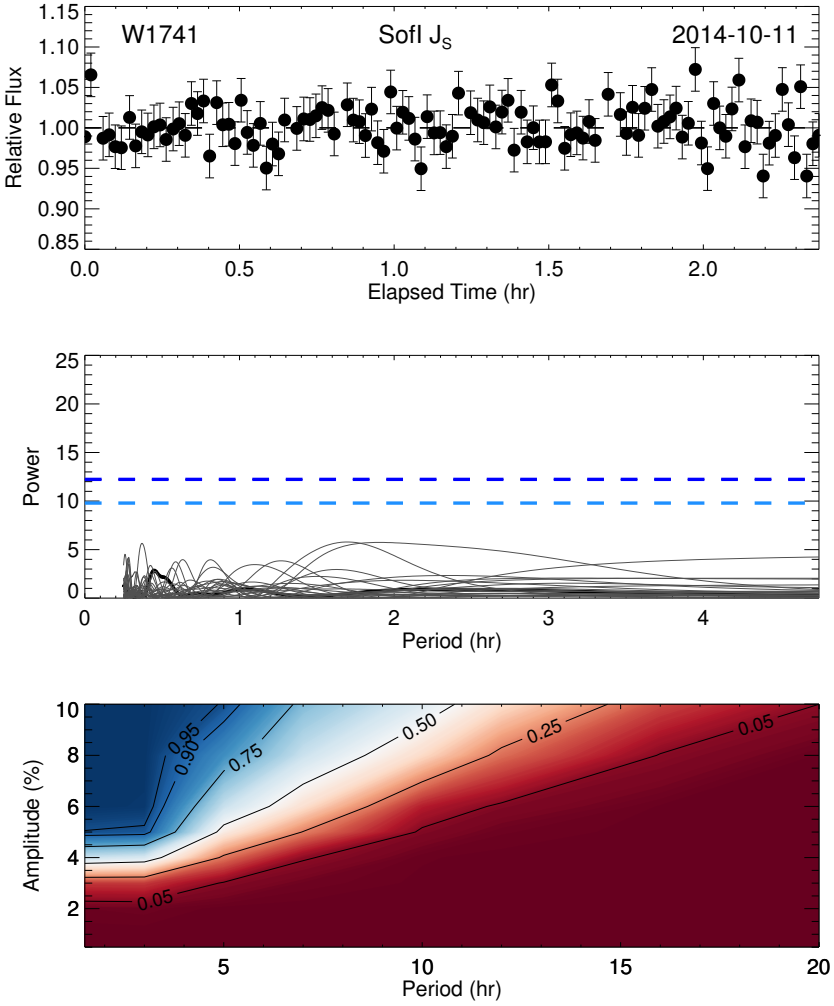

Figure A.3 Lightcurves, periodograms and sensitivity plots for non-variable objects.

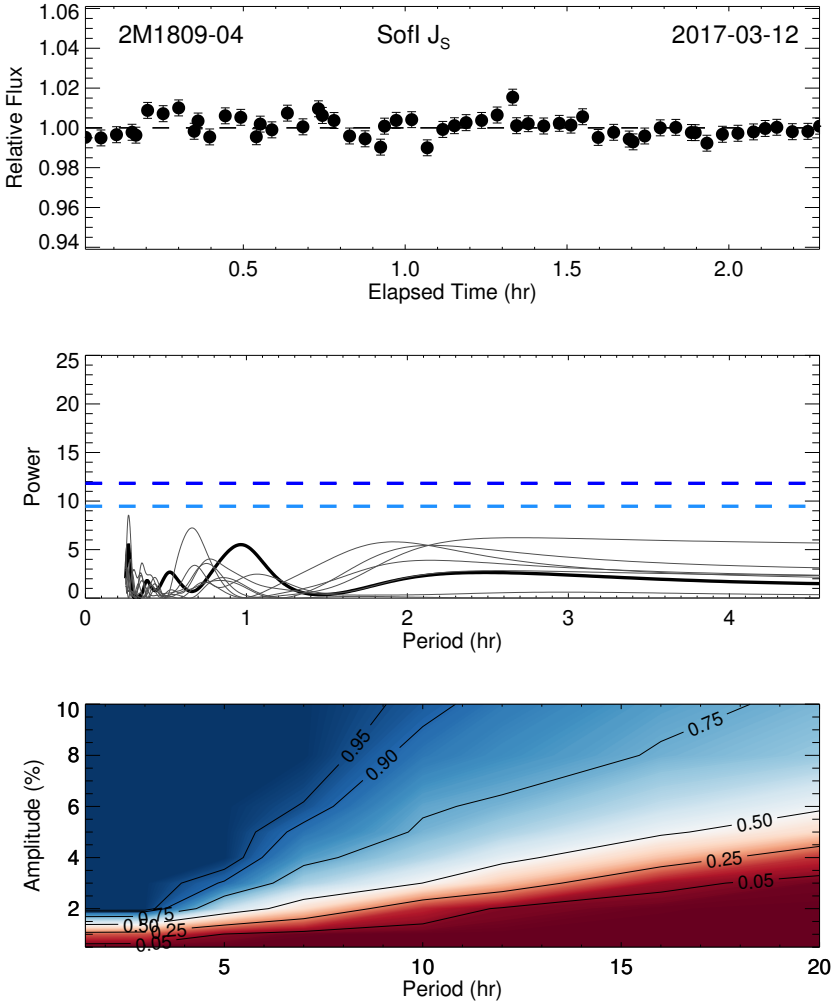

Figure A.3 Lightcurves, periodograms and sensitivity plots for non-variable objects.

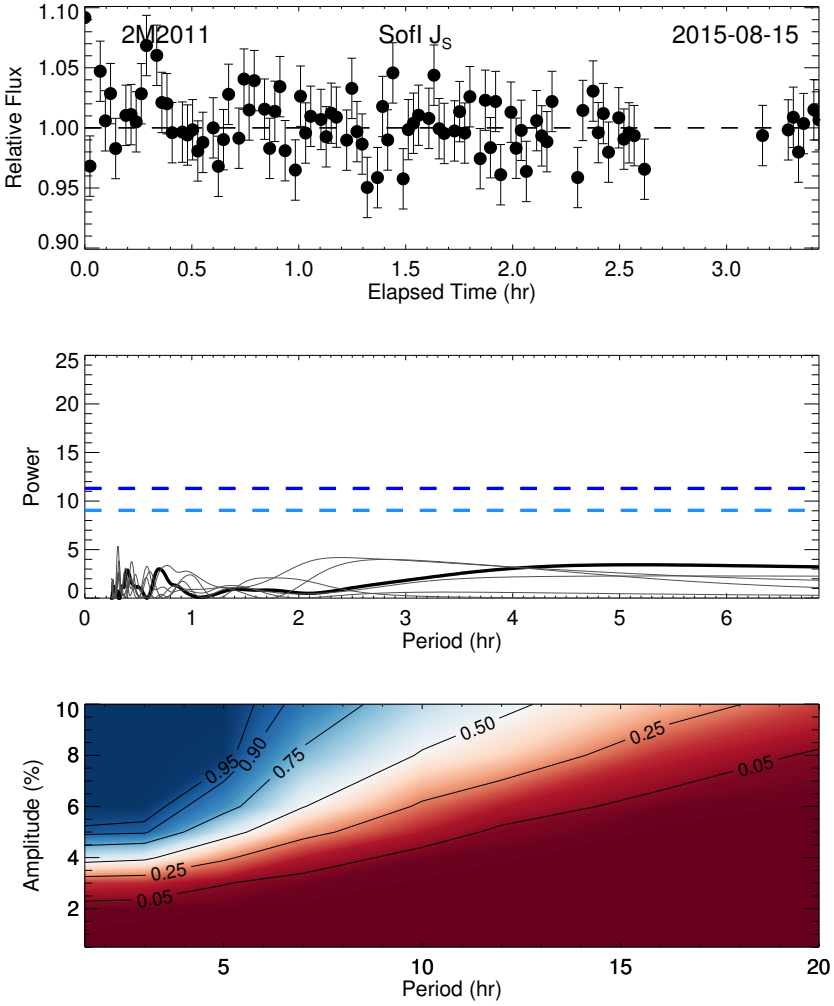

Figure A.3 Lightcurves, periodograms and sensitivity plots for non-variable objects.

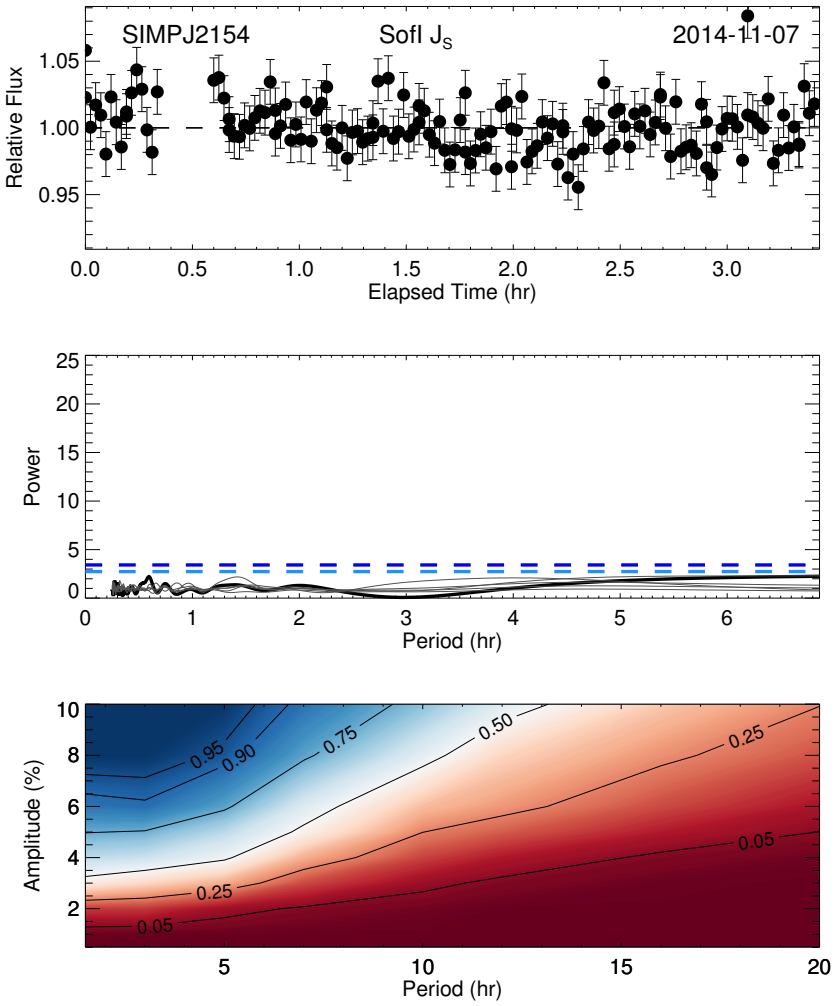

Figure A.3 Lightcurves, periodograms and sensitivity plots for non-variable objects.

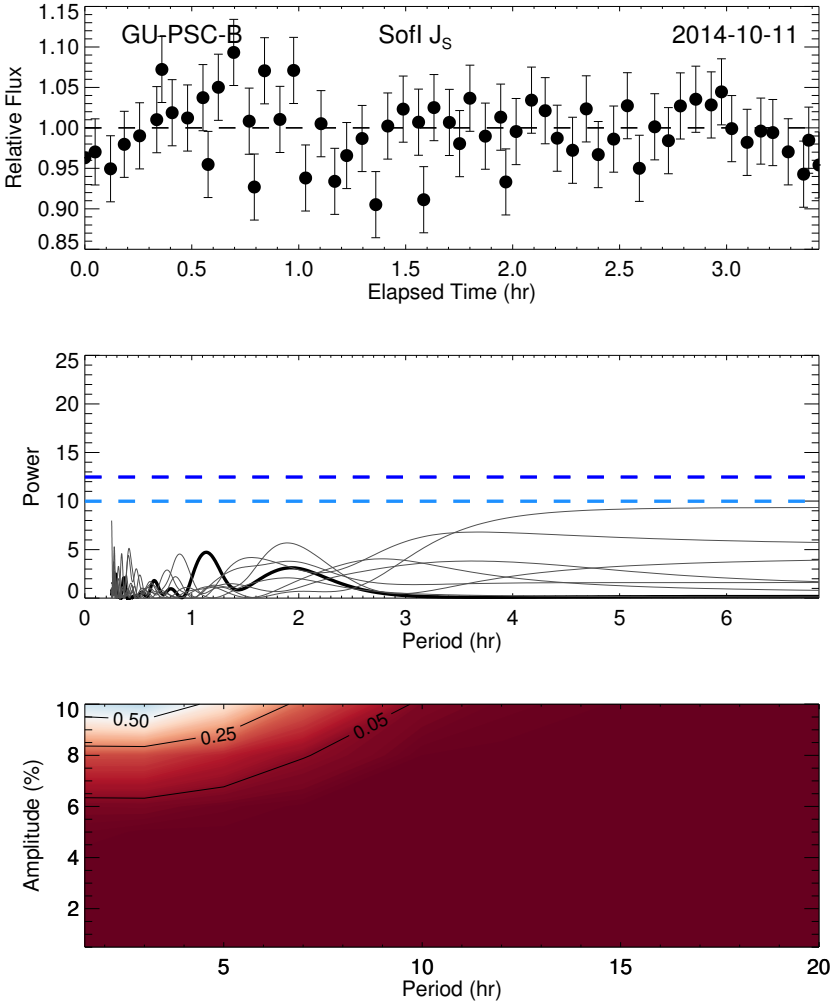

Figure A.3 Lightcurves, periodograms and sensitivity plots for non-variable objects.

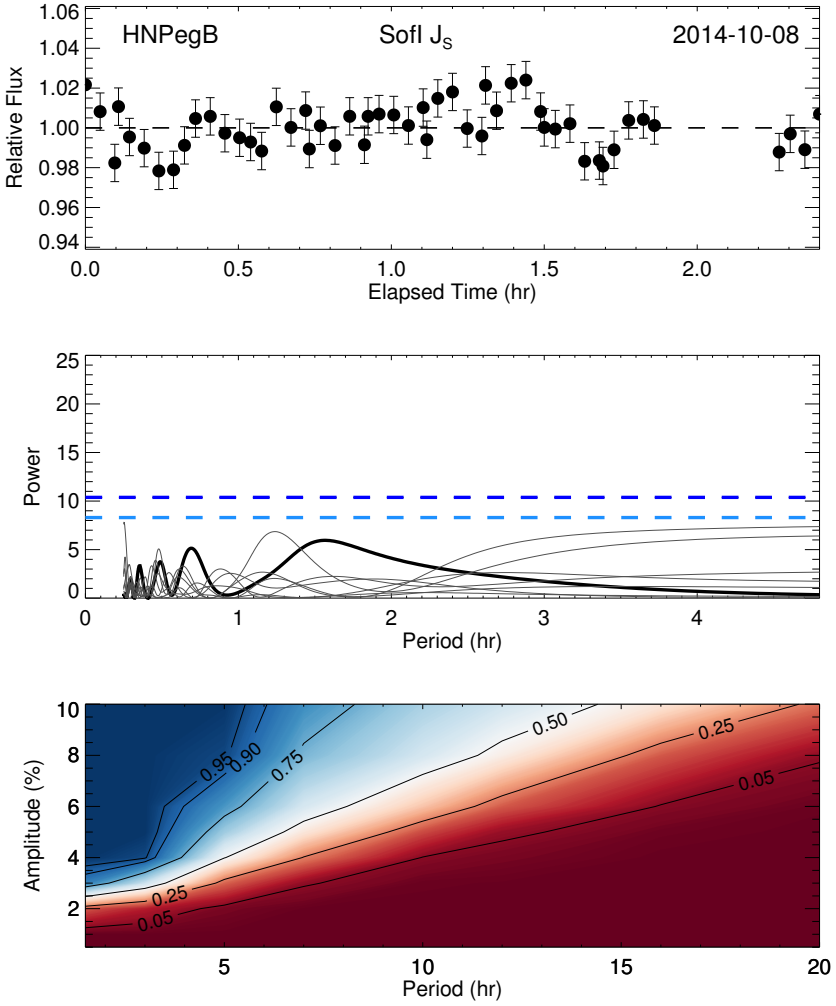

Figure A.3 Lightcurves, periodograms and sensitivity plots for non-variable objects.

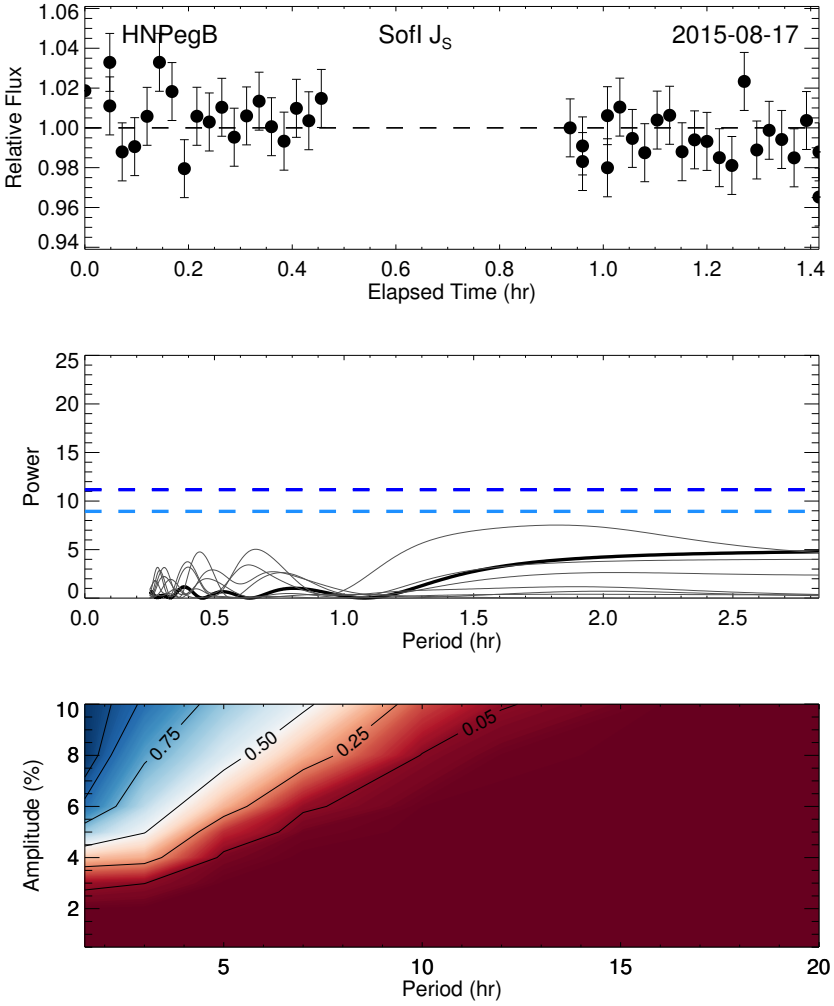

Figure A.3 Lightcurves, periodograms and sensitivity plots for non-variable objects.

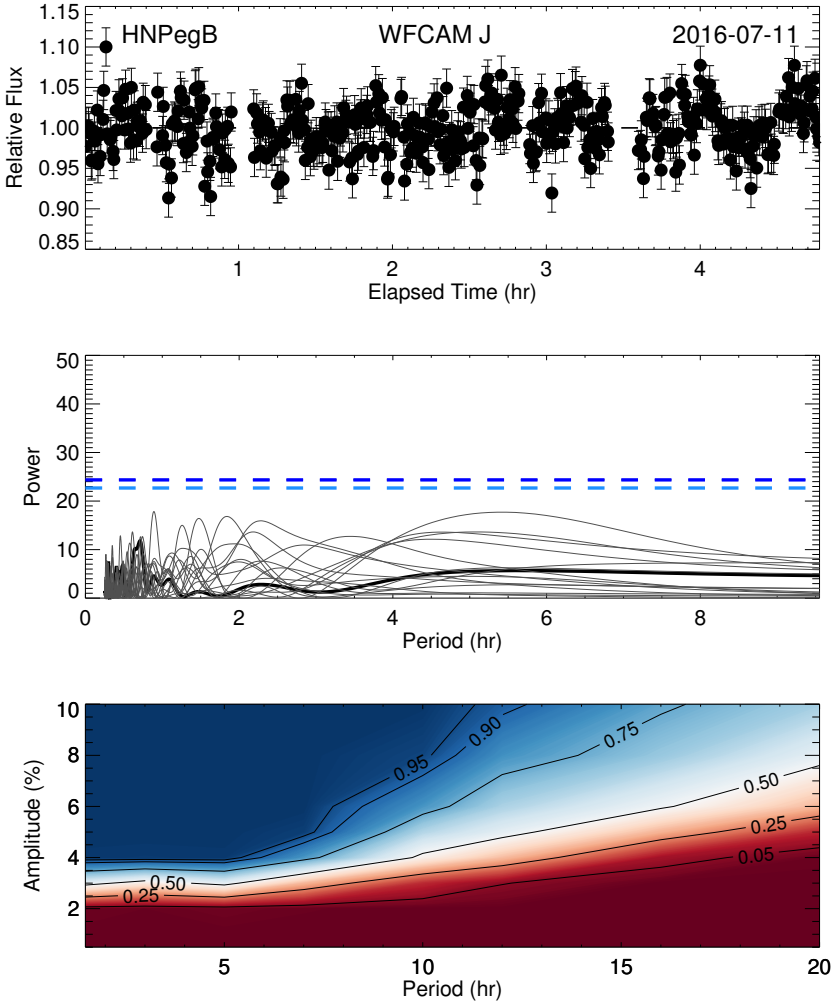

Figure A.3 Lightcurves, periodograms and sensitivity plots for non-variable objects.

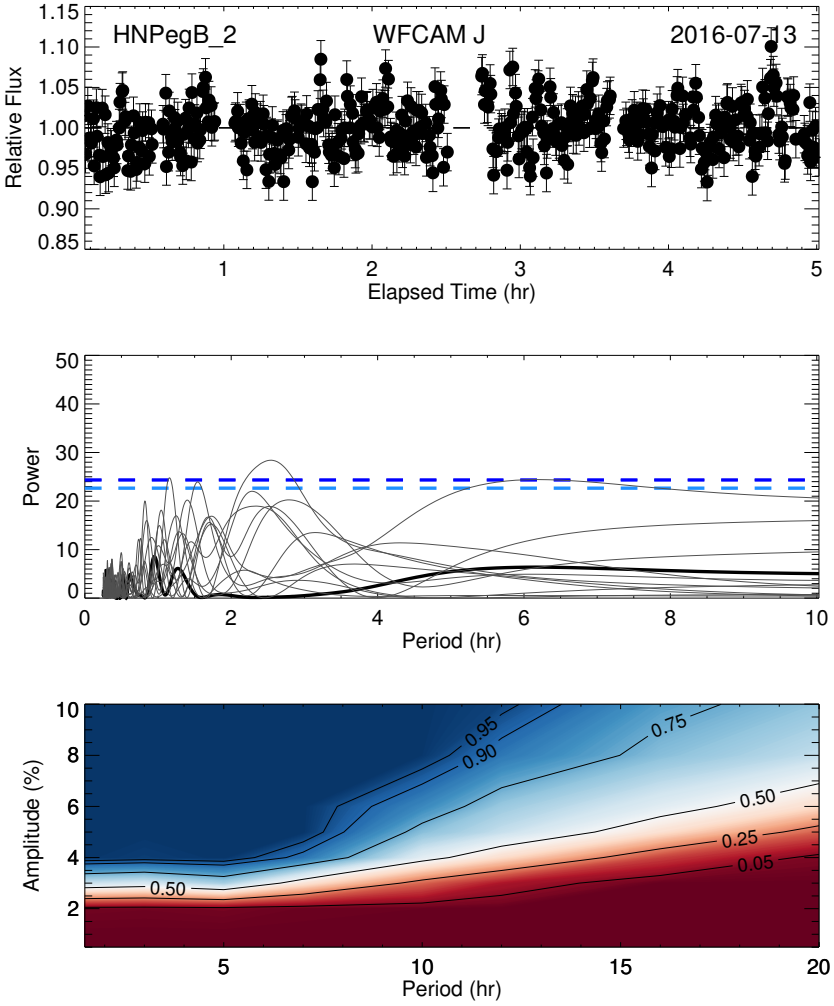

Figure A.3 Lightcurves, periodograms and sensitivity plots for non-variable objects.

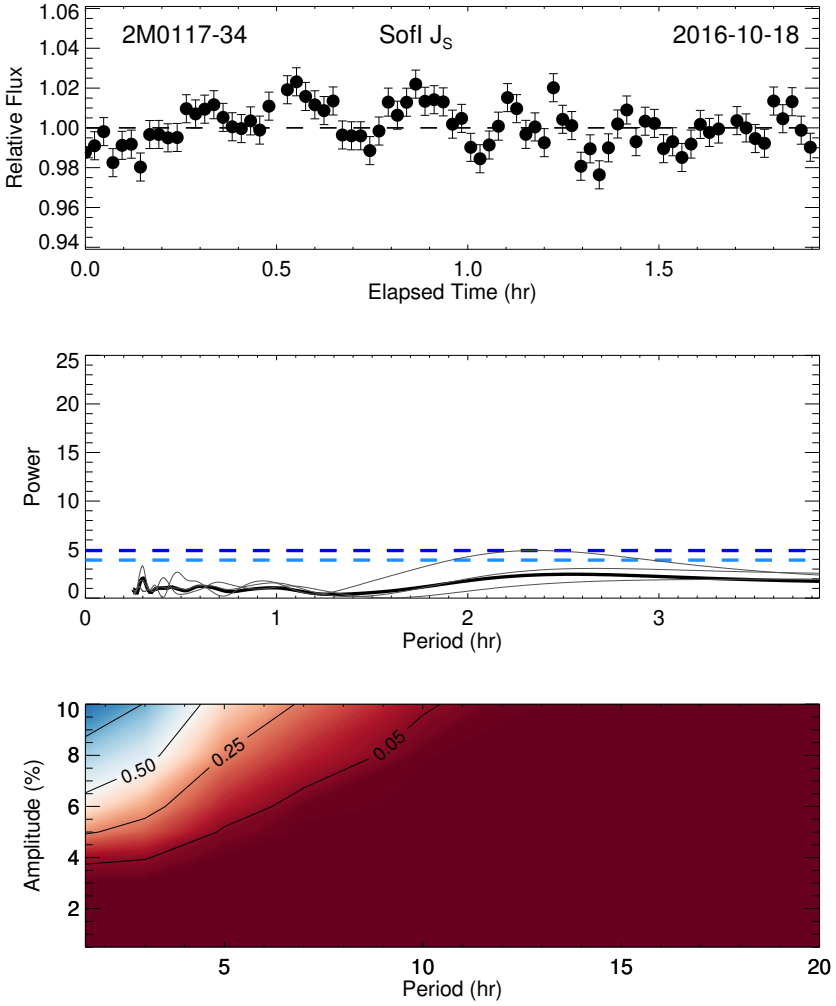

Figure A.4 Lightcurves, periodograms and sensitivity plots for poor quality observations

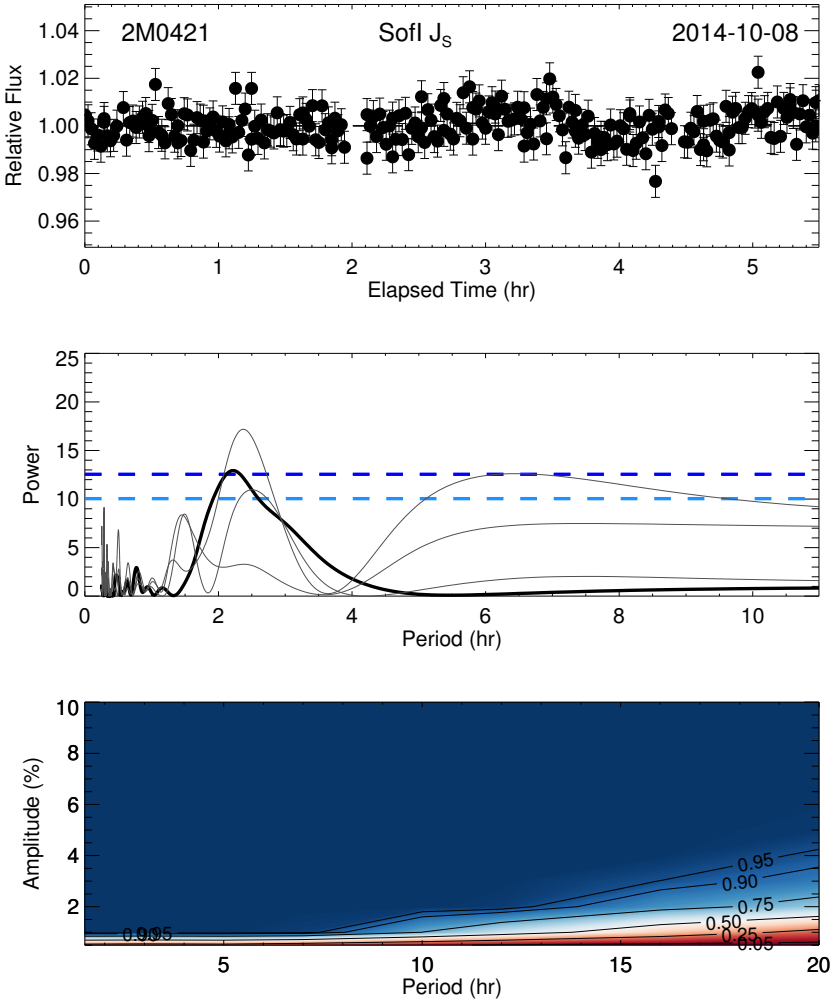

Figure A.4 Lightcurves, periodograms and sensitivity plots for poor quality observations

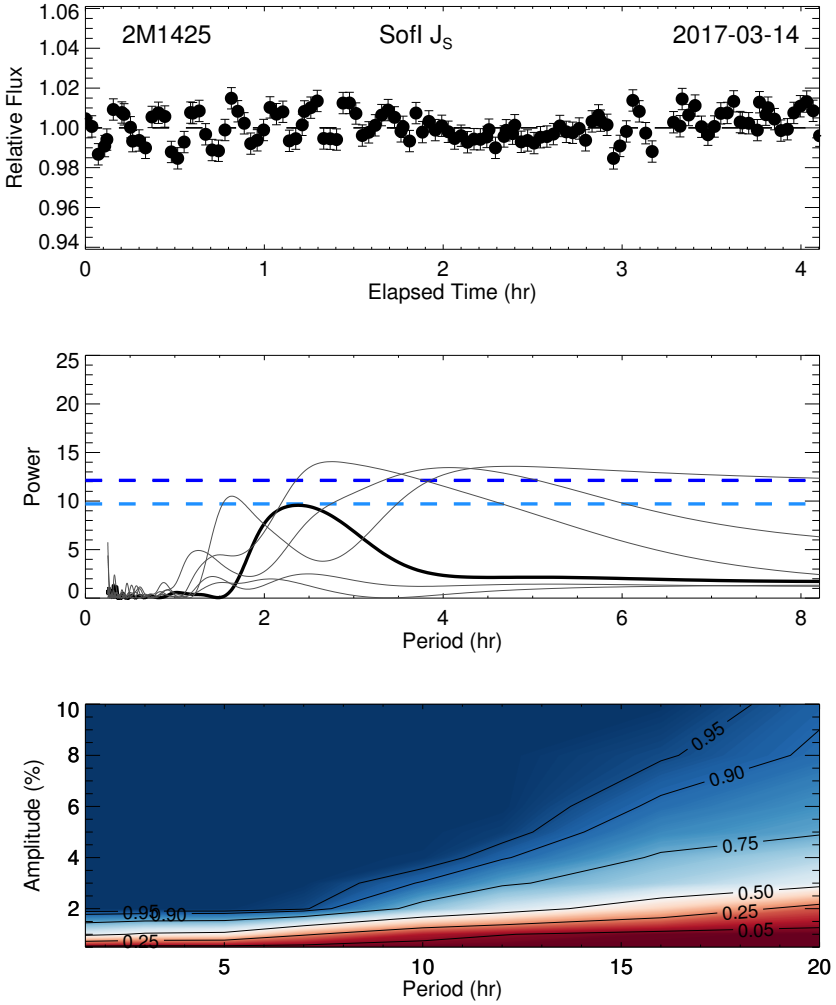

Figure A.4 Lightcurves, periodograms and sensitivity plots for poor quality observations

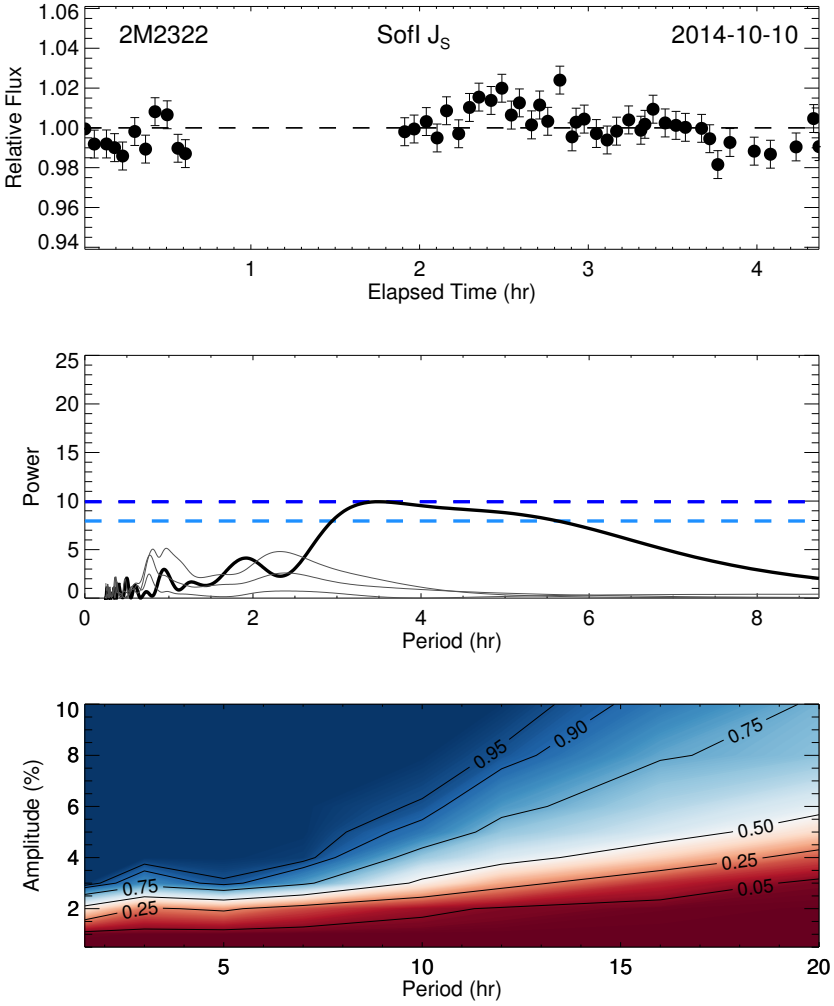

Figure A.4 Lightcurves, periodograms and sensitivity plots for poor quality observations

Bibliography

Ackerman, A. S., & Marley, M. S. 2001, Astrophysical Journal, 765, 872

Akritas, M. G., & Siebert, J. 1996, Monthly Notices of the Royal Astronomical Society, 278, 919

Allard, F., Homeier, D., & Freytag, B. 2012, Philosophical Transactions of the Royal Society A: Mathematical, Physical and Engineering Sciences, 370, 2765

Allard, N. F., Allard, F., Hauschildt, P. H., Kielkopf, J. F., & Machin, L. 2003, Astronomy & Astrophysics, 411, L473

Allers, K. N., Gallimore, J. F., Liu, M. C., & Dupuy, T. J. 2016, The Astrophysical Journal, 819, 133

Allers, K. N., & Liu, M. C. 2013, The Astrophysical Journal, 772, 79

Apai, D., Radigan, J., Buenzli, E., et al. 2013, The Astrophysical Journal, 768, 121

Apai, D., Kasper, M., Skemer, A., et al. 2016, The Astrophysical Journal, 820, 40

Apai, D., Karalidi, T., Marley, M. S., et al. 2017, Science, 357, 683

Artigau, É., Bouchard, S., Doyon, R., & Lafrenière, D. 2009, The Astrophysical Journal, 701, 1534

Bailer-Jones, C. A. L. 2004, Astronomy and Astrophysics, 419, 703

Baraffe, I., Chabrier, G., Allard, F., & Hauschildt, P. H. 2002, Astronomy & Astrophysics, 382, 563

Barenfeld, S. A., Bubar, E. J., Mamajek, E. E., & Young, P. A. 2013, The Astrophysical Journal, 766, 6

Barman, T. S., Macintosh, B., Konopacky, Q. M., & Marois, C. 2011, The Astrophysical Journal, 735, L39

Basri, G., Mohanty, S., Allard, F., et al. 2000, The Astrophysical Journal, 538, 363

Batygin, K. 2018, The Astronomical Journal, 155, 178

Bell, C. P. M., Mamajek, E. E., & Naylor, T. 2015, Monthly Notices of the Royal Astronomical Society, 454, 593

Berger, E., Rutledge, R. E., Reid, I. N., et al. 2005, The Astrophysical Journal, 627, 960

Bertoldi, F., Timmermann, R., Rosenthal, D., Drapatz, S., & Wright, C. M. 1999, Astronomy & Astrophysics, 346, 267

Best, W. M. J., Liu, M. C., Magnier, E. A., et al. 2015, The Astrophysical Journal, 814, 118

Beuzit, J.-L., Feldt, M., Dohlen, K., et al. 2008in (SPIE Digital Library), 12

Biller, B. 2013, Proceedings of the International Astronomical Union, 8, 1

—. 2017, Astronomical Review, 2857, 1

Biller, B. A., Allers, K., Liu, M. C., Close, L. M., & Dupuy, T. J. 2011, The Astrophysical Journal, 730, 39

Biller, B. A., Close, L. M., Masciadri, E., et al. 2007, The Astrophysical Journal Supplement Series, 173, 143

Biller, B. A., Crossfield, I. J. M., Mancini, L., et al. 2013, The Astrophysical Journal, 778, L10

Biller, B. A., Vos, J., Bonavita, M., et al. 2015, Astrophysical Journal Letters, 813, 1

Biller, B. A., Vos, J., Buenzli, E., et al. 2018, The Astronomical Journal, 155, 95

Blake, C. H., Charbonneau, D., & White, R. J. 2010, The Astrophysical Journal, 723, 684

Bonavita, M., de Mooij, E. J. W., & Jayawardhana, R. 2013, Publications of the Astronomical Society of the Pacific, 125, 849

Bonavita, M., Desidera, S., Thalmann, C., et al. 2016, Astronomy & Astrophysics, 593, A38

Bonnefoy, M., Marleau, G.-D., Galicher, R., et al. 2014, Astronomy & Astrophysics, 567, L9

Bonnefoy, M., Zurlo, A., Baudino, J. L., et al. 2016, Astronomy & Astrophysics, 587, A58

Bouvier, J., Matt, S. P., Mohanty, S., et al. 2014, in Protostars and Planets VI (University of Arizona Press)

Bouy, H., Brandner, W., Mart, E. L., Delfosse, X., & Allard, F. 2003, The Astronomical Journal, 1526

Bowler, B. P. 2016, Publications of the Astronomical Society of the Pacific, 128, 1

Buenzli, E., Apai, D., Radigan, J., Reid, I. N., & Flateau, D. 2014, The Astrophysical Journal, 782, 77

Buenzli, E., Marley, M. S., Apai, D., et al. 2015a, The Astrophysical Journal, 812, 163

Buenzli, E., Saumon, D., Marley, M. S., et al. 2015b, The Astrophysical Journal, 798, 127

Buenzli, E., Apai, D., Morley, C. V., et al. 2012, The Astrophysical Journal, 760, L31

Burgasser, A. J., Reid, I. N., Siegler, N., et al. 2007in

Burgasser, A. J., Kirkpatrick, J. D., Brown, M. E., et al. 2002, The Astrophysical Journal, 564, 421

Burgasser, A. J., Simcoe, R. A., Bochanski, J. J., et al. 2010, Astrophysical Journal, 725, 1405

Burrows, A., Hubbard, W. B., Lunine, J. I., & Liebert, J. 2001, Reviews of Modern Physics, 73, 719

Burrows, A., Sudarsky, D., & Hubeny, I. 2006, The Astrophysical Journal, 640, 1063

Burrows, A., Marley, M., Hubbard, W. B., et al. 1997, The Astrophysical Journal, 491, 856

Casali, M., Adamson, A., Alves de Oliveira, C., et al. 2007, Astronomy & Astrophysics, 467, 777

Casewell, S. L., Jameson, R. F., & Burleigh, M. R. 2008, Monthly Notices of the Royal Astronomical Society, 390, 1517

Chauvin, G., Lagrange, A., Dumas, C., et al. 2004, Astronomy and Astrophysics, 425, L29

Cho, J. Y., & Polvani, L. M. 1996, Physics of Fluids, 8, 1531

Clarke, F. J., Hodgkin, S. T., Oppenheimer, B. R., Robertson, J., & Haubois, X. 2008, Monthly Notices of the Royal Astronomical Society, 386, 2009

Clarke, F. J., Tinney, C. G., & Hodgkin, S. T. 2003, Monthly Notices of the Royal Astronomical Society, 341, 239

Cody, A. M., & Hillenbrand, L. A. 2014, The Astrophysical Journal, 796, 129

Conover, W. J., & Iman, R. L. 1980, Communications in Statistics - Theory and Methods, doi:10.1080/03610928008827895

Cox, A. N., ed. 2002, Allen's Astrophysical Quantities (New York, NY: Springer New York), doi:10.1007/978-1-4612-1186-0

Croll, B., Muirhead, P. S., Han, E., et al. 2016, arXiv:1609.03586

Crossfield, I. J. M. 2014, Astronomy & Astrophysics, 566, A130

Crossfield, I. J. M., Biller, B., Schlieder, J. E., et al. 2014, Nature, 505, 654

Cruz, K. L., Kirkpatrick, J. D., & Burgasser, A. J. 2009, The Astronomical Journal, 137, 3345

Cruz, K. L., Reid, I. N., Kirkpatrick, J. D., et al. 2007, The Astronomical Journal, 133, 439

Currie, T., Fukagawa, M., Thalmann, C., Matsumura, S., & Plavchan, P. 2012, The Astrophysical Journal, 755, L34

Cushing, M. C. 2014, in 50 Years of Brown Dwarfs: From Prediction to Discovery to Forefront of Research, ed. V. Joergens, Astrophysics and Space Science Library (Cham: Springer International Publishing), 113–140

Cushing, M. C., Vacca, W. D., & Rayner, J. T. 2004, Publications of the Astronomical Society of the Pacific, 116, 362

Cushing, M. C., Marley, M. S., Saumon, D., et al. 2008, The Astrophysical Journal, 678, 1372

Cushing, M. C., Kirkpatrick, J. D., Gelino, C. R., et al. 2011, Astrophysical Journal, 743, arXiv:1108.4678

Cushing, M. C., Hardegree-Ullman, K. K., Trucks, J. L., et al. 2016, The Astrophysical Journal, 823, 152

Dupuy, T. J., & Liu, M. C. 2012, The Astrophysical Journal Supplement Series, 201, 19

Enoch, M. L., Brown, M. E., & Burgasser, A. J. 2003, The Astronomical Journal, 126, 1006

Epchtein, N., De Batz, L., Caponi, L., Chevallier, E., & Copet, P. 1997, Messenger, 87

Eriksson, S. 2016, MSc thesis, Stockholm University

Esplin, T. L., Luhman, K. L., Cushing, M. C., et al. 2016, The Astrophysical Journal, 832, 58

Faherty, J. K., Burgasser, A. J., Walter, F. M., et al. 2012, The Astrophysical Journal, 752, 56

Faherty, J. K., Riedel, A. R., Cruz, K. L., et al. 2016, The Astrophysical Journal Supplement Series, 225, 1

Fazio, G. G., Hora, J. L., Allen, L. E., et al. 2004, The Astrophysical Journal Supplement Series, 154, 10

Feigelson, E. D. P. S. U., & Babu, G. J. P. S. U. 2013 (Cambridge University Press), arXiv:arXiv:1011.1669v3

Filippazzo, J. C., Rice, E. L., Faherty, J., et al. 2015, The Astrophysical Journal, 810, 158

Folkes, S. L., Pinfield, D. J., Kendall, T. R., & Jones, H. R. A. 2007, Monthly Notices of the Royal Astronomical Society, 378, 901

Foreman-Mackey, D., Hogg, D. W., Lang, D., & Goodman, J. 2013, Publications of the Astronomical Society of the Pacific, 125, 306

Freytag, B., Allard, F., Ludwig, H., Homeier, D., & Steffen, M. 2010, Astronomy and Astrophysics, 513, 19

Gagné, J., Allers, K. N., Theissen, C. A., et al. 2018a, The Astrophysical Journal, 854, L27

Gagné, J., Burgasser, A. J., Faherty, J. K., et al. 2015a, The Astrophysical Journal, 808, L20

Gagné, J., Faherty, J. K., Cruz, K., et al. 2014a, The Astrophysical Journal, 785, L14

Gagné, J., Lafrenière, D., Doyon, R., et al. 2014b, Astrophysical Journal Letters, 792, arXiv:1407.5344

Gagné, J., Lafrenière, D., Doyon, R., Malo, L., & Artigau, É. 2014c, The Astrophysical Journal, 783, 121

—. 2015b, The Astrophysical Journal, 798, 73

Gagné, J., Faherty, J. K., Cruz, K. L., et al. 2015c, The Astrophysical Journal Supplement Series, 219, 33

Gagné, J., Faherty, J. K., Burgasser, A. J., et al. 2017, The Astrophysical Journal, 841, L1

Gagné, J., Mamajek, E. E., Malo, L., et al. 2018b, The Astrophysical Journal, 856, 23

Gelino, C. R., & Marley, M. S. 2000in (Cambridge: Cambridge University Press), 1–30

Gelino, C. R., Marley, M. S., Holtzman, J. A., Ackerman, A. S., & Lodders, K. 2002, The Astrophysical Journal, 577, 433

Gillon, M., Triaud, a. H. M. J., Jehin, E., et al. 2013, Astronomy & Astrophysics, 555, L5

Girardin, F., Artigau, É., & Doyon, R. 2013, The Astrophysical Journal, 767, 61

Gizis, J. E., Allers, K. N., Liu, M. C., et al. 2015, The Astrophysical Journal, 799, 203

Gizis, J. E., Burgasser, A. J., Berger, E., et al. 2013, The Astrophysical Journal, 779, 172

Gizis, J. E., Faherty, J. K., Liu, M. C., et al. 2012, The Astronomical Journal, 144, 94

Goodman, J., & Weare, J. 2010, Communications in Applied Mathematics and Computational Science, 5

Harding, L. K., Hallinan, G., Boyle, R. P., et al. 2013, The Astrophysical Journal, 779, 101

Hayashi, C., & Nakano, T. 1963, Progress of Theoretical Physics, 30, 460

Heinze, A. N., Metchev, S., & Kellogg, K. 2015, Astrophysical Journal, 801, arXiv:1412.6733

Heinze, A. N., Metchev, S., Apai, D., et al. 2013, The Astrophysical Journal, 767, 173

Helling, C., Jardine, M., & Mokler, F. 2011, Astrophysical Journal, 737, arXiv:arXiv:1105.4409v1

Helling, C., Ackerman, A., Allard, F., et al. 2008, Monthly Notices of the Royal Astronomical Society, 391, 1854

Hiranaka, K., Cruz, K. L., Douglas, S. T., Marley, M. S., & Baldassare, V. F. 2016, The Astrophysical Journal, 830, 96

Hodgkin, S. T., Irwin, M. J., Hewett, P. C., & Warren, S. J. 2009, Monthly Notices of the Royal Astronomical Society, 394, 675

Irwin, J., Hodgkin, S., Aigrain, S., et al. 2008, Monthly Notices of the Royal Astronomical Society, 383, 1588

Irwin, M. J., Lewis, J., Hodgkin, S., et al. 2004, Optimizing Scientific Return for Astronomy through Information Technologies. Edited by Quinn, 5493, 411

Jackson, R. J., & Jeffries, R. D. 2010, Monthly Notices of the Royal Astronomical Society, 402, 1380

Joergens, V., Fernandez, M., Carpenter, J. M., & Neuhauser, R. 2003, The Astrophysical Journal, 594, 971

Kao, M. M., Hallinan, G., Pineda, J. S., et al. 2016, The Astrophysical Journal, 818, 24

Karalidi, T., Apai, D., Marley, M. S., & Buenzli, E. 2016, The Astrophysical Journal, 825, 90

Karalidi, T., Apai, D., Schneider, G., Hanson, J. R., & Pasachoff, J. M. 2015, The Astrophysical Journal, 814, 65

Kirkpatrick, J. D. 2005, Annual Review of Astronomy and Astrophysics, 43, 195

Kirkpatrick, J. D., Barman, T. S., Burgasser, A. J., et al. 2006, Astrophysical Journal, 639, 1120

Kirkpatrick, J. D., Reid, I. N., Liebert, J., et al. 1999, The Astrophysical Journal, 519, 802

—. 2000, The Astronomical Journal, 120, 447

Kirkpatrick, J. D., Cruz, K. L., Barman, T. S., et al. 2008, The Astrophysical Journal, 689, 1295

Kirkpatrick, J. D., Looper, D. L., Burgasser, A. J., et al. 2010, The Astrophysical Journal Supplement Series, 190, 100

Kirkpatrick, J. D., Gelino, C. R., Cushing, M. C., et al. 2012, Astrophysical Journal, 753, arXiv:1205.2122

Knapp, G. R., Leggett, S. K., Fan, X., et al. 2004, The Astronomical Journal, 127, 3553

Koen, C. 2003, Monthly Notices of the Royal Astronomical Society, 346, 473

Kostov, V., & Apai, D. 2013, The Astrophysical Journal, 762, 47

Kumar, S. S. 1963, The Astrophysical Journal, 137, 1121

Lafreniere, D., Doyon, R., Marois, C., et al. 2007, The Astrophysical Journal, 670, 1367

Lagrange, A.-M. 2014, Philosophical Transactions of the Royal Society A: Mathematical, Physical and Engineering Sciences, 372, 20130090

Lagrange, A.-M., Bonnefoy, M., Chauvin, G., et al. 2010, Science, 329, 57

Leconte, J. 2018, Astrophysical Journal Letters, arXiv:1801.08142

Leggett, S. K., Tremblin, P., Esplin, T. L., Luhman, K. L., & Morley, C. V. 2017, The Astrophysical Journal, 842, 118

Leggett, S. K., Cushing, M. C., Hardegree-Ullman, K. K., et al. 2016, The Astrophysical Journal, 830, 141

Lew, B. W. P., Apai, D., Zhou, Y., et al. 2016, The Astrophysical Journal, 829, L32

Liu, M. C., Dupuy, T. J., & Allers, K. N. 2016, The Astrophysical Journal, 833, 96

Liu, M. C., Magnier, E. A., Deacon, N. R., et al. 2013, The Astrophysical Journal, 777, L20

Lodders, K. 2003, The Astrophysical Journal, 591, 1220

Lodders, K., & Fegley, B. J. 1999, I.A.U. Symposium - Asymptotic Giant Branch Stars, 191, 279

Looper, D. L., Kirkpatrick, J. D., Cutri, R. M., et al. 2008, The Astrophysical Journal, 686, 528

Luhman, K. L. 2014, The Astrophysical Journal, 786, L18

Luhman, K. L., Stauffer, J. R., & Mamajek, E. E. 2005, The Astrophysical Journal Letters, 628, L69

Luhman, K. L., Patten, B. M., Marengo, M., et al. 2007, The Astrophysical Journal, 654, 570

Macintosh, B., Graham, J. R., Barman, T., et al. 2015, Science, 350, 64

MacKay, D. 2003, Journal of the American Statistical Association, 100, 365

Madhusudhan, N., Burrows, A., & Currie, T. 2011, The Astrophysical Journal, 737, 34

Malo, L., Doyon, R., Lafrenière, D., et al. 2013, The Astrophysical Journal, 762, 88

Mamajek, E. E., & Bell, C. P. M. 2014, Monthly Notices of the Royal Astronomical Society, 445, 2169

Marley, M., & Robinson, T. 2015, Annual Review of Astronomy and Astrophysics, 53, 279

Marley, M. S., Ackerman, A. S., Cuzzi, J. N., & Kitzmann, D. 2013, in Comparative Climatology of Terrestrial Planets (University of Arizona Press), 1–51

Marley, M. S., Saumon, D., Cushing, M., et al. 2012, The Astrophysical Journal, 754, 135

Marley, M. S., Saumon, D., & Goldblatt, C. 2010, The Astrophysical Journal, 723, 14

Marley, M. S., Seager, S., Saumon, D., et al. 2002, The Astrophysical Journal, 568, 335

Marocco, F., Day-Jones, A. C., Lucas, P. W., et al. 2014, Monthly Notices of the Royal Astronomical Society, 439, 372

Marois, C., Macintosh, B., Barman, T. S., et al. 2008, Science, 322, 1348

Marois, C., Zuckerman, B., Konopacky, Q. M., Macintosh, B., & Barman, T. 2010, Nature, 468, 1080

Mayor, M., & Queloz, D. 1995, Nature, 378, 355

Mayor, M., Marmier, M., Lovis, C., et al. 2011, 1

Metchev, S., Apai, D., Radigan, J., et al. 2013, Astronomische Nachrichten, 334, 40

Metchev, S. A., Heinze, A., Apai, D., et al. 2015, The Astrophysical Journal, 799, 154

Miles-Páez, P. A., Metchev, S. A., Heinze, A., & Apai, D. 2017, The Astrophysical Journal, 840, 83

Moorwood, A., Cuby, J., & Lidman, C. 1998, ESO Messenger, 53, 1

Morales-Calderon, M., Stauffer, J. R., Kirkpatrick, J. D., et al. 2006, The Astrophysicsl Journal, 43, 544

Morley, C. V., Fortney, J. J., Marley, M. S., et al. 2012, The Astrophysical Journal, 756, 172

Morley, C. V., Marley, M. S., Fortney, J. J., & Lupu, R. 2014, The Astrophysical Journal, 789, L14

Nakajima, T., Oppenheimer, B. R., Kulkarni, S. R., et al. 1995, Nature, 378, 463

Naud, M.-e., Artigau, É., Doyon, R., et al. 2017, The Astronomical Journal, 154, 129

Naud, M.-E., Artigau, É., Malo, L., et al. 2014, The Astrophysical Journal, 787, 5

Palla, F., & Baraffe, I. 2005, Astronomy & Astrophysics, 432, L57

Pedlosky, J. 1987, Geophysical Fluid Dynamics (New York, NY: Springer New York), doi:10.1007/978-1-4612-4650-3

Pineda, J. S., Hallinan, G., Kirkpatrick, J. D., et al. 2016, The Astrophysical Journal, 826, 73

Pollack, J. B., Hubickyj, O., Bodenheimer, P., et al. 1996, Icarus, 124, 62

Prato, L., Mace, G. N., Rice, E. L., et al. 2015, The Astrophysical Journal, 808, 12

Press, W., Teukolsky, S., Vetterling, W., et al. 1987, 501, arXiv:arXiv:1011.1669v3

Radigan, J. 2014, The Astrophysical Journal, 797, 120

Radigan, J., Jayawardhana, R., Lafrenière, D., et al. 2012, The Astrophysical Journal, 750, 105

Radigan, J., Lafrenière, D., Jayawardhana, R., & Artigau, E. 2014, The Astrophysical Journal, 793, 75

Rameau, J., Chauvin, G., Lagrange, A.-M., et al. 2013, The Astrophysical Journal, 779, L26

Reid, I. N., & Hawley, S. L. 2005, New Light on Dark Stars, Springer Praxis Books (Springer Berlin Heidelberg), 590, doi:10.1007/3-540-27610-6

Reiners, A., & Basri, G. 2008, The Astrophysical Journal, 684, 1390

Rhines, P. 1970, Geophysical Fluid Dynamics, 1, 273

Rhines, P. B. 1975, J. Fluid Mech., 69, 417

Rice, E. L., Barman, T., Mclean, I. S., Prato, L., & Kirkpatrick, J. D. 2010, The Astrophysical Journal Supplement Series, 186, 63

Rice, J. B., Wehlau, W. H., & Khokhlova, V. L. 1989, Astronomy and Astrophysics, 208, 179

Riedel, A. R., Blunt, S. C., Lambrides, E. L., et al. 2017, The Astronomical Journal, 153, 1

Rodriguez, D. R., Zuckerman, B., Kastner, J. H., et al. 2013, The Astrophysical Journal, 774, 101

Saumon, D., & Marley, M. 2008, The Astrophysical Journal, 689, 1327

Scargle, J. D. 1982, The Astrophysical Journal, 263, 835

Schlawin, E., Burgasser, A. J., Karalidi, T., Gizis, J. E., & Teske, J. 2017, The Astrophysical Journal, 849, 163

Schmidt, S. J., West, A. A., Hawley, S. L., & Pineda, J. S. 2010, The Astronomical Journal, 139, 1808

Schneider, A. C., Cushing, M. C., Kirkpatrick, J. D., et al. 2014, The Astronomical Journal, 147, 34

Schneider, A. C., Windsor, J., Cushing, M. C., & Kirkpatrick, J. D. 2017, The Astronomical Journal, 153, 1

Scholz, A., & Eislffel, J. 2004, Astronomy and Astrophysics, 421, 259

Scholz, A., Kostov, V., Jayawardhana, R., & Mužić, K. 2015, The Astrophysical Journal, 809, L29

Shkolnik, E. L., Allers, K. N., Kraus, A. L., Liu, M. C., & Flagg, L. 2017, The Astronomical Journal, 154, 69

Showman, A., Cho, J. Y.-K., & Menou, K. 2010, in Exoplanets, ed. S. Seager, Vol. 1 (University of Arizona Press), 471–516

Showman, A. P., & Kaspi, Y. 2013, The Astrophysical Journal, 776, 85

Sing, D. K., Fortney, J. J., Nikolov, N., et al. 2016, Nature, 529, 59

Skemer, A. J., Hinz, P. M., Esposito, S., et al. 2012, The Astrophysical Journal, 753, 14

Skrutskie, M. F., Cutri, R. M., Stiening, R., et al. 2006, The Astronomical Journal, 131, 1163

Snellen, I., Brandl, B., de Kok, R., et al. 2014, Nature, 509, 63

Ter Braak, C. J. F., & Vrugt, J. A. 2008, Statistics and Computing, 18, 435

Tinney, C. G., & Tolley, A. J. 1999, Monthly Notices of the Royal Astronomical Society, 304, 119

Torres, C. a. O., Quast, G. R., Melo, C. H. F., & Sterzik, M. F. 2008, Handbook of Star Forming Regions, II, 757

Tremblin, P., Amundsen, D. S., Chabrier, G., et al. 2016, The Astrophysical Journal, 817, L19

Tremblin, P., Amundsen, D. S., Mourier, P., et al. 2015, The Astrophysical Journal, 804, L17

Tremblin, P., Chabrier, G., Baraffe, I., et al. 2017, The Astrophysical Journal, 850, 46

Tsuji, T., Ohnaka, K., & Aoki, W. 1999, The Astrophysical Journal, 520, L119

Venot, O., Hébrard, E., Agúndez, M., et al. 2012, Astronomy & Astrophysics, 546, arXiv:1208.0560v1

Vogt, S. S., Penrod, G. D., & Hatzes, A. P. 1987, The Astrophysical Journal, 321, 496

Vos, J. M., Allers, K. N., & Biller, B. A. 2017, The Astrophysical Journal, 842, 78

Vos, J. M., Allers, K. N., Biller, B. A., et al. 2018, Monthly Notices of the Royal Astronomical Society, 474, 1041

Walkowicz, L. M., Basri, G., & Valenti, J. a. 2013, The Astrophysical Journal Supplement Series, 205, 17

Wang, J. J., Graham, J. R., Pueyo, L., et al. 2016, The Astronomical Journal, 152, 97

Wilson, P. A., Rajan, A., & Patience, J. 2014, Astronomy & Astrophysics, 566, A111

Yang, H., Apai, D., Marley, M. S., et al. 2015, The Astrophysical Journal, 798, L13

—. 2016, The Astrophysical Journal, 826, 8

York, D. G., Adelman, J., Anderson, J. E., et al. 2000, The Astronomical Journal, 120, 1579

Zapatero Osorio, M. R., Caballero, J. A., Béjar, V. J. S., & Rebolo, R. 2003, Astronomy & Astrophysics, 408, 663

Zapatero Osorio, M. R., Martin, E. L., Bouy, H., et al. 2006, The Astrophysical Journal, 647, 1405

Zhang, X., & Showman, A. P. 2014, The Astrophysical Journal, 788, L6

Zhou, Y., Apai, D., Schneider, G. H., Marley, M. S., & Showman, A. P. 2016, The Astrophysical Journal, 818, 176

Zuckerman, B., Bessell, M. S., Song, I., & Kim, S. 2006, The Astrophysical Journal, 649, L115